Contract F49620-91-C-0077

A Mechanistic Study of Microalloying Effects in NiAl

Final Report

Covering the Period 1 July 1991 through 31 March 1995

Prepared for
Air Force Office of Scientific Research
United States Air Force
Bolling Air Force Base, Washington DC 20332-6448

Prepared by
R. Darolia, R. D. Field, R. D. Noebe, A. Garg and W. S. Walston

Principal Investigator

R. Darolia

GE Aircraft Engines

Engineering Materials Technology Laboratories
Cincinnati, Ohio 45215-6301

DISCLAIMER NOTICE

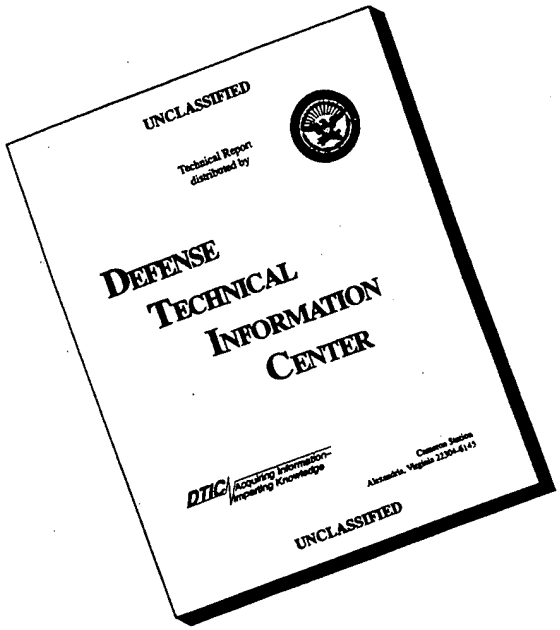

THIS DOCUMENT IS BEST QUALITY AVAILABLE. THE COPY FURNISHED TO DTIC CONTAINED A SIGNIFICANT NUMBER OF PAGES WHICH DO NOT REPRODUCE LEGIBLY.

REPORT DOCUMENTATION PAGE

Form Approved
OMB No 0704 0188

1. AGENCY USE ONLY (Leave blank)	2. REPORT DATE	3. REPORT TYPE AND DATES COVERED	
	May 31, 1995	Final	July 1, 1991 - March 31, 1995

4. TITLE AND SUBTITLE

A Mechanistic Study of Microalloying Effects in NiAl

5. FUNDING NUMBERS

61102F2306A1

6. AUTHOR(S)

R. Darolia, R. D. Field, R. D. Noebe, A. Garg and W. S. Walston

AFOSR-TR-96

0077

7. PERFORMING ORGANIZATION NAME(S) AND ADDRESS(ES)

General Electric Aircraft Engines
1 Neumann Way
Cincinnati, OH 45215-6301

9. SPONSORING / MONITORING AGENCY NAME(S) AND ADDRESS(ES)

AFOSR/NA
110 Duncan Avenue, Suite B115
Bolling AFB D. C. 20332-001

10. SPONSORING / MONITORING AGENCY REPORT NUMBER

F49620-91-C-0077

11. SUPPLEMENTARY NOTES

12a. DISTRIBUTION / AVAILABILITY STATEMENT

Approved for public release
Distribution unlimited

12b. DISTRIBUTION CODE

13. ABSTRACT (Maximum 200 words)

The objective of this study was to determine the mechanisms for ductility improvements in NiAl resulting from low level alloying additions (≤ 0.1at% of Mo, Ga, Fe, etc.) and low temperature heat treatments, and the relationship between these phenomena and embrittling effects of interstitial impurities.

The approach taken was to investigate the effect of microalloying additions on deformation behavior in single crystals. This included slip systems, critical resolved shear stresses (CRSS), and tensile ductility as a function of crystallographic orientation and temperature. TEM studies were also performed to determine dislocation structures. Investigations of point defects and their interactions with dislocations were pursued. These included resistivity measurements as well as internal friction studies. In the course of this study, serrated yielding was observed suggesting dislocation/point defect interactions. Further study of the strain aging phenomenon was carried out. as a function of composition, specimen heat treatments, test temperature and strain rates. In addition, the effect of multiple microalloying additions on ductility wasstudied on an alloy containing 0.1 at% Fe and 0.05 at% Ga. The effect of impurities on the deformation behavior of NiAl was studied by utilizing ultra-high purity single crystals. Studies were also carried out to better understand the deformation behavior in a strong NiAl alloy. (Continued on back page).

14. SUBJECT TERMS

Nickel aluminide, microalloying, ductility

15. NUMBER OF PAGES

208

16. PRICE CODE

17. SECURITY CLASSIFICATION OF REPORT	18. SECURITY CLASSIFICATION OF THIS PAGE	19. SECURITY CLASSIFICATION OF ABSTRACT	20. LIMITATION OF ABSTRACT
Unclassified	Unclassified	Unclas	

NSN 7540-01-280-5500

A considerable amount of scatter in the room temperature tensile ductility was observed throughout the course of this study. A systematic study of the cause of scatter was undertaken which included the effect of composition, especially carbon content, batch to batch variation, specimen machining, specimen surface preparation after machining and specimen alignment in the tensile test set up. Tests were also conducted at two test vendors to determine any test vendor related variability. Surface preparation techniques for the machined tensile specimens were found to play the most critical role in affecting the measured ductility.

Lastly, the effect of pre-straining was studied on a binary NiAl and a strong NiAl. An experimental plan consisting of tensile, compression and toughness tests was carried out to understand the mechanisms responsible for improvements obtained by pre-straining.

Abstract

The objective of this study was to determine the mechanisms for ductility improvements in NiAl resulting from low level alloying additions (≤ 0.1at% of Mo, Ga, Fe, etc.) and low temperature heat treatments, and the relationship between these phenomena and embrittling effects of interstitial impurities.

The approach taken was to investigate the effect of microalloying additions on deformation behavior in single crystals. This included slip systems, critical resolved shear stresses (CRSS), and tensile ductility as a function of crystallographic orientation and temperature. TEM studies were also performed to determine dislocation structures. Investigations of point defects and their interactions with dislocations were pursued. These included resistivity measurements as well as internal friction studies. In the course of this study, serrated yielding was observed suggesting dislocation/point defect interactions. Further study of the strain aging phenomenon was carried out. as a function of composition, specimen heat treatments, test temperature and strain rates. In addition, the effect of multiple microalloying additions on ductility was studied on an alloy containing 0.1 at% Fe and 0.05 at% Ga. The effect of impurities on the deformation behavior of NiAl was studied by utilizing ultra-high purity single crystals. Studies were also carried out to better understand the deformation behavior in a strong NiAl alloy.

A considerable amount of scatter in the room temperature tensile ductility was observed throughout the course of this study. A systematic study of the cause of scatter was undertaken which included the effect of composition, especially carbon content, batch to batch variation, specimen machining, specimen surface preparation after machining and specimen alignment in the tensile test set up. Tests were also conducted at two test vendors to determine any test vendor related variability. Surface preparation techniques for the machined tensile specimens were found to play the most critical role in affecting the measured ductility.

Lastly, the effect of pre-straining was studied on a binary NiAl and a strong NiAl. An experimental plan consisting of tensile, compression and toughness tests was carried out to understand the mechanisms responsible for improvements obtained by pre-straining.

Table of Contents

Abstract i
Table of Contents ii
List of Tables iv
List of Figures v
I. Introduction 1
II. Approach 3
2.1 Characterization of Microalloying Effects 3
2.2 Dislocation/Point Defect Interactions 4
2.3 Strain-Aging Effects 4
2.4 Low Temperature Heat Treatment Effects 4
2.5 Effect of Carbon 5
2.6 Effects of Multiple Microalloying Additions 5
2.7 Ultra-High Purity NiAl 7
2.8 Study of Scatter in the Room Temperature Tensile Properties 8
2.9 Pre-Strain Effects 8
III. Results and Discussion 13
3.1 Material Processing and Chemical Analysis 13
3.2 Mechanical Testing Procedure 15
3.3 Vacancy Concentration Experiments 15
3.4 Resistivity Measurements 17
3.5 Internal Friction Studies 18
3.6 Mechanical Property Tests 33
3.6.1 Mechanical Test Results from −196 to 250°C 33
3.6.2 TEM Studies and Deformation Behavior of D5, D5HT and D183 Compression Specimens 40
3.7 Serrated Yielding 57
3.7.1 Serrated Yielding Experiments with Constant Strain Rate 57
3.7.2 Serrated Yielding Experiments with Constant Cross Head Speed ... 73
3.8 Strain-Aging Effects 86
3. 9 Effect of Carbon 88
3.10 High Purity NiAl 88
3.10.1 Compression Tests 89
3.10.2 Room Temperature Tensile Tests 89
3.10.2.1 Fractography of Tensile Test Specimens 92
3.10.3 Fracture Toughness 98
3.10.3.1 Fractography of Toughness Test Specimens 98
3.10.4 Deformation Behavior 100
3.11 Effect of Specimen Surface Preparation 104
3.12 Pre-Strain Effects 119
3.12.1 Tensile Tests 119
3.12.2 Fracture Toughness Tests 122
3.13 Multiple Microalloying Additions 124
3.13.1 Multiple Microalloying Additions Fe and Ga 124
3.13.2 Multiple Microalloying Additions Hf and Ga 124
3.13.2.1 Characterization of the As-Homogenized Alloy D176 125
3.13.2.2 Temperature Dependence of the Yield Strength 125
3.13.2.3 Deformation Behavior of D176 128
3.13.2.4 Identification of Deformation Regimes 128

Table of Contents (Cont.)

3.13.2.5 Deformation Processes in Each Regime 131
3.13.2.5.1 <001> Orientation 131
3.13.2.5.2 <011> Orientation 151
3.13.2.6 Deformation Mechanisms in Alloy D176 Versus Binary NiAl 166
3.13.2.7 Correlation of Deformation Behavior with the DBTT. 169
3.13.2.8 Effect of Pre-strain on the Deformation Behavior 171
IV. Conclusions 174
V. References 177
VI. Publications 179
VII. Acknowledgments 181
Appendix A 182

List of Tables

I Strain Aging Effects Test Plan
II Pre-Strain Effects Test Plan
III Nominal Compositions of Single Crystal Alloys (Atomic and Weight %)
IV Results from Chemical Analysis of Single Crystal Castings and Tested Specimens
V Results from Resistivity Measurements
VI Resolved Shear Stress for <100>/(100) and <100>/(110) Systems
VII Resolved Shear Stress Factors Versus Mode of Applied Sound Waves
VIII Results from Initial Investigation of the Effects of Low Temperature Heat Treatments
IX Effect of Low Temperature Strain Aging Heat Treatments on Room Temperature Tensile Properties
X Fracture Toughness of <110> Oriented High Purity Specimens
XI Carbon Analysis of Representative Castings and Specimens and Room Temperature Plastic Elongations
XII Effect of Surface Finishing Step on Room Temperature Plastic Elongation in Fe-Containing NiAl Alloy
XIII Data from Pre-Straining Treatments of NiAl (D5) Compression Blocks
XIV Data from Pre-Straining Treatments of NiAl Alloy D176 Compression Blocks
XV Tensile Elongation Data for Pre-strained D5 Specimens
XVI Tensile Elongation Data for Pre-strained D176 Specimens
XVII Fracture Toughness of Pre-strained D5 Specimens
XVIII Fracture Toughness of Pre-strained D176 Specimens

List of Figures

Figure 1. The composition dependence of (a) ductility and (b) 0.2% yield strength of NiAl single crystals tested in tension along <110> direction at room temperature.

Figure 2. Drawing of compression blocks used in pre-straining studies. The block is compressed along one of the crystallographically oriented long directions and test specimens may be taken either parallel or perpendicular to the pre-strain axis.

Figure 3. Drawing of the constraining fixture used to prevent specimen buckling during compression pre-straining of the blocks shown in Figure 2.

Figure 4. Calculated vacancy concentration as a function of heat treatment for stoichiometric NiAl (D5) as determined by density and lattice parameter measurements.

Figure 5. Density as a function of heat treatment for stoichiometric NiAl and D182 (50.0Ni-49.75Al-0.25Fe in atomic %). Changes in density with heat treatment are believed to be caused by changes in vacancy concentration.

Figure 6. Geometry and crystallographic orientation of specimens used in internal friction experiments.

Figure 7. Stress (σ) and attenuation (α) data for three successive compressive loadings of a stoichiometric NiAl specimen which received an 800°C heat treatment (D5HT). The compression axis was [110] and the attenuation was measured using a 70MHz longitudinal [1$\bar{1}$0] ultrasonic wave.

Figure 8. Plot of stress (σ), attenuation (α), and modulus defect (ϕ) as a function of time for a compressive loading experiment of a stoichiometric NiAl specimen. The compression axis was [110]. The attenuation and modulus defect data were measured using a 10MHz longitudinal [1$\bar{1}$0] ultrasonic wave. Attenuation was also measured using a 70MHz [100] longitudinal wave (data not shown).

Figure 9. Plots of dislocation density (Λ) and dislocation segment length (L) as a function of time, calculated from the data shown in Figure 8. The segment length is given in terms of $\sqrt{\omega\tau}$, which is proportional to L, where ω is the ultrasonic frequency and τ is the relaxation time for dislocation motion.

Figure 10. Velocity (ϕ) and stress change (open circles in $Kg/cm^{2)}$ with time (in seconds) for D183 at 10 MHz for a shear <100> wave polarized along <110>.

Figure 11. Attenuation ($\Delta\alpha_2$) with time (in seconds) for D183 at 10 MHz for a shear <100> wave polarized along <110>.

Figure 12. Attenuation ($\Delta\alpha_2$) and stress change (open circles in $Kg/cm^{2)}$ with time (in seconds) for D183 at 30 MHz for a shear <100> wave polarized along <110>.

Figure 13. Flow stress (given in terms of critical resolved shear stress (CRSS) on the {110} and {100} planes) as a function of temperature taken from compression and tensile tests for stoichiometric NiAl given the standard heat treatment (D5). CRSS values for the {110} plane were derived from specimens strained along the <111> direction. CRSS values for the {100} plane were derived from specimens strained along the <110> direction.

Figure 14. Flow stress (given in terms of critical resolved shear stress (CRSS) on the {110} and {100} planes) as a function of temperature taken from compression and tensile tests for stoichiometric NiAl given an 800°C anneal (D5HT). CRSS values for the {110} plane were derived from specimens strained along the <111> direction. CRSS values for the {100} plane were derived from specimens strained along the <110> direction.

Figure 15. Flow stress (given in terms of critical resolved shear stress (CRSS) on the {110} and {100} planes) as a function of temperature taken from compression and tensile tests for NiAl microalloyed with Fe (D183). CRSS values for the {110} plane were derived from specimens strained along the <111> direction. CRSS values for the {100} plane were derived from specimens strained along the <110> direction.

Figure 16. Flow stress (given in terms of critical resolved shear stress (CRSS) on the {110} and {100} planes) as a function of temperature taken from compression and tensile tests NiAl microalloyed with Ga (D128). CRSS values for the {110} plane were derived from specimens strained along the <111> direction. CRSS values for the {100} plane were derived from specimens strained along the <110> direction.

Figure 17. 0.2% yield stress as a function of temperature for <110> oriented tensile specimens.

Figure 18. Plastic elongation as a function of temperature for <110> oriented tensile specimens.

Figure 19. Low magnification TEM image taken from compression specimens of stoichiometric NiAl given the standard heat treatment (D5), tested at -196°C. Stress axis: a) [111], b) [101].

Figure 20. Low magnification TEM image taken from compression specimens of stoichiometric NiAl given the standard heat treatment (D5), tested at 100°C. Stress axis: a) [111], b) [101].

Figure 21. Low magnification TEM image taken from compression specimens of stoichiometric NiAl given an 800°C anneal (D5HT), tested at -196°C. Stress axis: a) [111], b) [101].

Figure 22. Low magnification TEM image taken from compression specimens of stoichiometric NiAl given an 800°C anneal (D5HT), tested at 100°C. Stress axis: a) [111], b) [101].

Figure 23. Low magnification TEM image taken from compression specimens of NiAl microalloyed with Fe (D183), tested at -196°C. Stress axis: a) [111], b) [101].

Figure 24. Low magnification TEM image taken from compression specimens of NiAl microalloyed with Fe (D183), tested at 100°C. Stress axis: a) [111], b) [101].

Figure 25. Weak beam TEM micrograph taken from a [111] oriented D183 compression specimen tested to ~2% plastic strain at –196°C. The dislocations in this slip band have [001] Burgers vectors. Trace analyses were performed on the bowed dislocation, labeled "1", and on the elongated loops, labeled "2" and "3".

Figure 26. Weak beam TEM micrograph taken from a [101] oriented D183 compression specimen tested to ~2% plastic strain at –196°C. Trace analyses were performed on the elongated loop, labeled "1", and bowed dislocation, labeled "2". Both have [001] Burgers vectors. Note the jagged nature of the dislocation line.

Figure 27. Weak beam TEM micrograph taken from a [101] oriented D183 compression specimen tested to ~2% plastic strain at –196°C. Same area as shown in Figure 26, but with a different beam direction. Trace analyses were performed on the elongated loop, labeled "1", and bowed dislocation, labeled "2". Both have [001] Burgers vectors. Note the smoothness of the dislocation as viewed from this orientation, compared to the image in Figure 26.

Figure 28. Weak beam TEM micrograph taken from a [111] oriented D5 specimen tested to ~2% plastic strain at 100°C. Trace analyses were performed on the two curved dislocations labeled "1" (b=[001]) and the elongated loop labeled "2" (b=[010]).

Figure 29. Bright field TEM micrograph taken from a [101] oriented D5HT compression specimen tested to ~2% plastic strain at 100°C. Trace analyses were performed on the dislocations labeled "1" and "2". Both have [100] Burgers vectors.

Figure 30. Weak beam TEM micrograph taken from a [101] oriented D5HT compression specimen tested to ~2% plastic strain at 100°C. Higher magnification micrograph showing details of the b=[100] dislocation labeled "2" in Figure 29. Note that this image is rotated approximately 135° clockwise with respect to the image in Figure 29.

Figure 31. Weak beam TEM micrographs taken from a [101] oriented D183 compression specimen tested to ~2% plastic strain at 100°C. Trace analyses were performed on the bowed dislocation, labeled "1" , and the straight dislocation, labeled "2". Both have [001] Burgers vectors. The dislocation labeled "1" moved during the analysis. Micrographs a) and b) were taken before and after the dislocation moved, respectively.

Figure 32. Weak beam TEM micrograph showing an example of a faceted void observed in all of the D5HT specimens. The micrograph was taken from a [101] oriented D5HT compression specimen tested to ~2% plastic strain at 100°C.

Figure 33. Stress-strain curves showing serrated yielding in -125°C compression tests. a) D5, b) D183.

Figure 34. Stress-strain curves showing serrated yielding in 100°C compression tests. a) D5, b) D183.

Figure 35. Stress-strain curve for a 200°C compression test of stoichiometric NiAl (D5-1738) conducted at a strain rate of $8.3x10^{-5}$/s. The test was changed from strain to stroke control at approximately 1% plastic strain.

Figure 36. Stress-strain curve for a 400°C compression test of stoichiometric NiAl (D5-1738) conducted at a strain rate of $8.3x10^{-5}$/s in stroke control.

Figure 37. Stress-strain curve for a 200°C compression test of stoichiometric NiAl (D5-1738) conducted in strain control. The strain rate was increased from $1x10^{-5}$ to $1x10^{-3}$/s at approximately 1% plastic strain.

Figure 38. Stress-strain curve for a 200°C compression test of stoichiometric NiAl (D5-2154) conducted at a strain rate of $8.3x10^{-5}$/s with a loop gain of 20.

Figure 39. Stress-strain curve for a 200°C compression test of stoichiometric NiAl (D5-2154) conducted at a strain rate of $8.3x10^{-5}$/s with a loop gain of 30. Note the difference in the nature of the serrations as compared to Figure 38.

Figure 40. Stress-strain curve for a room temperature compression test of stoichiometric NiAl (D5-2154) conducted at a strain rate of $8.3x10^{-5}$/s with a loop gain of 20.

Figure 41. Stress-strain curve for a room temperature compression test of stoichiometric NiAl (D5-2154) conducted at a strain rate of $8.3x10^{-5}$/s with a loop gain of 30. Note the difference in the nature of the serrations as compared to Figure 40.

Figure 42. Stress-strain curve for a room temperature compression test of stoichiometric NiAl (D5-2154). The strain rate was increased from $1x10^{-5}$ to $1x10^{-3}$/s at approximately 1% plastic strain.

Figure 43. Stress-strain curve for a 200°C compression test of stoichiometric NiAl (D5-2154). The strain rate was increased from of $1x10^{-5}$ to $1x10^{-3}$/s at approximately 1% plastic strain.

Figure 44. Stress-strain curve for a room temperature compression test of stoichiometric NiAl given an 800°C heat treatment (D5-2154HT). The strain rate was increased from $1x10^{-5}$ to $1x10^{-3}$/s at approximately 1% plastic strain.

Figure 45. Stress-strain curve for a 200°C compression test of stoichiometric NiAl given an 800°C heat treatment (D5-2154HT). The strain rate was increased from $1x10^{-5}$ to $1x10^{-3}$/s at approximately 1% plastic strain.

Figure 46. Stress-strain curve for a room temperature compression test of a 0.1 at% Fe-containing NiAl alloy (D183-1675). The strain rate was increased from $1x10^{-5}$ to $1x10^{-3}$/s at approximately 1% plastic strain.

Figure 47. Load-displacement curve for a room temperature compression test of stoichiometric NiAl (D5-1738A) at a strain rate of $8.3x10^{-5}$/s.

Figure 48. Load-displacement curve for a room temperature compression test of 0.1 at% Fe-containing NiAl alloy (D183-1675A) at a strain rate of $8.3x10^{-5}$/s.

Figure 49. Load-displacement curve for a room temperature compression test of high purity NiAl (Oliver 2-1) at a strain rate of $8.3x10^{-5}$/s.

Figure 50. Load-displacement curve for a 400°C compression test of stoichiometric NiAl (D5-1738B) at a strain rate of $8.3x10^{-5}$/s.

Figure 51. Load-displacement curve for a 400°C compression test of 0.1 at% Fe-containing NiAl alloy (D183-1675B) at a strain rate of $8.3x10^{-5}$/s.

Figure 52. Load-displacement curve for a 400°C compression test of high purity NiAl (Oliver 2-2) at a strain rate of $8.3x10^{-5}$/s.

Figure 53. Load-displacement curve for a 500°C compression test of stoichiometric NiAl (D5-1738C) at a strain rate of $8.3x10^{-5}$/s.

Figure 54. Load-displacement curve for a 500°C compression test of 0.1 at% Fe-containing NiAl alloy (D183-1675D) at a strain rate of $8.3x10^{-5}$/s.

Figure 55. Load-displacement curve for a 500°C compression test of high purity NiAl (Oliver 2-3) at a strain rate of $8.3x10^{-5}$/s.

Figure 56. Load-displacement curve for a 600°C compression test of stoichiometric NiAl (D5-1738D) at a strain rate of $8.3x10^{-5}$/s.

Figure 57. Load-displacement curve for a 600°C compression test of 0.1 at% Fe-containing NiAl alloy (D183-1675E) at a strain rate of $8.3x10^{-5}$/s.

Figure 58. Load-displacement curve for a 600°C compression test of high purity NiAl (Oliver 2-4) at a strain rate of $8.3x10^{-5}$/s.

Figure 59. Load-strain curve for a room temperature tensile test of high purity NiAl (Oliver 2-1) at a strain rate of $8.3x10^{-5}$/s showing 12.85% plastic elongation.

Figure 60. Load-strain curve for a room temperature tensile test of high purity NiAl (Oliver 2-2) at a strain rate of $8.3x10^{-5}$/s showing only 1.14% plastic elongation.

Figure 61. Scanning electron micrographs of high purity NiAl (Oliver 1-1) showing slip bands or scratches at the fracture origin of low ductility specimens. a) shows fracture origin, b) shows slip bands or scratches at the surface near the fracture origin, c) higher magnification of the slip bands or scratches.

Figure 62. Scanning electron micrographs of high purity NiAl (Oliver 1-2) showing slip bands or scratches at the fracture origin of low ductility specimens. a) shows fracture origin, b) shows slip bands or scratches at the surface, c) higher magnification of the slip bands or scratches, d) still higher magnification of the slip bands or scratches.

Figure 63. Scanning electron micrographs of high purity NiAl (Oliver 1-3) showing what appears to be slip bands at the fracture origin of low ductility specimens. These slip bands were indexed to establish {100} and {110} slip planes.

Figure 64. Fracture toughness of high purity NiAl as a function of temperature compared with conventional purity NiAl.

Figure 65. Bright-field images close to the [011] zone axis, showing the deformed microstructures in a) Oliver 2-2 ($\varepsilon_f = 2.1\%$), b) Oliver 2-1 ($\varepsilon_f = 12.9\%$).

Figure 66. Dislocation contrast analysis showing a) strong visibility of dislocations with **g**01-1, b) invisibility with **g**100, c) weak residual contrast with **g**10-1, and d) strong visibility of dislocations with **g**-110. Dislocations marked "A" and "B" act as reference points.

Figure 67. Optical micrographs showing surface of D183-2448-5 specimen (8.2% plastic elongation) after electropolishing. Note a complete absence of grinding marks.

Figure 68. Optical micrograph showing surface of an as-ground specimen (D183-2449-10).

Figure 69. Optical micrograph showing surface of D183-2449-3 specimen (1.6% plastic elongation) after electropolishing.

Figure 70. Optical micrographs showing surface of D183-2448-4 specimen (5.4% plastic elongation) after electropolishing. Remnants of the grinding marks are still visible.

Figure 71. Optical micrographs showing surface of D183-2448-6 specimen (7.2% plastic elongation) after electropolishing. Remnants of the grinding marks are still visible.

Figure 72. Load-displacement curve for a room temperature tensile test of D183-2448-5 at a strain rate of $8.3x10^{-5}/s$.

Figure 73. Optical micrographs showing surfaces of chem milled specimens. a) D183-2448-3, b) D183-2170X-2.

Figure 74. Load-displacement curve for a room temperature tensile test of D183-2448-3 at a strain rate of $8.3x10^{-5}/s$.

Figure 75. Load-strain curve for a room temperature tensile test of D183-2448-7 at a strain rate of $8.3x10^{-5}/s$.

Figure 76. Load-strain curve for a room temperature tensile test of D183-2448-8 at a strain rate of $8.3x10^{-5}/s$.

Figure 77. Load-strain curve for a room temperature tensile test of D183-2448-9 at a strain rate of $8.3x10^{-5}/s$.

Figure 78. Plastic elongation vs. temperature curves for pre-strained and non-pre-strained D176.

Figure 79. As-homogenized NiAl alloy D176(1695) showing the extremely high density of G-phase cuboidal precipitates in the alloy and some G-phase platelets on the edge-on {110} planes. Arrows indicate <100> dislocations.

Figure 80. Yield strength of NiAl alloy D176 and binary NiAl (alloy D5) as a function of temperature for both the <001> and <011> orientations.

Figure 81. Arrhenius representation of the compression yield strength of <001> oriented NiAl alloy D176 showing three distinct deformation regimes. Solid symbols represent samples examined by TEM.

Figure 82. Arrhenius representation of the compression yield strength of <011> oriented NiAl alloy D176 showing two distinct deformation regimes with a gradual transition from region I to region II. Solid symbols represent samples examined by TEM.

Figure 83. Dislocation structure and g•b analysis for NiAl alloy D176 deformed along [001] at room temperature. a) general area of analysis, b) g110, c) g01I close to the Z.A. [011], d) g10I, e) g110, and f) g011 close to the Z.A. [01I].

Figure 84. (a) Typical dislocation structure for [001] oriented D176 deformed at 500 K to 1.4% plastic strain. The dislocation g · b analysis is shown in: b) WBDF 4g110, c) g1I0, and d) g10I.

Figure 85. The wavy appearance of the dislocations observed at 500 K. a) bright field image of a region with low dislocation density, and b) WBDF image that associates the waviness with both a cross-slip phenomenon (e.g. at "X") and pinning of the dislocation segments by the G-phase precipitates (e.g. at "Y").

Figure 86. (a) Duplex <111> slip observed in a [001] oriented D176 sample deformed at 600 K to 1.5% plastic strain. Dislocation g•b analysis of the area shown in (a) with: b) WBDF 4g110 (A : Visible, B : Inv.), c) g1I0 (A : Inv., B : Visible), and d) g011 (A : Visible, B : Weak Contrast). R denotes the reference point in each micrograph.

Figure 87. Typical dislocation microstructure in [001] D176 deformed to 2.1% plastic strain at 800 K. a) overall dislocation structure indicating slip on two primary systems, b) a region between slip bands where the dislocation density is low, and c) WBDF micrograph of intersecting slip bands showing the morphology of individual dislocations and loops (arrows).

Figure 88. a) Higher magnification image of the thin band marked with an arrow in Fig. 87(b), and (b-f) dislocation g•b analysis of the area in (a) with: b) g100, c) g01I, d) g020, e) gI10, and f) g110.

Figure 89. Typical dislocation structure for [001] D176 deformed at 1300 K to 2.0% plastic strain. a) general area of analysis, and (b-f) corresponding dislocation g•b analysis of the area with: b) g010, c) g100, d) g110, e) gI10, and f) g011.

Figure 90. Dislocation structure in [011] D176 samples deformed in Region I. a) deformed at room temperature to 0.3% plastic strain and b) deformed at 400 K to 1.3% plastic strain.

Figure 91. Dislocation g•b analysis of the [011] D176 sample tested at room temperature with: a) Z.A. [111], b) g100, c) g10I, d) g101, e) g01I, and f) g020. Arrows in (a) show the dislocation loops.

Figure 92. Dislocation structure in [011] D176 sample deformed at a) 1000 K and b) 1144 K. Both samples were deformed to approximately 2% plastic strain toward the end of region I.

Figure 93. Dislocation g•b analysis for the [011] D176 sample tested at 1000 K with: a) g200, b) g01I, c) g020, d) g002, e) gI01. (f) shows the view of the (010) slip plane and arrow in (b, f) shows the formation of a dislocation loop by cross-slip of a screw dislocation.

Figure 94. Dislocation structure of [011] D176 deformed at 1255 K to approximately 2% strain. a) BF micrograph showing the overall low dislocation density retained at this temperature and b) WBDF micrograph showing edge dislocations bypassing G-phase particles by Orowan looping.

Figure 95. Typical dislocation structure and (b-f) g.b analysis with: b) g1I0, c) g020, d) g10I, e) g100, and f) g01I for the [011] D176 sample deformed at 1300 K to 2% strain. Unmarked arrows in (b, d) denote dislocations of type "B" and "A", respectively.

Figure 96. Correspondence of the tensile DBTT with the onset of region III deformation behavior for [001] oriented NiAl alloy D176.

Figure 97. Observation of two distinct deformation regimes in binary NiAl and the correspondence of the tensile DBTT with the onset of region III deformation behavior for <001> oriented binary NiAl. Note that binary <001> NiAl does not exhibit a region II behavior as does alloy D176.

Figure 98. Correspondence of the tensile DBTT with the onset of region II deformation behavior for <011> oriented NiAl alloy D176.

I. Introduction

The need for high temperature, low density materials for applications in aircraft engines has led to extensive development activities in intermetallic compounds such as NiAl. One of the potential applications of NiAl is as a high and low pressure turbine blade and vane material. Low density (~2/3 that of a typical Ni base superalloy) NiAl turbine blades can reduce the turbine rotor weight (blades and disk) by as much as 40%. A major portion of this reduction in weight comes from reduction in the weight of the rotating disk due to reduced blade weight and centrifugal stresses. NiAl also has a thermal conductivity approximately 5 to 8 times that of a typical superalloy. Because of the higher conductivity, the temperature distribution in a turbine blade is much more uniform and the life-limiting "hot spot" temperature is reduced by as much as 50°C. Also, the oxidation resistance of NiAl is well proven, having served as the major component of the protective 'aluminide' coating on virtually all high pressure turbine blades and vanes of aircraft engines.

A major limitation to the application of NiAl based alloys in turbine engines is low room temperature ductility. For single crystal NiAl, no RT plastic elongation is seen in <100> oriented tensile specimens, whereas for <110> and <111> oriented NiAl (so called "soft" orientations), plastic elongation up to 2% can be obtained [1]. The plastic behavior is highly sensitive to composition and impurity content. The stoichiometric dependence of strength and ductility has been explained in terms of vacancies and anti-site defects within the structure [2]; however, the effects of impurities are not well understood.

Extensive alloying studies conducted at GEAE have shown beneficial effects of microalloying on the room temperature tensile ductility of "soft" oriented NiAl single crystals [3]. In room temperature tensile tests, up to 6% plastic elongation to failure has been obtained in <110> oriented NiAl alloys containing 0.1 and 0.25 at% Fe (Figure 1). Very significant improvements in ductility have also been made by alloying with Ga or Mo as shown in Figure 1. In the case of a 0.1at% Ga addition, 4.5% plastic elongation in room temperature tensile tests can be obtained in <110> oriented specimens. For the Fe additions, the ductility improvements are accompanied by a reduction in yield strength. While ductility enhancements are obtained at microalloying levels, the beneficial effects are either reduced or disappear at higher levels.

Intermediate temperature heat treatments have also been found to increase RT ductility in NiAl. This was first observed in polycrystalline specimens [4], and work at GEAE has confirmed a ductility enhancement in "soft" oriented single crystal specimens. The increased ductility is accompanied by a decrease in yield strength.

The objective of this study was to determine the mechanisms for ductility improvements in NiAl resulting from low level alloying additions. The approach taken was to investigate the effect of microalloying additions on deformation behavior in single crystals. This included slip systems, critical resolved shear stresses (CRSS) and tensile ductility as a function of crystallographic orientation and temperature. In the course of this study, serrated yielding was observed suggesting dislocation/point defect interactions. Further study of the strain aging phenomenon was carried out as a function of composition, specimen heat treatments, test temperature and strain

rates. Internal friction measurements were carried out to define dislocation/point defect interactions. In addition, the effect of multiple microalloying additions on ductility was studied on an alloy containing 0.1 at% Fe and 0.05 at% Ga. The effect of impurities was studied by growing ultra-high purity single crystals at the University of Tennessee.

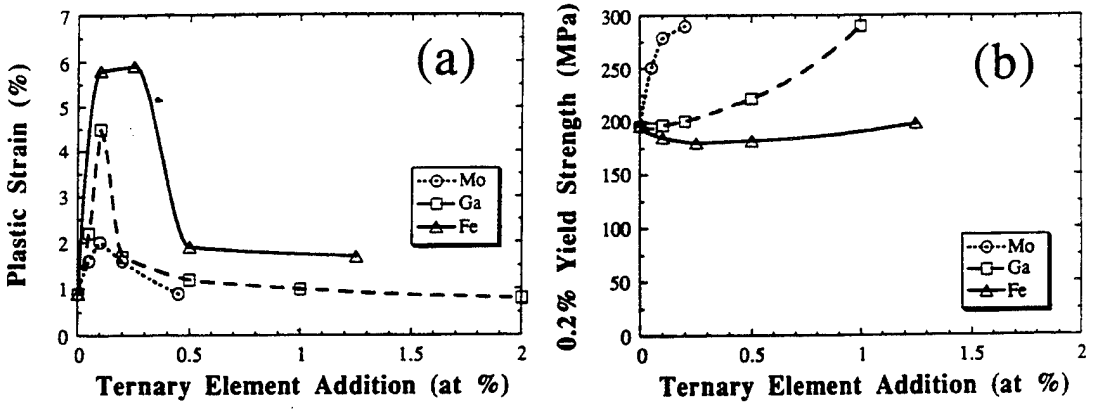

Figure 1. The composition dependence of (a) ductility and (b) 0.2% yield strength of NiAl single crystals tested in tension along <110> direction at room temperature.

A considerable amount of scatter in the room temperature tensile ductility was observed throughout the course of this study. A systematic study of the cause of scatter was undertaken which included the effect of composition, especially carbon content, batch to batch variation, specimen machining, specimen surface preparation and alignment in the tensile test set up. Tests were also conducted at two test vendors to determine any test vendor related variability.

Compared to other intermetallics, binary NiAl has a relatively low DBTT of 200°C for the <110> orientation and 400°C for the <001> orientation. Several investigators have studied the DBTT behavior in binary NiAl, however the mechanisms for the change in deformation behavior from brittle to ductile are not well understood. While Fe additions decrease DBTT, the majority of alloying additions increase DBTT. Also, as the level of alloying addition increases, the DBTT tends to increase. For example, in "strong" NiAl alloys such as D176 containing 0.5 at.% Hf and 0.05 at% Ga, even with these minor additions, the DBTT can increase beyond 800°C for the <110> orientation. Of significant interest is the shift in orientation dependence of the DBTT. In binary NiAl, the <110> has a DBTT about 200°C lower than the <001> orientation, however in strong NiAl alloys, this behavior is reversed. No studies have been previously performed on the DBTT behavior in strong NiAl alloys. Studies were carried out to understand the deformation behavior and mechanisms responsible for the orientation dependence anomaly of the DBTT in alloy D176.

Lastly, the effect of pre-straining was studied on a binary NiAl and a strong NiAl (alloy D176). Room temperature tensile fracture strength, tensile ductility, toughness and DBTT of NiAl have been found previously to be improved by high temperature pre-straining. An experimental plan consisting of tensile, compression and toughness tests was carried out in an attempt to differentiate between various possible mechanisms.

II. Approach

The objective of this study was to determine the mechanisms for ductility improvements in NiAl resulting from low level alloying additions (≤ 0.1 at%) and low temperature heat treatments, and the relationship between these phenomena and embrittling effects of interstitial impurities. The effects of alloying additions and heat treatments on ductility, active slip systems and yield stress as a function of temperature were characterized and dislocation/point defect interactions investigated. In addition, the ductile to brittle transition phenomenon was studied, which included the effect of high temperature pre-straining. In the course of this study, serrated yielding was observed suggesting dislocation/point defect interactions. Further study of the strain aging phenomenon was carried out as a function of composition, specimen heat treatments, test temperature and strain rates. A considerable amount of scatter in the room temperature tensile ductility was observed throughout the course of this study. A systematic study of the cause of scatter was undertaken which included effect of composition especially carbon content, batch to batch variation, specimen machining, specimen surface preparation after machining and specimen alignment in the test set up. Tests were also conducted at two test vendors to determine any vendor related variability. The program objective was accomplished by carrying out the following tasks:

2.1 Characterization of Microalloying Effects

Several alloying elements increase the room temperature ductility of NiAl in "soft" (non-<100>) orientations [3]. These elements include Mo, Ga, and Fe. The effect occurs at very low levels (≤ 0.1%). This increase in ductility is often accompanied by a reduction in yield stress. Low temperature heat treatments have also been found to increase room temperature ductility and reduce yield stress in stoichiometric NiAl. In the current investigation, the effects of two representative alloying elements, Fe and Ga, and a low temperature heat treatment were studied in detail to determine the mechanisms for this effect. Four different alloy/heat treatment combinations: 1) standard heat treated stoichiometric NiAl, 2) stoichiometric NiAl with a intermediate temperature (800°C) heat treatment, 3) NiAl with 0.1 at% Fe addition, 4) NiAl with 0.05 at% Ga addition were initially studied. Later on, high purity NiAl was added to the investigation. In addition, the effect of multiple microalloying additions on ductility was studied on an alloy containing 0.1 at% Fe and 0.05 at% Ga. A 'strong' alloy containing 0.5 at% Hf and 0.05 at% Ga was also studied. The first objective of this study was to characterize the effects of microalloying additions and low temperature heat treatments on mechanical properties. Initially, tension and/or compression testing were performed in the temperature range from -196 to 250°C to determine RT ductility and ductile to brittle transition temperature (DBTT) behavior. These tests provided information on the thermal activation of slip. Compression tests were performed in both <110> and <111> oriented specimens in order to determine the relative values of critical resolved shear stress (CRSS) for {110} versus {100} slip, which would be expected to affect cross slip behavior. Transmission electron microscopy (TEM) dislocation analysis was performed to determine the nature of slip in deformed specimens. Later on higher temperature tests to 600°C were added to investigate the strain aging effects.

2.2 Dislocation/Point Defect Interactions

A major emphasis of the study was the effect of point defects on deformation. The alloying elements may affect the deformation behavior of NiAl directly, or by the gettering or trapping of interstitials. Resistivity measurements and vacancy concentration determinations were performed as a preliminary indication of point defect concentrations in the alloys. Attempts were also made to study dislocation/point defect interactions using internal friction techniques by Professor A. Granato of the University of Illinois Physics Department. Of particular interest is the presence of "dislocation amplified" Snoek peaks, resulting from elastic interactions between dislocations and point defects. Most of the effort of the program concentrated on the development of experimental techniques to simultaneously measure wave velocity (related to elastic constants) and internal friction losses in multiple orientations during straining. In this manner, dislocation dynamics can be studied on different slip systems during deformation. Specifically, dislocation pinning effects could be investigated and related to point defect interactions.

2.3 Strain-Aging Effects

During the first year study, serrated yielding effects were observed as a function of temperature and alloy/heat treatment in compression tests. The observation of serrated yielding suggested that a strain aging effect might be active in NiAl and its alloys at relatively low temperatures. These effects were investigated further. Tests were carried out to verify this effect and further characterize the phenomenon using compression specimens. The test plan shown in Table I included an investigation of binary NiAl behavior at higher temperatures under the same testing conditions (strain rate, experimental set-up) to determine if there is a high temperature limit for this behavior, as expected for strain-aging effects. In addition, an investigation of the effect of strain rate on the serrated yielding behavior (the presence and intensity of serrated yielding) was carried out for standard heat treated NiAl (D5), NiAl given an 800°C ductilization anneal (D5HT), and the NiAl 0.1 at% Fe alloy (D183). Tests were also carried out with the high purity NiAl single crystals to determine whether the strain aging behavior is absent in the high purity single crystals due to low impurity content.

2.4 Low Temperature Heat Treatment Effects

The effect of low temperature heat treatments on the yield stress and ductility of NiAl and an Fe microalloyed alloy was also studied in response to the results on heat treatment effects on toughness for single crystal alloys [5-7], in which exposures in the range of 200-400°C (around the DBTT for NiAl) were observed to dramatically affect toughness values. Low temperature anneals have also been observed to affect tensile properties of polycrystalline NiAl [8]. In both cases, the observed behavior has been interpreted in terms of strain-aging effects. In the current investigation, room temperature tensile testing was carried out for both binary NiAl and the Fe-containing alloy in three conditions: 1) standard age (furnace cooled from a 1316°C/50hr. anneal), 2) a subsequent 1316°C anneal followed by air cooling, and 3) the above followed by a 400°C/2 hr. heat treatment. The heat treatment for condition 2 is expected to un-pin the dislocations with respect to any impurities. The 400°C anneal is expected to re-pin the dislocations. If this is occurring, both the yield strength and the ductility should be affected.

Table I. Strain Aging Effects Test Plan

1) Effect of 400°C HT on Ductility and Yield Strength
Purpose: Determine effect of low temperature HT on yield behavior
Alloys: NiAl, NiAl + 0.1 at% Fe
Heat Treatments: standard HT, 400°C/12 hrs., 400°C/12 hrs. + 200°C/2 hrs.
Orientation: <110>
Test: 2 RT tensile tests per alloy/condition

2) High Temperature Limit for Serrated Yielding
Purpose: Determine temperature dependence of serrated yielding effects
Alloy: NiAl
Heat Treatment: standard HT
Orientation: <110>
Test: compression tests at 8x10-5/s (5 tests). Start at 200°C and increase temperature incrementally to determine upper T limit

3) Strain Rate Effect
Purpose: Determine effect of strain rate sensitivity of serrated yielding and flow stress
Alloys/Heat Treatment: NiAl standard HT, NiAl/800°C, NiAl + 0.1 at% Fe
Orientation: <110>
Test: compression tests at -125°C, 200°C. 3 strain rates: 10^{-5}, 10^{-3}, 10^{-1} (2 strain rates/test)

2.5 Effect of Carbon

Based on the observation of dynamic and static strain aging, it was postulated that interstitial impurities may be controlling dislocation movement and thereby affecting ductility. Initially, common impurities such as oxygen, nitrogen, carbon and sulfur were analyzed for many representative castings. It was observed that oxygen, nitrogen and sulfur contents were essentially the same in all the castings whereas carbon level varied from casting to casting. Therefore, carbon was analyzed for many additional castings and representative tensile specimens at one chemical laboratory to eliminate analysis errors originating from various laboratories. Leco Corporation was selected because they manufacture the majority of equipment for carbon determination, and they yielded the best results in a round robin study previously conducted at GEAE. Room temperature plastic elongation data were correlated with the carbon content of the specimens.

2.6 Effects of Multiple Microalloying Additions

a) Ga and Fe combination in NiAl

Alloying development efforts conducted at GEAE in the past have revealed that combinations of microalloying additions can lead to higher ductilities than for individual additions. This suggests the possibility of synergistic effects between alloying elements. It was subsequently

discovered that Fe microadditions surpassed all other elements, either individually or in combinations, with regards to ductilizing NiAl [3]. In the second and third year of this program, a combination of the two most potent microalloying additions, Ga and Fe, was evaluated. The alloy composition chosen for this study was Ni-49.85Al-0.1Fe-0.05Ga (in at%). The plan called for tensile testing of <110> oriented specimens at room temperature and near the DBTT. Thus, the effect of these simultaneous microalloying additions tensile ductility was determined.

b) Ga and Hf combination in NiAl

In addition to improvements in ductility in ternary alloys, microalloying additions have been found to improve rupture strength in alloys containing Heusler phase forming strengthening elements such as Hf [9-10]. These effects are likely to be related. The strengthening effect is extremely important technologically, since the high temperature strength of binary NiAl must be improved significantly in order for this class of materials to be exploited in the high temperature, high stress applications of aircraft engines. Therefore, a set of experiments were carried out to determine the role of microalloying elements in quaternary alloys containing Hf additions. For this study alloy, a Hf containing alloy D176 was chosen. In this alloy, a 0.5 at% addition of Hf significantly improves the high temperature tensile and rupture properties. Also, 0.05 at% Ga was added to this alloy to improve the room temperature tensile properties based on the known beneficial effect of Ga in NiAl.

The objective of this task was to identify the operative deformation mechanisms in single crystal alloy D176 as a function of crystallographic orientation (hard : <001> and soft : <011>) and temperature. The aim of such an endeavor was to develop a complete description of the deformation behavior of alloy D176 including the temperature range over which each distinct deformation regime exists and to determine in detail the operative deformation mechanisms within each regime for both hard and soft single crystal orientations. Once this detailed description of the deformation behavior of high-strength single crystal NiAl has been developed, it will then be possible to identify the processes responsible for the brittle-to-ductile transition in this material and to explain the effect of pre-strain on mechanical properties.

While numerous investigators have characterized the dislocation structure in binary single crystal NiAl at particular temperatures, no single systematic study has been performed to quantify the temperature range over which various deformation processes occur and to correlate these mechanisms with specific behaviors such as the brittle to ductile transition temperature (DBTT). However, a review of the literature [11] indicates that two distinct types of slip behavior are observed for binary NiAl single crystals depending on the orientation of the sample. Non-<001> oriented crystals generally deform by <100> slip on either {100} or {110} planes. However, the critical resolved shear stress (CRSS) for <100> slip is zero for <001> oriented crystals and consequently, deformation proceeds by slip of <111> or <110> dislocations, though at high temperatures even the non-conservative motion of <100> dislocations probably contributes to the deformation of these crystals. One consequence of these differences in deformation behavior as a function of orientation, is that the DBTT of non-<001> crystals is approximately 100-150°C lower in temperature than for <001> crystals.

Very little is known about the effect that alloying additions may have on altering these deformation processes; but it is clear, especially for high-strength Hf-alloyed NiAl single crystals, that the effect must be considerable. For example, the DBTT of D176 single crystals of all orientations is significantly increased over that of comparably oriented binary NiAl. Furthermore, the influence of orientation on the relative DBTTs of D176 crystals becomes reversed; the DBTT for <001> D176 crystals is 100-200°C lower than that for <011> oriented crystals. This unusual behavior for the high-strength Hf-doped NiAl single crystals made it imperative to study both <001> and a non-<001> crystal orientations in this study. The approach involved the determination of yield stress, σ_y , of the alloy as a function of temperature, T, at a given strain-rate. When this data is plotted in the form of an Arrhenius plot of $\ln(\sigma_y)$ versus 1/T, the slope of the plot becomes proportional to the activation energy for deformation. Any deviation in the slope of the plot indicates a change in deformation mechanism. It is usually one of these changes in deformation mechanism which shows up as a change in slope on the Arrhenius plot that is responsible for the brittle-to-ductile transition in the material. This approach has been successful in identifying the various deformation regimes and the DBTT in polycrystalline binary NiAl as well as high-strength Re and Zr-doped polycrystalline NiAl alloys [12-14]. Furthermore, this approach has proved effective in accurately identifying the DBTT of <001> oriented Ni-50Al and Ni-40Al single crystal alloys [15].

The accuracy in determining the temperature at which a change in deformation mechanism occurs depends on the temperature range between the yield strength measurements. Therefore, it is preferred to run mechanical tests at as many different temperatures as practical, especially over the temperature range that a transition is expected. However, an advantage to this technique is the fact that the tests can be run in compression. Furthermore, for many high-strength alloys it is difficult to determine the tensile yield strength at lower temperatures since the material may fracture before yielding, though with careful testing procedures it is possible to determine the yield strength in compression.

Once the Arrhenius plot was established, transmission electron microscopy (TEM) was then performed on samples from each identifiable deformation regime to determine the operative deformation mechanisms and to verify that each regime does represent an individually unique set of active deformation processes. Consequently, another advantage to this technique is that the individual deformation regimes are already delineated from the Arrhenius plot and TEM is used to characterize the actual mechanisms that operate in each regime. Therefore, through a combination of mechanical testing, Arrhenius analysis, and systematic TEM studies it was possible to map the deformation behavior of D176 single crystals of <001> and <011> orientations.

2.7 Ultra-High Purity NiAl

Although the alloys produced at GEAE typically contain extremely low levels of impurities, these levels, particularly with respect to interstitial elements, could have significant effects on mechanical properties if strain-aging effects are occurring. Indeed, higher purity NiAl has been observed to display lower yield stresses [16]. For this segment of the study, we collaborated with Professor Ben Oliver at the University of Tennessee. We supplied him with <110> seed crystals to produce high purity castings of binary NiAl using a containerless levitation zone processor.

Tensile, compression and toughness tests were carried out as a function of temperature. The test results were compared with the results obtained with the GEAE produced material. The results were analyzed using TEM and scanning electron microscopy.

2.8 Study of Scatter in the Room Temperature Tensile Properties

During the course of this study, a considerable amount of scatter in the room temperature tensile ductility was observed. A systematic study of the cause of scatter was undertaken which included effect of composition, especially carbon content, batch to batch variation, specimen machining, specimen surface preparation after machining and specimen alignment in the tensile test set up. Tests were also conducted at two test vendors to determine any vendor related variability. Composition variations could exist from batch to batch, and small variations in the interstitial content could have a pronounced effect on the deformation behavior of NiAl. For this study, carbon, oxygen, sulfur and nitrogen contents were analyzed for many representative specimens. After the tensile specimens are ground to specified dimensions, they are electropolished to remove residual strains and grinding marks. It was observed that surface finish as well as the degree (depth and width) of grinding marks varied from specimen to specimen after electropolishing. It was also observed that etch pits were introduced during electropolishing. The size and depth of these etch pits varied from specimen to specimen. Therefore, variables in the electropolishing technique were systematically evaluated. Also other techniques such as chemical milling and diamond honing were evaluated. In all these techniques, conditions were varied to eliminate formation of etch pits and obtain different degrees of grinding mark removal. As will be discussed in Section 3.11, surface preparation prior to test was found to be the most critical variable affecting room temperature ductility.

2.9 Pre-Strain Effects

The room temperature tensile ductility and toughness of NiAl and its alloys has been found previously to be improved by high temperature pre-straining of the tensile specimen. Two mechanisms have been proposed for this effect. In the first mechanism, fracture is delayed by the formation of residual stress fields, formed by plastic deformation near the defects during the pre-straining. These defects are thus partially shielded during subsequent room temperature testing, reducing their effective stress concentration. Alternatively, the introduction of mobile dislocations by the pre-strain increase the inherent toughness of the material, thus increasing the strain to failure.

In order to differentiate between these two possible mechanisms, an experimental plan was devised in which the effects of high temperature pre-strain on both tensile and toughness properties were evaluated. If the mechanism involves shielding of defects, with no improvement in the inherent toughness of the material, increases in tensile ductility or fracture strengths would not be expected to be accompanied by improved toughness. If the mobile dislocation mechanism is operative, both tensile and toughness properties would be expected to improve.

The test matrix, shown in Table II, included experiments on two different alloys: binary NiAl, and a 0.5at%Hf containing alloy (D176). As mentioned earlier, the latter alloy has significantly

improved creep/rupture properties compared to the binary, but also has a significantly higher DBTT, in the range of 700-900°C (depending on orientation). Pre-straining at 1093°C has been found to lower this DBTT by as much as 200°C (also depending on orientation). It is interesting to note that, for this and other "strong" alloys of NiAl, the <001> orientation has a lower DBTT than the <110> orientation. This is in contrast to the binary, stoichiometric alloy, in which the <001> orientation is considerably stronger and less ductile than other orientations, due to the lack of a resolved shear stress on the preferred <100> slip systems.

In previous experiments on the effect of pre-strain on tensile ductility, a fully machined tensile specimen was pre-strained at temperature (538°C for stoichiometric NiAl and either 982 or 1093°C for strong alloys) and subsequently tested at the lower temperature. In the current study, pre-straining was performed in compression on oriented blocks (Figure 2). Various specimen geometries were then machined from these blocks, including tensile, toughness and compression bars. To prevent buckling, a restraining fixture was designed to restrict lateral movement of the specimen during the compression pre-strain (Figure 3).

The study of pre-strain effects was separated into two categories: 1) pre-straining and testing in the same orientation, and 2) pre-strain in one orientation, followed by testing in a second orientation. Pre-straining and testing was performed in two major crystallographic directions: <001> and <110>. Toughness and tensile testing was then performed on specimens with axes parallel to the pre-straining direction. Testing was conducted at room temperature and in the vicinity of the DBTT. For the high strength alloy, compression testing was also planned to assess the effect of pre-straining on the yield behavior below the tensile DBTT. Changes in this behavior may influence toughness and fracture strengths, for instance, even in the absence of macroscopic tensile ductility.

In the orientation effects portion of the study, pre-straining was performed in either <001> or <110> orientation, and testing conducted on specimens with axes parallel to the other crystallographic direction. In this manner, the effects of pre-strain on the properties in other directions was evaluated. It should be noted that the Burgers vectors of the dislocations created for the <001> and <110> directions will be different, with the preferred <100> slip direction active for <110> oriented specimens and the <111> (low temperature) or <110> (above the DBTT) slip directions active for the <001> "hard" orientation. Thus, the effect of the introduction of dislocations which are fundamentally different from those expected to be active for the given test orientation was studied using this set of experiments.

Table II. Pre-Strain Effects Test Plan

1) Pre-strain Effects - Single Orientation

Purpose: Determine the effect of pre-straining on yield behavior, toughness and ductility

Alloys: NiAl, NiAl alloy D176

Orientations: <100> and <110>

Test:

- Compression: RT + 3 elevated T's (2 tests ea. -> 8 per orient./alloy) (Hf containing alloy)
- Tensile: 4 T's near DBTT (2 tests ea. -> 8 per orient./alloy)
- Toughness test: RT + 3 elevated T's (2 tests ea. -> 8 per orient./alloy)

Experimental Procedure:

- EDM and machine oriented compression blocks
- Pre-strain in hot press
- Machine bars from block and test

2) Pre-strain Orientation Effects

Purpose: Determine the effect of pre-straining on properties in other orientations

Alloys: NiAl, NiAl alloy D176

Orientations: Pre-strain in <100> and test in <110>. Pre-strain in <110> and test in <100>

Testing:

- Tensile: 2 T's near DBTT (2 tests ea. -> 4 per orient./alloy)
- Toughness test: RT + 1 elevated T (2 tests ea. -> 4 per orient./alloy)

Experimental Procedure:

- EDM and machine double oriented compression blocks
- Pre-strain in hot press
- Machine bars from block perpendicular to pre-strain direction and test.

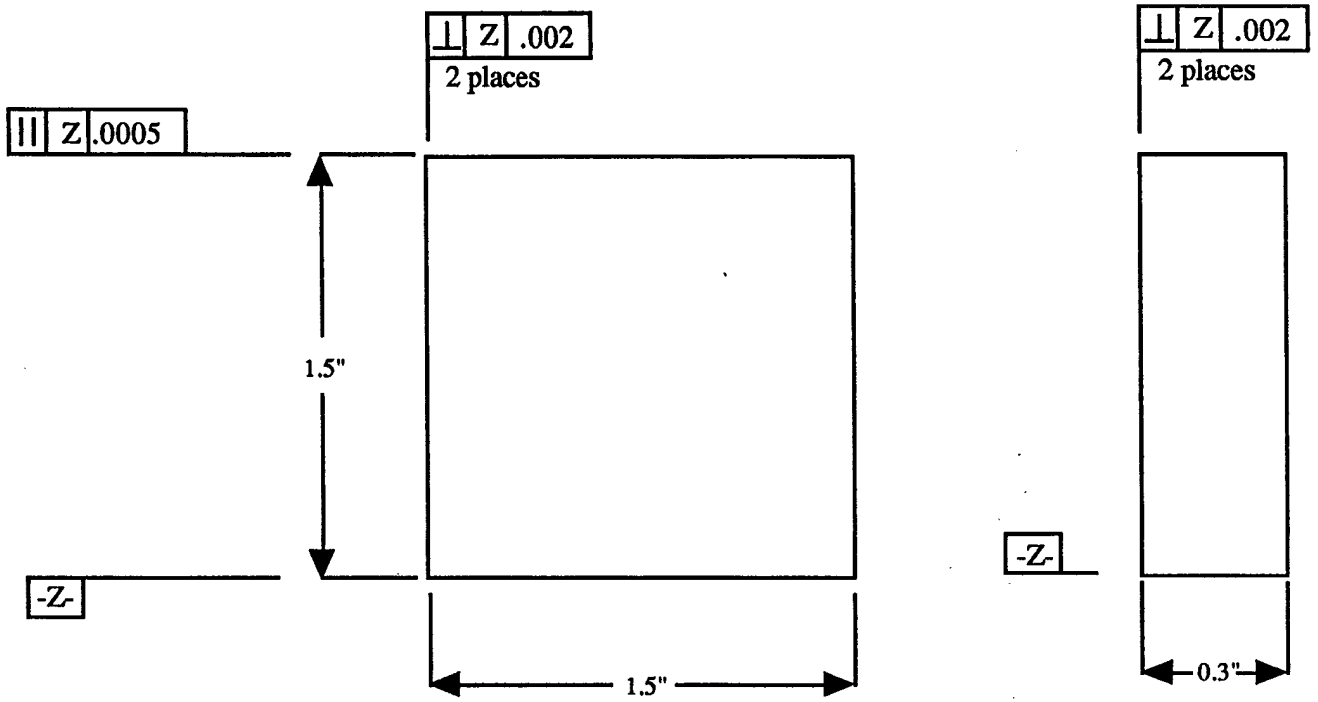

Notes: Drawing not to scale
Specimens will be provided as rectangular prisms, approximately 0.03" oversize
The ends of the specimen must be parallel to within 0.0005"
The faces of the specimen must be parallel to within 0.002"
Specimens to be low stress ground (see GE spec. 4013195-990 - Class B)

GE Aircraft Engines	
Specimen Name: Compression Block Specimen	Drawing Number: CB001

Figure 2. Drawing of compression blocks used in pre-straining studies. The block is compressed along one of the crystallographically oriented long directions and test specimens may be taken either parallel or perpendicular to the pre-strain axis.

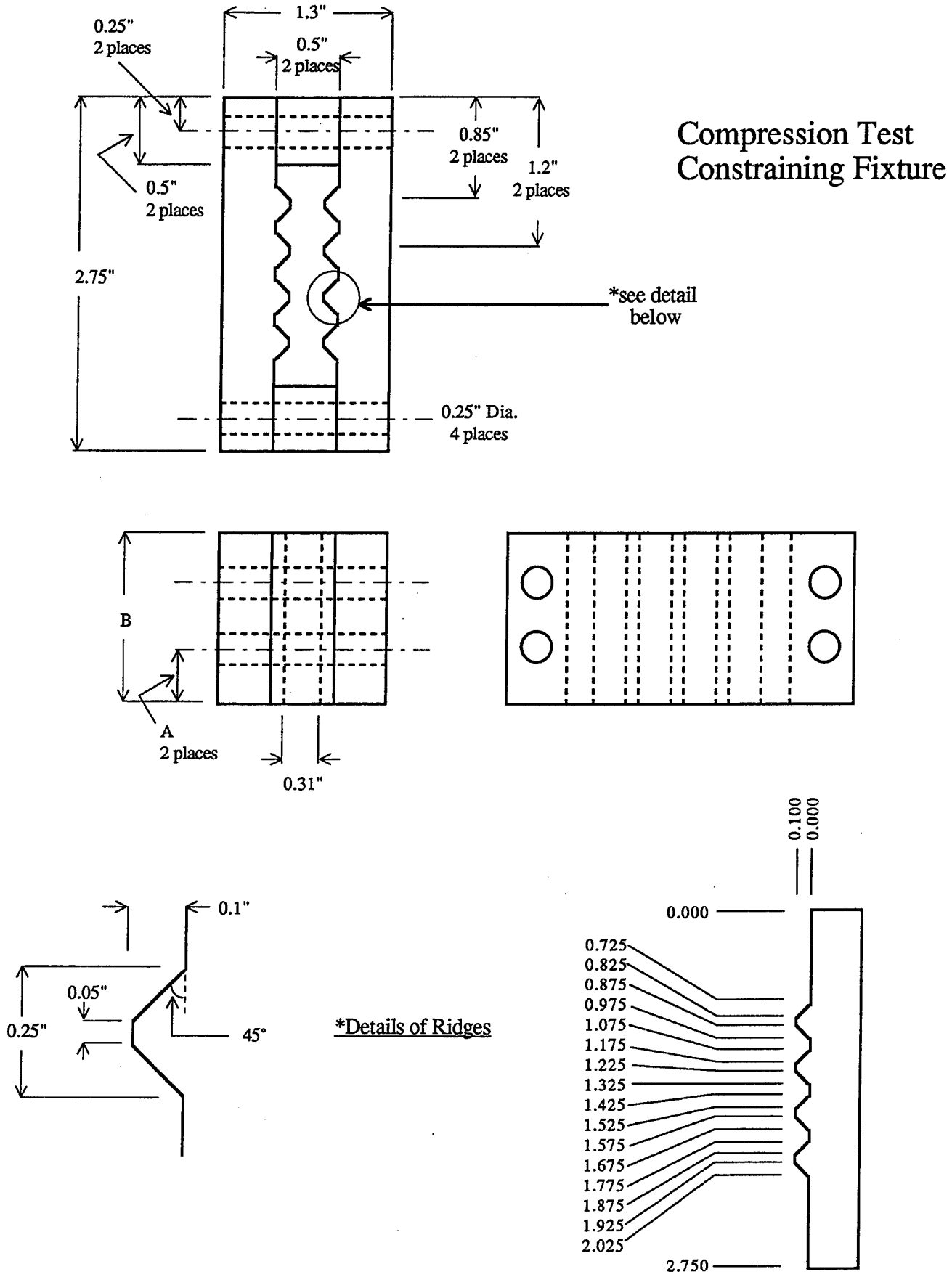

Figure 3. Drawing of the constraining fixture used to prevent specimen buckling during compression pre-straining of the blocks shown in Figure 2.

III. Results and Discussion

3.1 Material Processing and Chemical Analysis

The majority of single crystal slabs, 25mm x 32mm x 100mm, of the alloys used in this study were grown in an argon atmosphere using the Bridgman solidification method at GE Aircraft Engines (GEAE). The details of this method are described in reference [17]. The high purity single crystals of the stoichiometric composition of NiAl (50Ni:50Al) were grown in the <110> orientation by Prof. Ben Oliver of the University of Tennessee using <110> single crystal seeds supplied by GEAE. Six <110> oriented seed crystals were made to be used to produce the ultra-high purity NiAl crystals. NiAl crystals made at GEAE were oriented using back reflection Laue, and cylinders, approximately 23mm in diameter, were cut from the castings using wire EDM. Since these cylinders were not long enough to be used as seeds for Professor Oliver's apparatus, NiAl extenders, of random orientation, were bonded to the seeds using an activated diffusion bonding (ADB) process utilizing a Ni interlayer. These crystals were used as starter crystals for the containerless zone processor crystal growth apparatus. The containerless zone processing technique utilizes induction power to heat, levitate and constrain a liquid zone which is then directionally solidified. Since no crucible is used, contamination from the crucible material is avoided [18]

Nominal compositions for the alloys are listed in Table III. All of the single crystal castings tested in the first and second year of this study were subjected to chemical analysis for intentional alloying additions and selected impurities. The impurities chosen for analysis were those found to be present at significant levels in previous castings. During the third and fourth year of this study, the specimens were analyzed for interstitial elements such as carbon, oxygen, sulfur and nitrogen since they appear to be playing a role in the deformation behavior. Selected specimens which had shown high room temperature ductilities prior to start of this program were also analyzed for these elements. To eliminate variability in determining the carbon and oxygen contents, these elements were analyzed using the latest combustion techniques at Leco Corporation, who manufactures equipment for such analyses. Results from the analyses are listed in Table IV. For carbon and oxygen, only the values determined at Leco Corporation are reported in Table IV. The majority of the elements (e.g. Al, Si, P, S and O) are essentially the same in most of the castings and specimens which were analyzed except the High purity NiAl single crystals were analyzed to have much lower oxygen. Only carbon was found to vary from casting to casting. The effect of carbon on tensile properties is described in Section 3.9.

All the single crystals were homogenized in an argon atmosphere at 1316°C for 50 hours. The NiAl single crystals of the stoichiometric composition (50Ni:50Al) which received only the standard 1316°C/50 hour heat treatment will be referred to in this report as D5. D5 single crystals which were also given a subsequent 800°C/24 hour exposure will be referred to as D5HT. The high purity NiAl is designated as Oliver NiAl. The alloy containing 0.1 at% Fe is designated as D183. The alloy containing 0.05 at% Ga is designated as D128. The alloy containing both Fe and Ga is designated as D221. The Hf containing alloy is designated as D176. All heat treatments utilized in this program were conducted in the flowing argon atmosphere. All the mechanical tests were done in air.

Table III. Nominal Compositions of Single Crystal Alloys (Atomic and Weight %)

Alloy	Ni		Al		Fe		Ga	
	At%	Wt%	At%	Wt%	At%	Wt%	At%	Wt%
D5	50.00	68.51	50.00	31.49	--	--	--	--
D183	50.00	68.46	49.90	31.41	0.10	0.13	--	--
D128	50.00	68.48	49.95	31.44	--	--	0.05	0.08
D221	50.00	68.43	49.85	31.36	0.10	0.13	0.05	0.08
Oliver NiAl	50.00	68.51	50.00	31.49	--	--	--	--
D176	50.00	67.29	49.45	30.58	0.50 (Hf)	2.00 (Hf)	0.05	0.08

Table IV. Results from Chemical Analysis of Single Crystal Castings and Tested Specimens

	Weight %					Weight ppm	
Crystal	Ni	Al	Fe	Ga	Si	C	O
D5-1760	69.1	31.0	-	-	0.09	7	42
D5-1770	69.1	31.0	-	-	0.15	3	47
D5-1657HT	69.1	31.0	-	-	0.10	<2	43
D5-1667HT	68.4	31.4	-	-	0.11	30	48
D183-1682	68.6	31.1	0.15	-	0.15	<2	58
D183-1676	68.5	31.2	0.15	-	0.11	3	48
D128-1896	68.5	31.1	-	0.08	0.10	3	44
D5-1805	-	-	-	-	-	27	45
Oliver NiAl-1	68.62	31.38	-	-	-	9	7
Oliver NiAl-2-1	-	-	-	-	-	11	-
Oliver NiAl-2-2	-	-	-	-	-	6	-
D182-1124-3	-	-	-	-	-	8	36
D183-1126-3	-	-	-	-	-	12	41
D184-1092-3	-	-	-	-	-	3	39
D183-2448	-	-	-	-	-	6	32
D183-2449	-	-	-	-	-	11	33
D5-808-4	-	-	-	-	-	29	33
D5-2154	-	-	-	-	-	4	33
D5-2153-2	-	-	-	-	-	7	-

N and S were below detectable limits for all crystals (<3ppm S, <5ppm N). If a value is not reported under an element, either this element was not added to the alloy or it was not analyzed.

3.2 Mechanical Testing Procedure

Single crystal slabs were oriented using the back reflection Laue technique, and specimens were EDM wire cut from the slabs in the desired crystallographic orientations. The tensile and compression specimens were ground to specified dimensions using low stress grinding techniques. Button head type tensile specimens were used with gauge diameters of 2.5mm and gauge lengths of 19.1mm. For the majority of compression testing, 6.4mm diameter specimens were used, with a length of 15.9mm, resulting in a length to diameter ratio of 2.5/1. Unless otherwise specified, specimens were electropolished to remove the residual grinding strains and grinding marks. A solution of 7 to 10% perchloric and 90 to 93% methanol at -30°C was used. Electropolishing times of up to 2 minutes in 3 to 15 seconds interval were used to remove about a 25 μm surface layer. During the later stages of this program, electropolishing times were varied to examine surface condition of the specimens and its effect on the room temperature tensile elongation. Chemical milling was also evaluated in a selected group of specimens to compare surface finishes and evaluate their effect on the room temperature tensile elongation. For chemical milling, a solution of 15% nitric acid and 85% phosphoric acid at 125°C was used. The chemical milling time was varied from 5 minutes to 30 minutes. Unless otherwise specified, both the tensile and compression tests were run at a strain rate of 8.3×10^{-5}/s. The tensile tests were run to failure, while the compression tests were discontinued after approximately 2% plastic strain.

3.3 Vacancy Concentration Experiments

One of the possible effects of microalloying additions may to modify the vacancy concentrations, as a function of temperature, in the material. NiAl can display large thermal and constitutive vacancy concentrations [19]. The latter occurs on the Ni sublattice in Al rich alloys. High vacancy concentrations can affect strength and ductility in B2 compounds. This effect is particularly potent in FeAl [20]. In an effort to obtain some preliminary data on the effects of microalloying on vacancy concentrations in NiAl alloys, density measurements as a function of alloying and heat treatment were performed. Room temperature density measurements as a function of heat treatment, coupled with precise lattice parameter determinations, have previously been used to determine vacancy concentrations in NiAl alloys [19]. In the current investigation, difficulties were encountered in obtaining unambiguous precise lattice parameter values for the ternary alloys. Therefore, only density measurements were used as an indication of relative vacancy concentration as a function of heat treatment.

Three different heat treatments were chosen for the study. All of the samples were heat treated at 1316°C and slow cooled (~170°C/hour). Some of the samples were subsequently heat treated at either 1316°C/1 hour or 1093°C/2 hours, followed by a water quench. After heat treatment, the surfaces were ground off to remove any oxidation or depleted regions. Densities were measured by comparing weights of the sample measured in air versus water.

Figure 4 shows the calculated vacancy concentration as a function of heat treatment for the stoichiometric NiAl alloy. These data were obtained by comparing the actual densities with the theoretical densities, calculated using the lattice parameter as measured by x-ray diffraction. The vacancy concentrations of the water quenched specimens are 0.45% and 0.17% at 1316 and

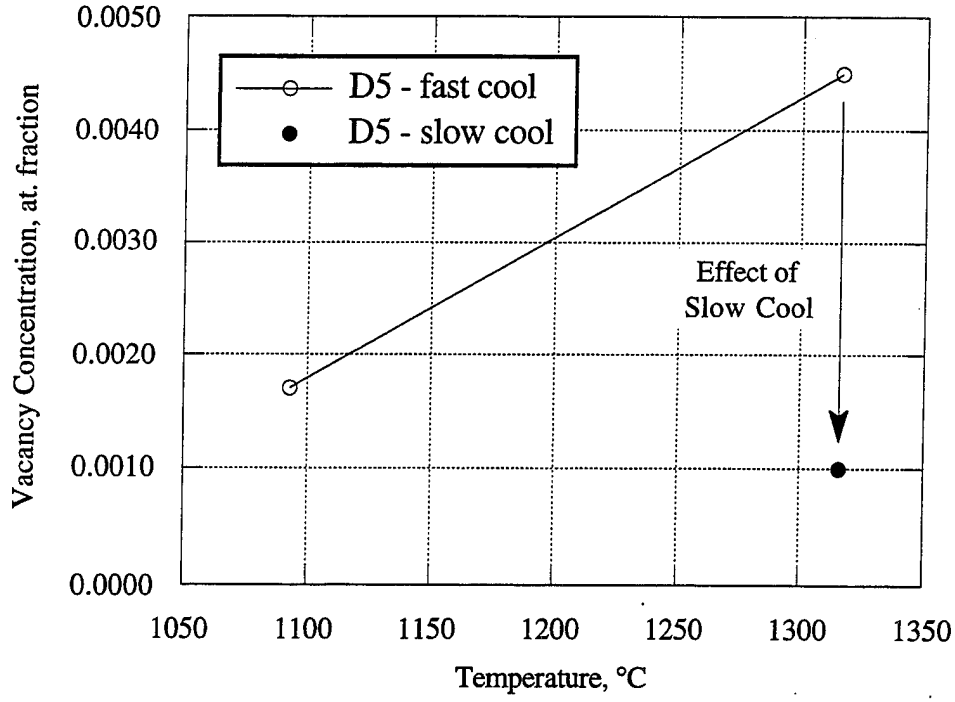

Figure 4. Calculated vacancy concentration as a function of heat treatment for stoichiometric NiAl (D5) as determined by density and lattice parameter measurements.

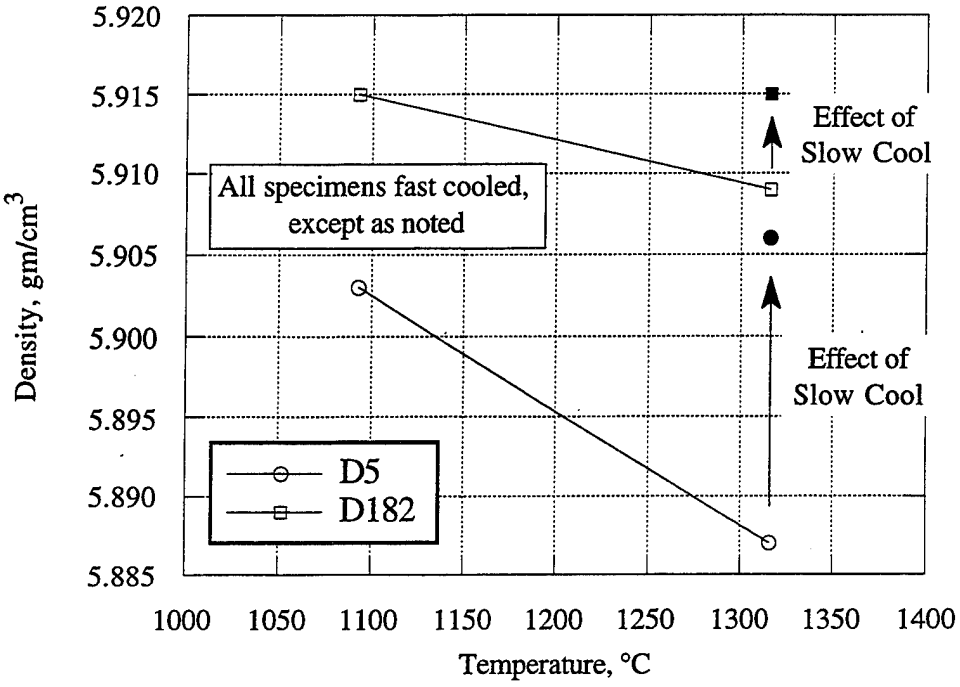

Figure 5. Density as a function of heat treatment for stoichiometric NiAl and D182 (50.0Ni-49.75Al-0.25Fe in atomic %). Changes in density with heat treatment are believed to be caused by changes in vacancy concentration.

1093°C, respectively. These values may be compared to 1.1% and 0.51%, measured for these temperatures by previous investigators [19]. The specimen which was slow cooled from 1316°C yielded a value of 0.12%.

Figure 5 shows the density as a function of heat treatment for stoichiometric NiAl and D182 (50.0Ni-49.75Al-0.25Fe in atomic %) The difference between the densities of the specimens which were quenched versus slow cooled from 1316°C is smaller for D182. This suggests that microalloying elements, specifically Fe, may decrease the concentration of vacancies formed during high temperature exposure in NiAl alloys. It should be emphasized that these are preliminary data and do not provide conclusive evidence for this effect. The application of more sophisticated experimental techniques to determine the concentration and nature of vacancies in these alloys will be required to properly characterize any possible interactions between microalloying elements and vacancies in NiAl.

3.4 Resistivity Measurements

Although resistivity measurements do not identify the specific defect giving rise to differences in the measured values, it can give an overall indication of the point defect concentration in the specimen. Resistivity measurements can be correlated with results from other techniques such as intensities of Snoek peaks in internal friction measurements.

Flat specimens measuring 35.1mm x 5.1mm x 0.5mm were prepared from D5, D5HT, D183, and D128 materials. For these measurements, the D5 and D5HT specimens were taken from the same casting (1657). Resistance measurements were performed at room temperature and –196°C, and the ratios of the resistance values at the two temperatures calculated. Since the temperature independent contribution to the resistivity is associated with the point defect concentration, an increase in this ratio indicates that the total point defect concentration has been reduced.

Results from the resistivity measurements are presented in Table V. The values listed are averages for two specimens for each alloy/heat treatment. The two values differed by less than 1.2% in all cases. Note that the D5 and D128 have essentially identical values. The value for D183 is slightly lower, possibly due to the presence of the Fe as a substitutional element. The value for D5HT is significantly higher, indicating a decrease in the total point defect concentration.

Table V. Results from Resistivity Measurements†

Specimen	Resistivity Ratio
D5	2.56
D5HT	3.62
D183	2.36
D128	2.54

† values are ratios of resistivity measured at RT to that measured at –196°C

The resistivity measurements indicate that only the stoichiometric alloy which received the 800°C heat treatment (D5HT) has a significantly lower total point defect concentration. This is

probably due to a decrease in vacancies. It must be kept in mind that this is a non-specific measurement, so that rearrangements in the point defects, e.g.. interactions between vacancies and solute elements or between substitutional and interstitial elements, might not be detected. Also, effects from decreases in one species may be offset by increases in another, and the microalloying elements themselves may act to increase resistivity.

3.5 Internal Friction Studies (at University of Illinois)

The internal friction studies were conducted at the University of Illinois, Urbana by Prof. Andy Granato. The purpose of the internal friction measurements was to distinguish between the possible mechanisms controlling dislocation flow for each of the slip systems found to be important in the associated mechanical and microscopic studies. This was done by analysis of attenuation and velocity changes during deformation using multiple sound waves with different polarization chosen to discriminate between different slip systems. Although this is possible in principle, it has not been done before, and the apparatus and technique were modified to conduct these measurements.

The first step was an analysis of the resolved shear stress factors applying to each of the slip systems for stresses arising from megahertz sound waves. These stress distributions differ from those imposed by static loading. It has been found that, unlike most metallic systems, it was possible to separate the response of different slip systems to an applied external load, and a configuration of measurements was designed specifically for this purpose. A summary of the calculations and configurations is given in Table VI. It has proven to be more difficult than anticipated to achieve good resolution of the attenuation and velocity data when using several modes simultaneously. The resolved shear stress factors for these modes are listed in Table VII. This appeared to be mainly a technical problem which may require improved control of parallel sample surfaces to find the optimal frequency to minimize interferences from diffraction and non-parallel effects. Also it will probably be necessary to use more electronic apparatus for the different waves than was originally anticipated.

Table VI. Resolved Shear Stress† for <100>/(100) and <100>/(110) Systems

<100>/{100} Slip Systems	(A) RSS	<100>/{110} Slip Systems	(B) RSS
1) [100]/(001)	σ_{31}	1) [001]/(I10)	$(\sigma_{23}+\sigma_{13})\sqrt{2}$
2) [010]/(001)	σ_{32}	2) [001]/(110)	$(\sigma_{13}+\sigma_{23})\sqrt{2}$
3) [100]/(010)	σ_{21}	3) [010]/(10I)	$(\sigma_{21}+\sigma_{23})\sqrt{2}$
4) [001]/(010)	σ_{23}	4) [010]/(101)	$(\sigma_{21}+\sigma_{23})\sqrt{2}$
5) [010]/(100)	σ_{12}	5) [100]/(011)	$(\sigma_{23}+\sigma_{13})\sqrt{2}$
6) [001]/(100)	σ_{13}	6) [100]/(01I)	$(\sigma_{21}+\sigma_{13})\sqrt{2}$

†referred to the cubic axes

Table VII. Resolved Shear Stress Factors Versus Mode of Applied Sound Waves

	Propagation Direction					
	[001]			[110]		
Polarization Direction	[001] long.	[100] shear	[010] shear	[110] long.	[1$\bar{1}$0] shear	[001] shear
Elastic Constant Measured	C_{11}	C_{44}	C_{44}	$(C_{11}+C_{12}+2C_{44})/2$	$(C_{11}-C_{12})/2$	C_{44}
Slip System A <100> {100}						
A1	0	1	0	0	0	0.5
A2	0	0	1	0	0	0.5
A3	0	0	0	0.403	0	0
A4	0	0	1	0	0	0.5
A5	0	0	0	0.403	0	0
A6	0	1	0	0	0	0.5
Slip System B <100> {110}						
B1	0	0.5	0.5	0	0	1
B2	0	0.5	0.5	0	0	0
B3	0	0	0.5	0.201	0	0.25
B4	0	0	0.5	0.201	0	0.25
B5	0	0.5	0	0.201	0	0.25
B6	0	0.5	0	0.201	0	0.25

$2C_{44}/(C_{11}+C_{12}+2C_{44})=0.403$

The specimens were compressed along the long <110> axis of a square cross section compression specimen, while longitudinal or shear waves were propagated along <001> and <110> directions. The specimen geometry and crystallographic orientation are shown in Figure 6.

Since a compression along [110] can activate systems A3 and A5, and B3, B4, B5 and B6, one sees from the table that [001] longitudinal and [110] shear waves polarized along [1$\bar{1}$0] see no effects for any of these slip systems. The longitudinal [110] wave was the only wave that detected deformation on slip system A, but it also detected deformation on slip systems B3-6, so that these two modes (longitudinal [110] and C44 shear [110]) can be used to separate the effects of the two slip systems. The [001] shear modes can be used for further checks and more detailed examination of {110} slip systems.

For each set of slip systems the attenuation and velocity measurements give the relaxation strengths and relaxation times, which in turn are used to separate out the dislocation drag and pinning forces. From these, together with Snoek effect measurements for interstitial impurities, it is expected that it will be possible to distinguish between long and short range pinning and drag mechanism for the dislocation-impurity interactions.

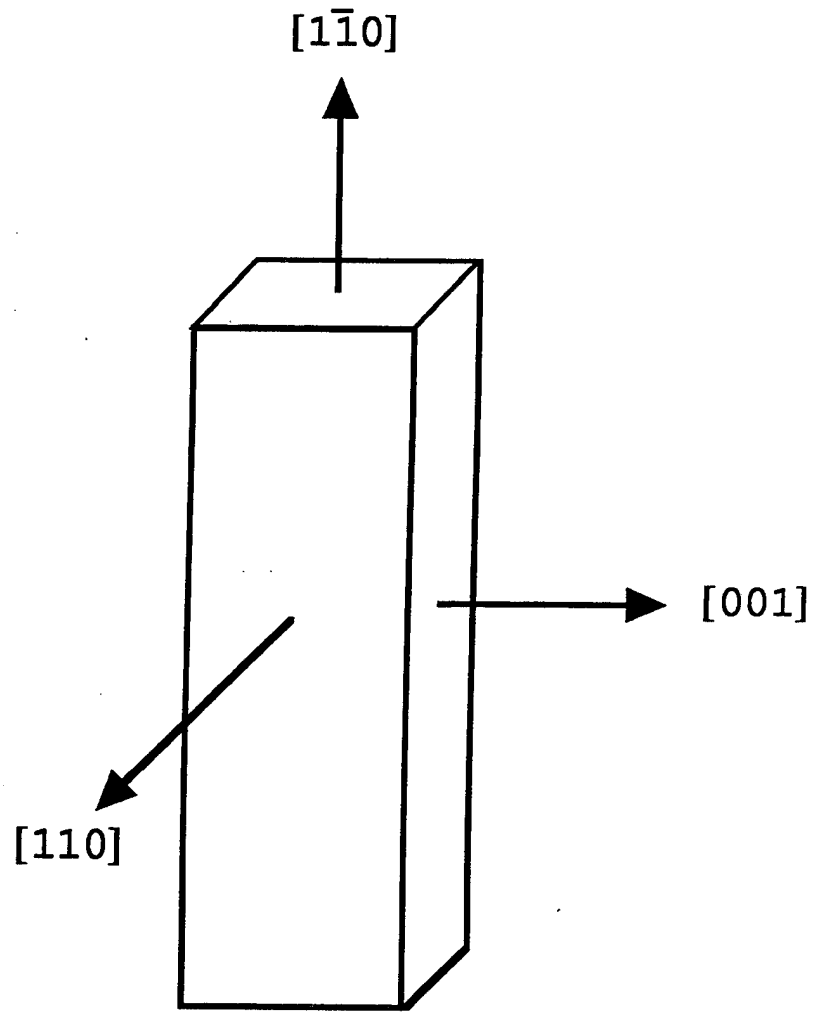

Figure 6. Geometry and crystallographic orientation of specimens used in internal friction experiments.

Ultrasonic measurements were made during <110> compression at constant strain rate on two NiAl specimens, intermediate temperature annealed (D5HT) and unannealed (D5). These are the first ultrasonic measurements in this new regime of material parameters. The measurements are therefore exploratory and incomplete. Because the measurements require simultaneous observation of several quantities in a new regime, a further development of the ultrasonic techniques has been required, and was pursued. Ideally, we wish to have simultaneous measurements of ultrasonic attenuation and velocity of at least two selected independent polarization modes with strain rate and strain. The sample geometry limits the possibilities to some extent. Although the measurements are so far incomplete, they are sufficient to demonstrate a number of important effects and to define the improvements required to obtain more complete quantitative results. It is found that the annealed and unannealed specimens have quite different behavior. The physics of the dislocation behavior is quite different from that known from earlier studies on purer materials, and the ultrasonic technique appears to be viable, promising to be a powerful tool in providing detailed quantitative results of the dislocation dynamics during deformation which can hardly be obtained with other measurements.

Measurements using a 70MHz longitudinal <1T0> ultrasonic wave in an annealed (D5HT) NiAl specimen compressed at constant strain rate along a <110> axis are shown in Figure 7. Curves for the stress and attenuation as a function of time for three successive loadings (A, B, and C) are shown. For each run the load is increased at constant strain rate, relaxed at zero strain rate, and then reduced at constant strain rate. In run A, the attenuation starts to increase as the strain approaches the maximum value applied near the flow stress, levels off during the relaxation, increases slightly when the load is first released, and then decreases but levels off at a value higher than the initial attenuation.

Subsequently, there is a small additional decrease in the attenuation, over a few hours, and the load is increased again for run B. In run B the strain rate has been increased over that of run A. When the stress exceeds the maximum value obtained in run A, the attenuation increases again to a much higher level. When the load decreases during the stress relaxation at constant strain, the attenuation decreases again about 20% and becomes constant. When the stress is reduced, the attenuation increases, and then subsequently decreases at zero stress, but by a smaller amount than during the relaxation. There is again a further slow decrease at zero stress over several hours before run C. With run C a similar pattern of behavior is obtained. However during unloading, the strain is held fixed for a minute at about half the maximum load and the attenuation oscillates slightly in a not very well defined way.

To interpret these results, we need to fall back on the basic relations describing plastic flow and ultrasonic attenuation and velocity. The total strain ε_T is given as the sum of the elastic strain ε_{el} and the dislocation strain ε_d:

$$\varepsilon_T = \varepsilon_{el} + \varepsilon_d \qquad (1)$$

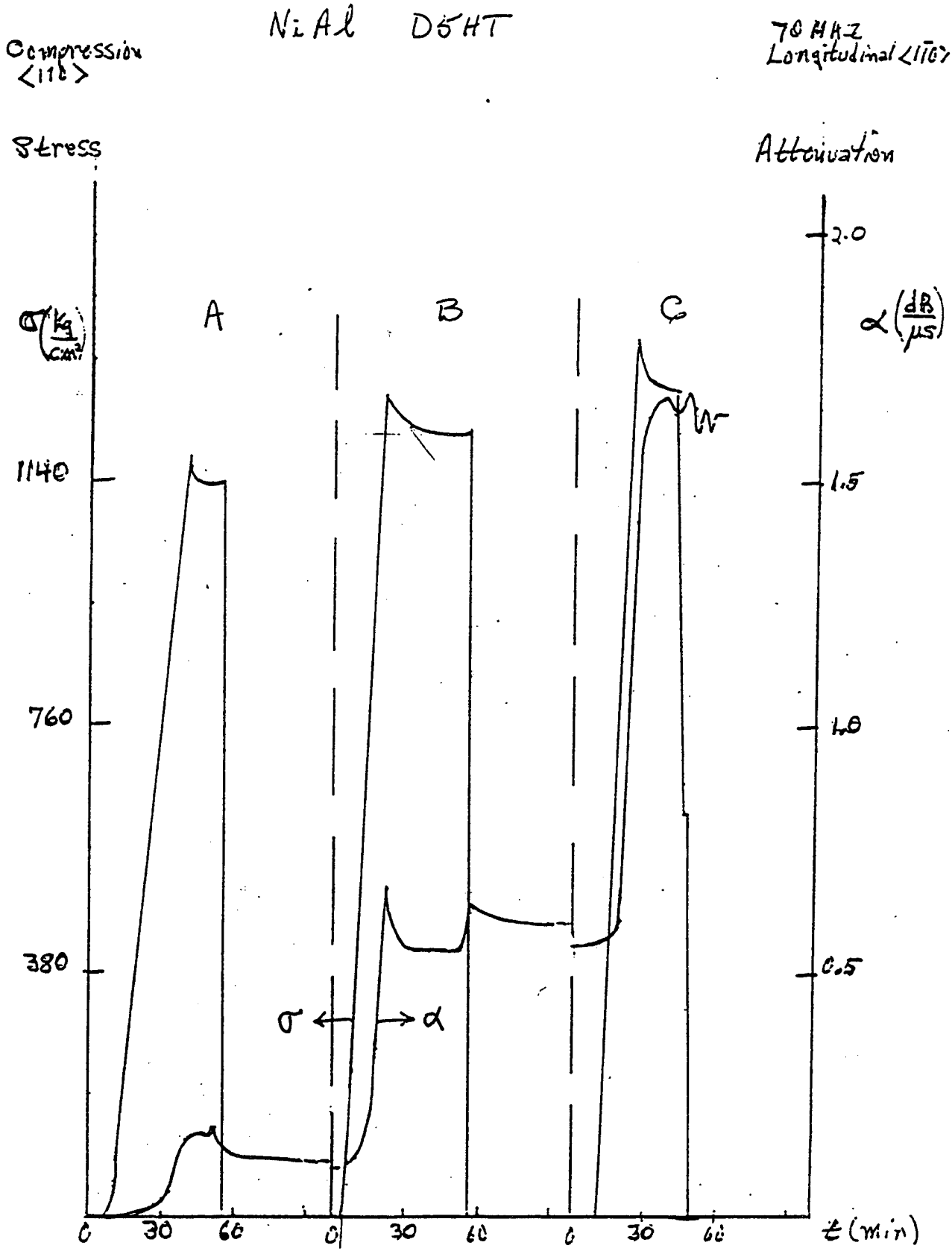

Figure 7. Stress (σ) and attenuation (α) data for three successive compressive loadings of a stoichiometric NiAl specimen which received an 800°C heat treatment (D5HT). The compression axis was [110] and the attenuation was measured using a 70MHz longitudinal [1$\bar{1}$0] ultrasonic wave.

The elastic strain is given by

$$\varepsilon_{el} = \sigma/E \qquad (2)$$

where σ is the applied stress and E is the Young's modulus. The dislocation strain and strain rate are given by

$$\varepsilon_d = \Lambda\, b\, \bar{x}, \text{ and}$$
$$\dot{\varepsilon}_d = \Lambda\, b\, \bar{v} \qquad (3)$$

where Λ is the dislocation density, b the Burgers vector, $\bar{x}$ and $\bar{v}$ are the average dislocation displacement and the average dislocation velocity, respectively. The average dislocation velocity is assumed to be limited by thermal activation and given by

$$\bar{v} = d\,\nu \exp(-U(\sigma))/kT \qquad (4)$$

where d is the distance advanced per thermal activation event, ν is the attack frequency, $U(\sigma)$ is the stress-dependent activation energy, k is Boltzmann's constant and T is the temperature. The activation energy may be taken in the form

$$U = U_o - b\sigma L \qquad (5)$$

where U_o is the activation energy in the absence of an applied stress on the dislocations and L is the dislocation segment length between pinning points of strength U_o.

The velocity v of the ultrasonic wave is given by

$$v = v_o - \Delta v \qquad (6)$$

where v is the velocity in a perfect crystal given by $v_o = \sqrt{C/\rho}$, where C is the elastic constant appropriate for the ultrasonic wave polarization employed, and ρ is the density. Δv may be related to the standard modulus defect by

$$\phi = \frac{\Delta C}{C} = \frac{2\Delta v}{v_o} = \Delta_R \frac{1}{1+\omega^2\tau^2} \qquad (7)$$

where Δ_R is the dislocation relaxation strength, $\omega = 2\pi f$, where f is the ultrasonic frequency and τ is the relaxation time for the dislocation motion. This measures the in-phase part of the ultrasonic response, while the out-of-phase part is given by:

$$\delta = Q^{-1} = \frac{\Delta}{\pi} = \frac{\alpha}{8.68\pi f} = \Delta_R \frac{\omega\tau}{1+\omega^2\tau^2} \qquad (8)$$

where δ is the loss tangent, Q^{-1} the inverse Q quality factor, Δ is the logarithmic decrement, and α is the ultrasonic attenuation in decibels per second. The dislocation relaxation strength and time are given by

$$\Delta_R = \Omega\Delta_0 \Lambda L^2 \tag{9}$$

$$\tau = BL^2/\pi^2 C \tag{10}$$

where $\Omega\Delta_0$ is a constant depending on orientation ~ 1/10, L is the dislocation segment length, C is the dislocation tension ~ $Gb^2/2$, and B is the dislocation viscosity occurring in the dislocation equation of motion

$$A \frac{d^2y}{dt^2} + B \frac{dy}{dt} + Ky = b\sigma \tag{11}$$

where A is the dislocation mass per unit length, y is the dislocation displacement, t is the time, and σ is the resolved shear stress on the dislocation system. For short-range pinning at a spacing L, the restoring force K is given by

$$K = \pi^2 C/L^2 \tag{12}$$

and for a viscous drag provided by phonon scattering, B ~ 2×10^{-4} in cgs. units for most of the cases where measurements are available.

In the system of equations given for the measurements of ε_d, $\dot{\varepsilon}_d$, δ and ϕ, the unknowns to be determined are Λ, L, B, $\bar{x}$, and U_0. This is one too many unknowns, but a useful approximation is made by supposing that $b^2 \sigma L \sim U_0/2$, where U_0 lies in the range of 0.1 to 1 ev for weak to strong pinning.

For the measurements shown in Figure 7, we have available only $\dot{\varepsilon}_T$ and α for loading, and also σ for the relaxation. This is not sufficient for a complete quantitative analysis, which would require both attenuation and velocity, as well as ultrasonic measurements with other polarizations to separate the contributions from different slips systems. 70 MHz is a convenient frequency for the ultrasonic attenuation measurements because diffraction effects become important for lower frequencies. This leads to interference effects in the ultrasonic pulse echo pattern for thin specimens, making measurements and interpretation more difficult. However, ultrasonic velocity measurements can only be made presently at lower frequencies, and so simultaneous measurements have been made, to be described later, at a lower frequency. Although the measurements given in Figure 7 are thus insufficient for a complete analysis, some useful observations are obtained from them by making some order of magnitude approximations and assumptions.

We first note, by comparison with the ultrasonic measurements available mainly for relatively pure materials such as copper, aluminum, and alkali halides, that we should be surprised to get any measurable attenuation at all in these materials. The fact that a conveniently measured value occurs

for the attenuation change implies both that something unusual and interesting is occurring in this material and that ultrasonic measurements should provide a useful probe of the behavior. In previous measurements on other materials, typical values of the parameters found have been

$\Lambda \sim 10^6\ cm^{-2}$
$L \sim 10^{-4}$ cm
$B \sim 2 \times 10^{-4}$.

This gives a relaxation strength Δ_R of

$$\Delta_R \sim \frac{\Lambda L^2}{10} \sim 10^{-3}, \text{ and}$$

$$\omega\tau = \frac{\omega B L^2}{\pi^2 C} \sim 0.9, \text{ so that } \delta \text{ and } \phi \sim 10^{-3}.$$

However, we here expect, with an argument to be given presently, that L is almost two orders of magnitude smaller for the much stronger NiAl. This means that even if Λ is 3 to 4 orders of magnitude larger, that δ should still be about four orders of magnitude smaller and not detectable. The fact that an easily observable change in δ is found implies that the viscous drag must be much larger than the phonon drag.

That L must be much smaller follows by analysis of the strain rate data. From Eqs. (1) and (2), with $\sigma_{110} = 191 \times 10^{12}$ dynes/cm^2, one has $\dot{\sigma}_{el} = 5.8 \times 10^{-7}$ sec^{-1} for loading in run B below the plastic flow range. For the relaxation, one then obtains $\dot{\varepsilon}_d = 4.2 \times 10^{-8}$ sec^{-1}. Then with Eq. 3, d ~ b, and $\nu \sim 4 \times 10^{11}$ sec^{-1}, one has

$\exp [\upsilon(\sigma)/ kT] \sim 10^4 \Lambda$, so that for:

Λ	$U(\sigma)/kT$
10^7	25.3
10^8	27.6
10^9	29.9
10^{10}	32.2

Then for $U(\sigma) \sim 30\ kT \sim 3/4$ eV, $\frac{b^2 \sigma L}{2} \sim \frac{3}{4}$ eV, and $L \sim 2 \times 10^{-6}$cm.

Now, although a quantitative analysis for Λ and L during the deformation may not be found without velocity data, we may speculate on the behavior from the attenuation data in Figure 7. Focusing on run B, when the stress level reaches the flow stress, we suppose the dislocation density increases rapidly, giving the rapid increase in attenuation. During the relaxation, with the stress decreasing, we suppose the dislocation density Λ does not change much, but the length L decreases slightly. The attenuation stops decreasing however, and appears to decrease only as long as the dislocations are still moving. This could be accounted for if the reduction in L arises mainly from dislocation intersections, and not by point defect pinning by diffusing point defects,

since the latter process should continue. When the stress is removed, the attenuation increases again. Since the stress is below the maximum level achieved earlier, we suppose the dislocation density has not changed, but some segments become partly unpinned. Since the attenuation then decreases at zero stress, but much more slowly than during the relaxation, there may be some pinning by diffusing defects. If this is correct, we would expect the reduction during relaxation to be relatively insensitive to temperature, while the reduction at zero stress should be sensitive. This needs to be examined in future experiments.

In a fourth run (D) on the specimen both the velocity and attenuation were measured at a lower frequency. The data could not be analyzed however, since a reference point for the velocity before deformation was not known. A velocity defect $\phi \sim 10^{-3}$ was obtained, however, and this shows that velocity data are obtainable and are likely to be of a convenient magnitude for analysis in future measurements. The total deformation for all four runs was about 1.5% and estimated to be about 1/3% for run B. With Eq. 3, this would give $\bar{x} \sim 10^{-4}$cm for $\Lambda \sim 10^{9}$cm^{-2}.

An attempt was made to obtain simultaneous measurements of attenuation and velocity on the non heat-treated specimens D5. This necessitated going to lower frequencies where diffraction problems complicate the measurements. Also attenuation measurements were made of a longitudinal <100> mode simultaneously at 70 MHz. The measurements were only partly successful, giving data for the loading process, but failed before data could be obtained during relaxation. In this range, the behavior observed was different from that found for the heat treated specimen.

The attenuation α and modulus defect ϕ at 10MHz, and stress as a function of time for constant strain rate are shown in Figure 8. The flow stress in this specimen was almost twice that of the heat treated specimen. In the Figure, the stress is 40Kgm/cm^2 per unit, so that flow and ultrasonic changes occurred starting at about 2200Kgm/cm^2. Below 2200 sec in the loading, the constant strain rate imposed was provided entirely by the elastic strain. The rate of stress increase slows above 2400 sec as dislocation strain now contributes to the total strain. The velocity decreases, giving a modulus defect $\phi \sim 4 \times 10^{-3}$ in the range from 2400 to 3100 sec, after which the echo pattern became non-exponential and non-usable. In contrast to the heat treated specimen, however, the attenuation goes through a maximum at about 3000 sec.

The <100> longitudinal mode attenuation (not shown) should see no dislocations on either the {100} or {110} slip planes. However it starts to increase, but at a distinctly higher stress level than that for the <110> longitudinal mode, which sees dislocations on both the {100} and {110} planes. This was unexpected, and shows that dislocations on other than the {100} and {110} planes play a role in the deformation.

When these data are analyzed, using Eqs. 7, 8, and 12 to obtain quantities proportional to Λ and L, assuming a constant B, the results shown in Figure 9 are obtained. $\sqrt{\omega\tau}$ is proportional to L. On the figure, the dislocation density Λ' is that which would be obtained if B were given by the phonon drag $B = 2 \times 10^{-4}$. ($\Lambda = \Lambda'(B/2 \times 10^{-4})$. The highest dislocation density Λ' achieved at t = 3200 sec is 4×10^{6} cm^{-2}. If B is 4 orders of magnitude larger, as we suppose later, than Λ is 4×10^{10} cm^{-1} at this time.

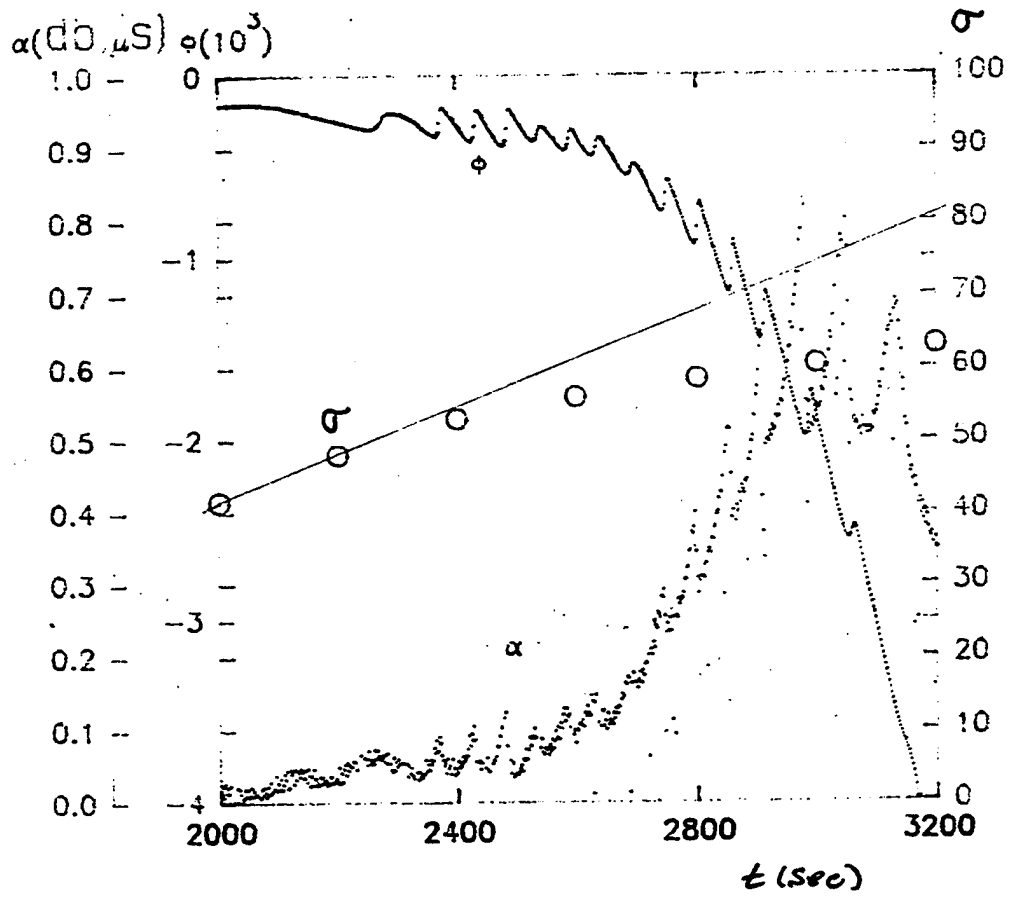

Figure 8. Plot of stress (σ), attenuation (α), and modulus defect (ϕ) as a function of time for a compressive loading experiment of a stoichiometric NiAl specimen. The compression axis was [110]. The attenuation and modulus defect data were measured using a 10MHz longitudinal [1T0] ultrasonic wave. Attenuation was also measured using a 70MHz [100] longitudinal wave (data not shown).

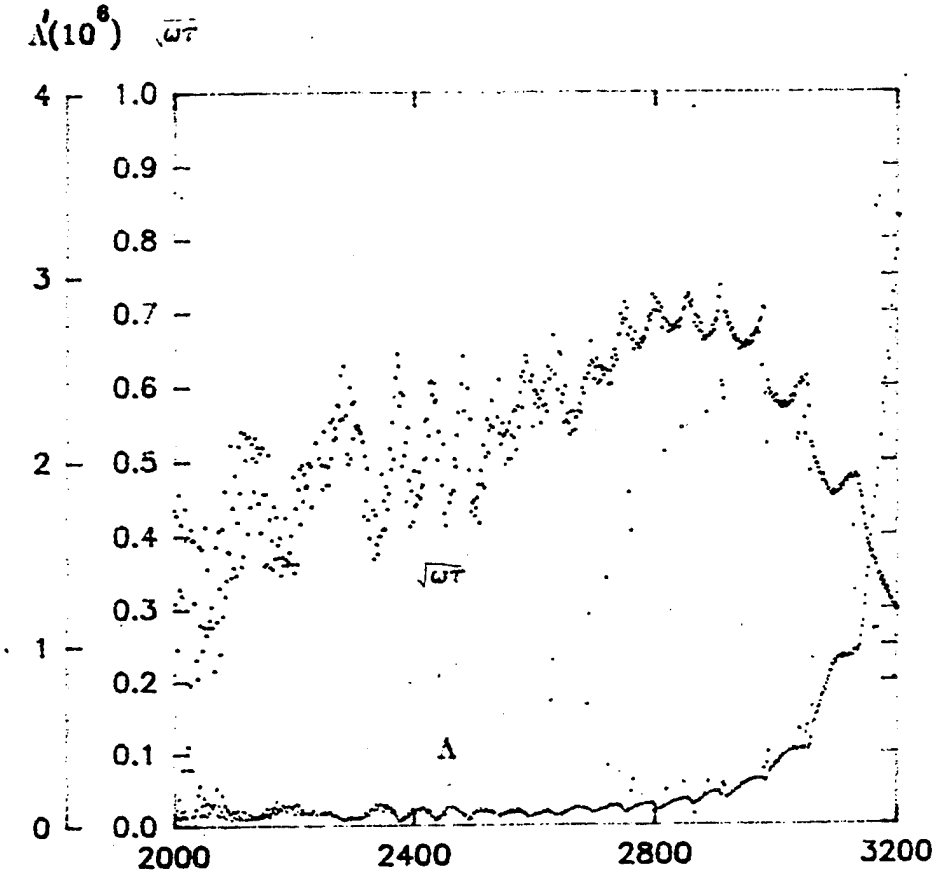

Figure 9. Plots of dislocation density (Λ) and dislocation segment length (L) as a function of time, calculated from the data shown in Figure 8. The segment length is given in terms of $\sqrt{\omega\tau}$, which is proportional to L, where ω is the ultrasonic frequency and τ is the relaxation time for dislocation motion.

For the interval from 2000 to 2800 sec, the dislocation density is approximately constant, while the loop segment length L slowly increases. Then, from 2800 to 3200 sec, L decreases while Λ increases greatly. The results suggest that the initial deformation arises by a stress induced increase of L from existing dislocations, but a later rapid increase in Λ actually decreases L, but not enough to compensate for the increasing Λ. The decrease in L may result from dislocation intersections, but a simultaneous shear wave <100> measurement is still required to separate the dislocation densities on the {100} and {110} planes. We tentatively conclude, subject to verification with additional measurements, that a second group of dislocations increase greatly in density after the initial deformation has begun.

From the change in stress-rates for the constant strain rate, one finds $\dot{\varepsilon}_d = 3 \times 10^{-7}$ at t = 3200 sec. By combining the expressions for $\dot{\varepsilon}_d$ and ϕ, the dislocation density can be eliminated to obtain

$$\frac{\dot{\varepsilon}_d}{\phi} = \frac{10}{L^2} b^2 \nu \exp [-U(\sigma)/kT].$$

Then with a first iteration for $L^{(o)} \sim 2 \times 10^{-6}$cm, $\nu = 4 \times 10^{11}$, $\phi = 4 \times 10^{-3}$, we obtain

$$\frac{U(\sigma)}{kT} \sim \frac{3}{4} \text{ eV, as before.}$$

Then $L \sim 10^{-6}$ cm, and

$$\Lambda = \frac{10\phi}{L^2} = 4 \times 10^{10} \text{ cm}^{-2}.$$

This is somewhat higher than expected. For this reason, and also because the pulse echo pattern was starting to deteriorate at this point (3200 sec), this measurement needs to be verified.

The measurements obtained during the first two years of these studies show that:

1) The ultrasonic technique promises to provide details of the behavior of NiAl alloys during deformation not obtainable in other ways. The magnitude of the attenuation and velocity changes are in a good range for this technique.

2) The effects found to date are unusual compared to those known from earlier work which was restricted to purer metals and alkali halides. A much larger viscosity drag coefficient than is provided by phonon drag is required. Dipole reorientation by interstitial dipoles may be a candidate for this. It is known, for example, that water molecule dipoles in ice (at concentration of 100%) lead to an increase in the dislocation viscosity of seven orders of magnitude.

3) The ultrasonic effects appear to be quite different in the heat treated (D5HT) and standard D5 specimens. There is evidence for dislocation cross slipping in the D5 specimen.

4) There is evidence of dislocation motion in planes other than the {100} and {110} planes. These preliminary results need verification, as well as extensions in subsequent experiments.

5) New experiments are needed using <100> shear modes to separate the {100} and {110} plane dislocations. The temperature dependence of the ultrasonic measurements near room temperature is needed to sort out possible mechanisms for the loop length (L) decreases found during relaxation and at zero stress after loading.

During the third year, ultrasonic measurements were made on D183 during first loading under <110> compression at constant strain rate. Attenuation and velocity at 10 MHz for a shear <100> wave, polarized along <110>, were measured simultaneously. The purpose of this measurement was to see if effects occurring on the primary and secondary slip systems can be separated and to see if important differences occur in the dislocation density, restoring forces and viscosities of specimens containing 0.1 at% Fe.

The velocity at constant strain rates and the stress on first loading are shown in Figure 10. The velocity change $\phi = \Delta v/v$ is in units of tenths of a percent, and the time is in seconds for constant deformation rates. The stress is given by the open circles. The velocity decreases sharply when the stress approaches the flow stress of about 1900 kg/cm^2. When the strain is then held constant, the velocity continues to increase but at a slower and decreasing rate. When the strain rate is then increased again to the previous value, this behavior is repeated, and when the load is decreased to zero, the velocity change stays nearly constant, decreasing at only a very slow rate. The small discontinuity near 5600 seconds is not a physical effect, but an artifact corresponding to a retuning of the ultrasonic frequency to improve the ultrasonic pattern at this point.

The simultaneously measured attenuation at 10 MHz is shown in Figure 11. The attenuation unexpectedly decreases at first even before substantial changes in the velocity occur, remains relatively unchanged through most of the deformation, and then increases back toward the initial level on unloading the specimen. This behavior is unexpected, strange, and awkward for analysis, since it requires that we know how the initial attenuation is divided between dislocation effects and geometrical background effects. The attenuation changes obtained for the 30 MHz signal on the secondary slip planes shown in Figure 12 is also anomalous, but less so. Because of these anomalies, the originally planned additional deformation was postponed until some additional testing could be done. The attenuation level was low in these tests because the frequency was low, and this made the uncontrollable component of the attenuation from geometrical effects, (diffraction, non-parallelism, ...) relatively large. It was apparent from earlier tests on D5HT that attenuation measurements at 70 MHz suffered less from these difficulties, but the velocity measurements must be made at 10 MHz with the present instrumentation.

Several tests were made with different electronic circuitry for a pulse overlap system to see if a velocity system with less sensitivity could be developed which would allow for measurements less susceptible to detuning from sample shape changes and usable at higher frequencies. Also circuit changes were made in an attempt to improve the stability and accuracy of the low-level attenuation measurement at low frequency. It was concluded from these tests that although 10 MHz attenuation measurements can be made more useful, the most practical measurements for

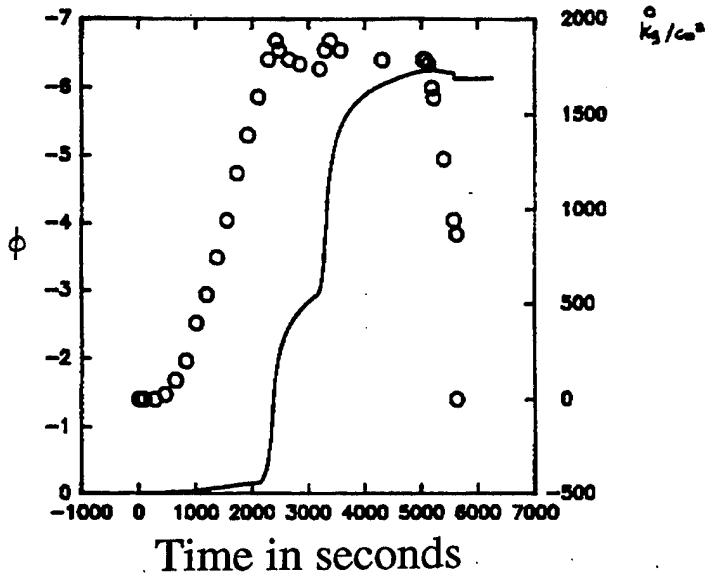

Figure 10. Velocity (ϕ) and stress change (open circles in $Kg/cm^{2)}$ with time (in seconds) for D183 at 10 MHz for a shear <100> wave polarized along <110>.

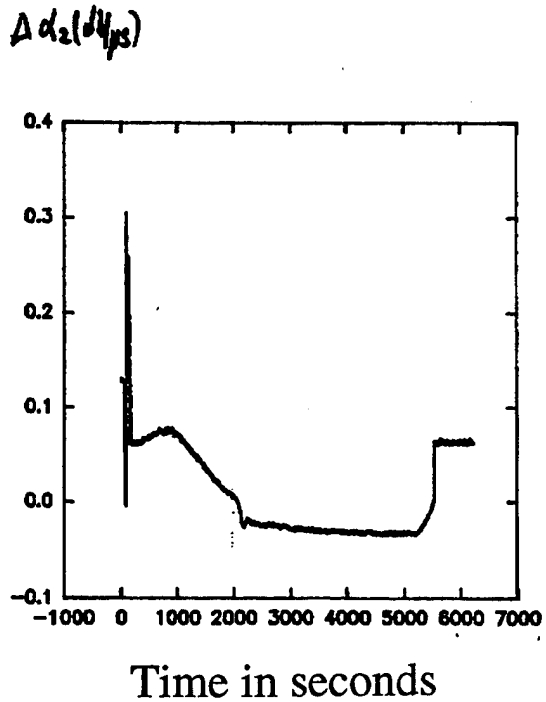

Figure 11. Attenuation ($\Delta\alpha_2$) with time (in seconds) for D183 at 10 MHz for a shear <100> wave polarized along <110>.

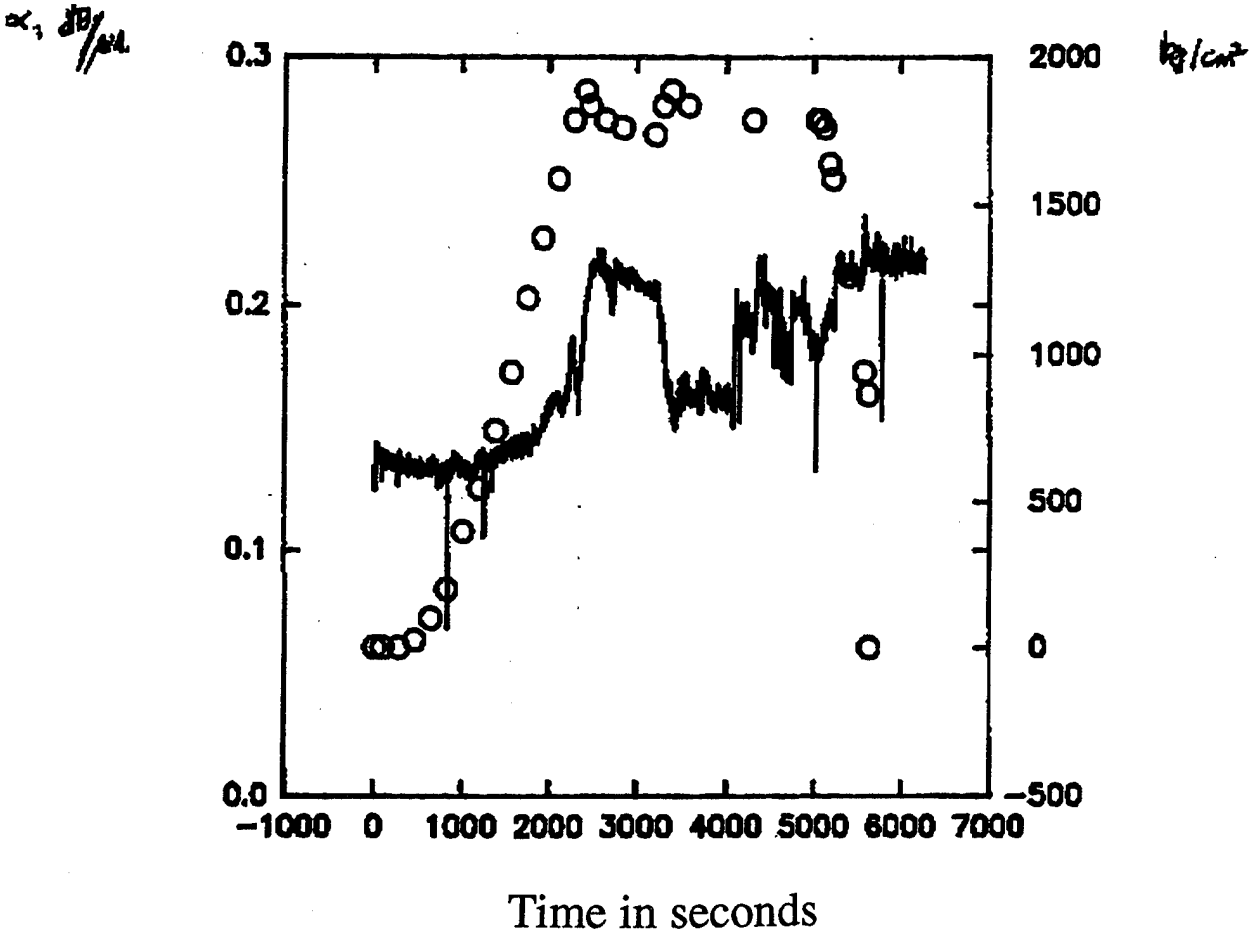

Figure 12. Attenuation ($\Delta\alpha_2$) and stress change (open circles in Kg/cm^2) with time (in seconds) for D183 at 30 MHz for a shear <100> wave polarized along <110>.

continuing deformation would be velocity measurements at 10 MHz with the original system, combined with attenuation measurements at 70 MHz on the two principle slip systems. It was also concluded that extensive additional instrumentation development will be required to obtain useful data. Since further instrument development was beyond the scope of this program, this study was terminated.

3.6 Mechanical Property Tests

3.6.1 Mechanical Test Results from –196 to 250°C

The effect of low temperature heat treatments on the yielding and DBTT behavior of D5 was studied. The effect of Fe and Ga additions also was evaluated. Tensile and compression tests were performed as a function of temperature and the deformation behavior was studied by transmission electron microscopy. Results from the tests are shown in Figures 13-18. The yield points for the compression tests were often not well defined, particularly for the low temperature tests. This may have resulted from slight misalignments of the platens and the specimen which "settled in" during the early stages of the test. As a result, reliable measurements of the 0.02 and 0.2% yield stresses were not always obtainable. However, the flow stresses, defined in this case as the point at which the stress-strain curve bends over into a linear work hardening rate, were very reproducible. Flow stress values measured from tests with well behaved yielding were comparable to those measured in tests which exhibited extremely poorly defined yielding. In the former, the flow stress was generally equal to the 0.2% yield stress. Therefore, the flow stress was used in lieu of an offset stress for the compression tests. For the tensile tests, 0.2% yield stresses were used. As can be seen in the plots, the compression flow stress and tensile yield stress values are essentially equivalent at temperatures for which both quantities were measured.

The data in Figures 13-16 are given in terms of the critical resolved shear stress (CRSS) values for the {110} and {100} planes. These were measured in <111> and <110> oriented specimens, respectively. As these are both "soft" orientations for NiAl, the slip direction is <100> in both cases. The behavior of the CRSS as a function of temperature and orientation was essentially similar in all of the alloys/heat treatments investigated. Inspection of the data reveals that the CRSS falls rapidly between –196 and -50°C for both orientations. The rate at which the CRSS falls with temperature decreases with increasing temperature. Above 0°C, the decline in CRSS with temperature is approximately linear. The CRSS for the {110} plane is generally slightly higher than that for {100}. This is consistent with previous results obtained at GEAE in room temperature tests [21], but contradicts the traditional belief that {110} is the preferred slip plane in NiAl [22-24].

Yield stress and plastic elongation values from the tensile tests are presented in Figures 17 and 18, respectively. The room temperature elongation for the D5 specimen was unusually high for this alloy/heat treatment. However, at 100 and 150°C, the D5HT and microalloyed specimens displayed markedly higher plasticity than the D5 specimens. The results also indicate that the ductile to brittle transition temperature (DBTT) for D5HT and D183 is lower than that of D5. The D128 data are somewhat more confusing. Although the RT ductility is quite high, the 100 and 150°C values are unusually low. Such unusual behavior and scatter in the tensile ductility was

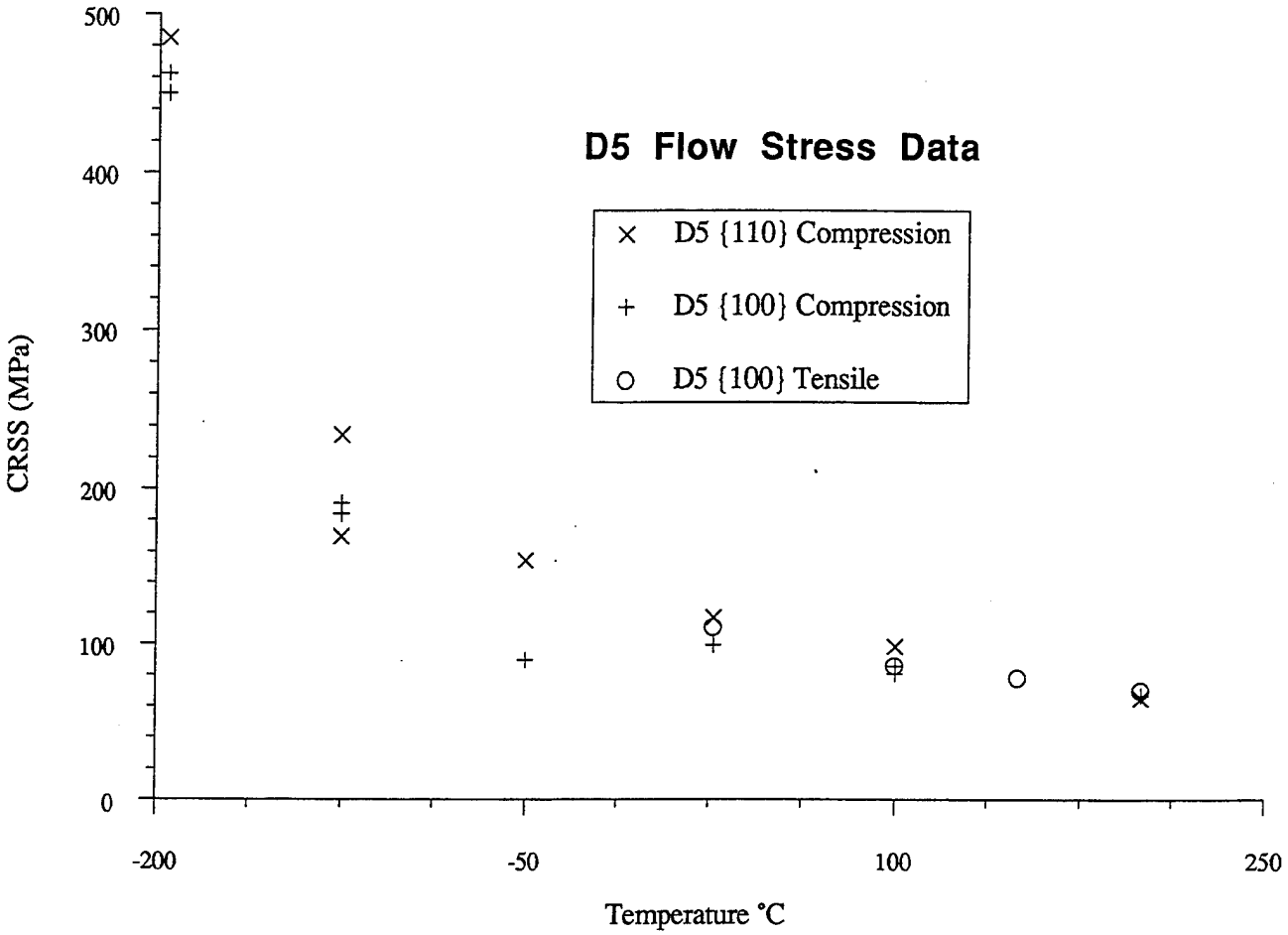

Figure 13. Flow stress (given in terms of critical resolved shear stress (CRSS) on the {110} and {100} planes) as a function of temperature taken from compression and tensile tests for stoichiometric NiAl given the standard heat treatment (D5). CRSS values for the {110} plane were derived from specimens strained along the <111> direction. CRSS values for the {100} plane were derived from specimens strained along the <110> direction.

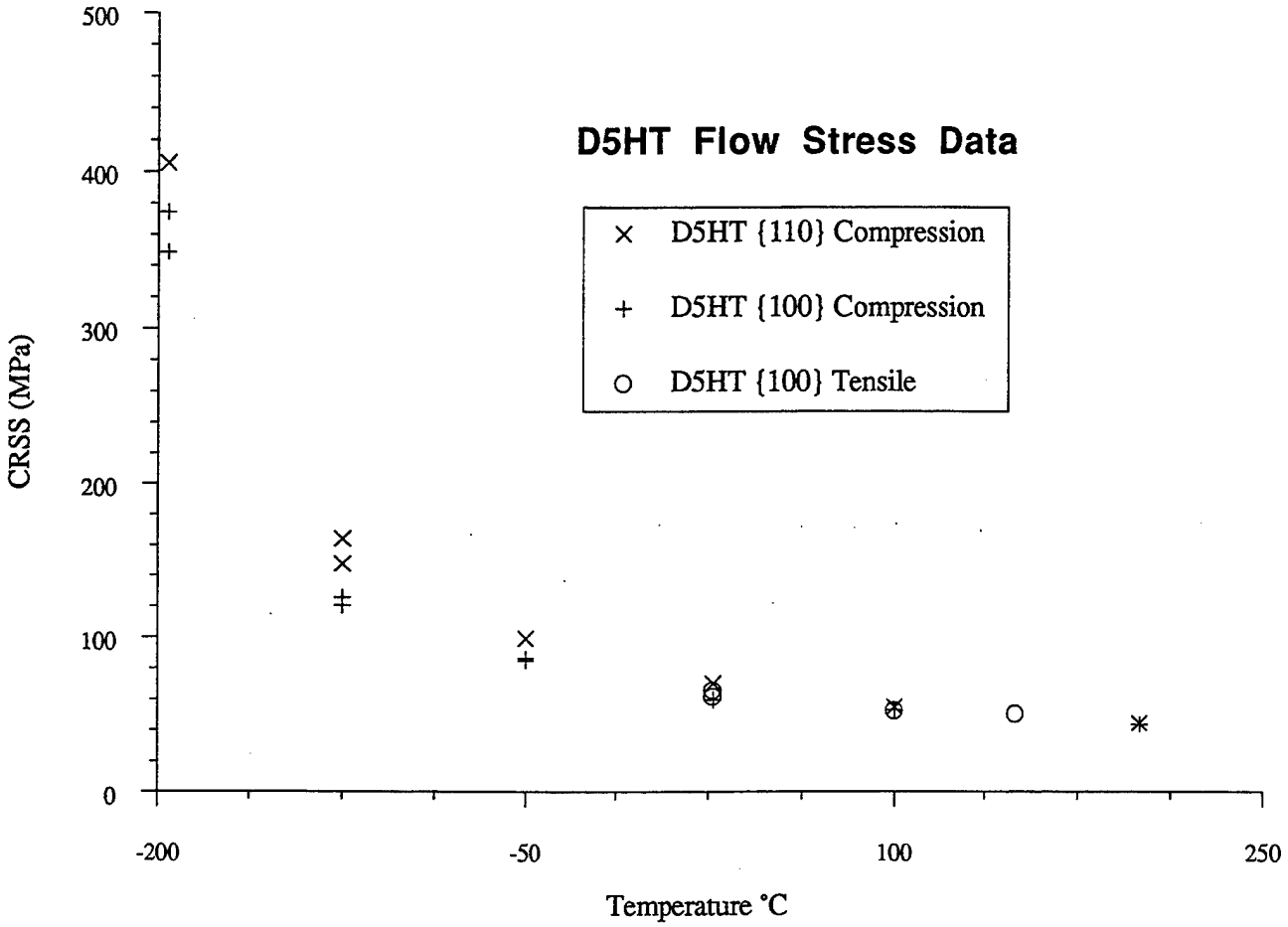

Figure 14. Flow stress (given in terms of critical resolved shear stress (CRSS) on the {110} and {100} planes) as a function of temperature taken from compression and tensile tests for stoichiometric NiAl given an 800°C anneal (D5HT). CRSS values for the {110} plane were derived from specimens strained along the <111> direction. CRSS values for the {100} plane were derived from specimens strained along the <110> direction.

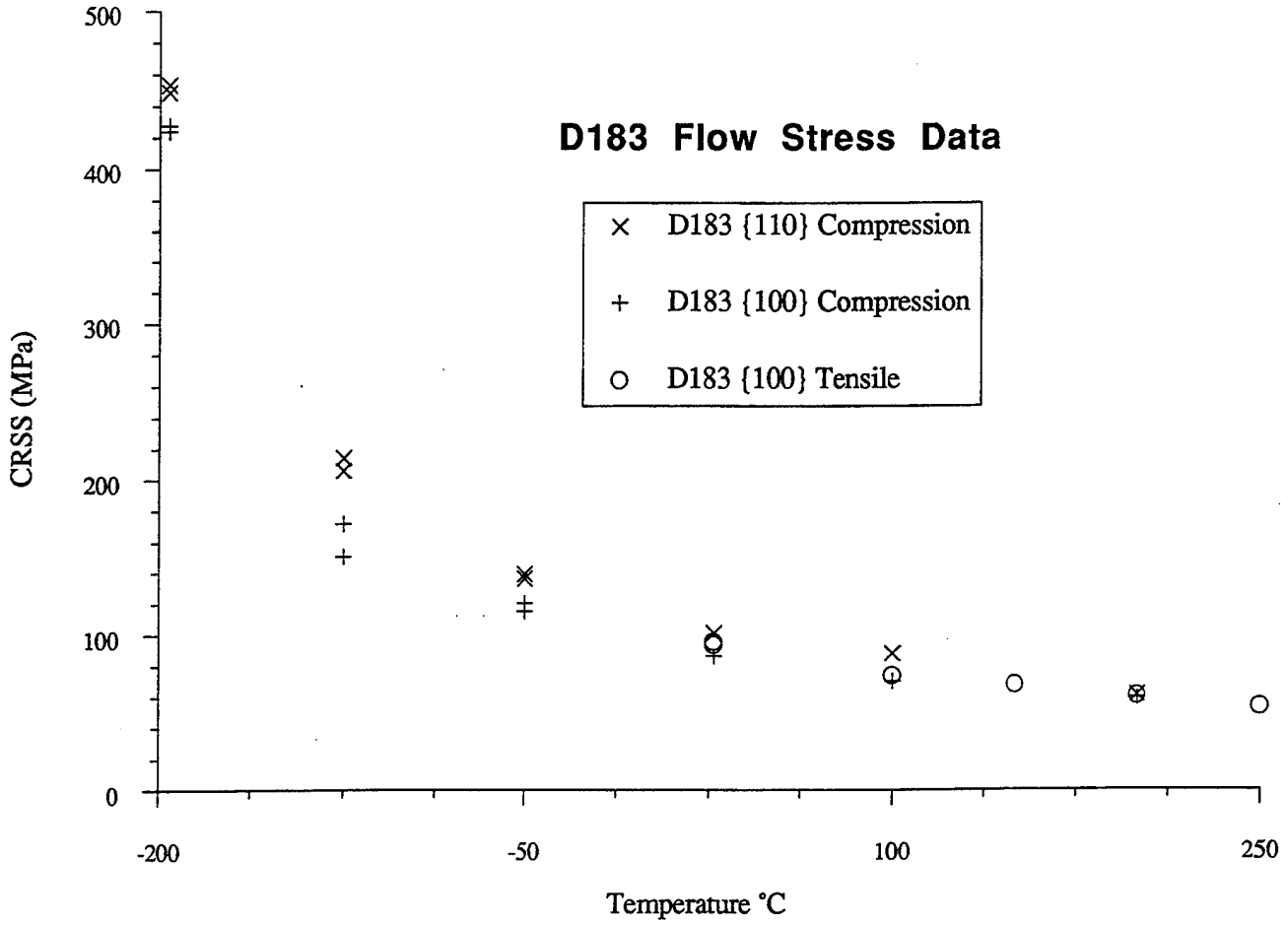

Figure 15. Flow stress (given in terms of critical resolved shear stress (CRSS) on the {110} and {100} planes) as a function of temperature taken from compression and tensile tests for NiAl microalloyed with Fe (D183). CRSS values for the {110} plane were derived from specimens strained along the <111> direction. CRSS values for the {100} plane were derived from specimens strained along the <110> direction.

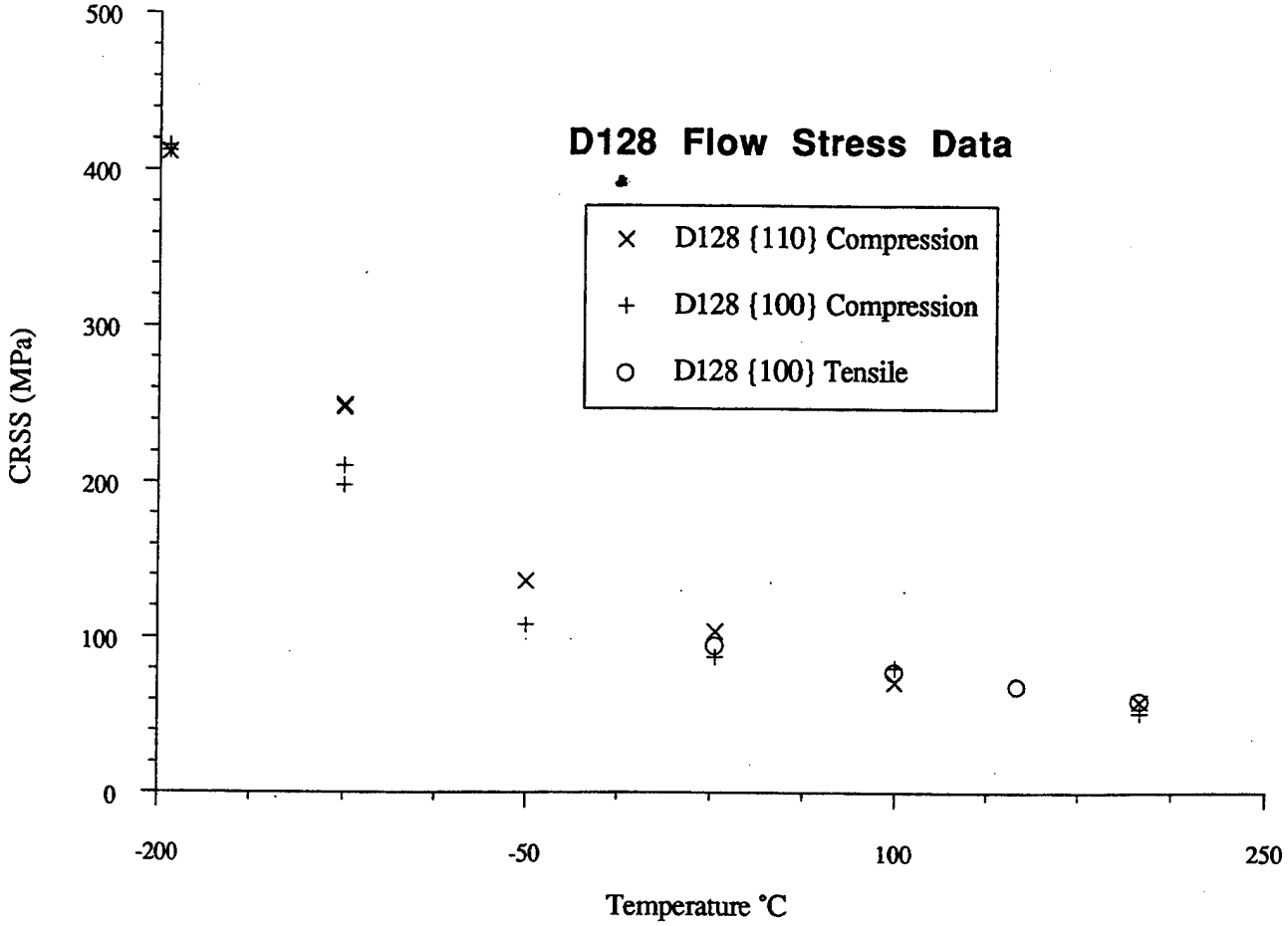

Figure 16. Flow stress (given in terms of critical resolved shear stress (CRSS) on the {110} and {100} planes) as a function of temperature taken from compression and tensile tests NiAl microalloyed with Ga (D128). CRSS values for the {110} plane were derived from specimens strained along the <111> direction. CRSS values for the {100} plane were derived from specimens strained along the <110> direction

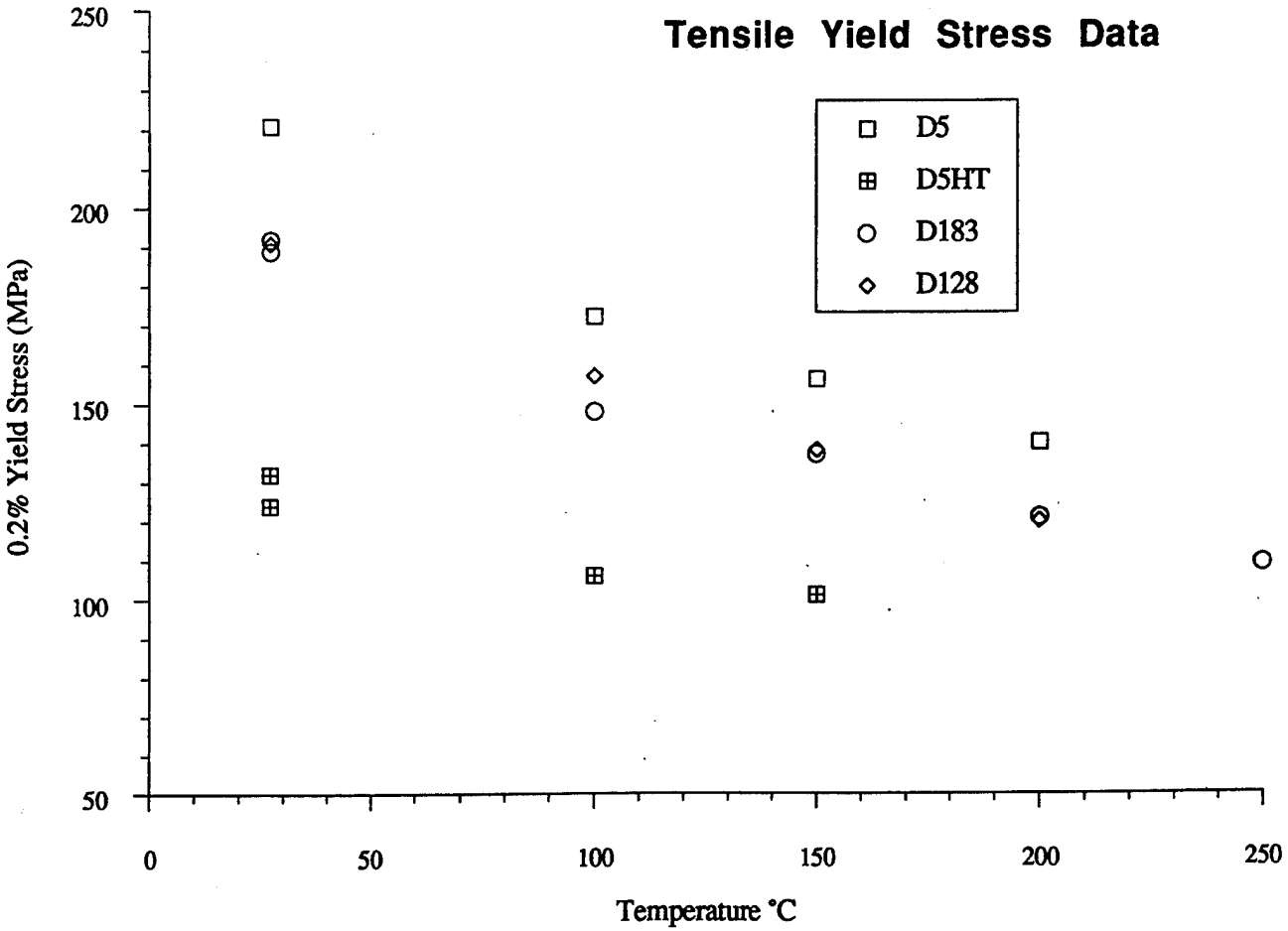

Figure 17. 0.2% yield stress as a function of temperature for <110> oriented tensile specimens.

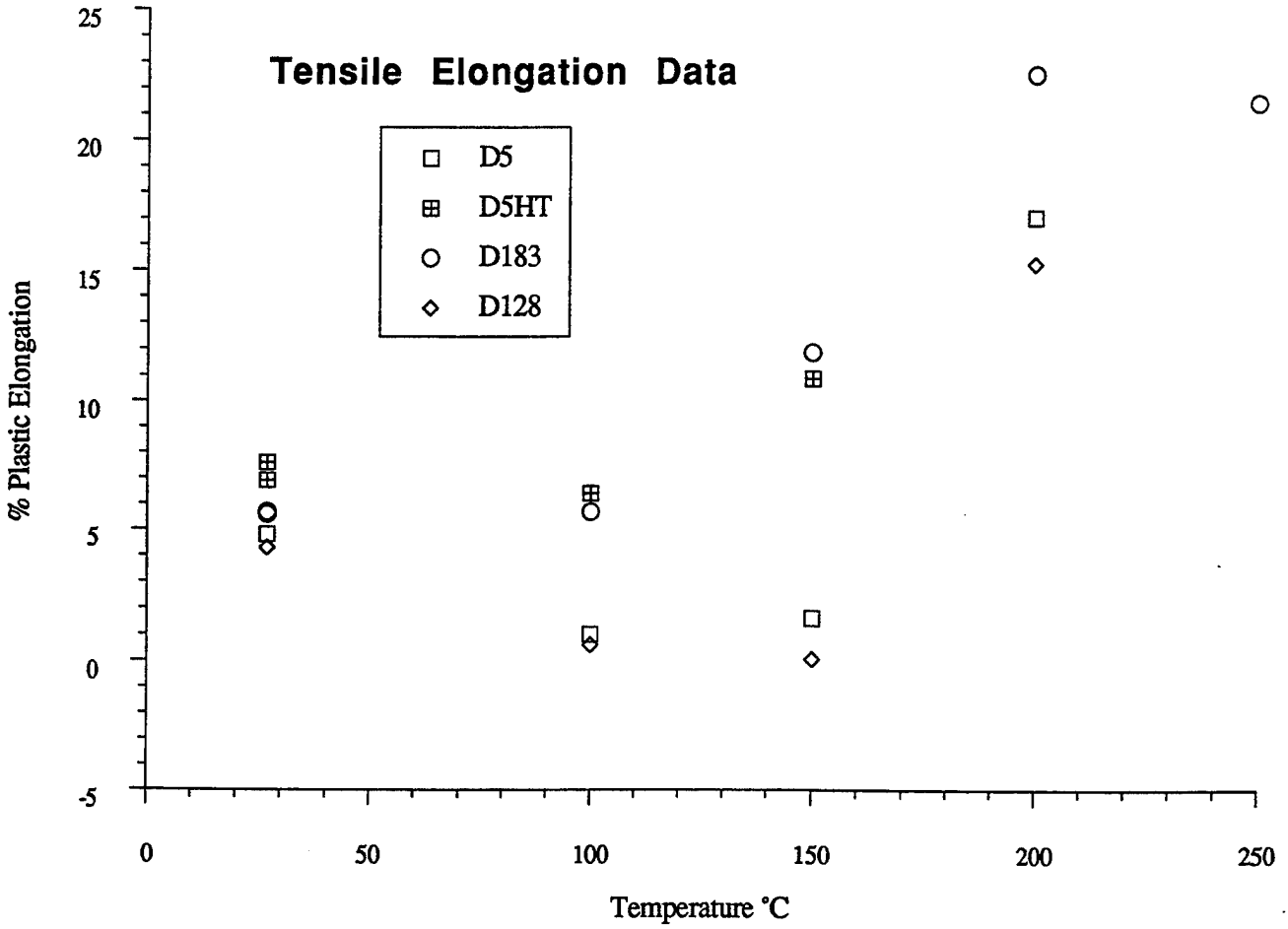

Figure 18. Plastic elongation as a function of temperature for <110> oriented tensile specimens.

seen throughout the course of this investigation. The values of the yield stress or the flow stress were reproducible and followed the expected trends, but scatter in the tensile ductility continued to plague the program. To understand this problem, a very systematic study was carried out to evaluate various variables which could affect the measured ductility. These included batch to batch variability of the single crystal castings particularly their carbon and oxygen contents, heat treatments, cooling rates, machining vendors, post grinding operations/surface preparation techniques such as electropolishing or chemical milling to remove the grinding marks introduced during machining and testing vendors particularly the alignment of the specimens. The results of this investigation are described in Section 3.11. It was concluded from this study that the surface preparation after machining played the most critical role in dramatically affecting the measured ductility. Room temperature tensile plastic elongations varied from about zero percent to about 8% for specimens with various post grinding operations/surface finishes while keeping all the other variables the same.

3.6.2 TEM Studies and Deformation Behavior of D5, D5HT and D183 Compression Specimens

TEM dislocation studies were performed on the D5, D5HT, and D183 compression specimens tested at –196 and 100°C in both <111> and <110> orientations, for a total of 12 specimens. All of the specimens were tested to approximately 2% plastic strain. For the purposes of relating specific Burgers vectors and slip planes in the TEM studies to the stress axes, these <111> and <110> axes are designated as [111] and [101], respectively. The –196°C specimens were studied since they represent the simplest cases in which thermal activation is minimized. At 100°C, the D5HT and D183 specimens displayed high levels of plastic elongation in tensile tests, while D5 was still below its DBTT at this temperature.

Burgers vector determinations were made using the invisibility criterion. Slip plane identifications were achieved by determining the planes on which bowed dislocations were lying, by means of trace analyses on two or more segments of each dislocation. Trace analyses of straight dislocations were also used, as well as the elongation directions of dipole loops. These last features were assumed to have been deposited from superjogs on moving screw dislocations, and thus elongated along directions perpendicular to their Burgers vectors in the slip plane [21,25,26].

Low magnification micrographs showing the general dislocation distributions in all of the specimens studied are shown in Figures 19-24. The dislocation structures in these specimens were similar for the same orientations and temperature, regardless of alloy and heat treatment. As expected, <100> Burgers vectors were observed in all of the specimens. All of the data indicate that the {110} slip planes are active in <111> oriented specimens and the {100} slip planes are active in <110> oriented specimens, at both temperatures studied. This is consistent with the resolved shear stresses on these planes for the two orientations: the {110} plane has the higher Schmid factor for the <111> orientation (0.47 vs. 0.33), while the {100} plane has the higher Schmid factor for the <110> orientation (0.5 vs. 0.35). Most of the dislocations present in the specimens were debris, rather than actively slipping dislocations. The debris consists of elongated loops and dislocations not lying on slip planes.

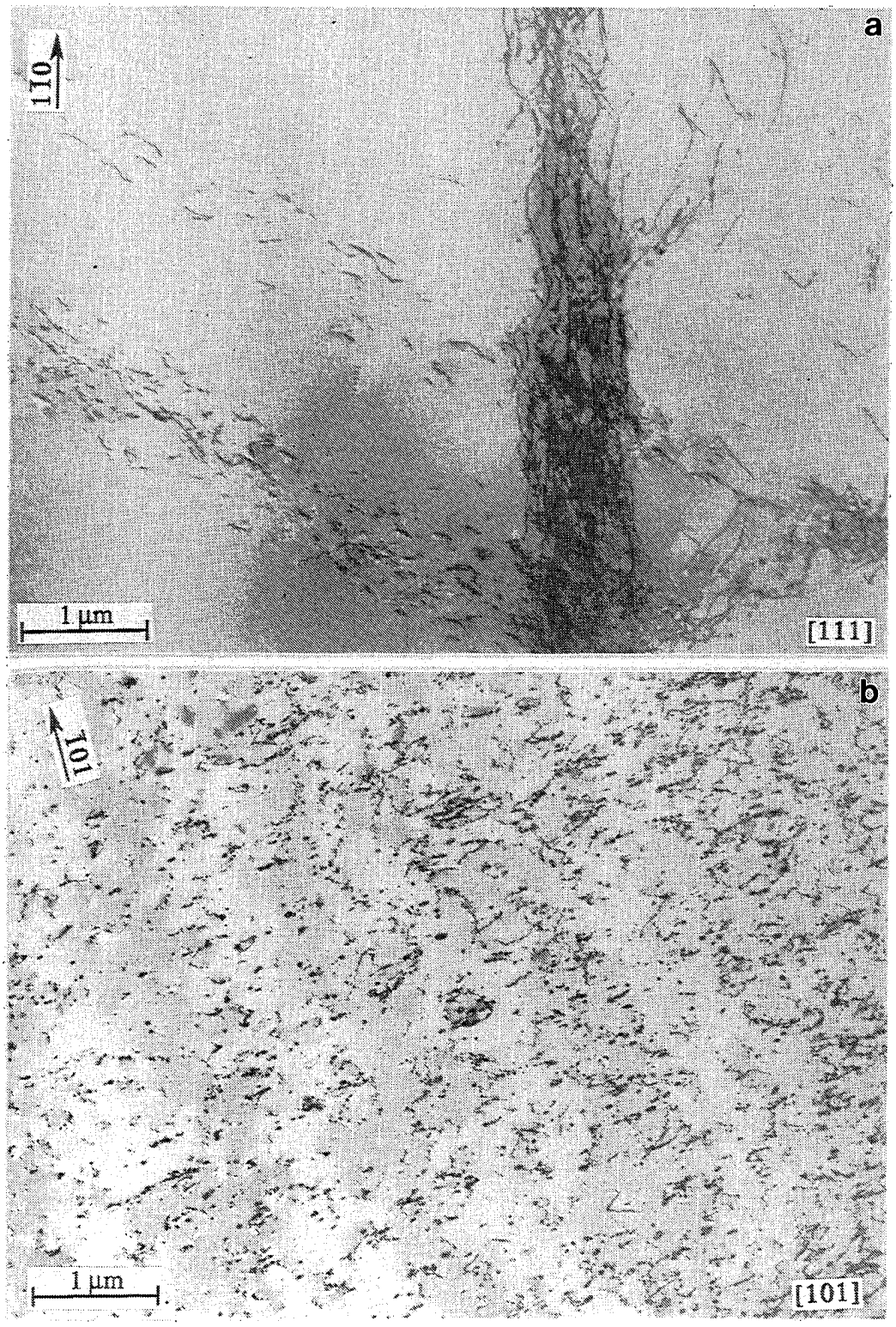

Figure 19. Low magnification TEM image taken from compression specimens of stoichiometric NiAl given the standard heat treatment (D5), tested at -196°C. Stress axis: a) [111], b) [101].

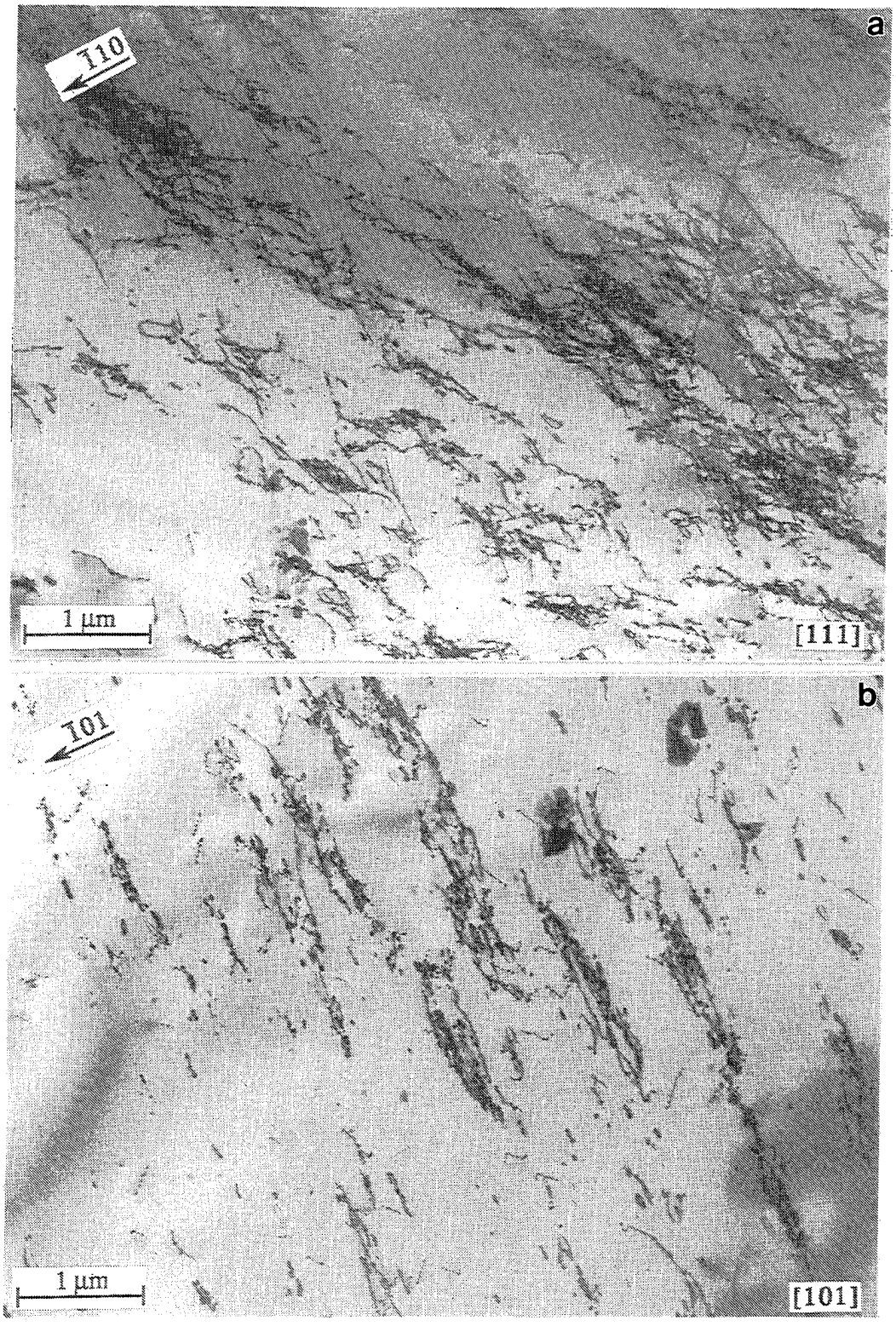

Figure 20. Low magnification TEM image taken from compression specimens of stoichiometric NiAl given the standard heat treatment (D5), tested at 100°C. Stress axis: a) [111], b) [101.

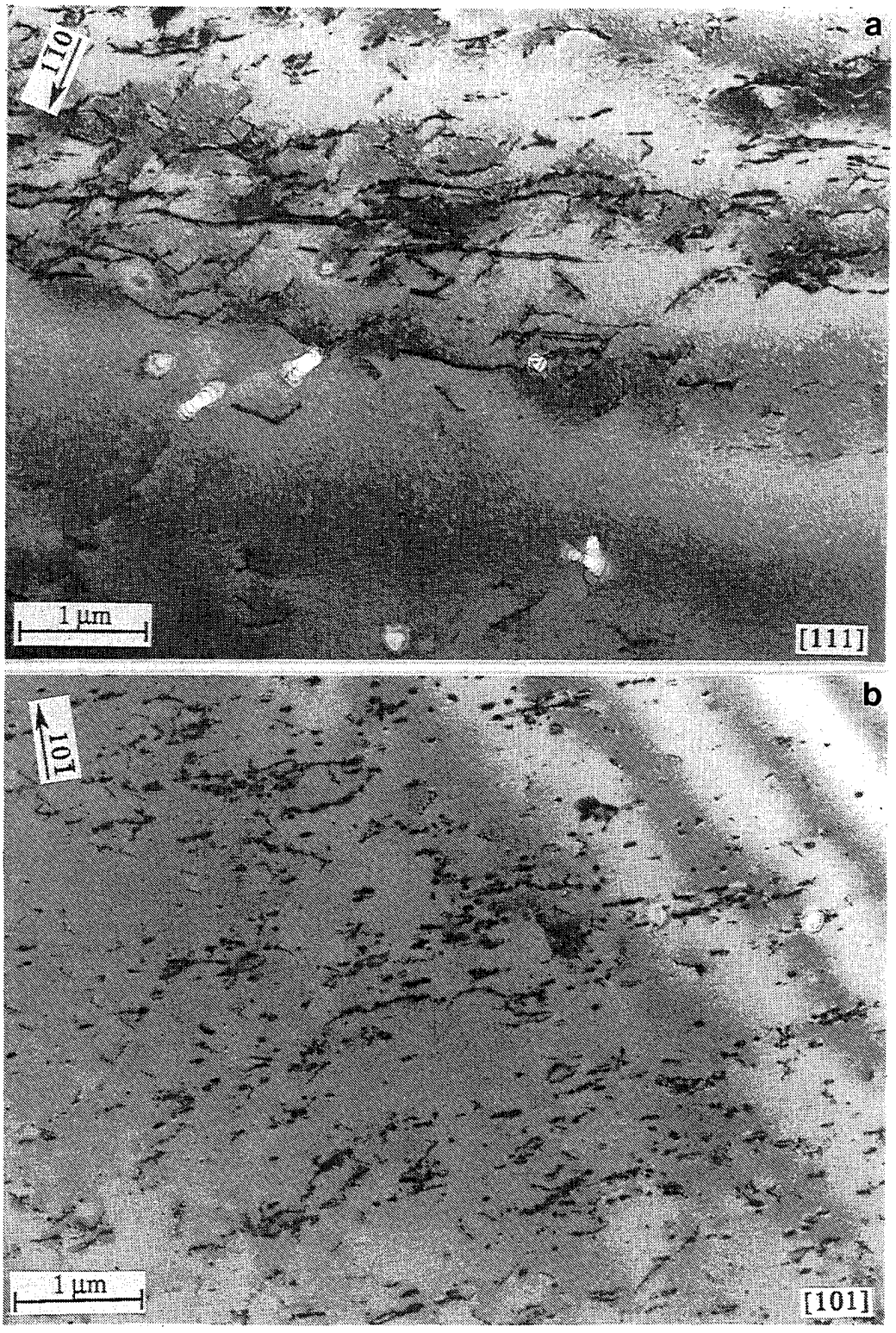

Figure 21. Low magnification TEM image taken from compression specimens of stoichiometric NiAl given an 800°C anneal (D5HT), tested at -196°C. Stress axis: a) [111], b) [101].

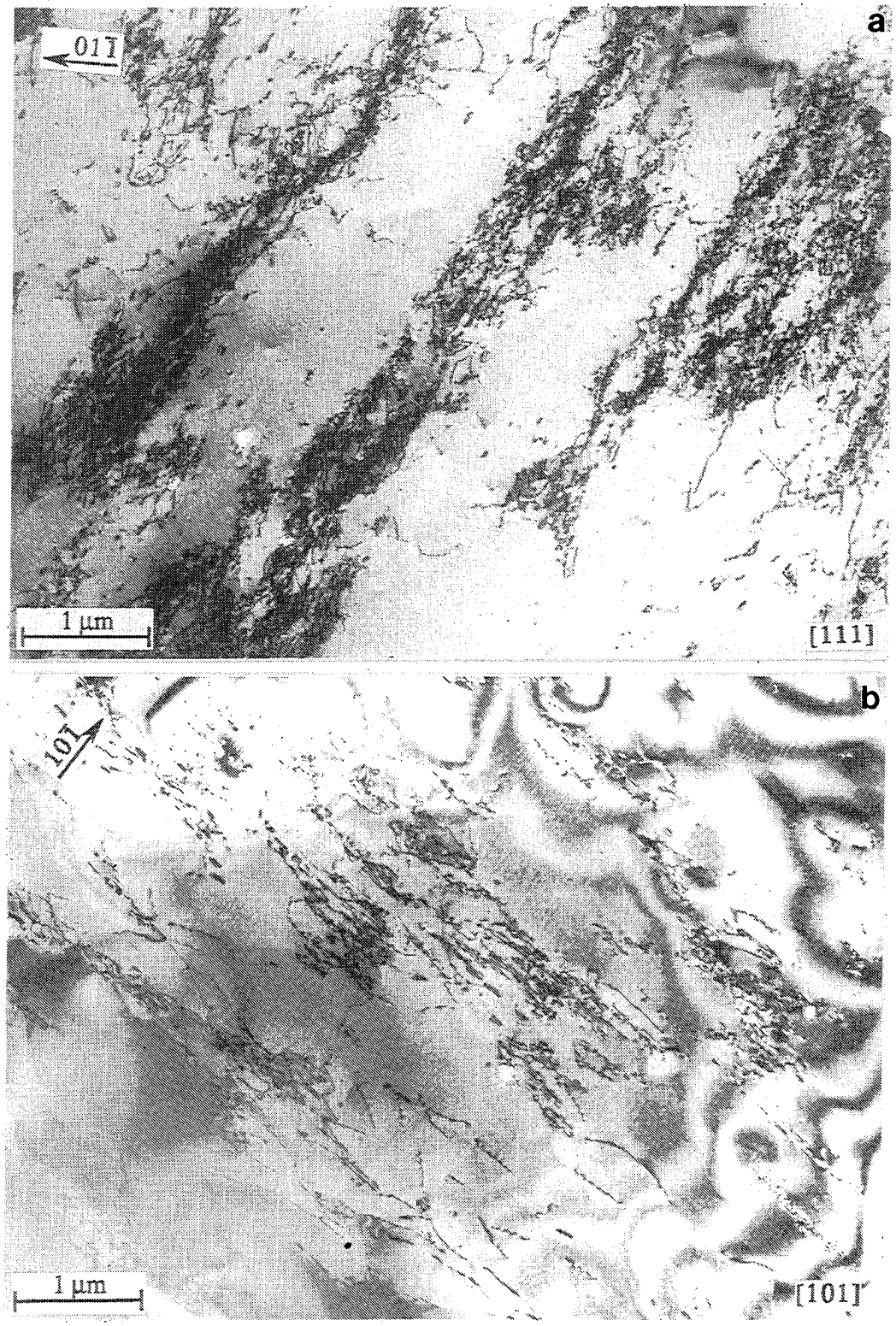

Figure 22. Low magnification TEM image taken from compression specimens of stoichiometric NiAl given an 800°C anneal (D5HT), tested at 100°C. Stress axis: a) [111], b) [101].

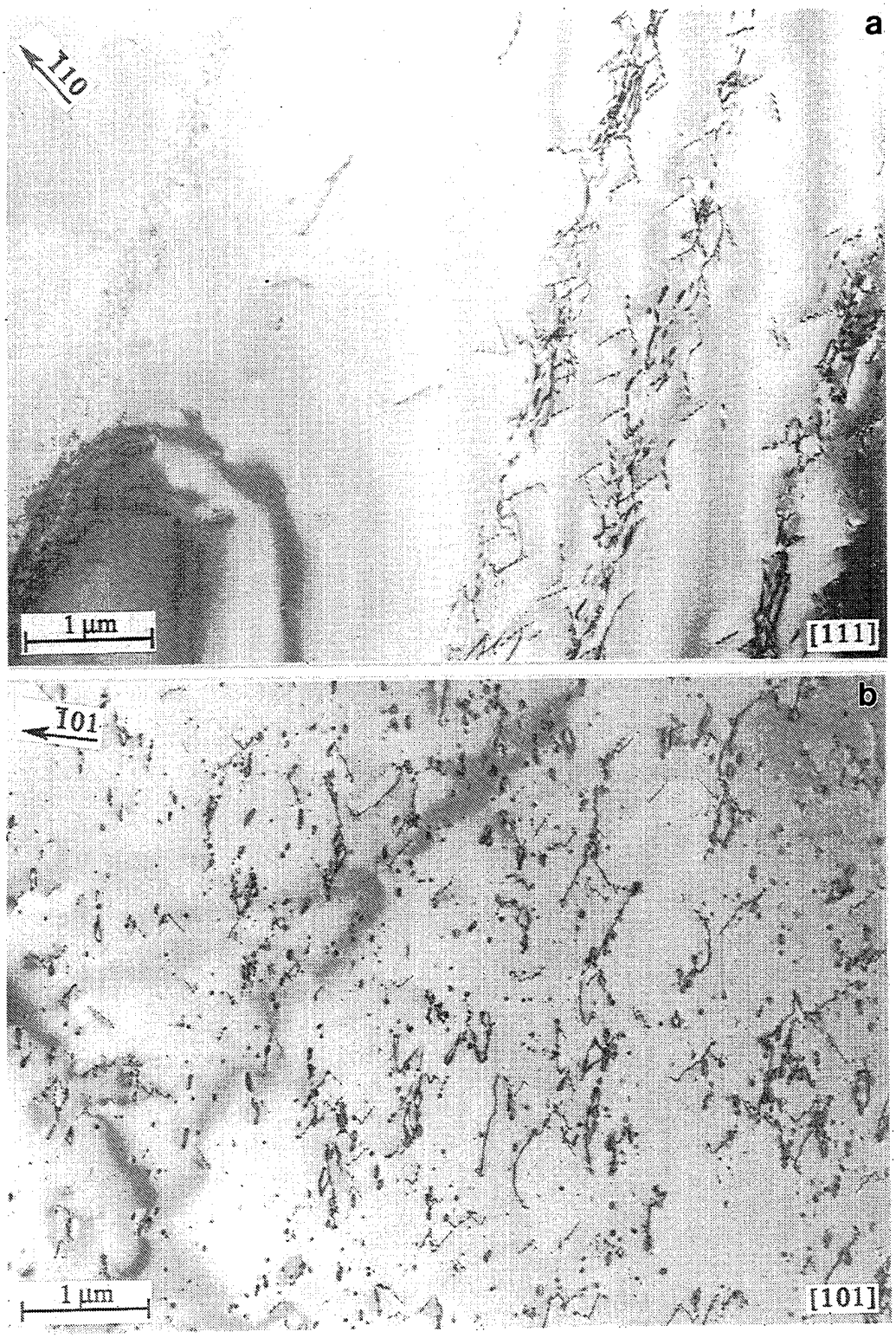

Figure 23. Low magnification TEM image taken from compression specimens of NiAl microalloyed with Fe (D183), tested at -196°C. Stress axis: a) [111], b) [101].

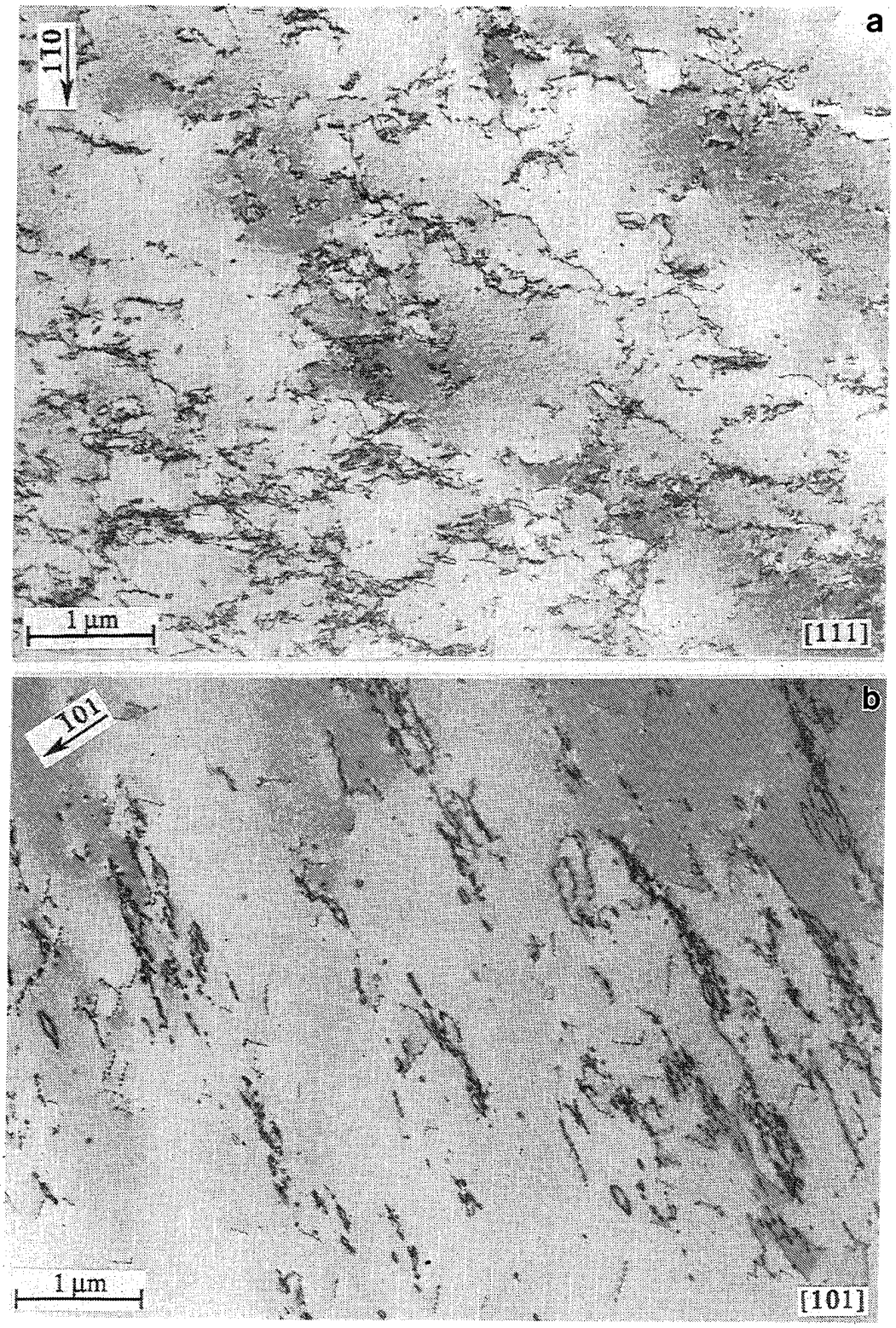

Figure 24. Low magnification TEM image taken from compression specimens of NiAl microalloyed with Fe (D183), tested at 100°C. Stress axis: a) [111], b) [101].

At –196°C, the <111> oriented specimens exhibited distinct slip bands, each containing dislocations all possessing the same Burger vector. This orientation and temperature yielded the highest percentage of dislocations actually on slip planes, and thus the most easily interpreted dislocation structures. It is interesting to note that the work hardening rates for <111> oriented specimens tested at –196°C were lower than those at any other temperature and orientation. This is consistent with the lower degree of dislocation interaction observed in these specimens. At 100°C, a cellular structure developed, with tight tangles surrounding areas of lower dislocation density. Many of the dislocations in the latter areas were found to lie on or close to slip planes. This may represent a further development of the slip band structure, forming as individual slip bands intersect and dislocation density increases. The <110> oriented specimens tested at –196°C had a very homogeneous dislocation distribution, consisting mostly of debris, with no evidence of slip bands or dislocation tangles. At 100°C, a cellular structure developed, similar to that for the <111> oriented specimens tested at the same temperature. As at –196°C, bowed dislocations seldom lay entirely on slip planes. Most of them appeared to have high densities of superjogs.

Figures 25-31 are higher magnification micrographs showing details of the dislocation structures. Since the same orientation and temperature gave similar dislocation structures, examples are given from different alloys to illustrate typically observed features for each orientation/temperature.

Figure 25 is a weak beam micrograph taken from a [111] oriented D183 specimen tested at –196°C, showing the details of the dislocation structure in an individual slip band. The dislocations in this band have a [100] Burgers vector. Several examples of bowed out dislocations and elongated loops can be seen in this micrograph. Trace analysis of two segments of a bowed dislocation (labeled "1" in the figure) showed it to lie on a (011) plane. Several other bowed dislocations appeared to be on the same plane when viewed in stereo pair micrographs. Two loops were analyzed; both were elongated along directions contained within the (011) plane, one along a direction ~6° from [01$\bar{1}$], the other ~24° away (labeled "2" and "3" in the figure, respectively). Stereo pair micrographs revealed that most of the other loops were approximately parallel to these, especially the loop elongated nearer to [01$\bar{1}$]. Several straight dislocations, parallel to each other, were also observed in the stereo pair micrographs. Trace analysis of one of these (labeled "4" in the figure) yielded a line direction of [32~2], consistent with a (011) slip plane. This orientation results in a minimum in line energy for b=[100] dislocations on (011) in NiAl, as determined from anisotropic elasticity calculations [27].

Figure 26 is a weak beam micrograph taken from a [101] oriented D183 specimen also tested at –196°C. Most of the dislocations appear to be debris, with large numbers of elongated loops. Trace analysis of one of these loops with b=[001] (labeled "1" in the micrograph) showed it to be elongated along [010]. Most of the other loops appeared to be approximately parallel to this one when viewed in stereo pair micrographs, consistent with a (100) slip plane. The bowed dislocation in the center of the micrograph (labeled "2") has a [001] Burgers vector and appears to be lying approximately on the (100) plane in the stereo pair micrographs, although it does not appear to lying entirely on a single plane. This observation was confirmed by trace analysis of 4 segments along its length. The segments were found to have line directions anywhere from ~0° (a segment near [010]) to 18° off of the (100) plane. This dislocation structure, consisting primarily

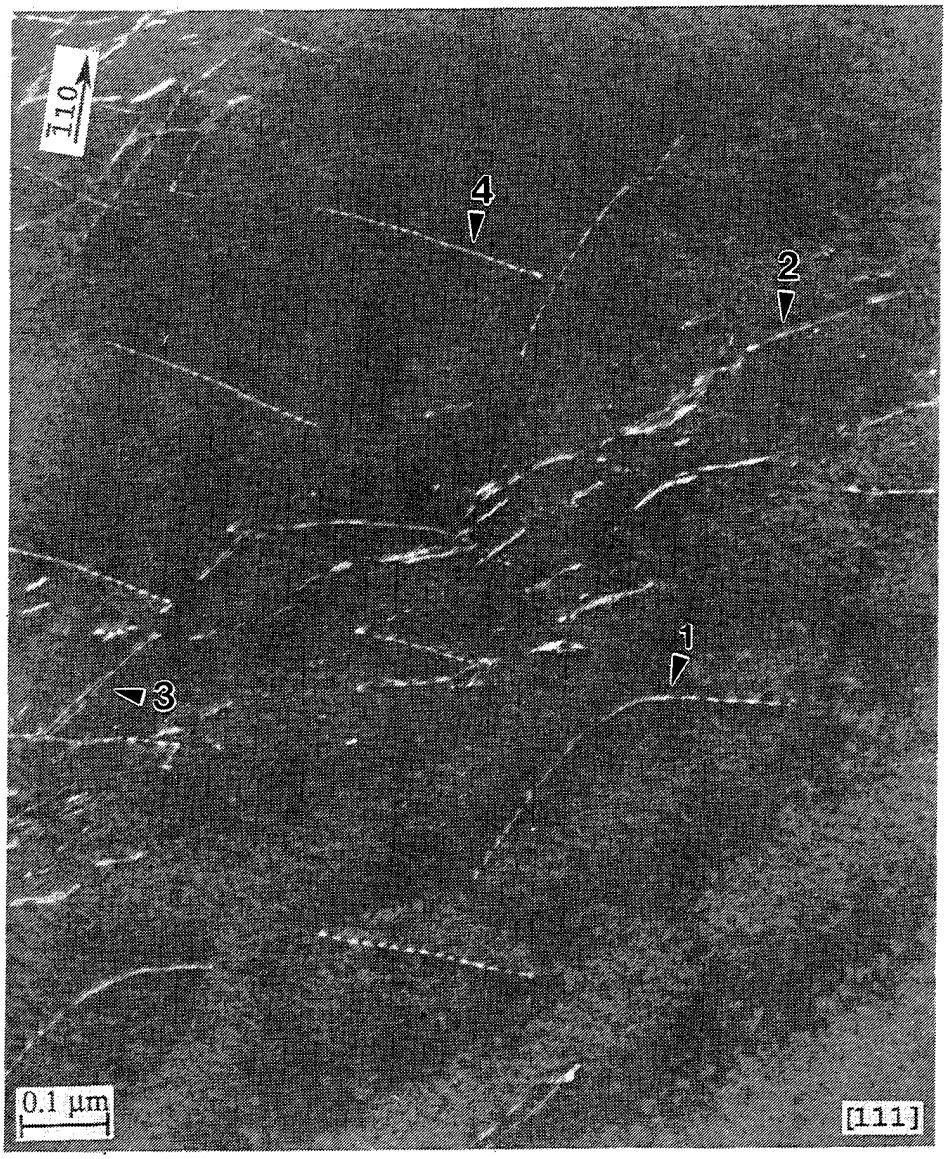

Figure 25. Weak beam TEM micrograph taken from a [111] oriented D183 compression specimen tested to ~2% plastic strain at –196°C. The dislocations in this slip band have [001] Burgers vectors. Trace analyses were performed on the bowed dislocation, labeled "1", and on the elongated loops, labeled "2" and "3".

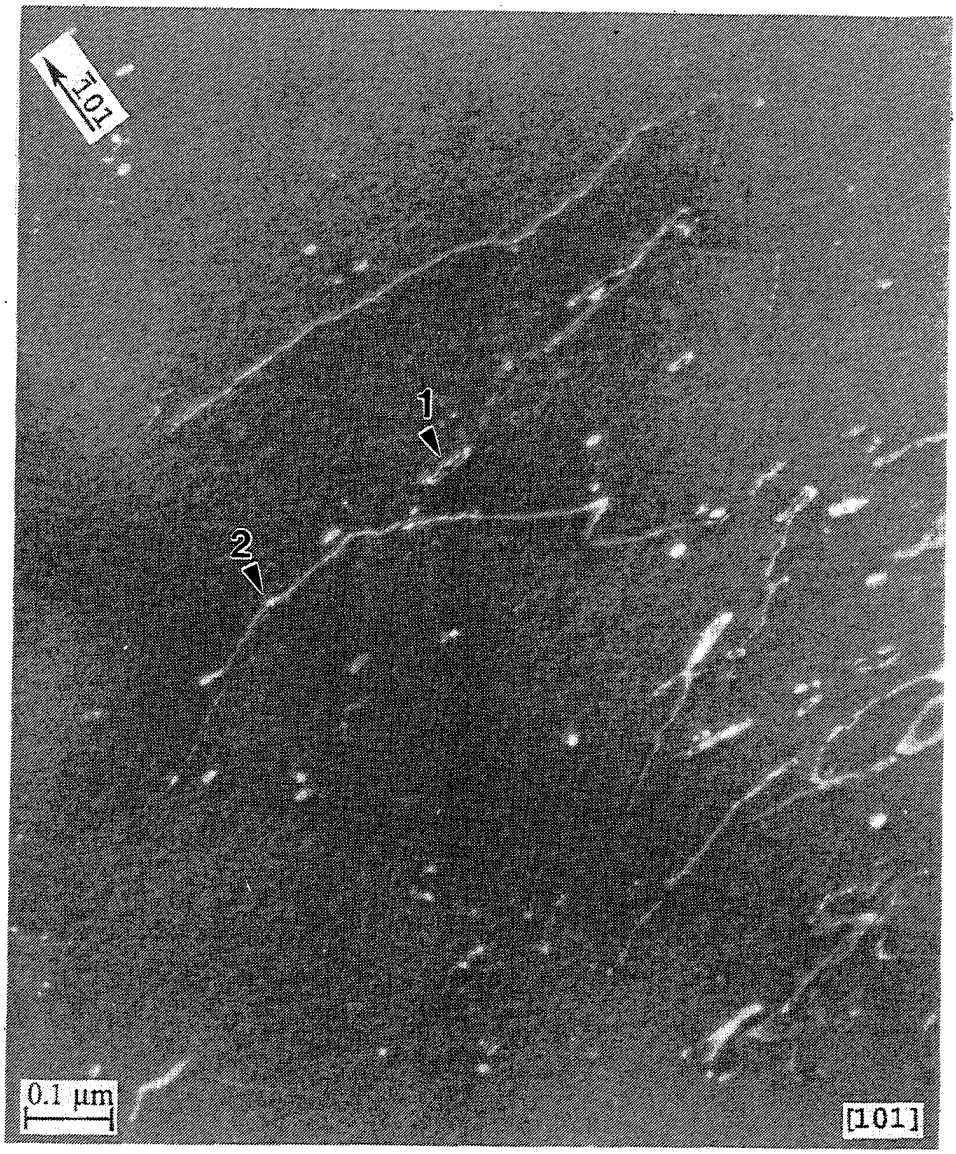

Figure 26. Weak beam TEM micrograph taken from a [101] oriented D183 compression specimen tested to ~2% plastic strain at –196°C. Trace analyses were performed on the elongated loop, labeled "1", and bowed dislocation, labeled "2". Both have [001] Burgers vectors. Note the jagged nature of the dislocation line.

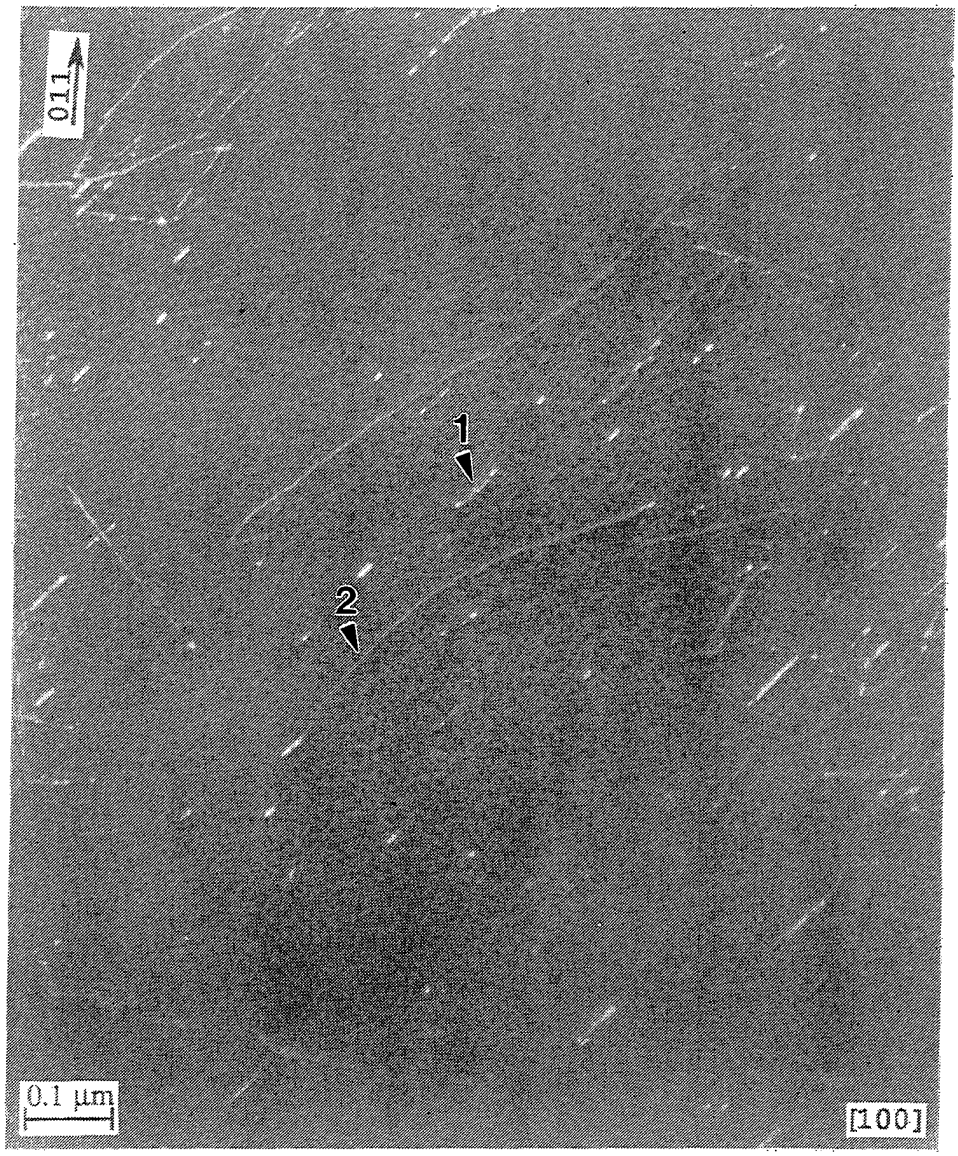

Figure 27. Weak beam TEM micrograph taken from a [101] oriented D183 compression specimen tested to ~2% plastic strain at –196°C. Same area as shown in Figure 26, but with a different beam direction. Trace analyses were performed on the elongated loop, labeled "1", and bowed dislocation, labeled "2". Both have [001] Burgers vectors. Note the smoothness of the dislocation as viewed from this orientation, compared to the image in Figure 26.

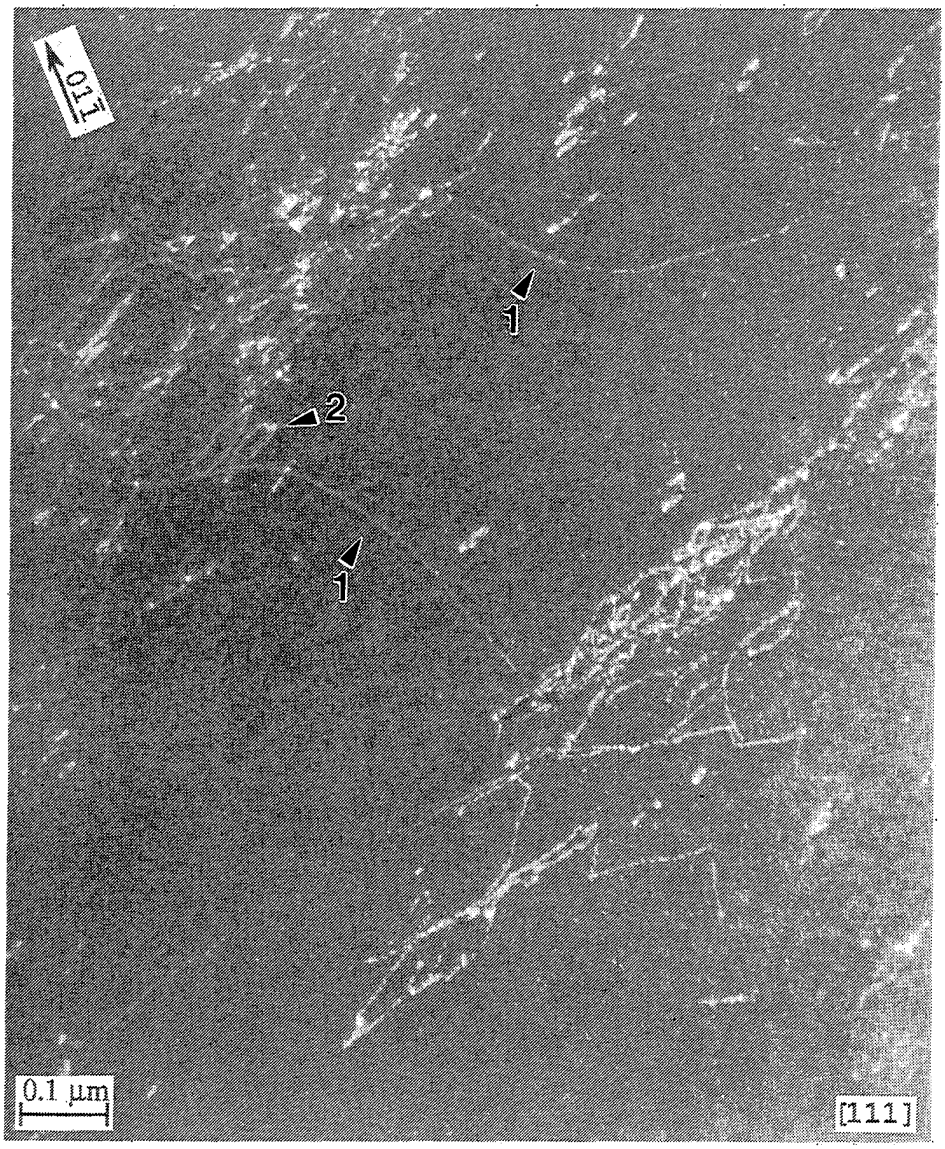

Figure 28. Weak beam TEM micrograph taken from a [111] oriented D5 specimen tested to ~2% plastic strain at 100°C. Trace analyses were performed on the two curved dislocations labeled "1" (b=[001]) and the elongated loop labeled "2" (b=[010]).

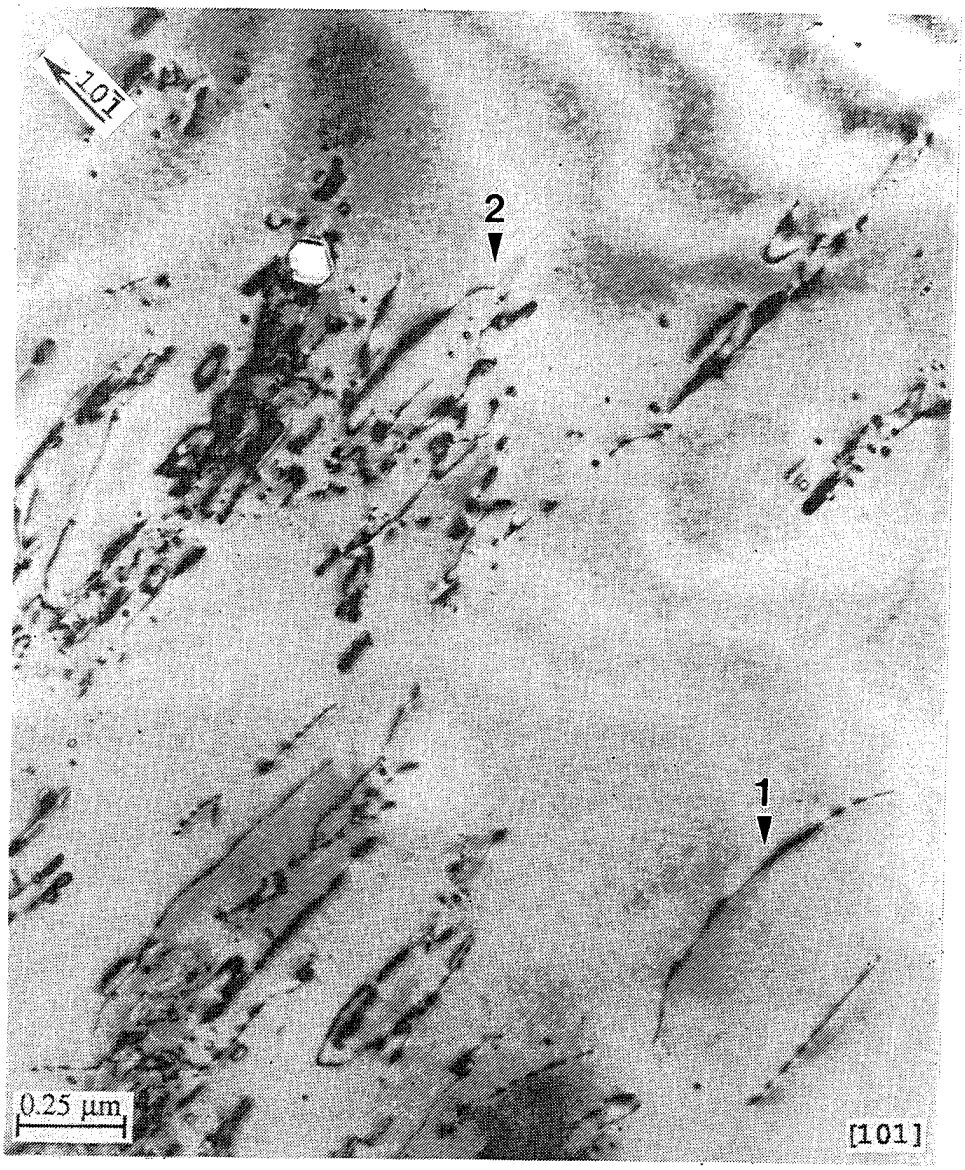

Figure 29. Bright field TEM micrograph taken from a [101] oriented D5HT compression specimen tested to ~2% plastic strain at 100°C. Trace analyses were performed on the dislocations labeled "1" and "2". Both have [100] Burgers vectors.

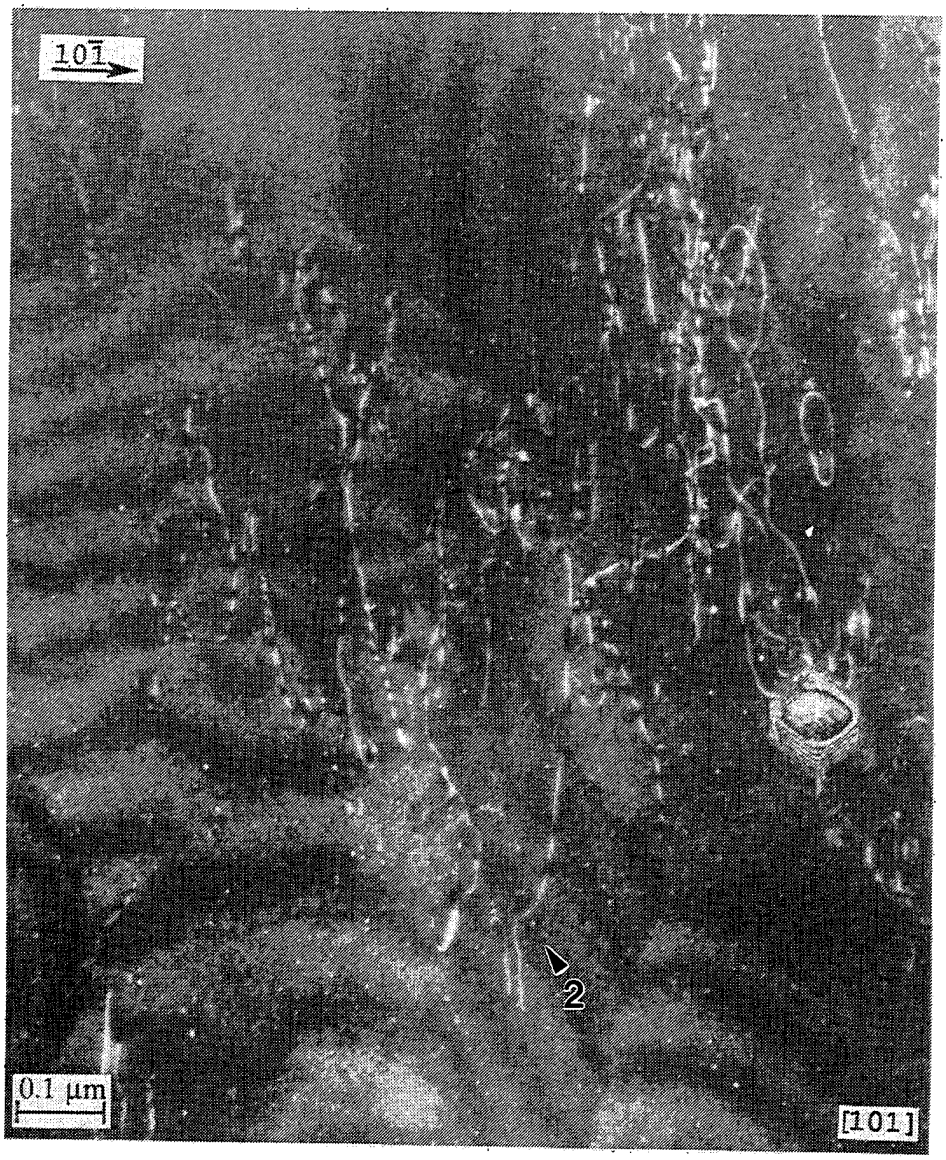

Figure 30. Weak beam TEM micrograph taken from a [101] oriented D5HT compression specimen tested to ~2% plastic strain at 100°C. Higher magnification micrograph showing details of the b=[100] dislocation labeled "2" in Figure 29. Note that this image is rotated approximately 135° clockwise with respect to the image in Figure 29.

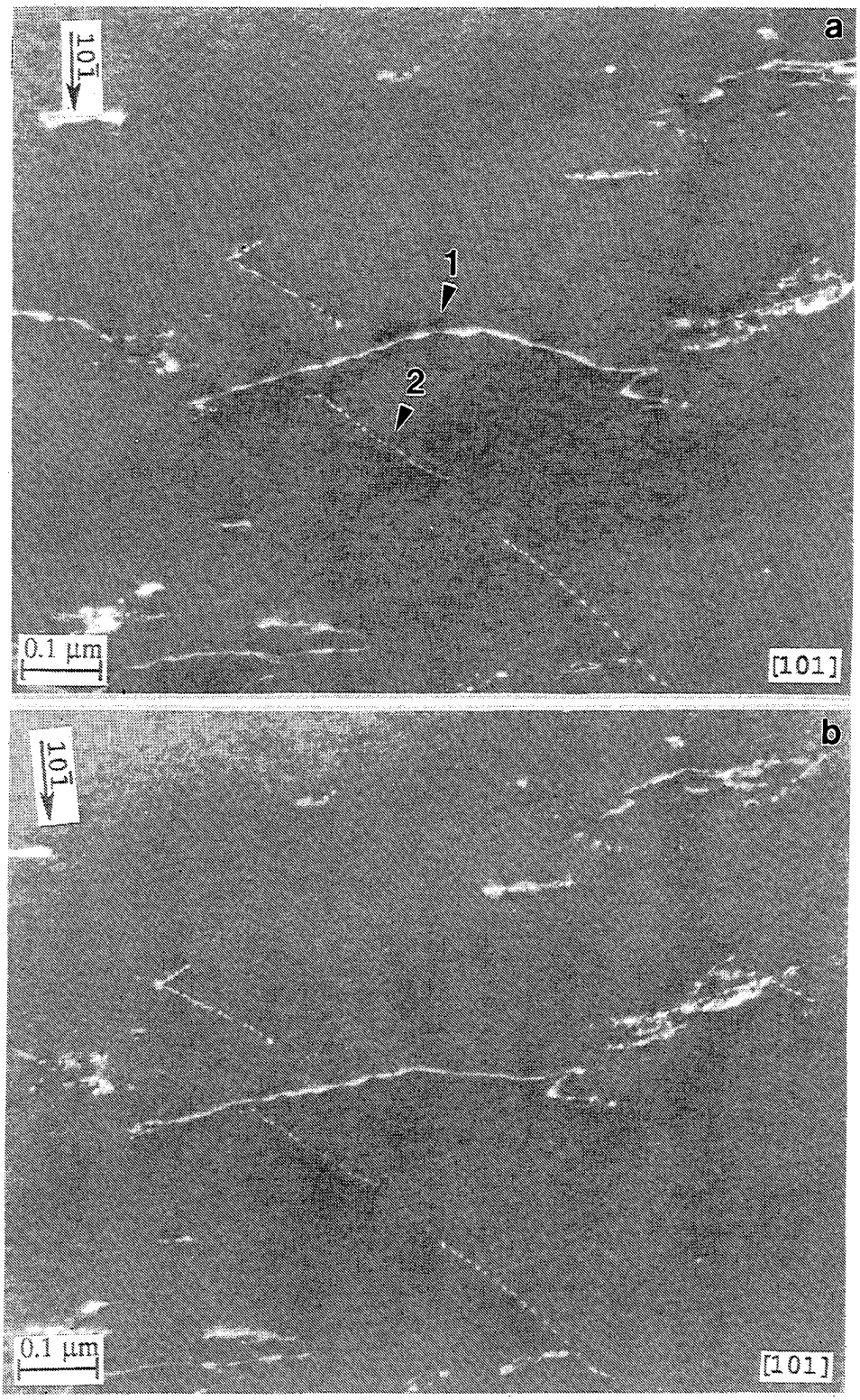

Figure 31. Weak beam TEM micrographs taken from a [101] oriented D183 compression specimen tested to ~2% plastic strain at 100°C. Trace analyses were performed on the bowed dislocation, labeled "1" , and the straight dislocation, labeled "2". Both have [001] Burgers vectors. The dislocation labeled "1" moved during the analysis. Micrographs a) and b) were taken before and after the dislocation moved, respectively.

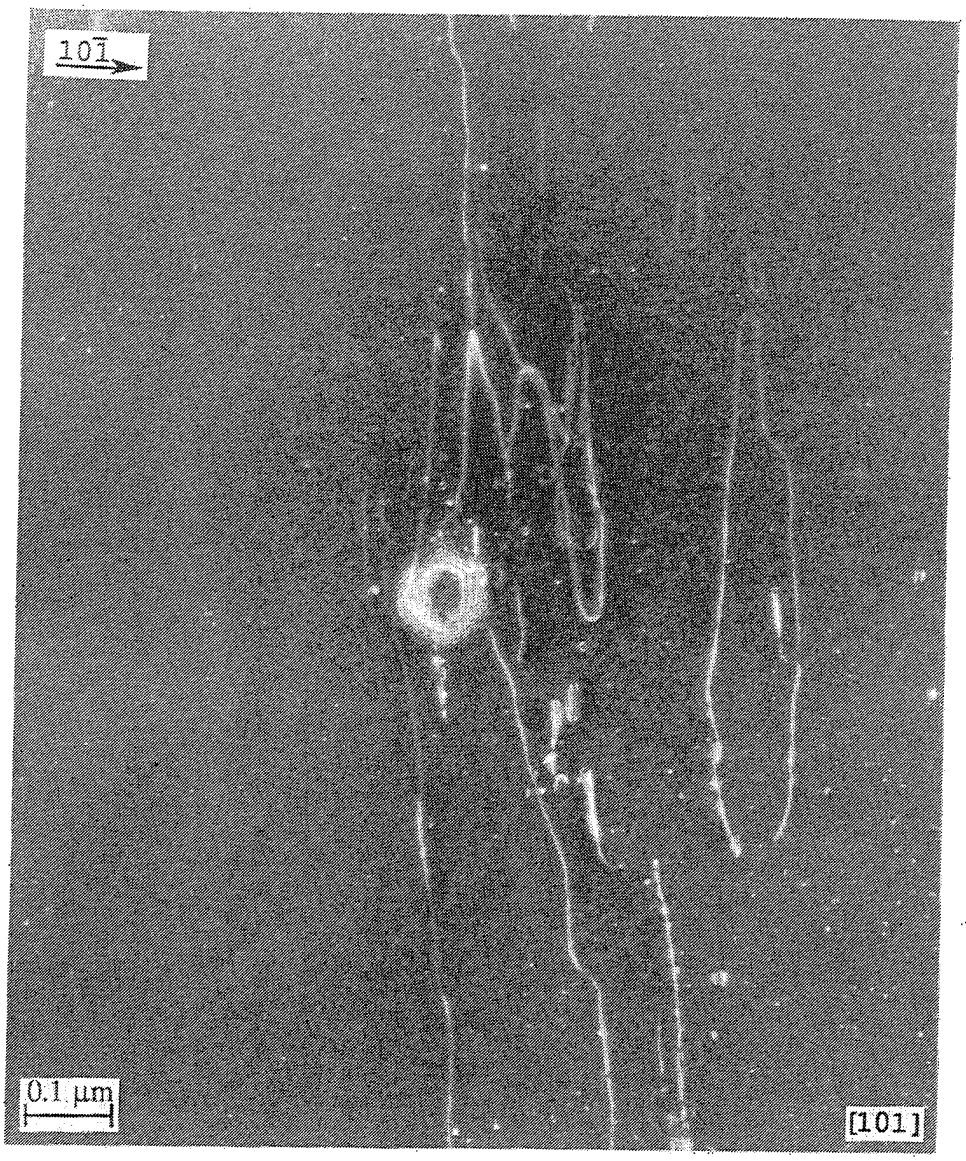

Figure 32. Weak beam TEM micrograph showing an example of a faceted void observed in all of the D5HT specimens. The micrograph was taken from a [101] oriented D5HT compression specimen tested to ~2% plastic strain at 100°C.

of debris with "non-planar" curved dislocations, is typical of NiAl specimens strained along [101]. Another feature of interest, also observed in other [101] specimens, is that the bowed b=[001] dislocation appears to be smooth when viewed using a [100] beam direction (ie. perpendicular to the (100) plane), as shown in Figure 27. The dislocation is jagged in appearance when view from other directions, as can be seen in Figure 26, which was taken using a [101] beam direction. If the slip plane for this dislocation is (100), this jagged appearance represents a high density of superjogs along its length. This would be expected to severely hamper the motion of the dislocation on the (100) plane and would also give rise to the large number of elongated loops.

Figure 28 is a weak beam micrograph taken from a [111] oriented D5 specimen tested at 100°C. Most of the dislocations have [010] Burgers vectors, but two bowed b=[001] dislocations are also present (labeled "1" in the micrograph). Trace analyses on these two bowed dislocations (2 segments on each) showed that they lie very close to (110) slip planes; plane traces for the two line directions intersected 8-10° from the (110). Large quantities of elongated loops are also observed. A trace analysis of one loop (labeled "2" in the micrograph) with b=[010] yielded an elongation direction ~5° from [101], consistent with a (101) slip plane. Most of the other loops appear to be approximately parallel to this one.

Figure 29 is a bright field micrograph taken from a [101] oriented D5HT specimen tested at 100°C. Although the dislocations for this orientation and temperature consist mainly of debris, as in the –196°C [101] oriented specimens, some bowed dislocations lying on slip planes were occasionally observed. The bowed dislocation marked "1" in Figure 29 is an example. This dislocation has a [100] Burgers vector. Three segments of a bowed b=[100] dislocation were analyzed. All three segments were found to be within a few degrees of lying on the (001), well within the errors of the trace analysis technique. The dislocation marked "2" in Figure 29 is seen at higher magnification in Figure 30. A dipole loop is still attached to this dislocation. The loop has a [100] Burgers vector and is elongated approximately along [010] (10° off), consistent with a (001) slip plane. The long segment of the dislocation line to which the loop is attached was also analyzed. Its line direction is contained within the (001) plane, approximately 10° from [010], further evidence of slip on (001).

Another example from a [101] oriented specimen tested at 100°C (D183) is shown in Figure 31. During the course of the analysis, the center of the bowed out section of a b=[001] dislocation (labeled "1" in Figure 31a) moved. Stereo pair micrographs taken before and after this event suggested that it was bowed out on a (100) slip plane and relaxed (ie. straightened) under the electron beam. The fact that it was able to relax, aided by the activation energy provided by heating of the specimen by the beam, suggests that it lay on a slip plane. Trace analysis was performed on 3 segments of the dislocation after it moved. A line direction of [071] was determined for the center section, consistent with a (100) slip plane. The other two segments are slightly off the (100) trace. Several parallel straight b=[001] dislocations can also be seen in the micrographs. Trace analysis of one of these (labeled "2" in Figure 31a) yielded a line direction of ~[0~23], again consistent with a (100) slip plane.

Faceted voids were observed in all of the specimens receiving the 800°C heat treatment (ie D5HT). These were studied in more detail in the [101] oriented specimen tested at 100°C. After

electropolishing, the specimen was ion milled for approximately 1/2 hour, thus eliminating the possibility that the voids resulted from particles being electropolished out of the foil. The features still appeared to be voids, even in relatively thick areas of the foil. A stereo pair was taken of the void shown in Figure 32, which was found in a thick region. The void appears to be totally enclosed within the foil when viewed in the stereo pair. There is no evidence of a precipitate (ie. extra reflections in diffraction patterns, contrast other than that of the matrix, or changes in EDS spectra with respect to the matrix). These voids probably formed from condensation of excess vacancies trapped from higher temperature heat treatments.

3.7 Serrated Yielding

In the first year of mechanical testing with some of the NiAl alloys, a serrated yielding phenomenon was observed. This was particularly evident in the compression specimens, but was also observed during the tensile tests. Serrated yielding was observed in two different temperature ranges for the D5 specimens: in the -125°C tests and in the 100 to 250°C range (ie. around the DBTT). The effect disappeared at -125°C for the D5HT and D128 specimens, and was significantly reduced for the D183 specimens; however, the serrated yielding persisted for all of the alloys/heat treatments at the higher temperatures. Examples of compression stress-strain curves for D5 and D183 are shown in Figures 33 and 34. Serrated yielding (or "jerky glide") suggests a point defect/dislocation interaction (i.e.. the dynamic strain aging effect) [28,29]. Therefore, the serrated yielding behavior was very systematically studied as a function of alloy composition, heat treatments, test temperatures and strain rate. For these experiments, compression tests were performed on solution heat treated NiAl (D5), NiAl with a subsequent 800°C exposure (D5HT), and NiAl + 0.1 at% Fe (D183). Later on, high purity NiAl was also evaluated for strain aging effects.

3.7.1 Serrated Yielding Experiments with Constant Strain Rate

The majority of the stress vs. strain plots generated in the first three years of this study had excessive instrument noises arising from testing apparatus set-up parameters which appear to exacerbate serrated yielding effects in these alloys, to the point where it is difficult to separate real effects from artifacts from the testing apparatus. Instabilities were also observed in the elastic regions of the curve. These were later identified as instrumentation artifacts. Examples of such stress vs. strain plots are shown in Figures 35-46. The tests were performed using an Instron 8561 frame with a 8.9kN load cell and an electric actuator. Experiments were conducted under strain rate control, in which the strain rate was kept constant via a feed-back loop/signal from the strain gage attached either to the specimen gage or to the cross head. In an attempt to keep a constant strain rate, signal from the strain gage was continually fed to the specimen displacement controls. Such an attempt caused excessive noise in the recording even though several loop gains (frequency of strain rate adjustments) were evaluated. Specimens from a single casting ((D5-2154) were used to assess the instrumental factors affecting the observed serration effects. By adjusting the loop gain (in strain control), the severity of the serrations was observed to vary in intensity. In Figure 38, for example, a loop gain of 20 in a 200°C test (8.3×10^{-5}/s) results in large amplitude, rounded serrations. Adjusting the loop gain to 30 gives rise to lower amplitude, less rounded serrations as shown in Figure 39. The same experiment at room temperature yields serrations only

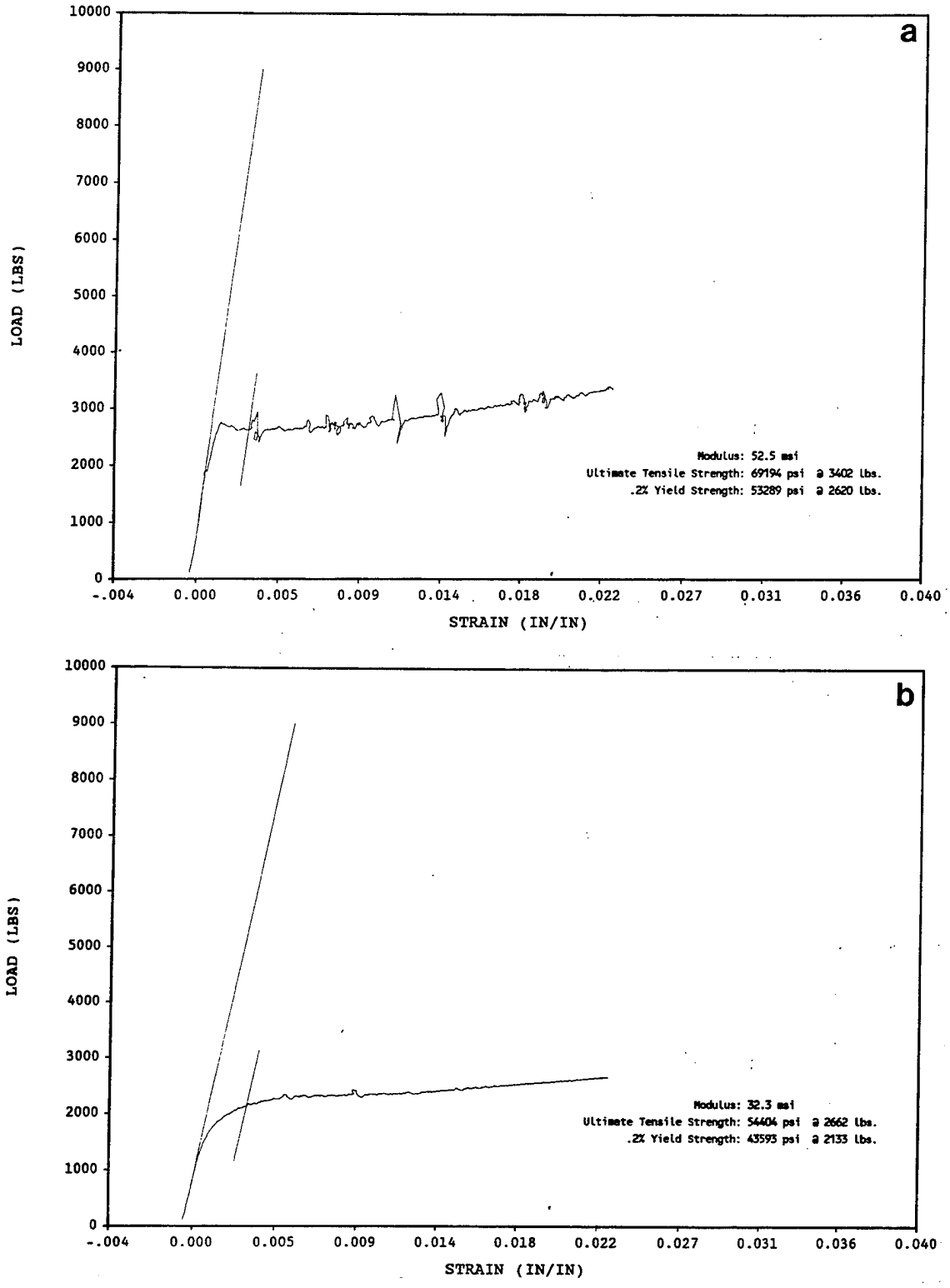

Figure 33. Stress-strain curves showing serrated yielding in -125°C compression tests. a) D5, b) D183.

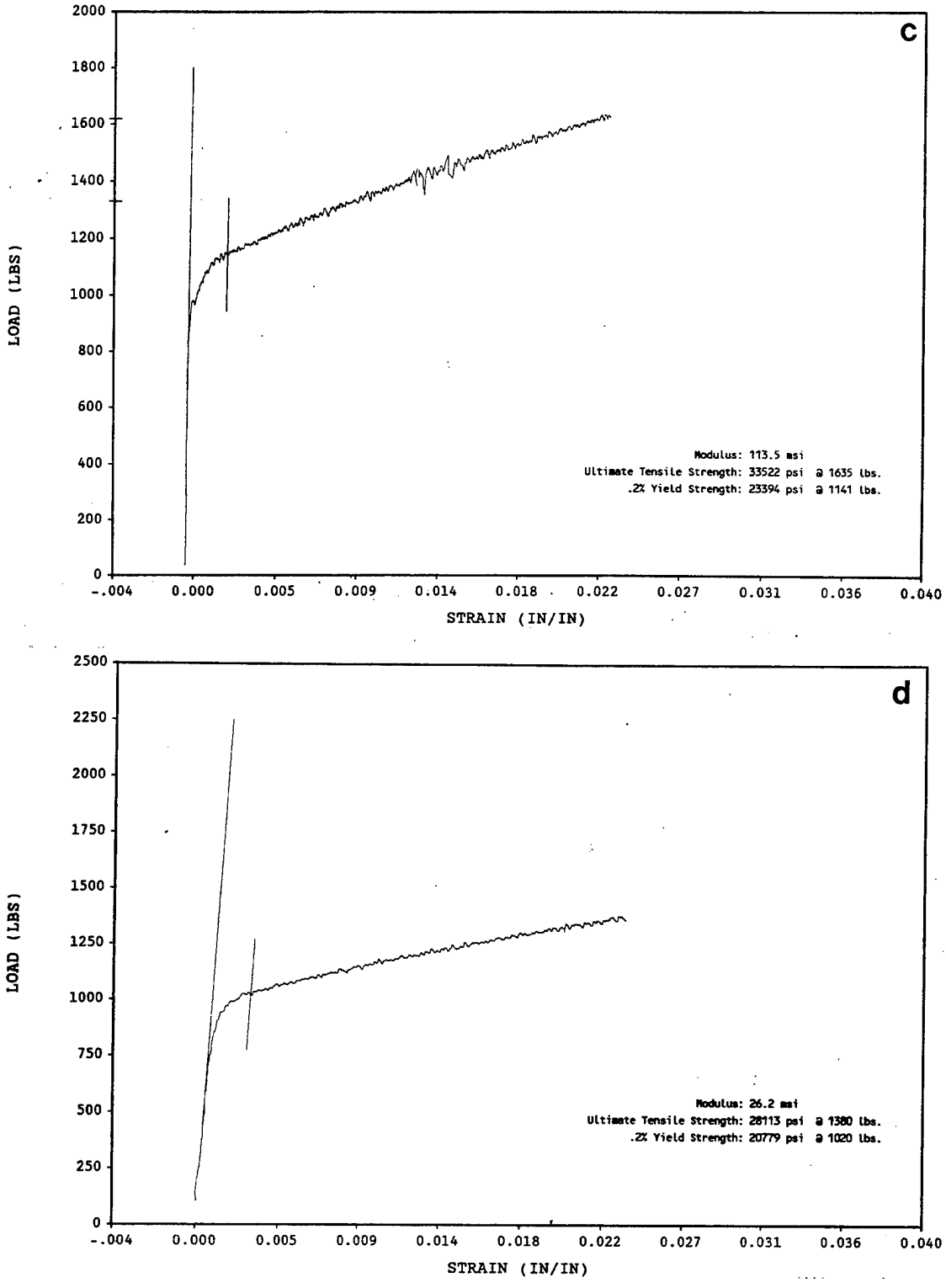

Figure 34. Stress-strain curves showing serrated yielding in 100°C compression tests. a) D5, b) D183.

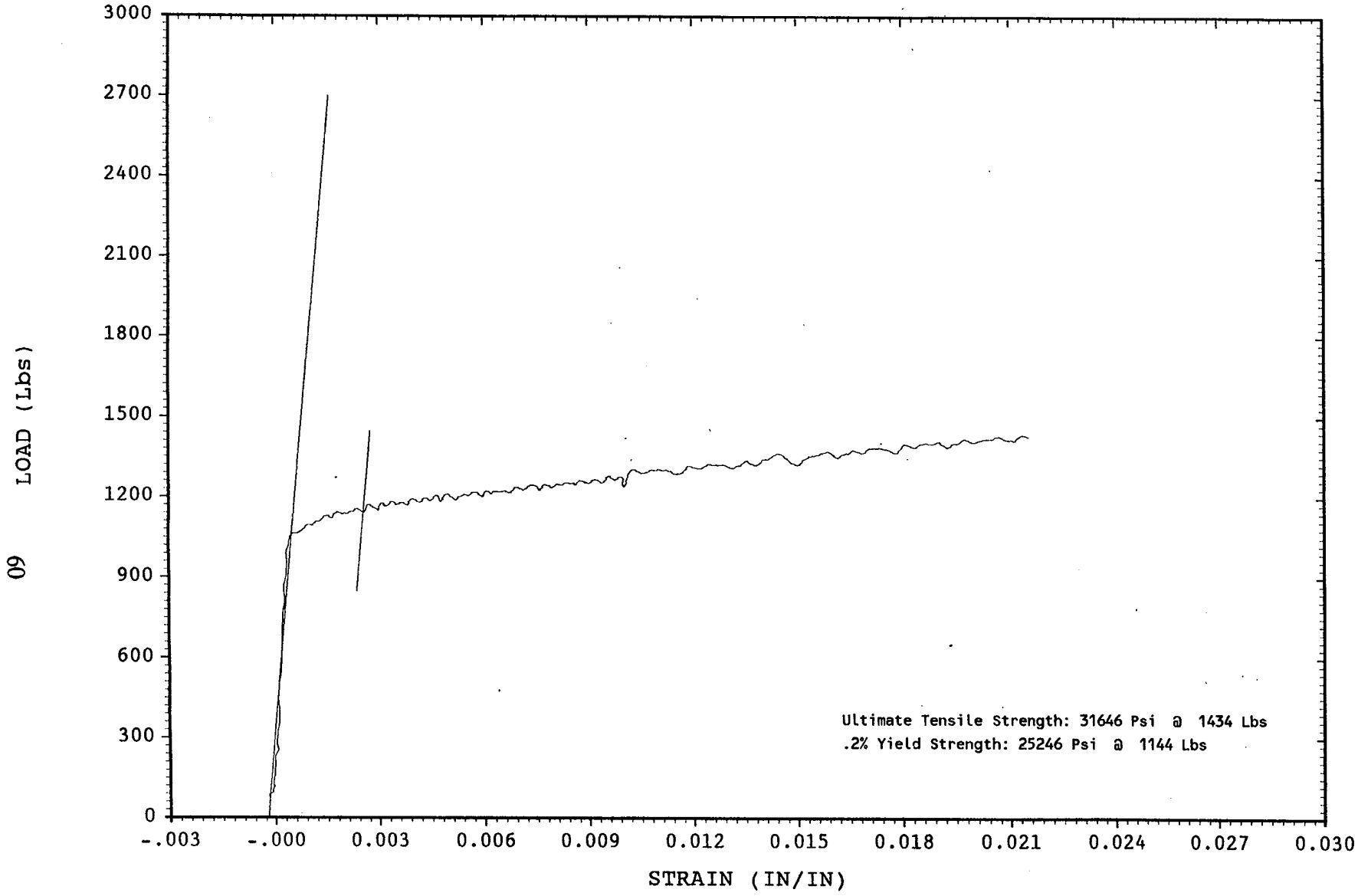

Figure 35. Stress-strain curve for a 200°C compression test of stoichiometric NiAl (D5-1738) conducted at a strain rate of 8.3×10^{-5}/s. The test was changed from strain to stroke control at approximately 1% plastic strain.

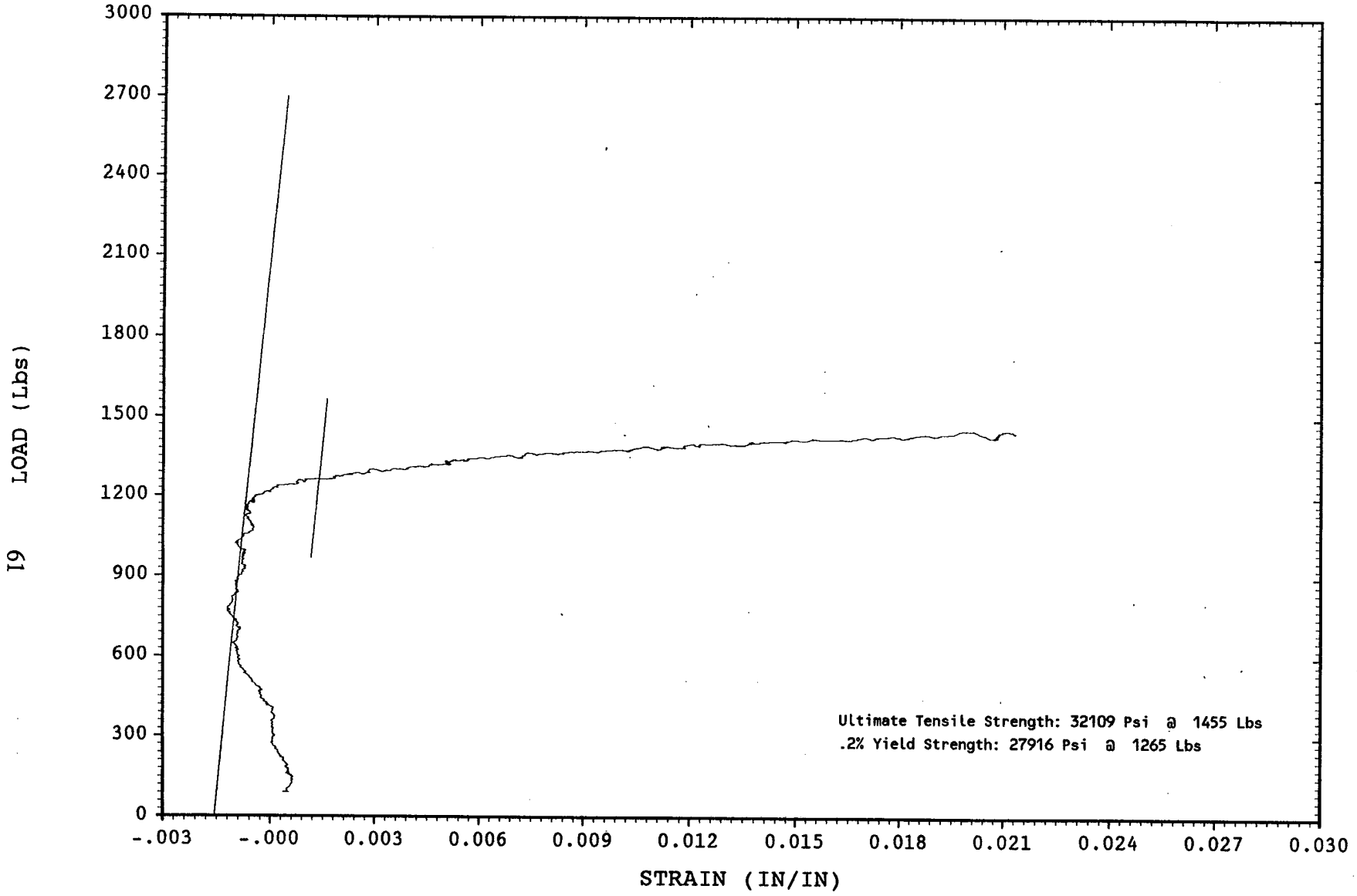

Figure 36. Stress-strain curve for a 400°C compression test of stoichiometric NiAl (D5-1738) conducted at a strain rate of 8.3×10^{-5}/s in stroke control.

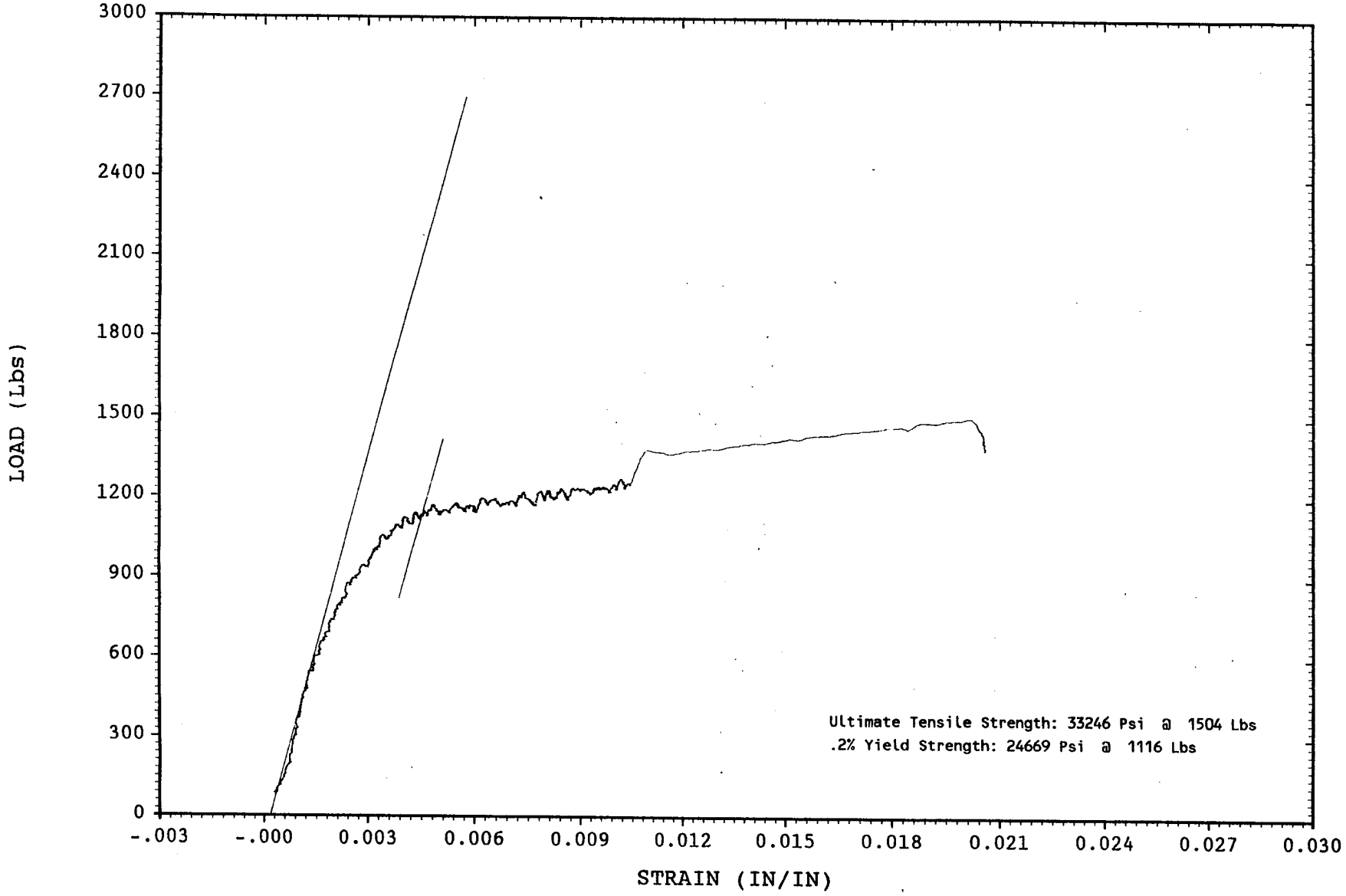

Figure 37. Stress-strain curve for a 200°C compression test of stoichiometric NiAl (D5-1738) conducted in strain control. The strain rate was increased from $1x10^{-5}$ to $1x10^{-3}$/s at approximately 1% plastic strain.

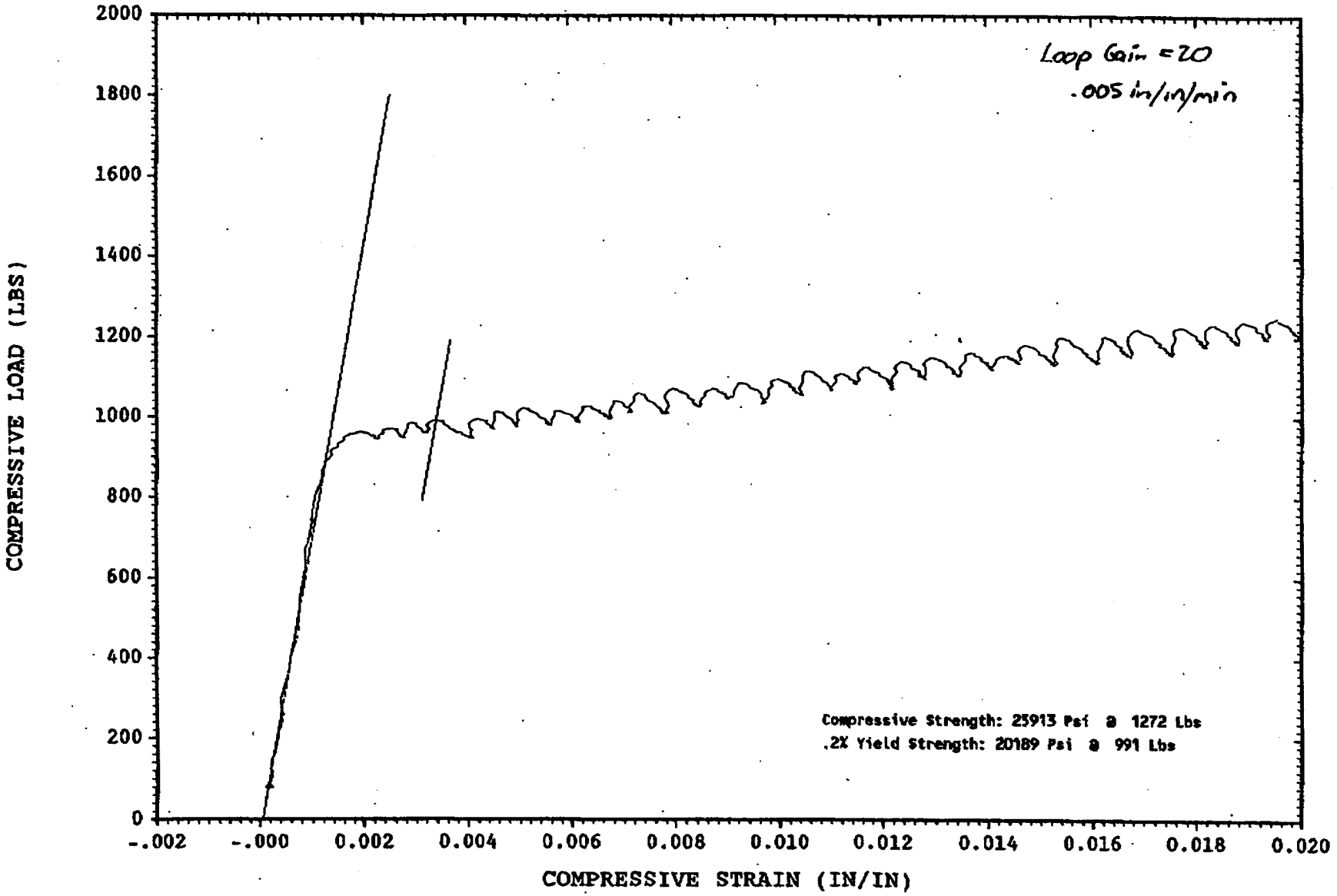

Figure 38. Stress-strain curve for a 200°C compression test of stoichiometric NiAl (D5-2154) conducted at a strain rate of 8.3×10^{-5}/s with a loop gain of 20.

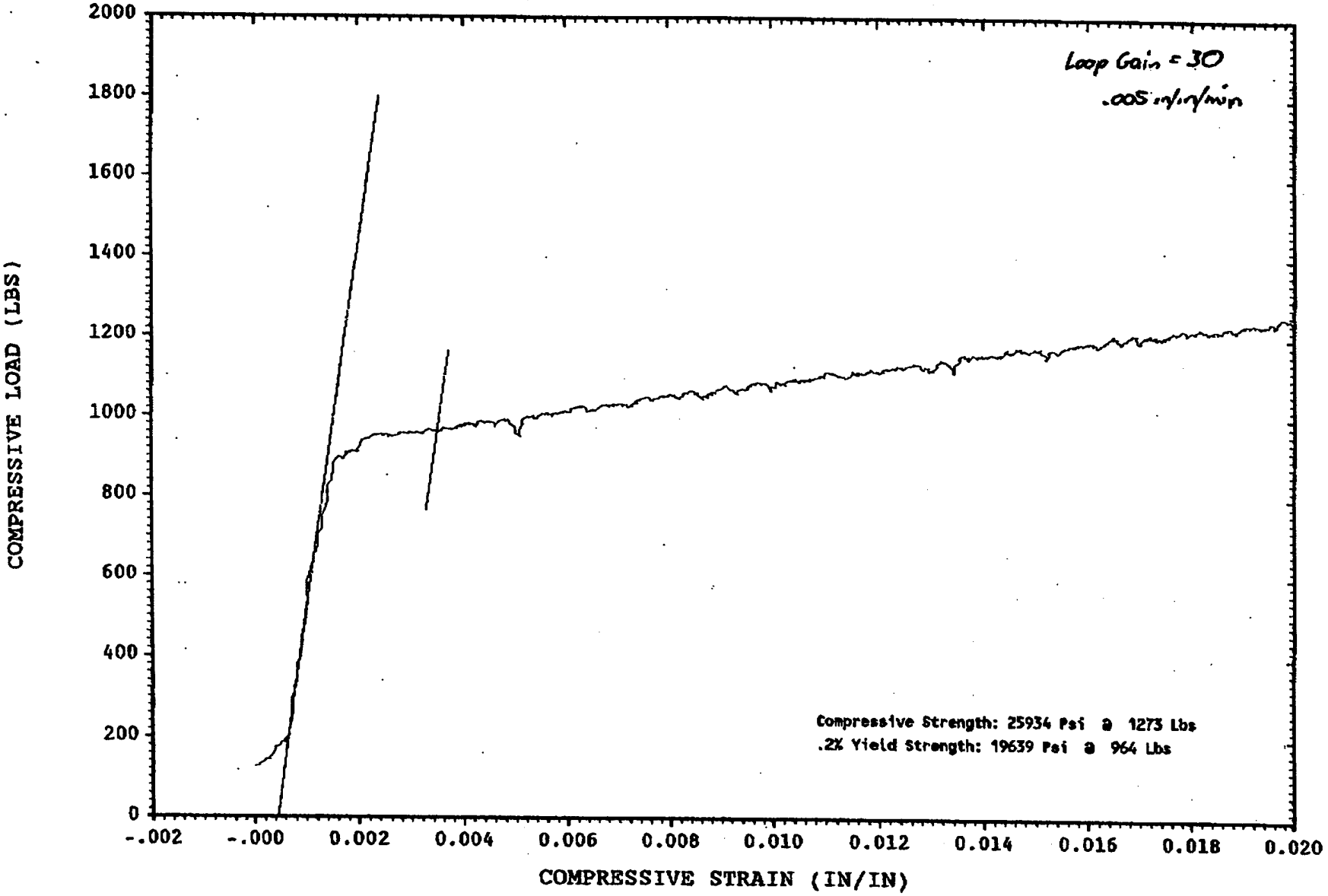

Figure 39. Stress-strain curve for a 200°C compression test of stoichiometric NiAl (D5-2154) conducted at a strain rate of 8.3×10^{-5}/s with a loop gain of 30. Note the difference in the nature of the serrations as compared to Figure 38.

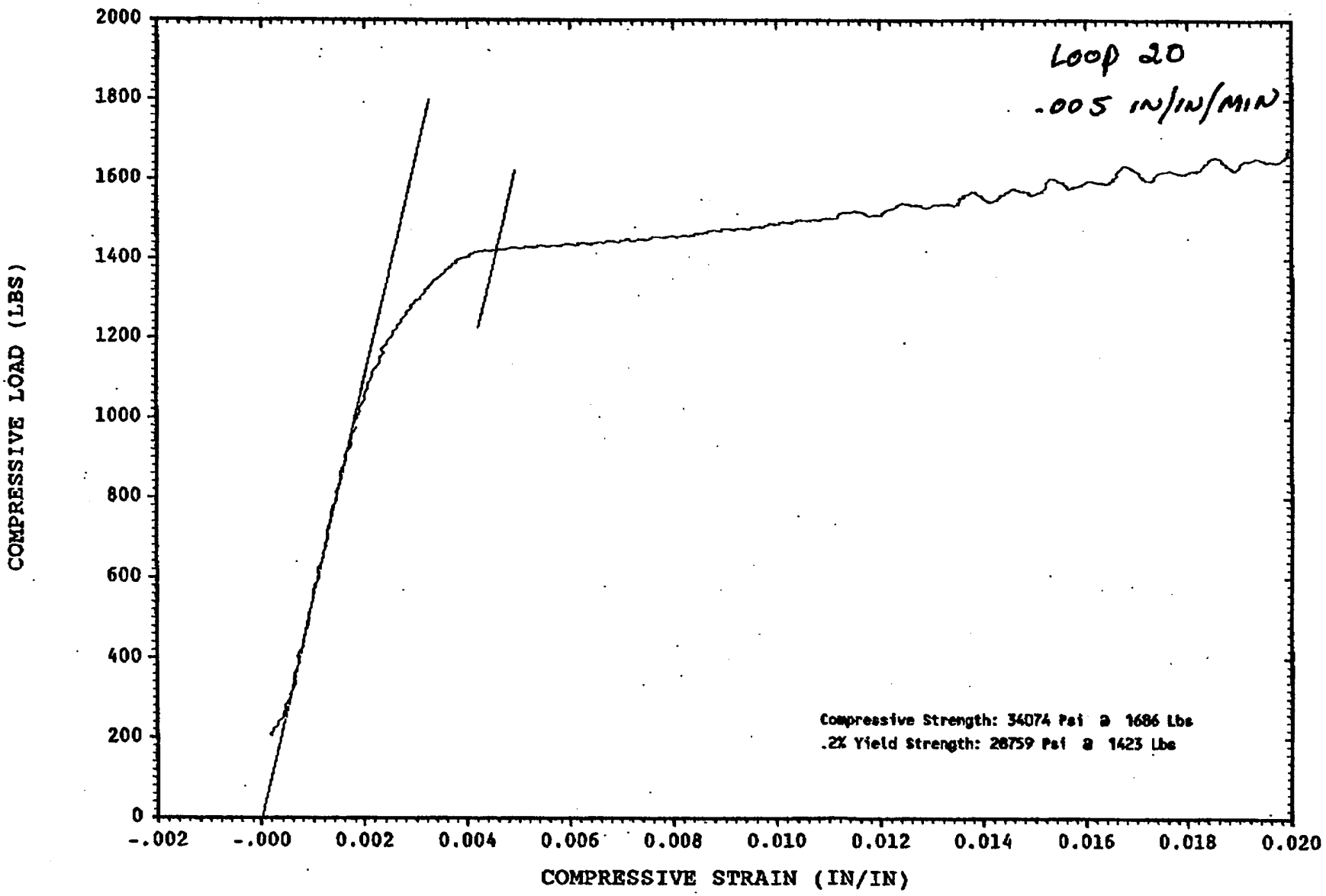

Figure 40. Stress-strain curve for a room temperature compression test of stoichiometric NiAl (D5-2154) conducted at a strain rate of 8.3×10^{-5}/s with a loop gain of 20.

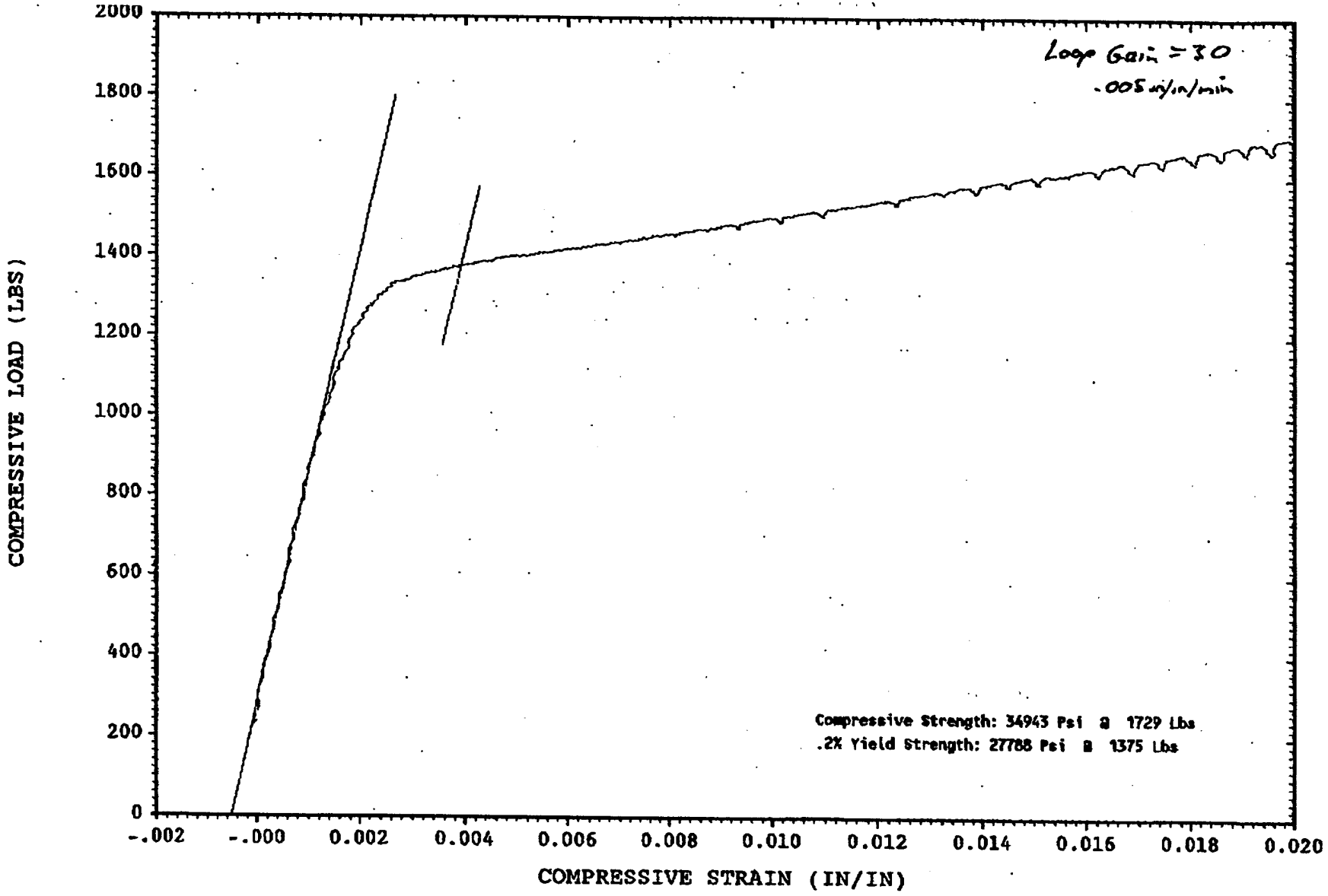

Figure 41. Stress-strain curve for a room temperature compression test of stoichiometric NiAl (D5-2154) conducted at a strain rate of 8.3×10^{-5}/s with a loop gain of 30. Note the difference in the nature of the serrations as compared to Figure 40.

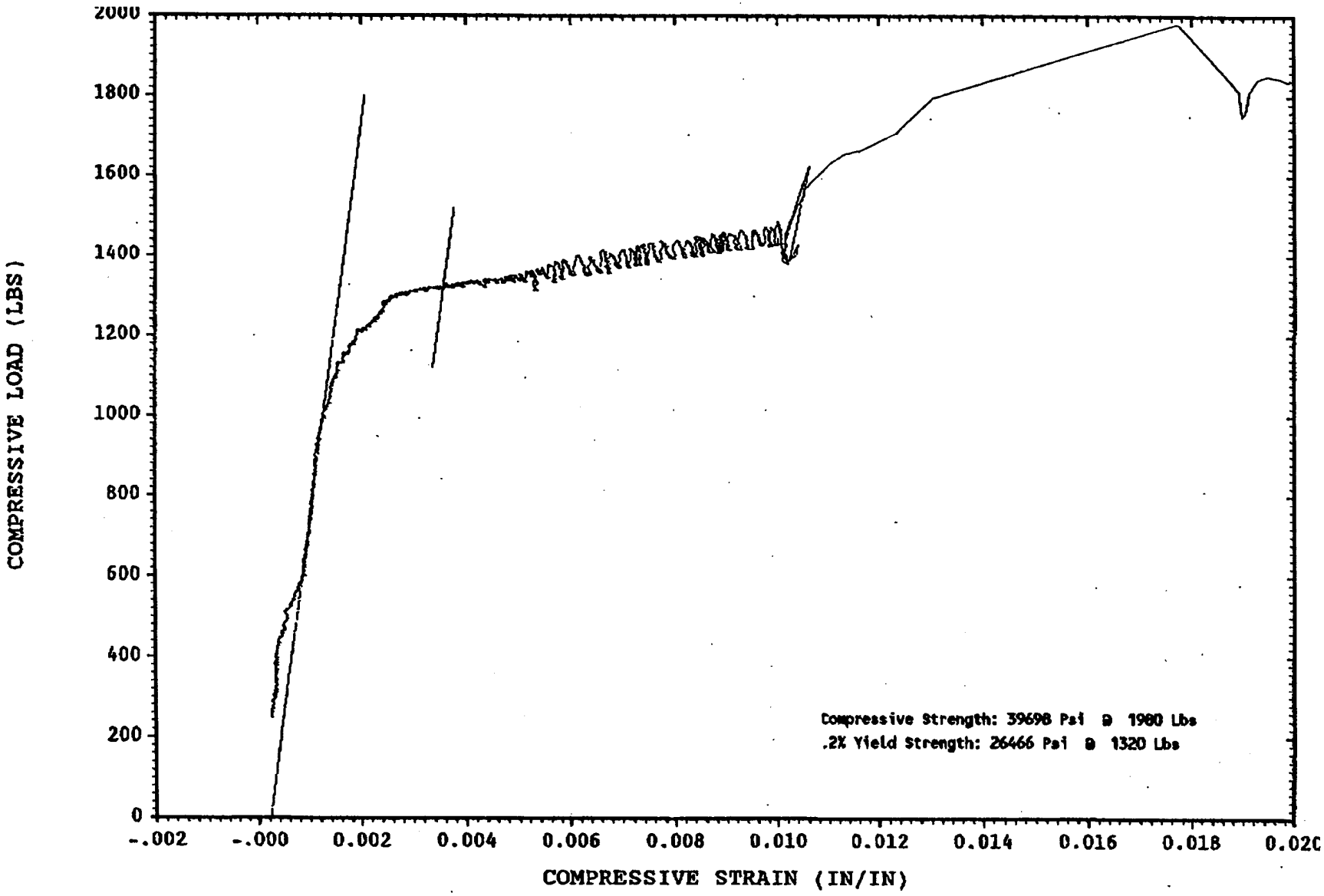

Figure 42. Stress-strain curve for a room temperature compression test of stoichiometric NiAl (D5-2154). The strain rate was increased from $1x10^{-5}$ to $1x10^{-3}$/s at approximately 1% plastic strain.

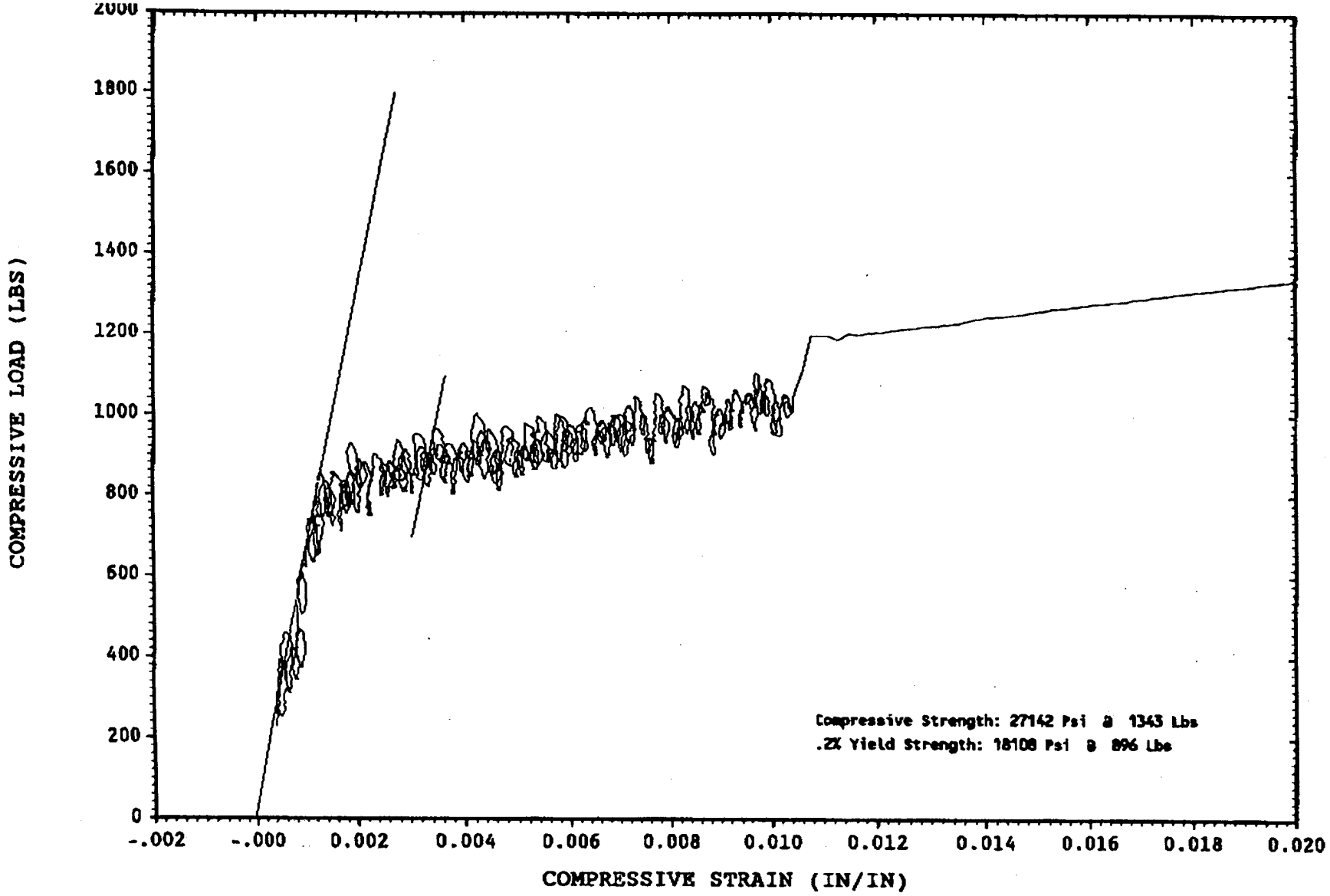

Figure 43. Stress-strain curve for a 200°C compression test of stoichiometric NiAl (D5-2154). The strain rate was increased from of $1x10^{-5}$ to $1x10^{-3}$/s at approximately 1% plastic strain.

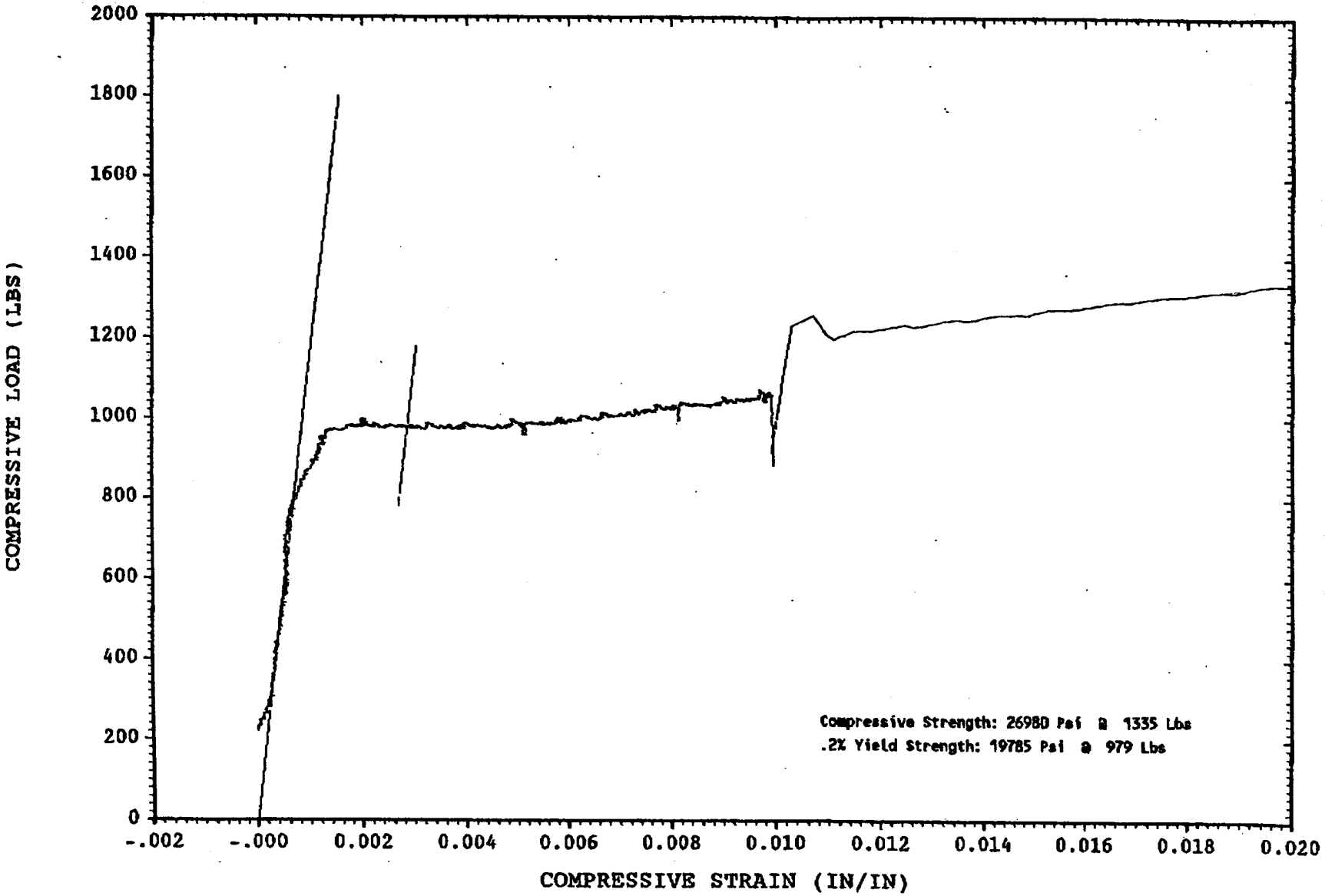

Figure 44. Stress-strain curve for a room temperature compression test of stoichiometric NiAl given an 800°C heat treatment (D5-2154HT). The strain rate was increased from $1x10^{-5}$ to $1x10^{-3}$/s at approximately 1% plastic strain.

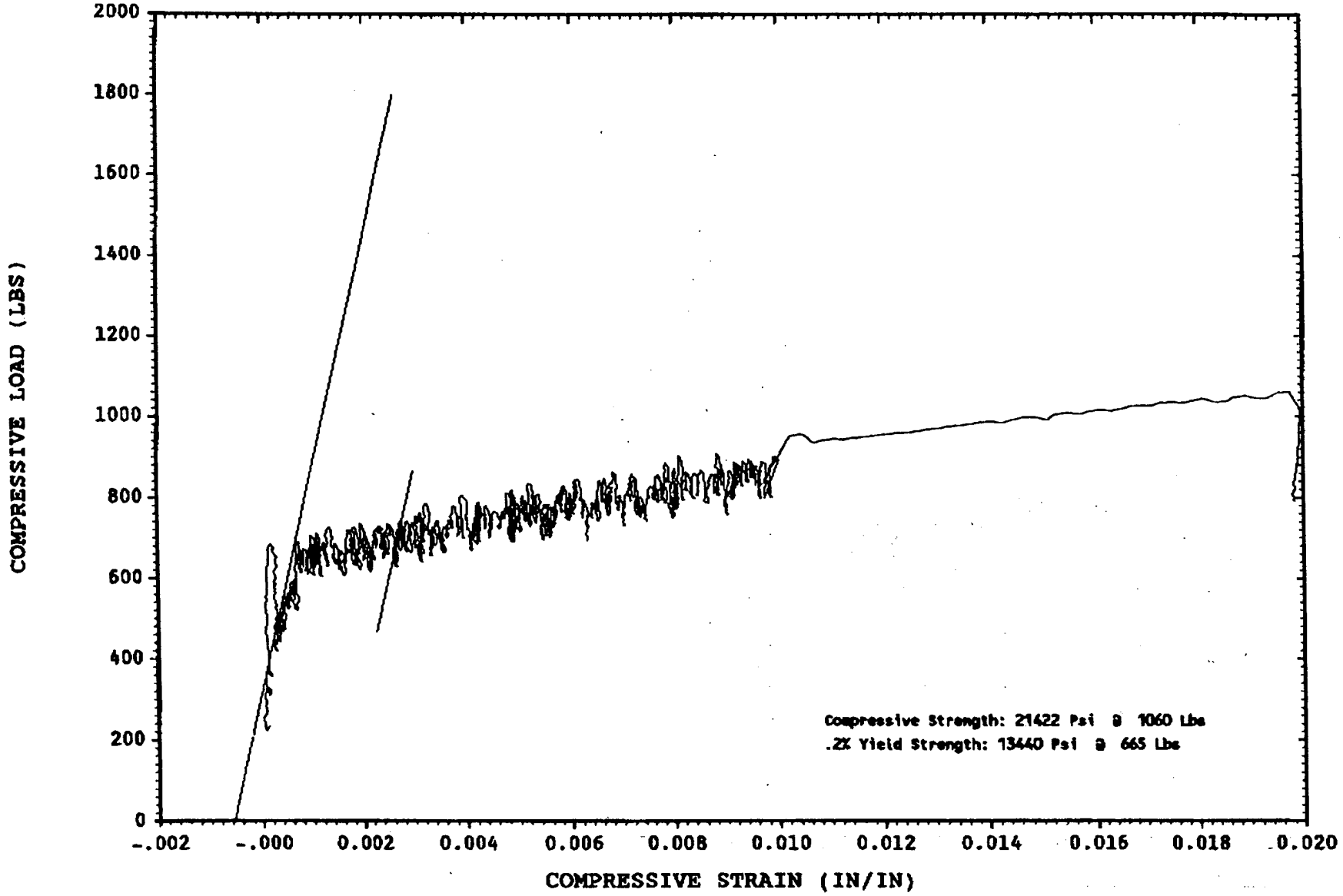

Figure 45. Stress-strain curve for a 200°C compression test of stoichiometric NiAl given an 800°C heat treatment (D5-2154HT). The strain rate was increased from $1x10^{-5}$ to $1x10^{-3}$/s at approximately 1% plastic strain.

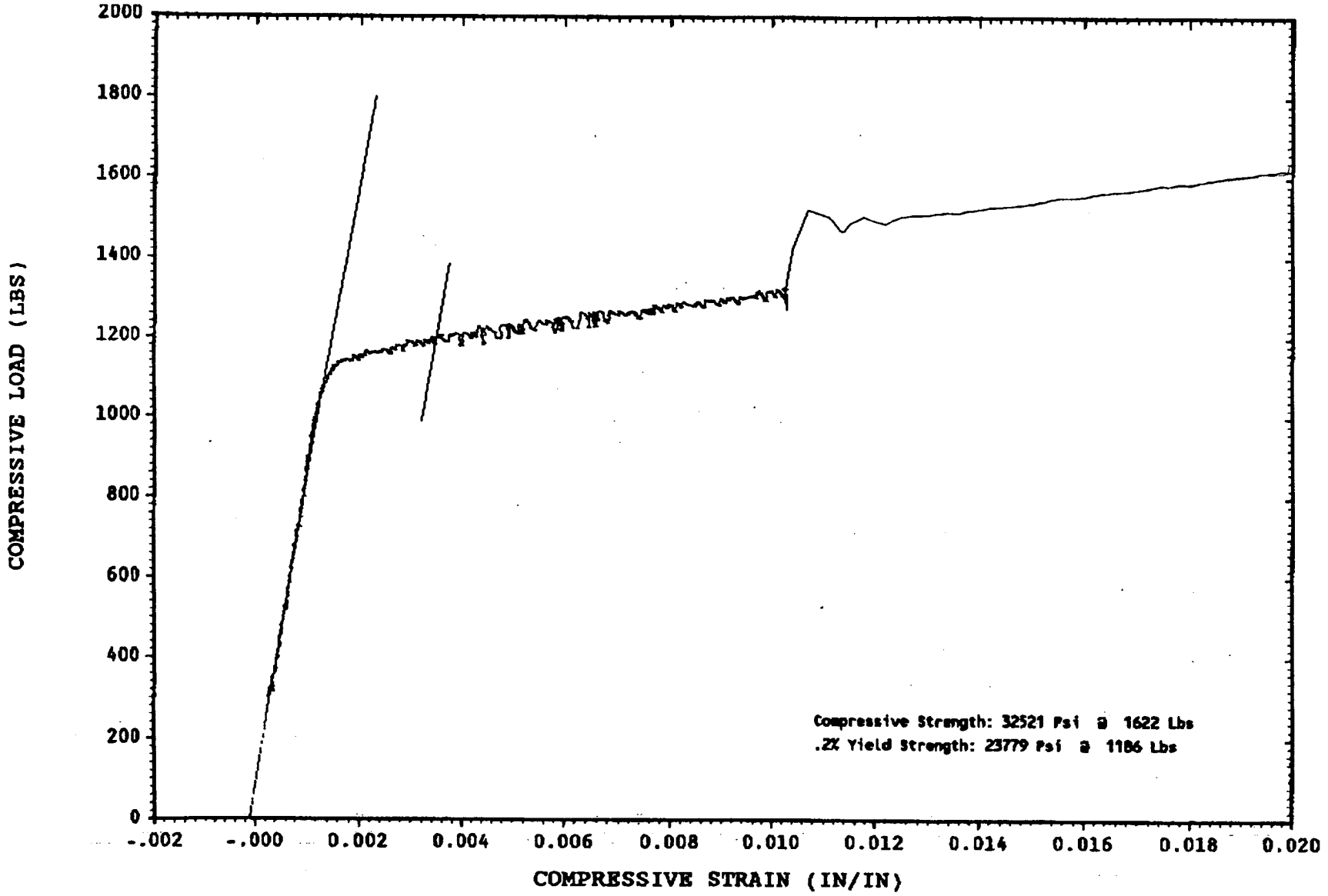

Figure 46. Stress-strain curve for a room temperature compression test of a 0.1at% Fe containing NiAl alloy (D183-1675). The strain rate was increased from $1x10^{-5}$ to $1x10^{-3}$/s at approximately 1% plastic strain.

after approximately 1% plastic strain as shown in Figure 40. Note that the serrations are similar in morphology for similar loop gains. Thus, the serrated yield behavior is seen to vary as a function of temperature (and, as will be discussed below, strain rate and alloy/heat treatment), but is affected by instrumental conditions. It is also likely that the strain gages were slipping during the tests. It appeared that the strain aging phenomenon was real, but information regarding temperature, alloying and heat treatment effects is suspect in trying to clearly understand the serrated yielding phenomenon. The yield/flow stress information obtained from these plots, however, is accurate. Once the instrument related problem was understood, tests in the fourth year of study were run in a screw driven machine under fixed cross head speed without a strain gage attached on the specimen. The load was plotted against the crosshead displacement. Tests were run with stoichiometric NiAl (D5), Fe-containing NiAl (D183) and high purity Oliver specimens as a function of temperature. Useful results were obtained which are described in Section 3.7.2.

As mentioned earlier, the stress vs. strain plots obtained with constant strain rates are not useful to extract precise information regarding strain aging. They, however, indicated serrated yielding trends as a function of temperature, strain rate, and alloy/heat treatment which are described below.

For the standard NiAl D5 specimens, testing was performed on specimens taken from two different crystals. The first crystal, D5-1738, displayed higher than normal yield stress values. Most of the tests were performed at 200°C, where considerable serrated yielding behavior had been observed previously. Experiments were conducted on the effect of performing the tests under stroke control, in which the stroke rate was kept constant via a feed-back loop from a cross-head displacement sensor, versus strain control, in which the stroke rate was determined by a feed-back signal from the strain gage attached to the specimen. Thus, in stroke control, the rate of deformation is controlled by keeping the cross-head displacement rate constant, while under strain control, the displacement rate within the specimen gage is kept constant. In both cases, serrations were observed in the stress-strain curve, although the frequency of the serrations appear to be greater in strain control (Figure 35).

Strain rate jump experiments were also performed, as shown in Figure 37. At 10^{-3}/s, the stress-strain behavior appears more smooth. The flow stress was observed to increase with increasing strain rate, with a slight yield point in the transition region. The activation volume (in units of b^3, where b is the Burger's vector) was calculated to be 163, compared to 292 in a previous investigation at GEAE [1] and 174 in a study by Kitano and Pollock [30]. The previous GEAE data were calculated from 0.2% yield stress data for two separate tensile tests, using specimens from different castings and are therefore less reliable.

The second D5 single crystal (D5-2154) had more typical yield stress values. Strain rate jump tests were also performed on this alloy. The serrations were more severe, and occurred at a smaller strain (~0.5% plastic), at 1 x 10^{-5}/s (Figure 42) as compared to 8.3x10^{-5}/s (Figure 41) for room temperature tests. Some apparent anomalies in the curve are observed after the jump to 1 x 10^{-3}/s in the room temperature test. The activation volume for this crystal was 116 at 200°C, somewhat smaller than for the D5-1738 crystal. Severe serrations are observed at 1 x 10^{-5}/s, even in the elastic region of the curve, which disappear at 1 x 10^{-3}/s (Figure 43).

For the heat treated specimens, the D5-2154 crystal was used, affording a back-to-back comparison with the standard heat treatment condition. Stress-strain curves for strain rate jump tests at room temperature and 200°C are shown in Figures 44 and 45, respectively. The stress-strain curve for the room temperature strain rate jump test of the 0.1 at% Fe alloy is shown in Figure 46. The activation volumes for the 800°C heat treated specimens were 83 and 199 at room temperature and 200°C, respectively. For the 0.1 at% Fe alloy tested at room temperature, the activation volume was 88, similar to the D5-2154HT specimen.

At room temperature, the serrations for both the 800°C heat treated specimen and the 0.1 at% Fe alloy appear to be reduced compared to the standard heat treated NiAl. This is consistent with the first year results, in which serrated yielding behavior was less pronounced in both of these alloy/heat treatment conditions. At 200°C, the 800°C heat treated specimen displays behavior similar to that of the standard heat treated specimen for the 1×10^{-5}/s and 1×10^{-3}/s strain rates.

3.7.2 Serrated Yielding Experiments with Constant Cross Head Speed

As mentioned earlier, once the instrument related problems were understood, compression tests in the fourth year of study were run in a screw driven machine under fixed cross head speed without a strain gage attached on the specimen. The cross head speed was preset to impose an initial strain rate of 8.3×10^{-5}/sec. The load was plotted against the crosshead displacement. Tests were run with stoichiometric NiAl (D5-1738), Fe-containing NiAl (D183-1675) and high purity Oliver (Oliver 2) specimens at room temperature, 400°C, 500°C and 600°C. The specimen dimensions for the cylindrical specimens were 6.03mm x 15.3mm, 6.3mm x 15.5mm and 4.82mm x 10.2mm for D5, D183 and Oliver specimens, respectively. At room temperature, no serrated yielding was observed in any of these three alloys as seen in Figures 47-49. A yield drop is seen in the Fe-containing NiAl (D183) alloy. It is also interesting to note the difference in the flow stresses of these alloys. The stoichiometric NiAl alloy (D5) has the highest strength. It is quite obvious that the Fe addition significantly reduces the flow strength. It is also very interesting to note that the high purity NiAl has about 40% lower flow strength. At 400°C, serrations appear in D5 and D183 whereas there is no indication of serrated yielding in the high purity specimens (Figures 50-52). At 500°C, serrations are quite prevalent in D5. The serrations are smaller in D183 at this temperature compared to those seen at 400°C. No serrations are seen in the high purity NiAl specimens (Figure 53-55). At 600°C, serrations are beginning to disappear in D5 whereas they have completely disappeared in D183. Again, no serrations are seen in the high purity NiAl single crystals (Figure 56-58). The serrated yielding information obtained above with a fixed cross head speed in a screw driven machine have provided data which are consistent with what is expected from a dynamic strain aging phenomenon, and points to the fact that impurities are playing an important role in the deformation behavior of NiAl. Addition of Fe appears to negate the strain aging effect. A complete absence of serrated yielding in the high purity NiAl has also been observed by Prof. John Hack of Yale [31] who has been studying the strain aging behavior in conventional and high purity NiAl single crystals as a collaborative effort with GE Aircraft Engines under the auspices of this program. Much lower flow stresses of D183 and high purity NiAl specimens at all test temperatures are also noteworthy.

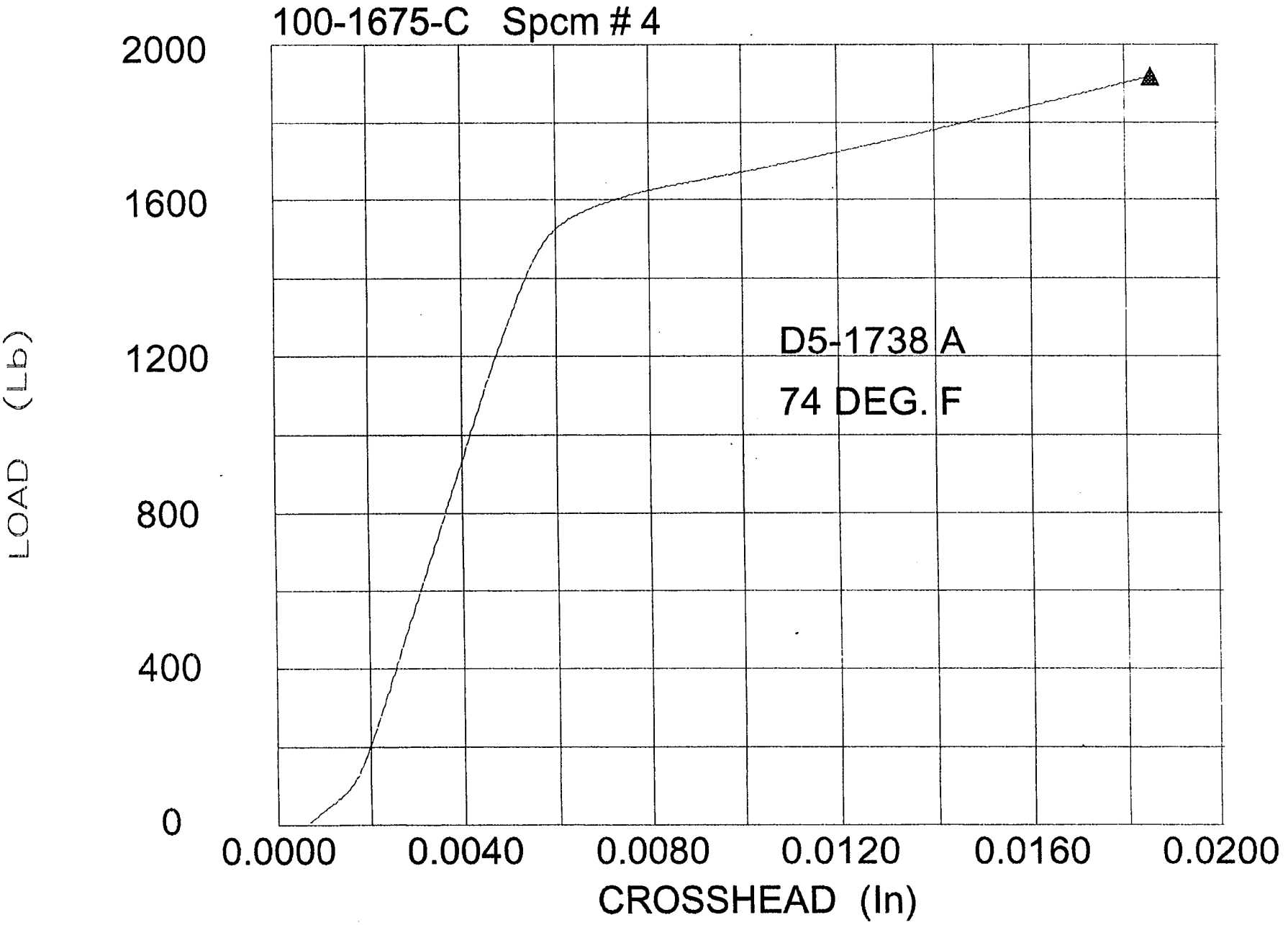

Figure 47. Load-displacement curve for a room temperature compression test of stoichiometric NiAl (D5-1738A) at a strain rate of 8.3×10^{-5}/s.

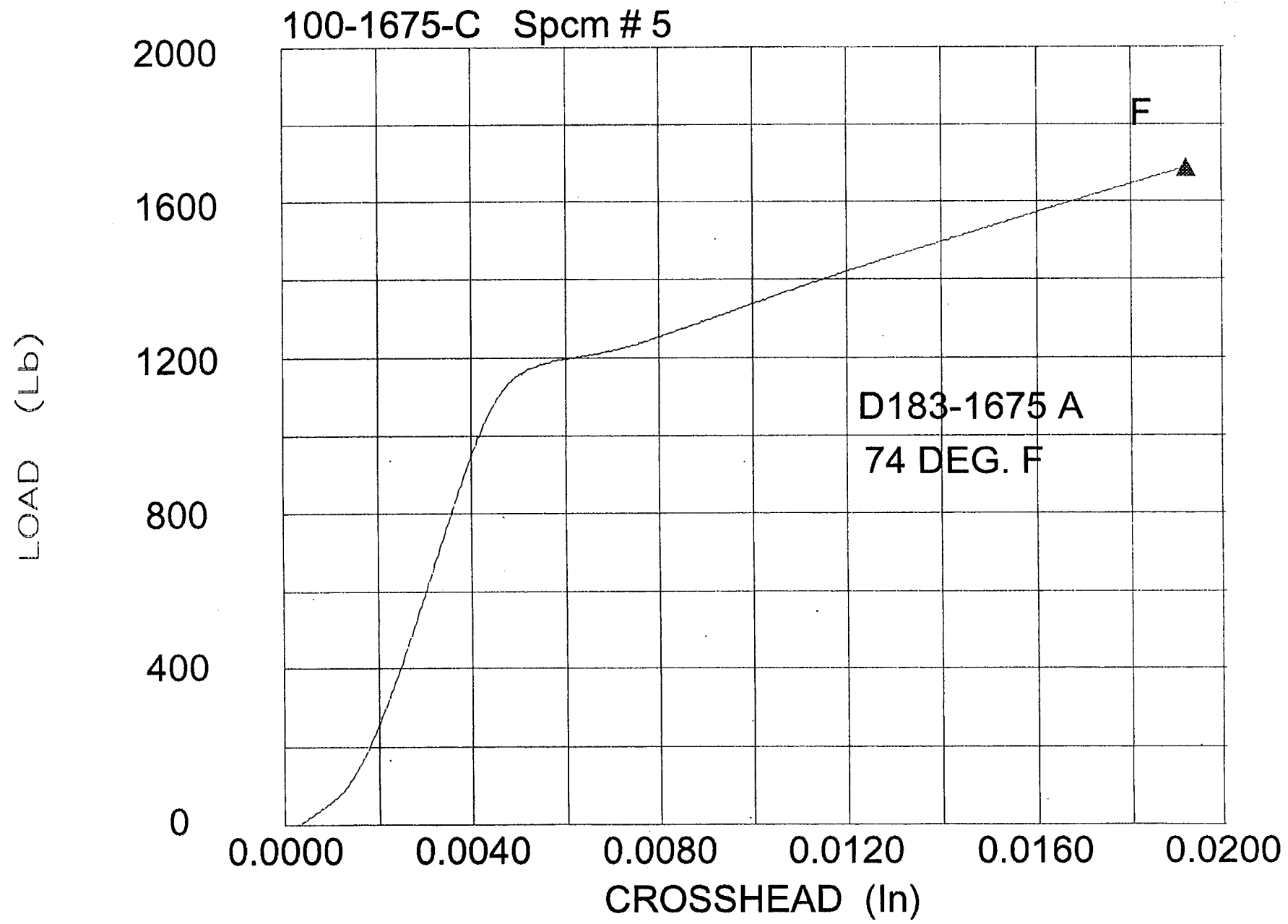

Figure 48. Load-displacement curve for a room temperature compression test of 0.1 at% Fe-containing NiAl alloy (D183-1675A) at a strain rate of 8.3×10^{-5}/s.

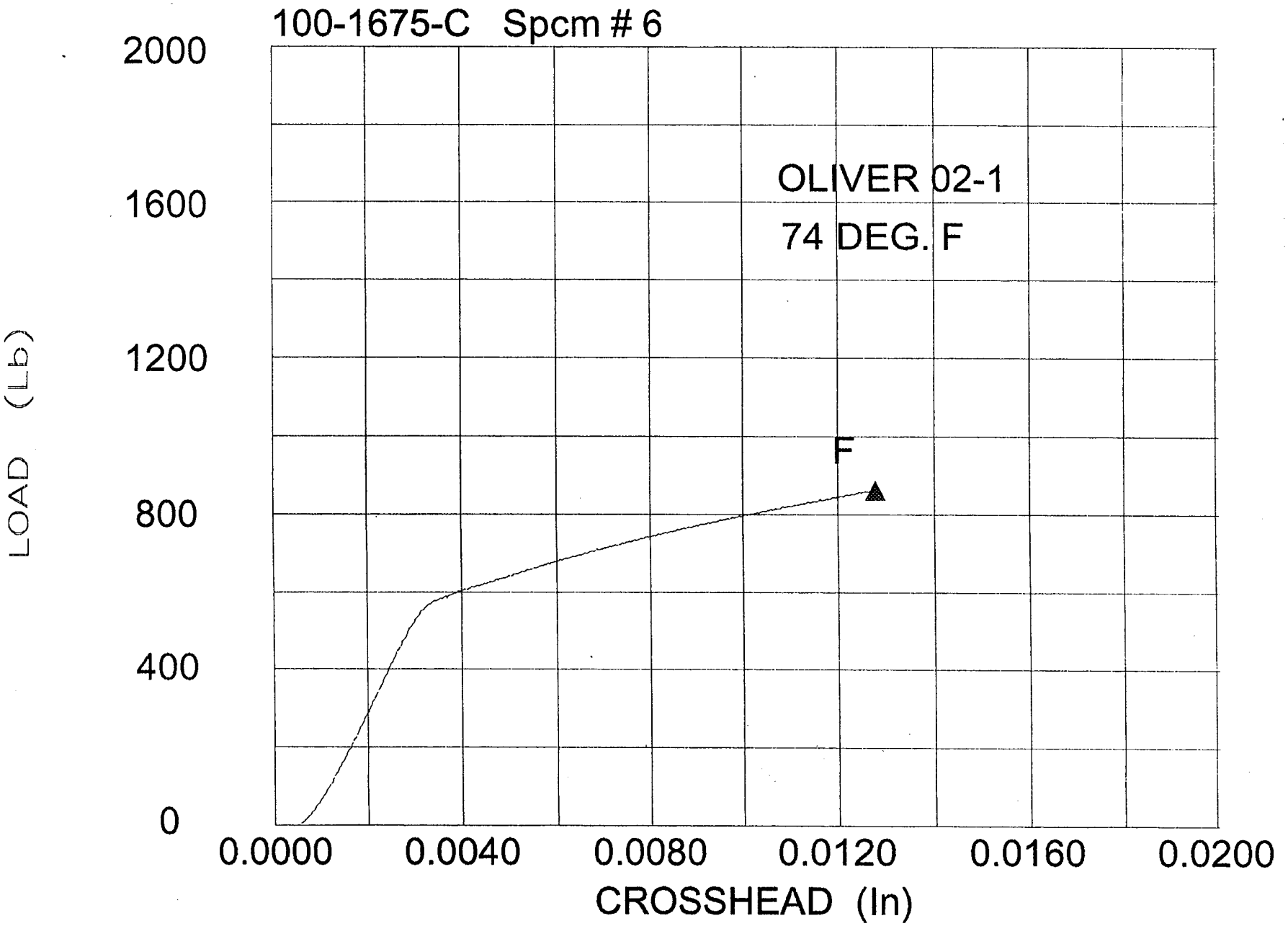

Figure 49. Load-displacement curve for a room temperature compression test of high purity NiAl (Oliver 2-1) at a strain rate of 8.3×10^{-5}/s.

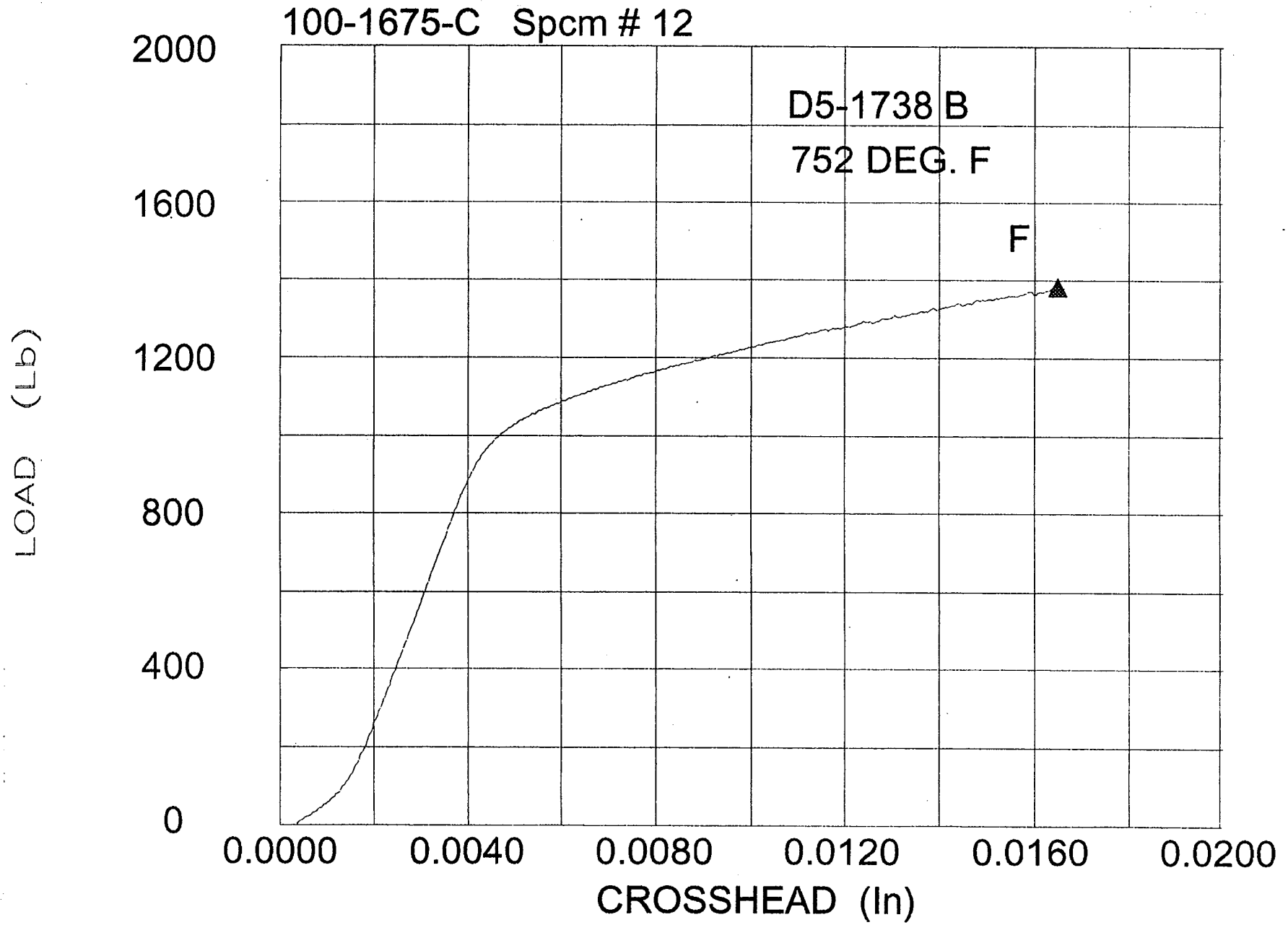

Figure 50. Load-displacement curve for a 400°C compression test of stoichiometric NiAl (D5-1738B) at a strain rate of 8.3×10^{-5}/s.

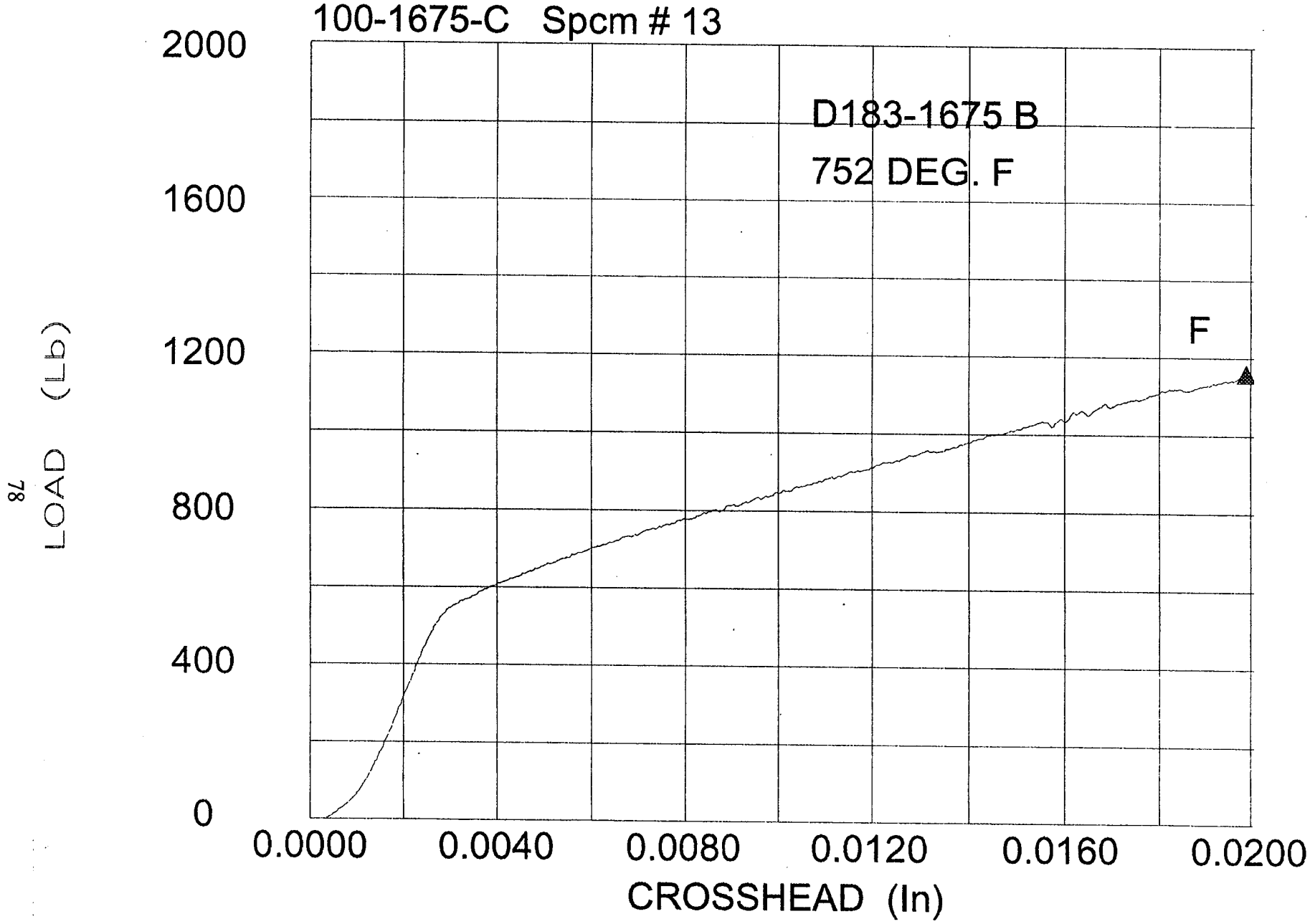

Figure 51. Load-displacement curve for a 400°C compression test of 0.1 at% Fe-containing NiAl alloy (D183-1675B) at a strain rate of 8.3×10^{-5}/s.

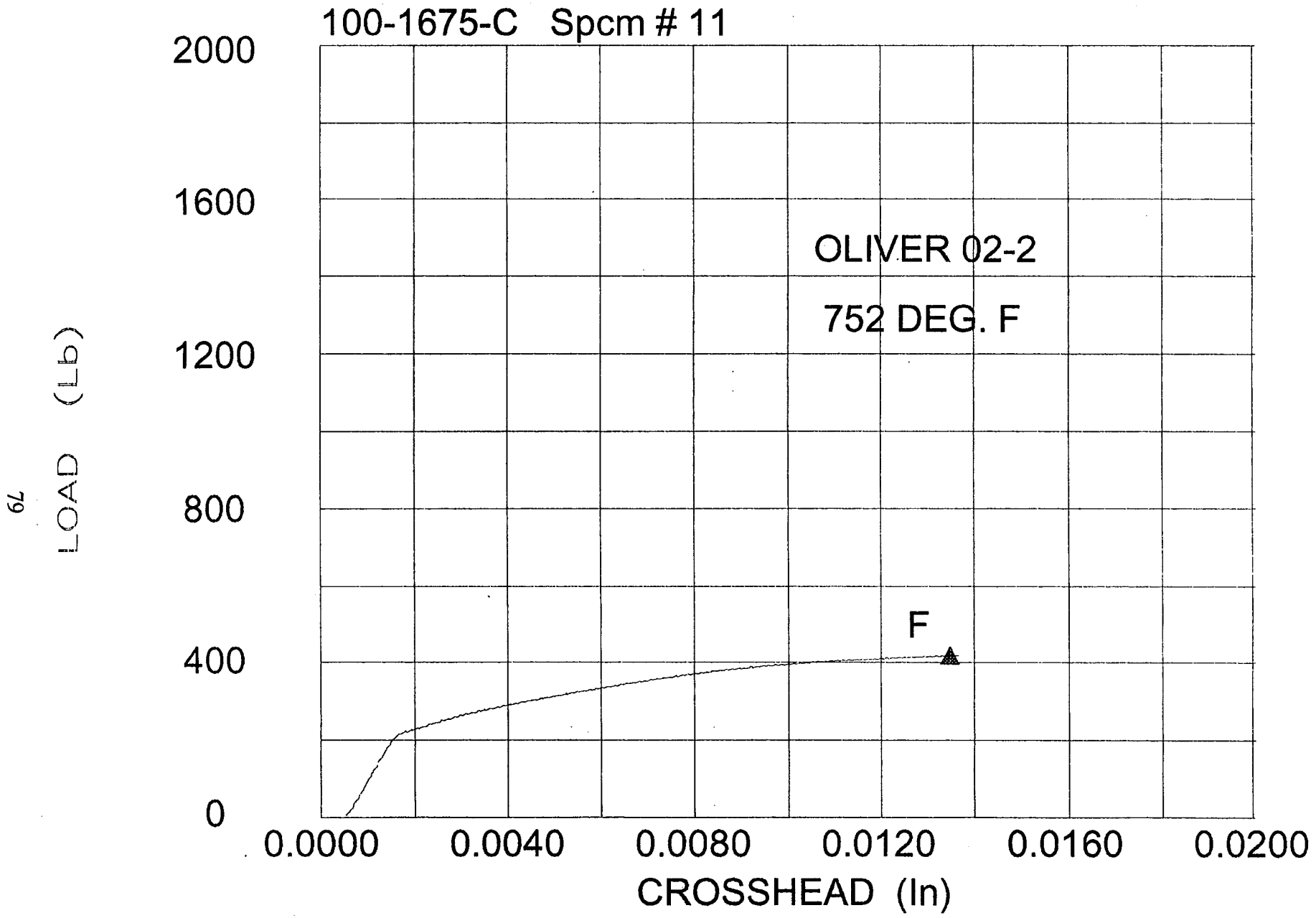

Figure 52. Load-displacement curve for a 400°C compression test of high purity NiAl (Oliver 2-2) at a strain rate of 8.3×10^{-5}/s.

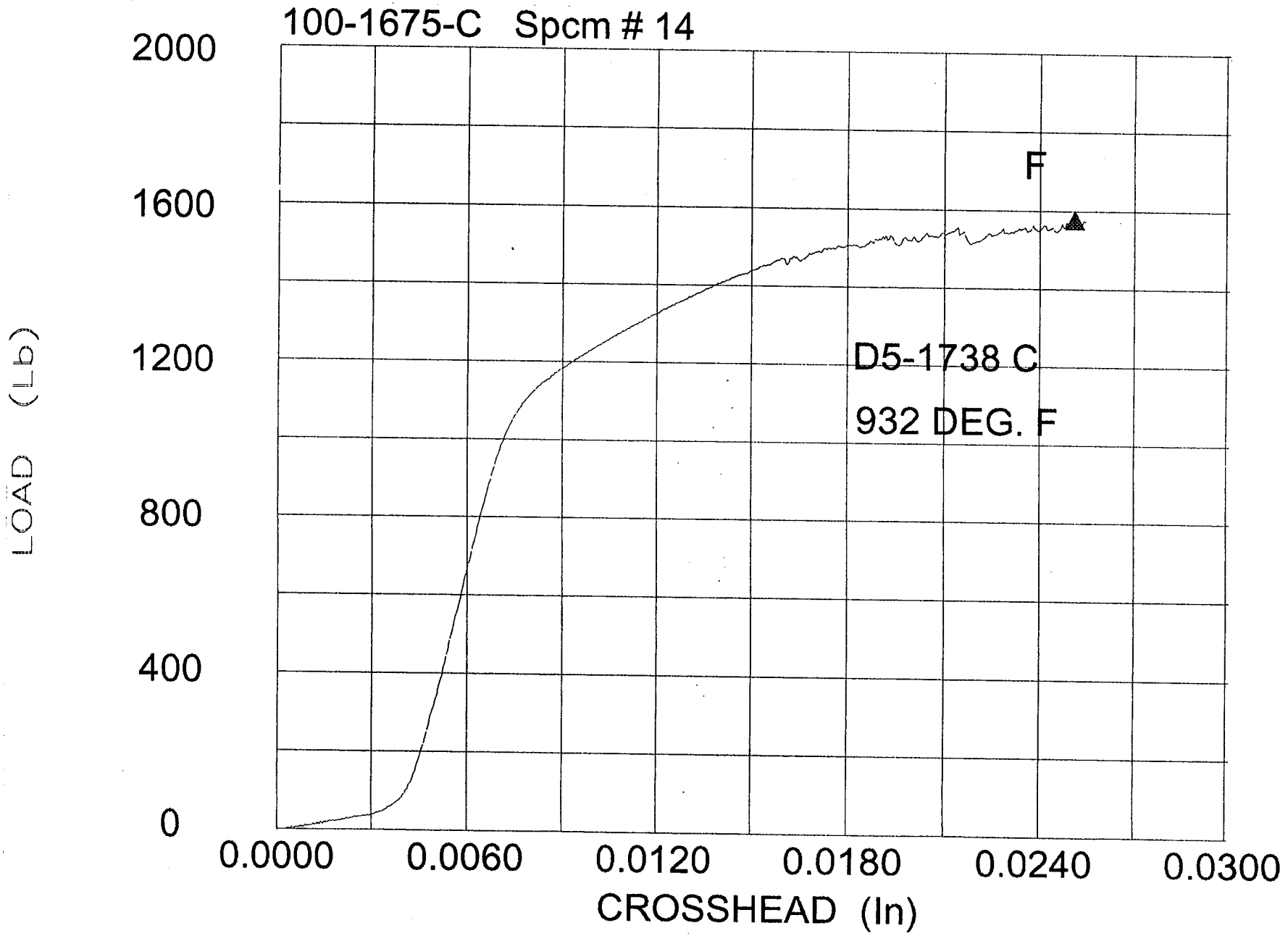

Figure 53. Load-displacement curve for a 500°C compression test of stoichiometric NiAl (D5-1738C) at a strain rate of 8.3×10^{-5}/s.

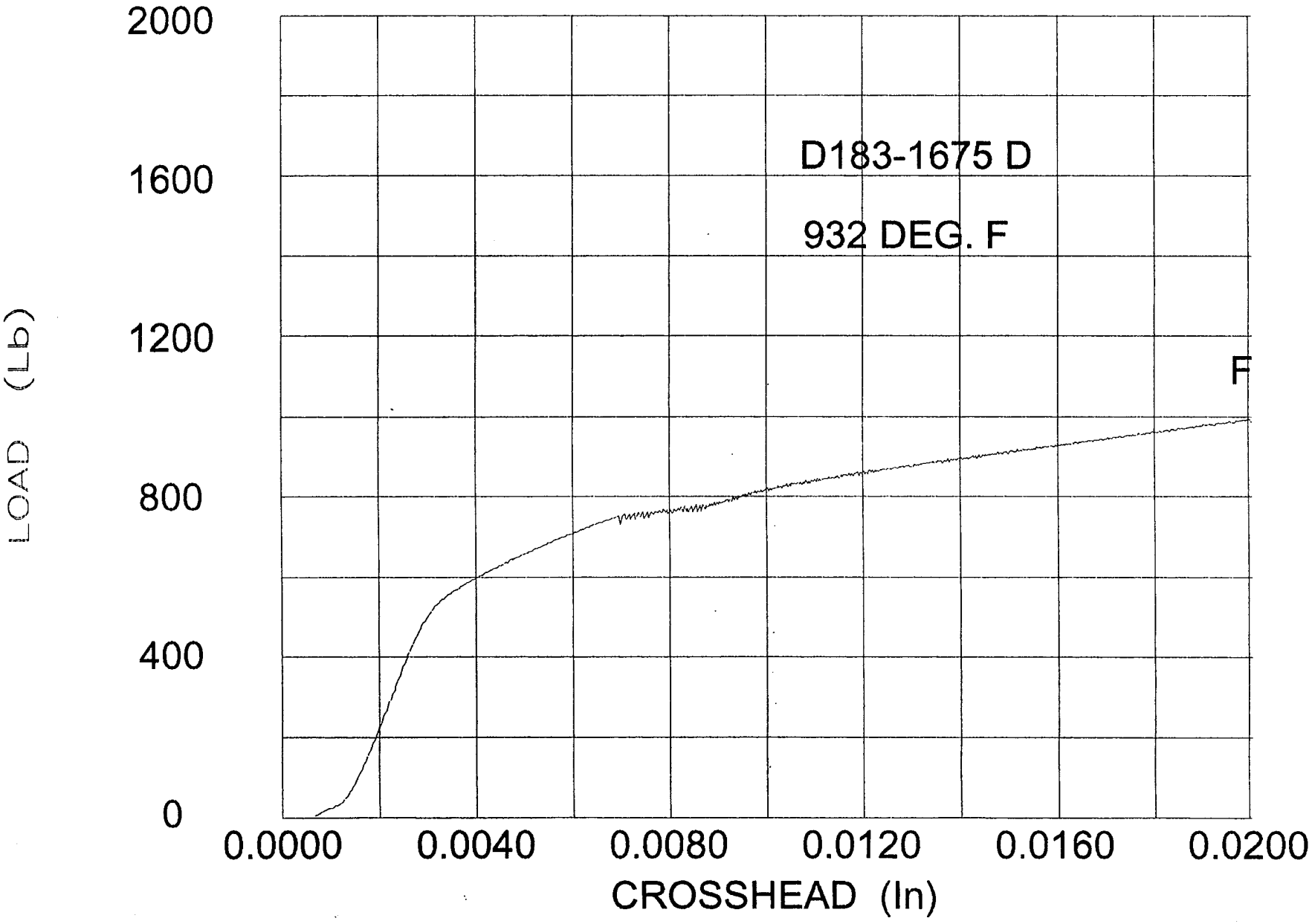

Figure 54. Load-displacement curve for a 500°C compression test of 0.1 at% Fe-containing NiAl alloy (D183-1675D) at a strain rate of 8.3×10^{-5}/s.

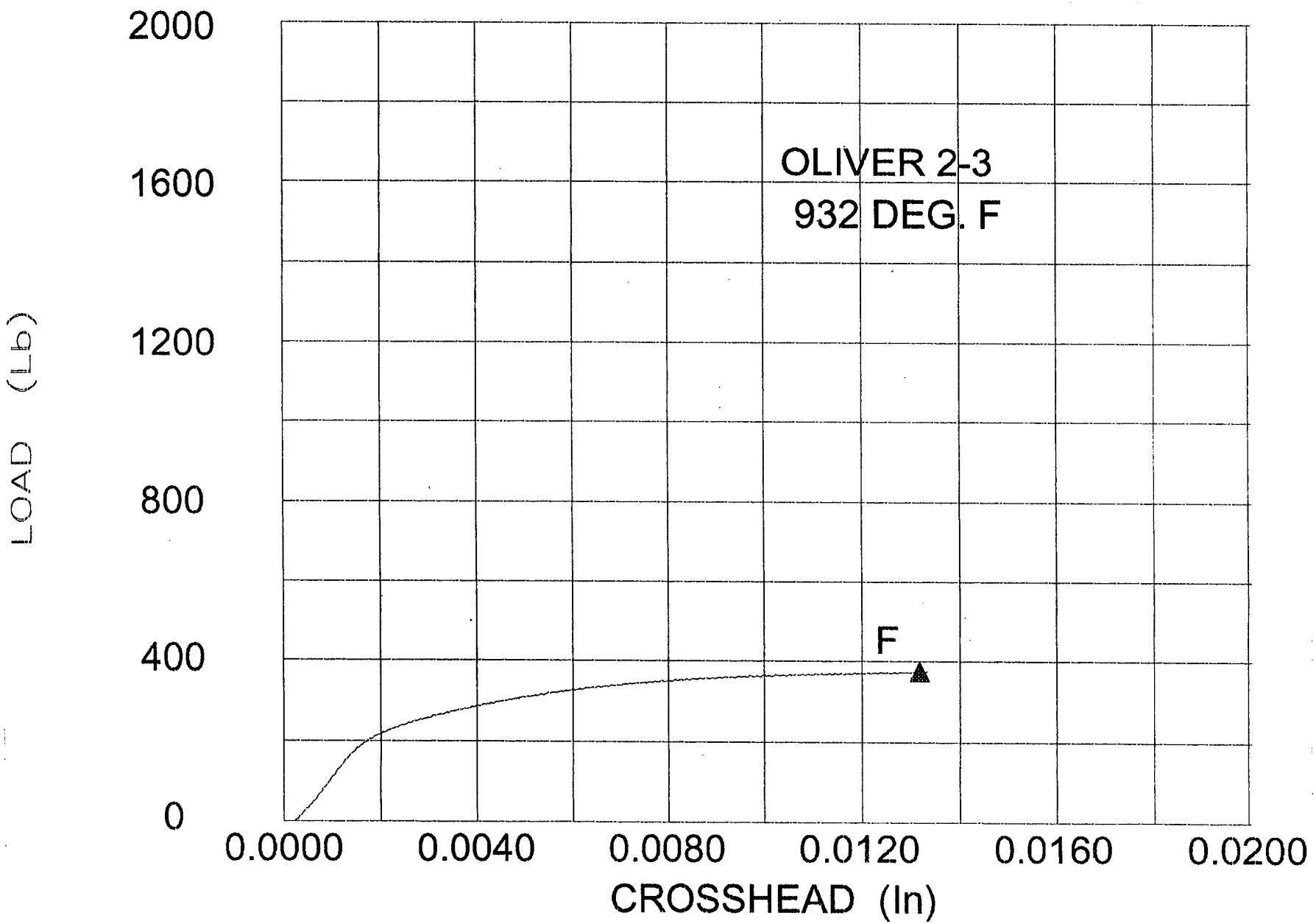

Figure 55. Load-displacement curve for a 500°C compression test of high purity NiAl (Oliver 2-3) at a strain rate of 8.3×10^{-5}/s.

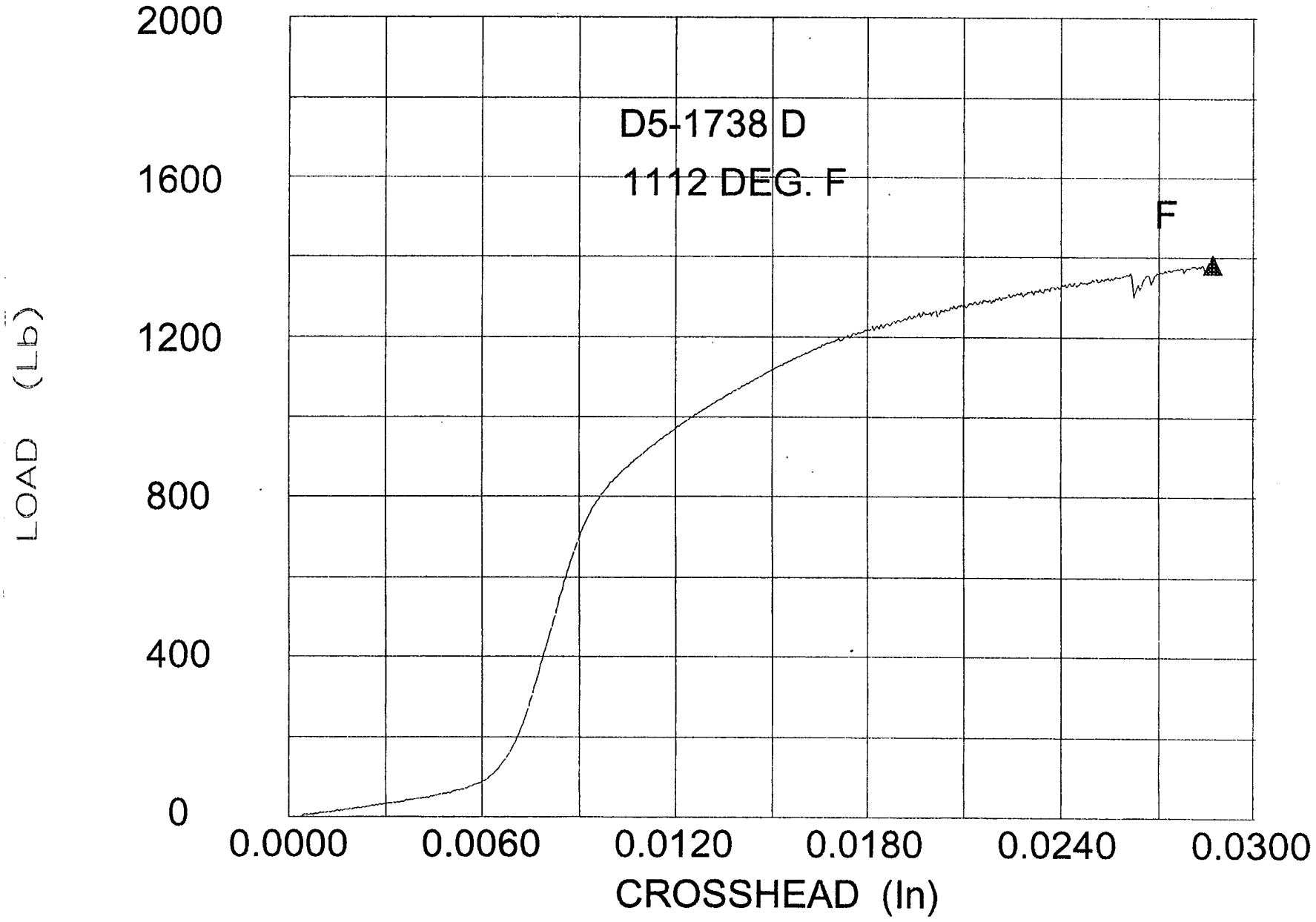

Figure 56. Load-displacement curve for a 600°C compression test of stoichiometric NiAl (D5-1738D) at a strain rate of 8.3×10^{-5}/s.

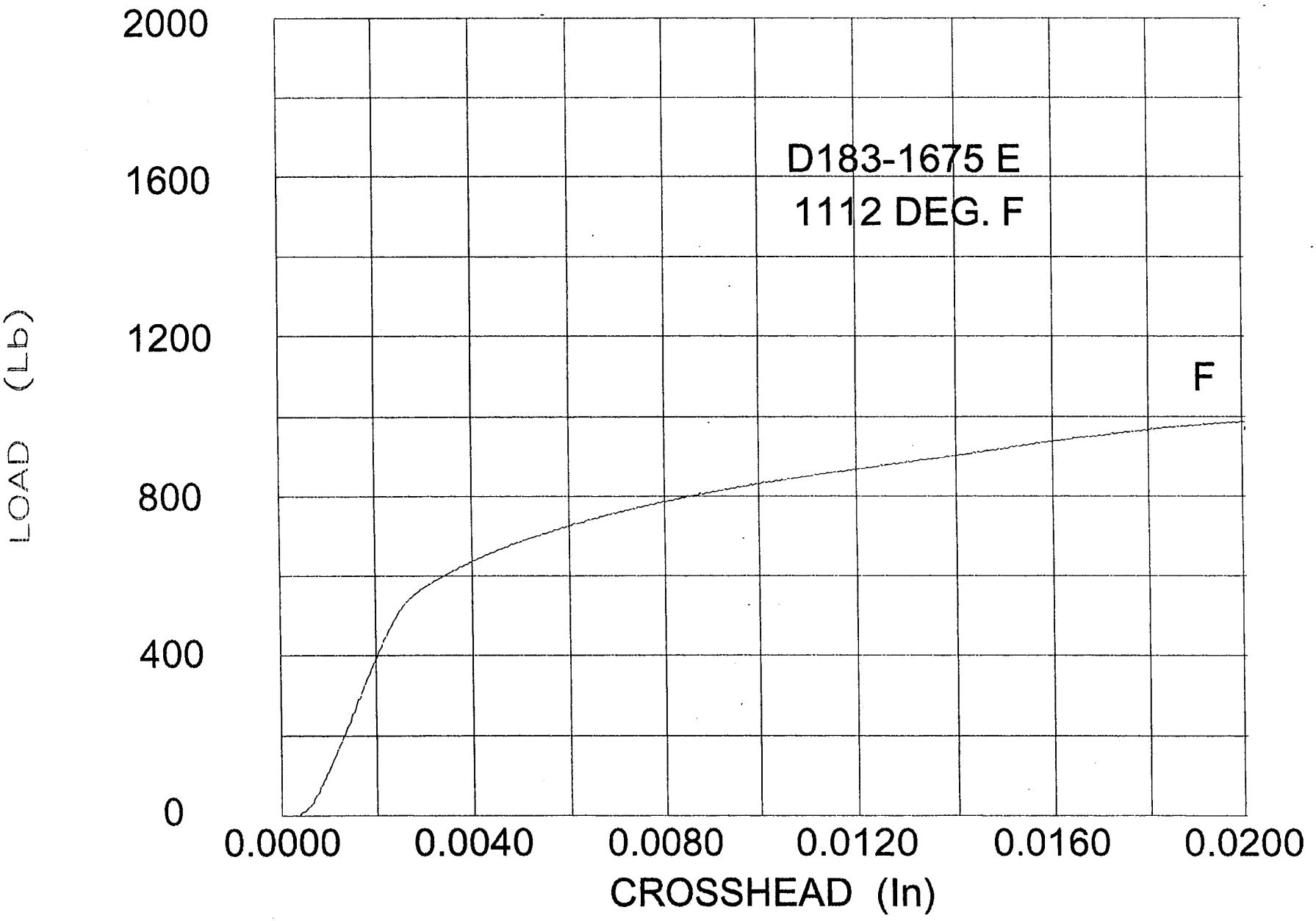

Figure 57. Load-displacement curve for a 600°C compression test of 0.1 at% Fe-containing NiAl alloy (D183-1675E) at a strain rate of 8.3×10^{-5}/s.

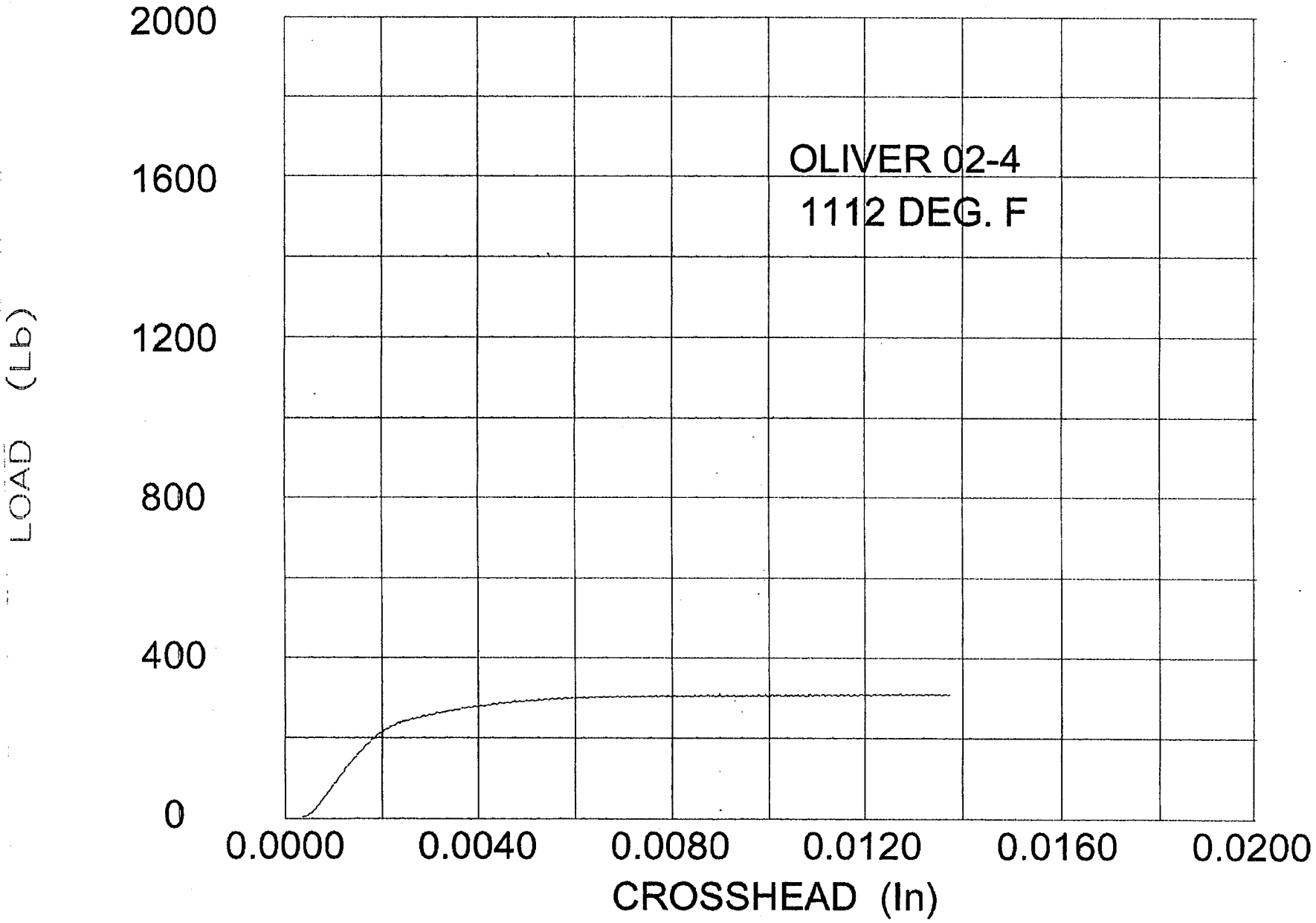

Figure 58. Load-displacement curve for a 600°C compression test of high purity NiAl (Oliver 2-4) at a strain rate of 8.3×10^{-5}/s.

3.8 Strain-Aging Effects

For this part of the study, we collaborated with Prof. John Hack of Yale University. In the first part of this study, tensile specimens of NiAl were subjected to low temperature heat treatments and tested at room temperature to observe possible changes in ductility and yield behavior often associated with strain aging effects. Based on experiments on the effects of such thermal exposures on fracture toughness, a 400°C heat treatment was selected as a potential un-pinning treatment (i.e.. remove point defects from the dislocations) and a subsequent 200°C exposure was selected as a treatment to re-establish the atmospheres around dislocations. As shown in Table VIII, preliminary results showed no significant effect of these heat treatments on ductility. The yield stress was observed to rise slightly for both low temperature heat treatments, suggesting that the 400°C heat treatment was too low in temperature to effect un-pinning of the dislocations. It must be mentioned that it is likely that surface finish effect mentioned in Section 3.11 might have played a role in determining the exact plastic elongation values.

Based on a re-evaluation of the fracture toughness data obtained by Prof. Hack on D5 NiAl [5-7], along with data on yield point behavior in polycrystalline alloys [8], a second set of experiments was then planned, for both NiAl and NiAl + 0.1 at% Fe alloys. In this set of experiments, three heat treatment conditions were evaluated: standard solution treatment, consisting of 1316°C/50hr hours followed by a furnace cool in flowing argon; re-solutioning at 1316°C, followed by a more rapid air cool; and all of the above plus a 400°C/2 hour anneal. The air cool is expected to prevent re-pinning of dislocations following the solution temperature exposure. The 400°C exposure is expected to re-pin the dislocations. The test results are shown in Table IX.

As seen in Table IX, there is very significant scatter in the room temperature elongation values. Because of the scatter in the data, distinct conclusions cannot be drawn. However, it can be concluded that the 400°C exposure does not degrade room temperature plasticity in D5 and D183. Earlier (see Table VIII), the 400°C exposure was shown not to increase the room temperature plastic elongation in D5. It appears (with limited data which are plagued with scatter) that the 400°C exposure has no effect on the room temperature plastic elongation. These results do not correlate well with toughness results [5,6] where the 400°C exposure was shown to significantly improve the room temperature toughness in D5. The yield stress appear to be slightly increased by the low temperature heat treatments. The 0.2% yield stress for D183 is also unexpectedly higher than that of D5. All other data have shown lower yield stress for D183. Such scatter in the elongation data led to a very systematic search for the sources of the scatter. This search led to the conclusions drawn in Section 3.11 'Effect of Specimen Surface Preparation'. The experiments to determine the effect of strain aging on room temperature plastic elongation and toughness should be repeated with test specimens which have been properly electropolished.

Table VIII. Results from Initial Study on Low Temperature Heat Treatment Effects

Specimen ID	HT Condition	0.2% Yield Stress	% Plastic Elongation
D5-1355 1A	1	184	1.4
D5-1355 1B	1	181	2.2
Average	1	183	1.8
D5-1355 2A	2	199	1.8
D5-1355 2B	2	198	1.9
Average	2	199	1.9
D5-1355 3A	3	210	2.2
D5-1355 3B	3	195	1.2
Average	3	203	1.7

Condition 1: Standard homogenization anneal (1316°C/50 hours/FC)
Condition 2: Standard heat treatment + 400°C/16 hours
Condition 3: Standard heat treatment + 400°C/16 hours + 200°C/2 hours

Table IX. Effect of Low Temperature Strain Aging Heat Treatments on Room Temperature Tensile Properties

Specimen ID	HT Condition	0.2% Yield Stress, MPa	% Plastic Elongation
D5-2153-1	1	189	3.1
D5-2153-2	1	184	4.0
D5-2153-3	2	201	2.5
D5-2153-4	2	199	6.8
D5-2153-5	3	198	4.9
D5-2153-6	3	201	6.6
D183-2170-2	1	207	3.0
D183-2170-3	2	215	5.4
D183-2170-4	2	217	1.4
D183-2170-5	3	223	4.3
D183-2170-6	3	220	2.1

Condition 1: Standard homogenization anneal (1316°C/50 hours/FC)
Condition 2: Standard homogenization anneal (1316°C/50 hours/rapid cool
Condition 3: Standard homogenization anneal (1316°C/50 hours/rapid cool+ 400°C/2 hours

3. 9 Effect of Carbon

Based on the observation of dynamic and static strain aging, it was postulated that interstitial impurities may be controlling dislocation movement and thereby affecting ductility. Initially, common impurities such as oxygen, nitrogen, carbon and sulfur were analyzed for many representative castings. The chemical analysis results are shown in Table IV. It was observed that oxygen, nitrogen and sulfur contents were essentially same in all the specimens whereas carbon level varied from casting to casting. Therefore, carbon was analyzed for many additional castings at one chemical laboratory to eliminate analysis errors originating from various laboratories. Leco Corporation was selected because they manufacture the majority of equipments for carbon determination. The chemical analysis results are shown in Table XI.

The following conclusions are drawn from the data: 1) the carbon levels vary from 2 ppm to 31 ppm in D5 whereas the carbon levels are below 11 ppm in Fe and Ga containing specimens. The carbon levels of the Oliver specimens are also in single digits. Since D5 with high carbon are the oldest castings in the Table XI, it is likely that the casting practices were improved with time such that carbon contents are being kept low. It is also possible that additions of Fe and Ga reduce carbon in the casting; however, we do not know of any mechanism for such a reduction in carbon. For example, since the densities of commonly formed iron carbides Fe_3C, Fe_2C and Fe_7C_3 are 7.681, 7.114 and 7.601 gm/cc^3 respectively, these carbides would not float on the top of the NiAl melt whose density is about 6.0 gm/cc^3. It is interesting to note that the majority of the specimens with high room temperature elongations have low carbon. The scatter in the data is probably related to the variation in post machining surface preparation procedure (electropolishing time) as has been discussed under Section 3.11.

The dependence of the room temperature ductility on carbon content correlates well with the strain aging phenomena observed in this study. Since D5 with low carbon also has high plastic elongation, it raises the question whether the Fe effect is real or the low carbon levels in the casting are responsible for high ductility. All the past room temperature elongation data on D5 generated under this study, as well under the GE IRAD program (about 20 data points) were re-examined, and it was observed that the majority of the elongation values in D5 were around 1 to 2 percent. The highest values on D5 did not approach the commonly obtained high values in the Fe-containing alloys. Also, the observed reduction of the flow stress in Fe-containing alloys and the propensity of the low carbon D5 alloys for serrated yielding (and reduced serrated yielding in Fe-containing alloys) appear to make the Fe effect real. In any case, a more systematic testing of D5 specimens which contain various carbon levels and which have been electropolished under controlled conditions and times is warranted.

3.10 High Purity NiAl

Three <110> oriented single crystals were received from Prof. Ben Oliver of the University of Tennessee. These crystals were given a 50 hour homogenization treatment at 1315°C. Compression, tensile and toughness tests were conducted as a function of temperature.

3.10.1 Compression Tests

The compression tests are described in Section 3.7.2 for the serrated yielding experiments. A complete absence of serrated yielding was observed in the high purity NiAl specimens at all test temperatures. The absence of serrated yielding in high purity NiAl is consistent with the expected behavior where the dislocation/impurities interactions have been eliminated in the high purity NiAl. The high purity NiAl also had much lower flow stresses compared to conventional purity NiAl at all test temperatures.

Table XI. Carbon Analysis of Representative Castings and Specimens and Their Room Temperature Plastic Elongations

Specimen ID	Carbon, ppm	RT Plastic Elong., %
D5-412	24	0.9
D5-808-4	31	0.6
D5-1667HT	2	6.9
D5-1667HT	30	7.6
D5-1760	7	0.0
D5-1770	3	4.8
D5-2153-2	7	4.0
D5-2154	4	3.6
D183-1682	2	3.9
D183-1676-6	3	6.8
D183-1676-1	3	2.9
D183-1126-3	11	4.0
D183-2448	6	1.9-8.2*
D183-2449	11	0.4-6.6*
D128-1896	4	4.3
D182-1124-3	8	6.6
D184-1092-3	3	5.7
Oliver 1	9	1.3
Oliver 2-1	11	12.9
Oliver 2-2	6	1.1

* Range of values with various specimen surface preparations

3.10.2 Room Temperature Tensile Tests

Initially, six tensile tests (three each from Oliver NiAl single crystals 1 and 2) were conducted at room temperature. One of these specimens (Oliver 2-1) showed a room temperature plastic elongation of 12.85%. The load vs. strain curve for Oliver 2-1 is shown in Figure 59. The other five specimens exhibited plastic elongations ranging from 1.14 to 2.38%, typical of conventional purity NiAl. The load vs. strain curve for one of the specimens (Oliver 2-2) typical for these low

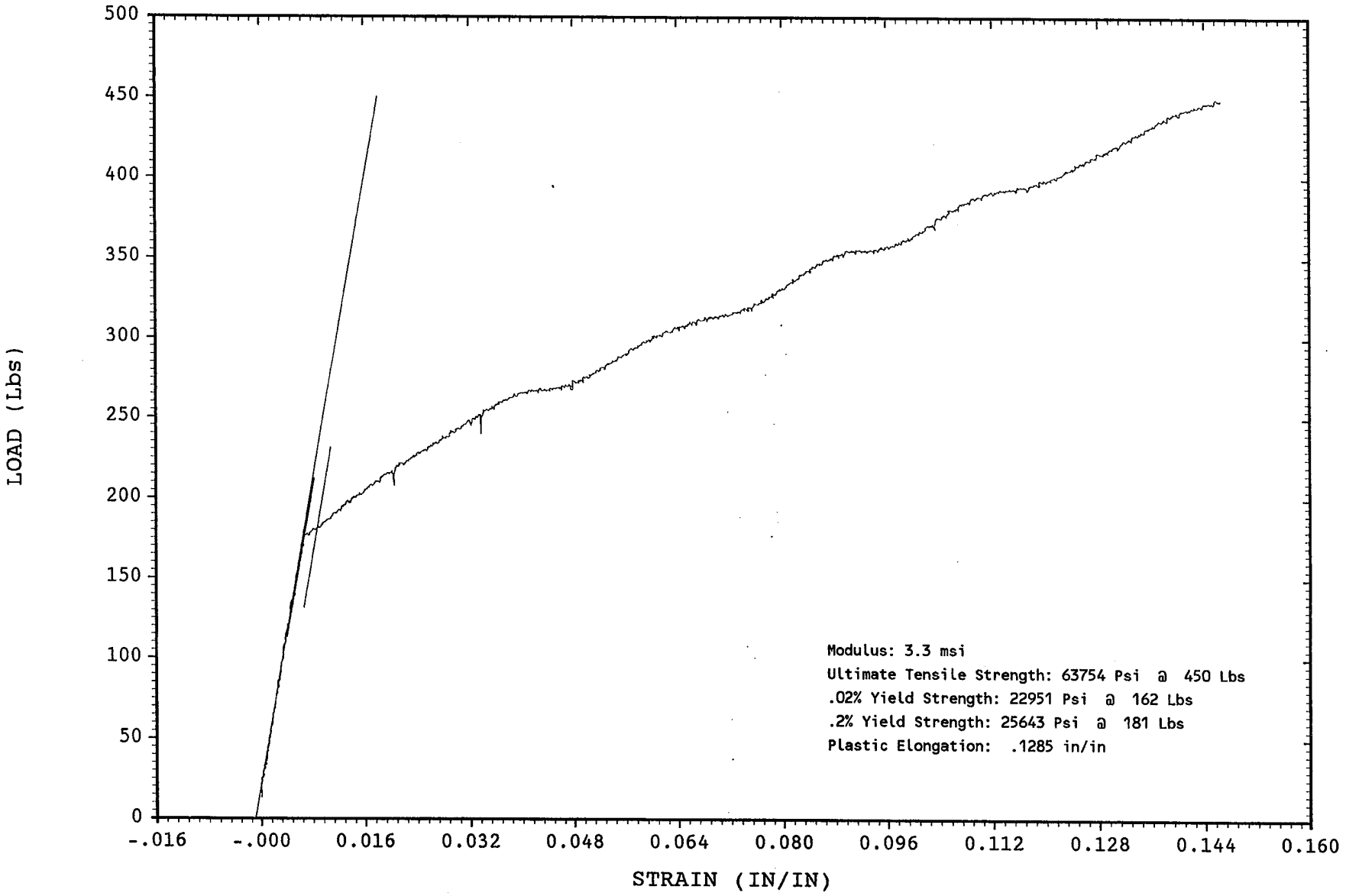

Figure 59. Load-strain curve for a room temperature tensile test of high purity NiAl (Oliver 2-1) at a strain rate of 8.3×10^{-5}/s showing 12.85% plastic elongation.

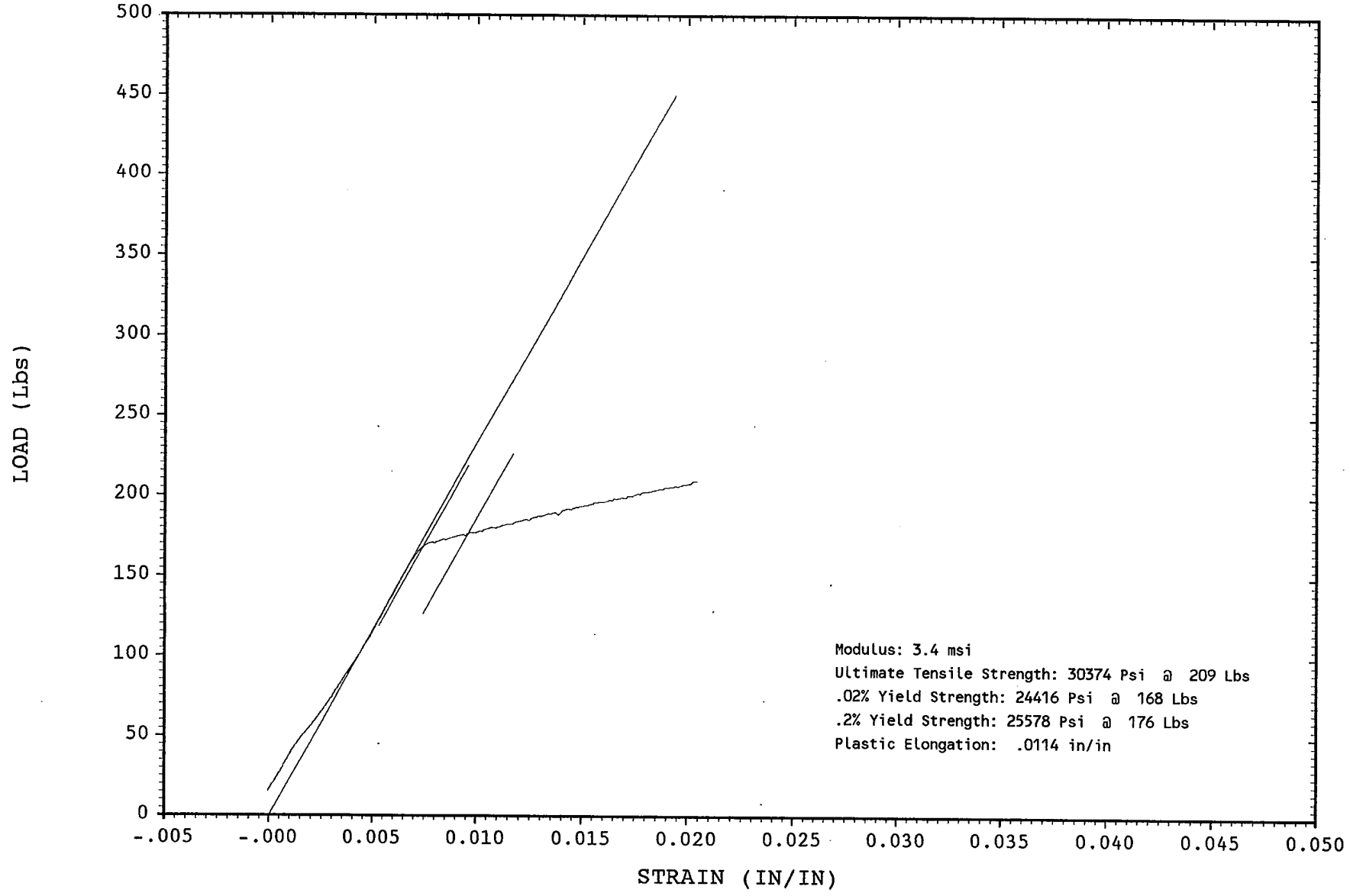

Figure 60. Load-strain curve for a room temperature tensile test of high purity NiAl (Oliver 2-2) at a strain rate of 8.3×10^{-5}/s showing only 1.14% plastic elongation.

ductility specimens is shown in Figure 60. The complete test data set and load vs. strain curves are shown in Appendix A. It is interesting to note that the 0.2% yield strength for the six specimens are essentially the same, around 172 MPa. The ultimate tensile strength (UTS) of the specimens are dependent on the final elongation prior to fracture. The specimen with the 12.85% elongation had an UTS of 439.2 MPa which is amazingly very high. This indicates that higher fracture loads are obtainable even in highly pure NiAl provided premature failures are avoided.

Another set of four specimens (Oliver 3-1, 3-2, 3-3 and 3-4) from Oliver NiAl single crystal 3 were machined and tested at room temperature. Two of the specimens (Oliver 3-1 and 3-2) were pre-strained to 2% plastic strain at 540°C and subsequently tested at room temperature. One of the specimens (Oliver 3-1) exhibited an elongation of 4.52% and the second specimen (Oliver 3-2) failed after only 0.4% elongation. Oliver 3-3 was given the 800°C/24 hrs high temperature heat treatment. This specimen showed an elongation of 7.68% which is similar to the heat treatment effect observed in conventional purity NiAl (D5HT) specimens. Oliver 3-4 was given a 1000°C pre-oxidizing treatment (oxide softening) to improve room temperature ductility per observations by Noebe and Gibala [32]. This specimen failed after only 0.47% plastic elongation at room temperature indicating no improvement by the pre-oxidation treatment.

A very thorough investigation was carried out to understand the scatter in the room temperature plastic elongation values. This included composition verification, fractography of the failed specimens by scanning electron microscopy (SEM), TEM analysis of the dislocation structures and vendor test procedure audit. The consistency of yield stress values in the Oliver 1-1, 1-2, 1-3, 2-1, 2-2 and 2-3 specimens indicated that the specimens had no microstructural and compositional variations. It can also be inferred from the yield stress data that there were no discrepancies related to testing procedure, such as specimen misalignment, etc. The composition analysis of several tested specimens did not reveal any significant differences (Table IV). The TEM observations on the high (Oliver 2-1) and low ductility (Oliver 2-2 and 2-3) specimens are described in Section 3.10.5 It was concluded that the deformation behavior (dislocation structure, type, and slip planes) was similar for the high and low ductility specimens. The deformation behavior was also similar to that seen in the conventional purity D5 specimens. It is quite likely , though, that the tensile elongation values may have been affected by variation in the post surface finishing step. Since higher elongation values are generally obtained with specimens with either a high temperature pre-strain or a 800°C heat treatment, it is likely that these treatments make test specimens less susceptible to surface condition effects.

3.10.2.1 Fractography of Tensile Test Specimens

The fracture surface examination by scanning electron microscopy of the failed tensile specimens revealed an indication of either surface scratches or slip bands at the initiation sites of all the low ductility specimens as shown in Figures 61-63. Such indications were not present in the three high ductility specimens. These indications appear to be slip bands, but it was not possible to unequivocally determine whether the indications were slip bands or scratches. Very careful indexing of these lines in one of the specimens (Oliver 1-3) with respect to the specimen axis by SEM and X-ray indicated that these could be slip bands with slip occurring on both {100} and {110} planes, which is consistent with the slip planes observed in NiAl. As will be discussed in

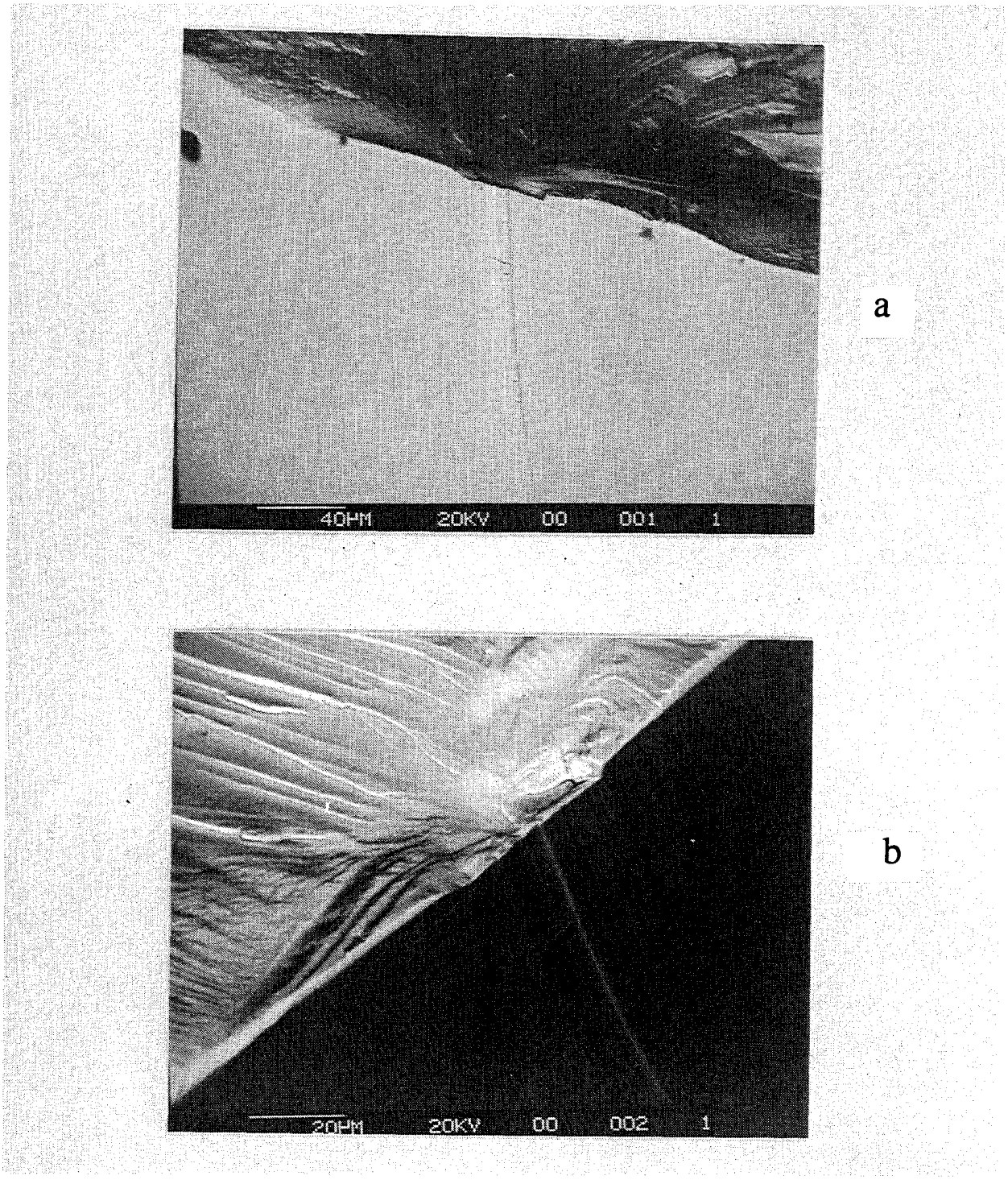

Figure 61. Scanning electron micrographs of high purity NiAl (Oliver 1-1) showing slip bands or scratches at the fracture origin of low ductility specimens. a) shows fracture origin, b) shows slip bands or scratches at the surface near the fracture origin, c) higher magnification of the slip bands or scratches.

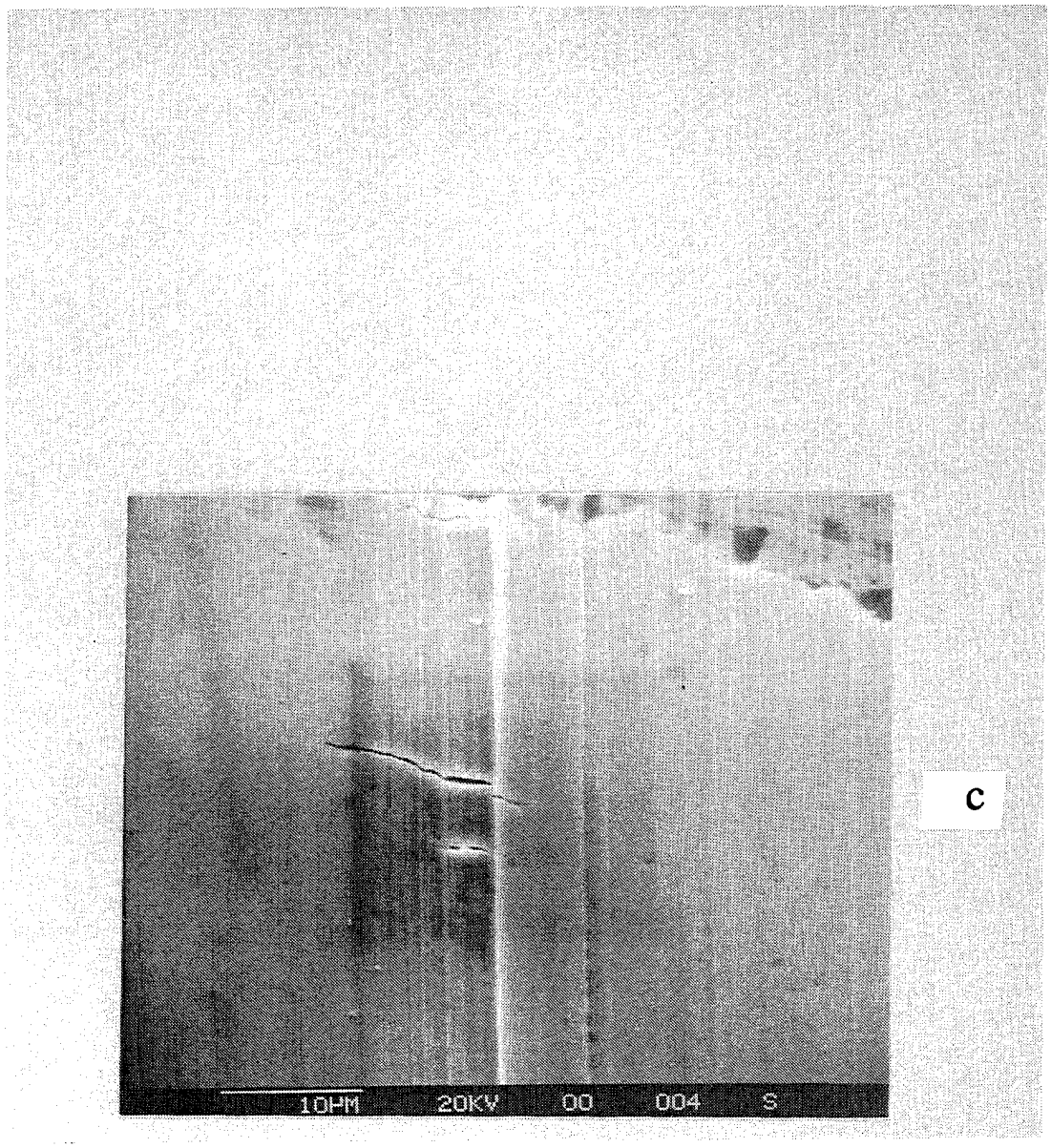

Figure 61(cont.). Scanning electron micrographs of high purity NiAl (Oliver 1-1) showing slip bands or scratches at the fracture origin of low ductility specimens. a) shows fracture origin, b) shows slip bands or scratches at the surface near the fracture origin, c) higher magnification of the slip bands or scratches.

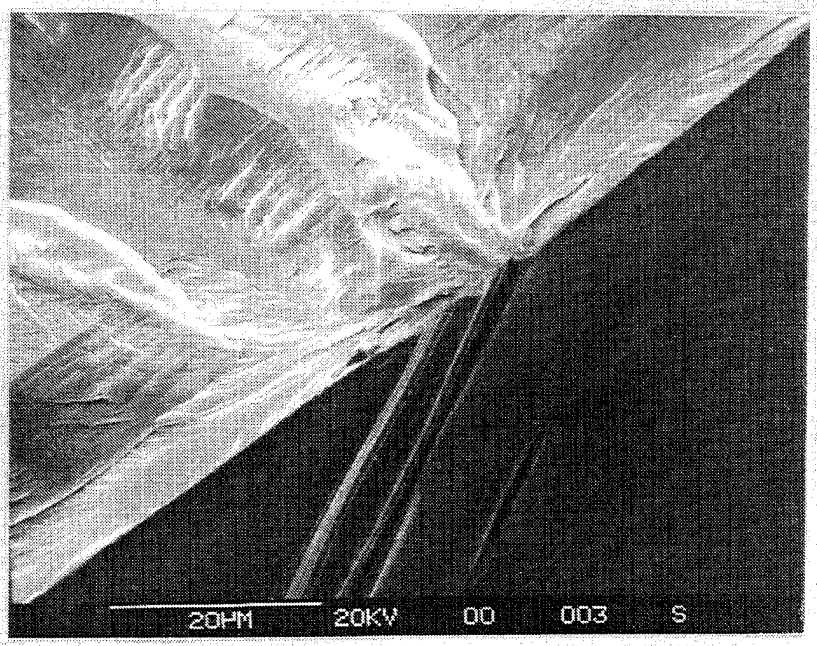

a

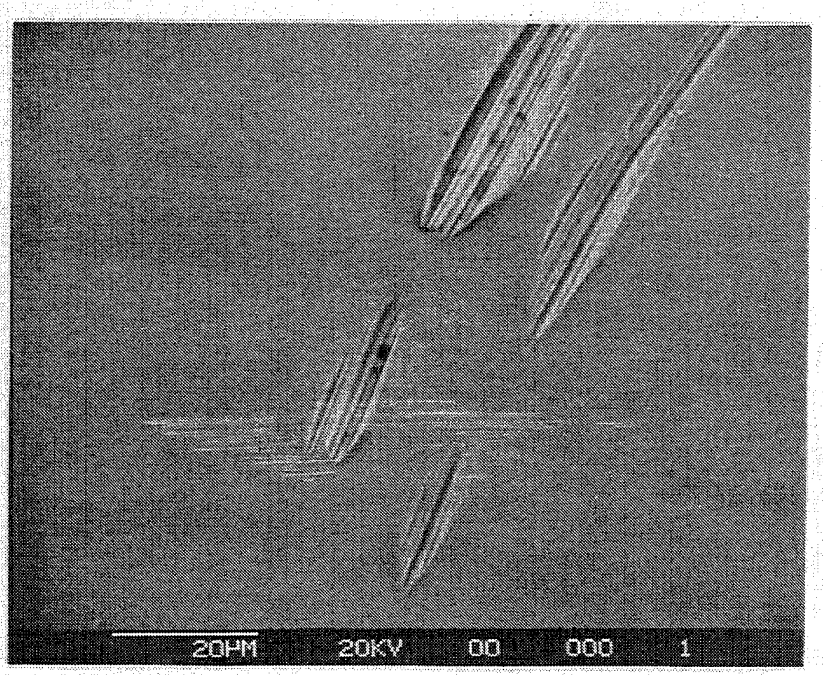

b

Figure 62. Scanning electron micrographs of high purity NiAl (Oliver 1-2) showing slip bands or scratches at the fracture origin of low ductility specimens. a) shows fracture origin, b) shows slip bands or scratches at the surface, c) higher magnification of the slip bands or scratches, d) still higher magnification of the slip bands or scratches.

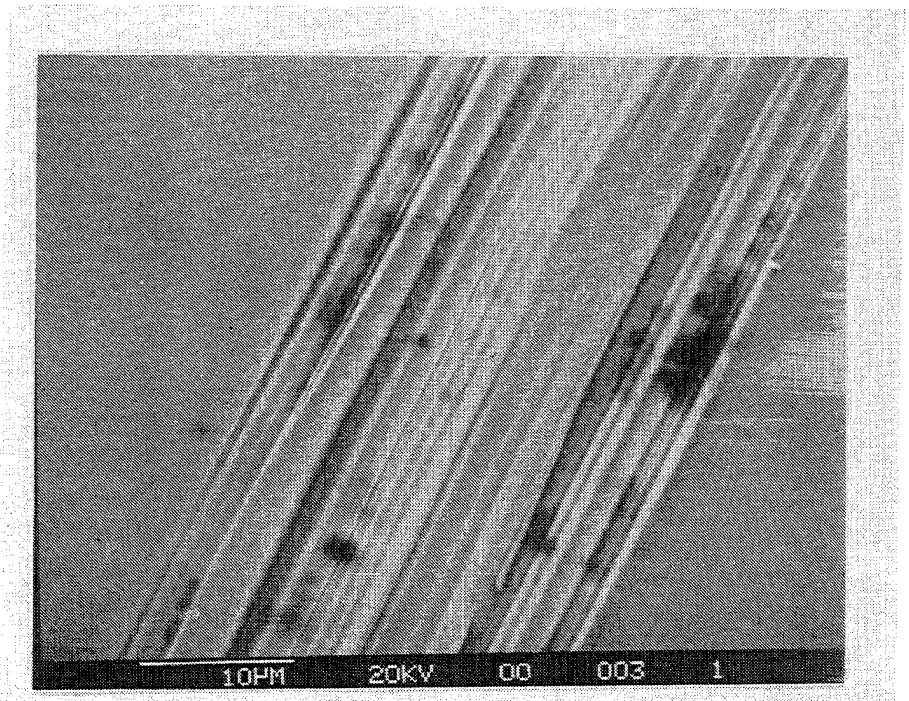

c

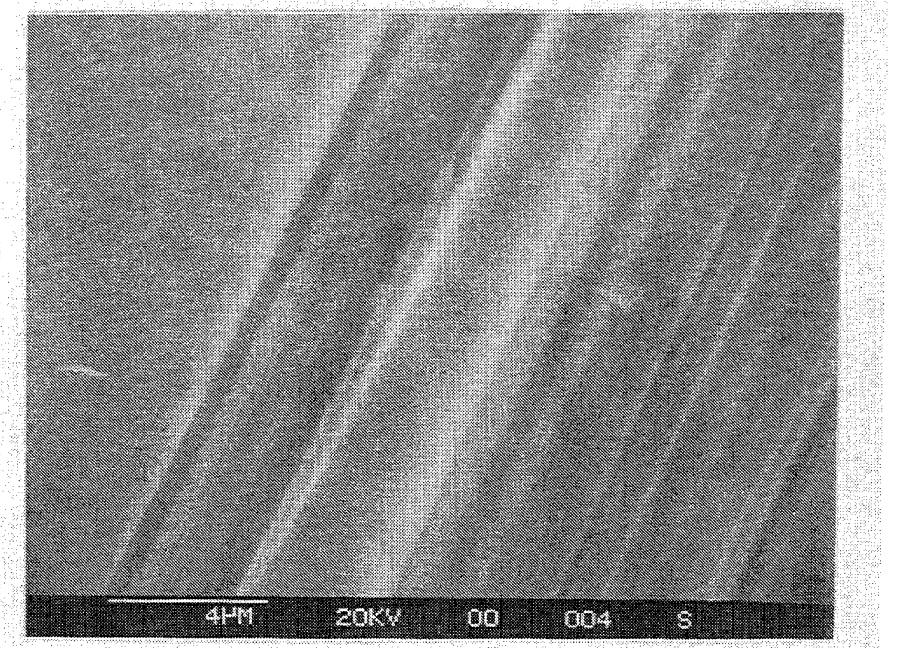

d

Figure 62(cont.). Scanning electron micrographs of high purity NiAl (Oliver 1-2) showing slip bands or scratches at the fracture origin of low ductility specimens. a) shows fracture origin, b) shows slip bands or scratches at the surface, c) higher magnification of the slip bands or scratches, d) still higher magnification of the slip bands or scratches.

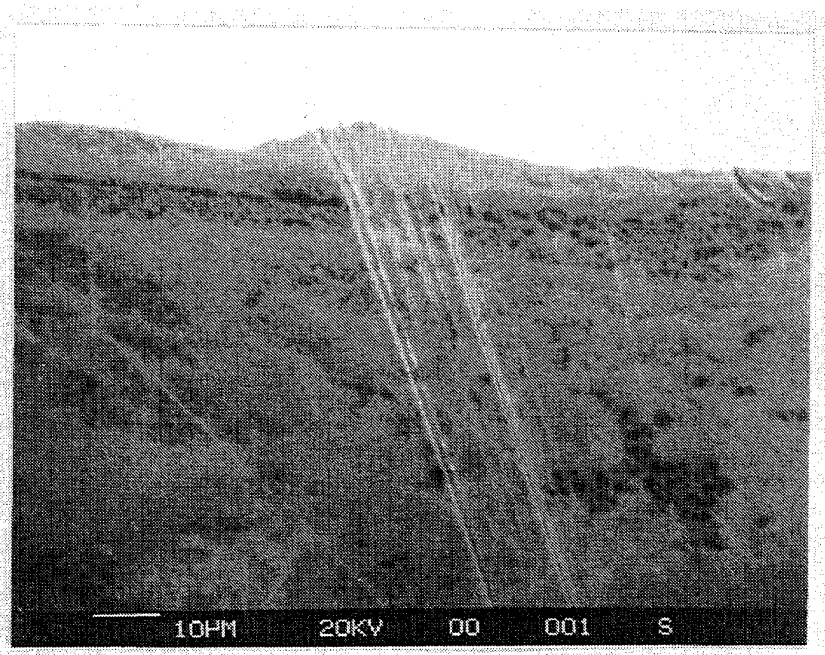

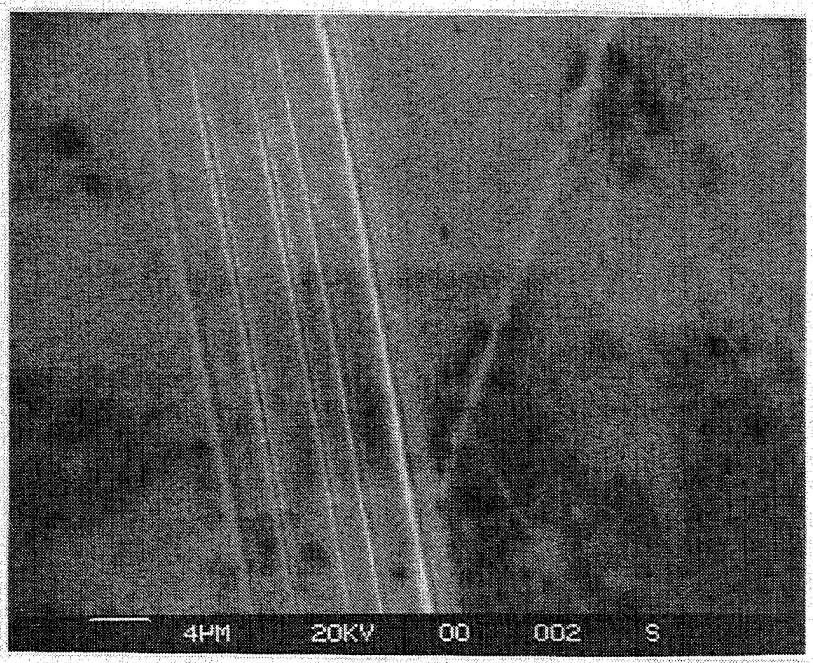

Figure 63. Scanning electron micrographs of high purity NiAl (Oliver 1-3) showing what appears to be slip bands at the fracture origin of low ductility specimens. These slip bands were indexed to establish {100} and {110} slip planes.

Section 3.11, the surface grinding marks can have a dramatic influence on ductility. However, the grinding marks are generally nearly perpendicular to the specimen axis, whereas the surface indications observed on these specimens were nearly parallel to the specimen axis. Further analysis of these indications is warranted.

3.10.3 Fracture Toughness

<110> oriented three-point bend fracture toughness specimens with a chevron notch were machined and tested as a function of temperature. The test results are shown in Table X. The fracture toughness results are compared with the values obtained with the conventional purity NiAl in Figure 64. It is obvious from the comparison of the data that no significant improvement in fracture toughness is obtained with the high purity single crystals. These results are surprising since the high purity NiAl specimens contained very low levels of interstitial impurities, and showed an absence of serrated yielding as discussed in Section 3.7.2. It was believed that the high purity NiAl would have higher dislocation mobility, thereby providing higher fracture toughness. It is quite obvious that the deformation behavior in NiAl is not well understood, and additional study is warranted to further understand its deformation behavior.

Table X. Fracture Toughness of <110> Oriented High Purity NiAl

Specimen ID	Temperature, °C	K_{ic}, MPa•$m^{1/2}$
Oliver 3-1	RT	5.8
Oliver 3-2	RT	4.4
Oliver 3-3	93 (200°F)	4.9
Oliver 3-4	149 (300°F)	6.3
Oliver 3-5	204 (400°F)	8.2
Oliver 3-6	260 (500°F)	4.5

3.10.3.1 Fractography of Toughness Test Specimens

The fracture surfaces of all the specimens were examined, and the fracture planes were estimated to be {110} based on the fact that the fracture facets were parallel to the specimen orientation of <110> in specimens with toughness values ranging from 4.5 to 6.3 MPa.•$m^{1/2}$. The lone specimen (Oliver 3-5) which exhibited a toughness of 8.2 MPa.•$m^{1/2}$ at 204°C (400°F) had cleavage facets of high index planes. These observations on fracture planes are identical to the observations on conventional purity NiAl [33-34].

In summary, the high purity NiAl specimens did not exhibit any significant improvement in room temperature ductility and toughness. These results are rather surprising. It is probably easy to explain low ductility values on poor surface condition of the specimens, but lack of improvement in fracture toughness is difficult to explain. These specimens did show an absence of strain aging, and had much lower yield strengths compared to the conventional purity NiAl.

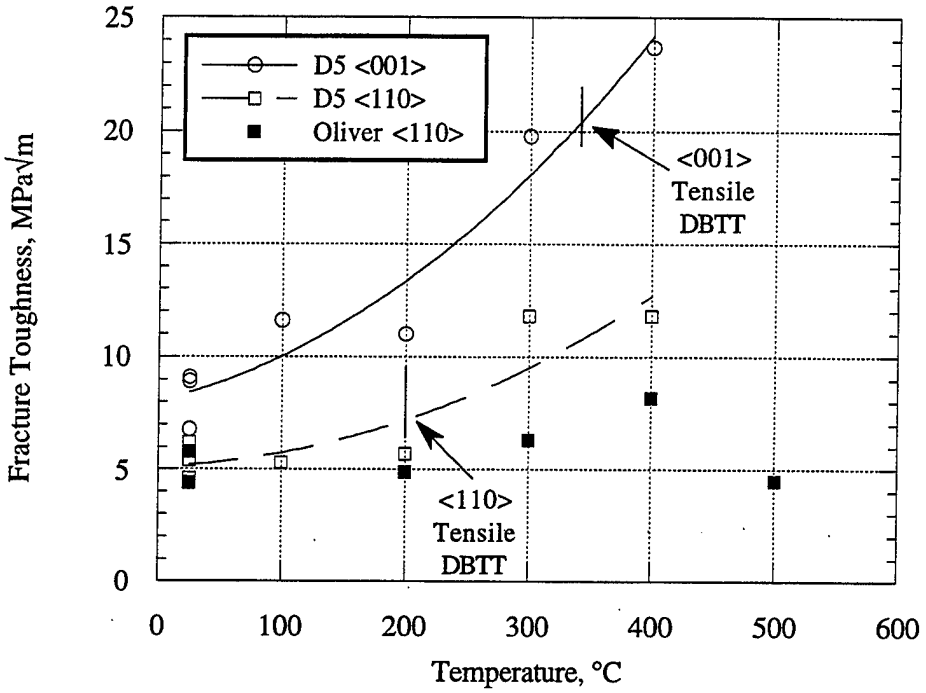

Figure 64. Fracture toughness of high purity NiAl as a function of temperature compared with conventional purity NiAl.

3.10.4 Deformation Behavior (at NASA Lewis Research Center)

Three tensile samples designated Oliver 2-1, 2-2, and 2-3 were sent to NASA Lewis Research Center, Cleveland for post-test analysis to determine the origin of the scatter in the room temperature ductility. Transmission Electron Microscopy (TEM) was performed on a low ductility sample (Oliver 2-2) and the high ductility sample (Oliver 2-1). TEM foils were prepared from the gage section of the fractured tensile samples just below the fracture surface. General microstructural examination and dislocation analysis were conducted in a Philips EM420 TEM equipped with a double-tilt goniometer. At least three foils from each sample were examined.

Representative TEM bright-field images close to the [011] zone axis, showing the deformed microstructures from samples Oliver 2-2 ($\varepsilon_f = 2.1\%$) and Oliver 2-1 ($\varepsilon_f = 12.9\%$) are shown in Figure 65a and 65b, respectively. The microstructure of the deformed samples consist of jogged and curved dislocation segments and dislocation debris in the form of numerous elongated loops. These loops are clearly visible in sample Oliver 2-2, where the dislocation density is much lower. As deformation proceeds the dislocation structure becomes arranged in a cellular network (Fig. 65(b). This type of observation is common for near stoichiometric binary NiAl and is attributed to the prolific cross-slip of screw dislocations during room temperature deformation [35,36].

Dislocation contrast analysis was conducted for both samples and it was found that deformation occurred by <010> type dislocations. Details of the g•b analysis for sample Oliver 2-2 are shown in Figure 66, where dislocations marked as "A" and "B" act as reference points for each micrograph taken under the different diffracting conditions. Dislocations as well as loops were strongly visible with the operating reflections g011 (Fig. 66(a)) and g110 (Fig. 66(d)), invisible with g100 (Fig. 66(b)), and showed weak residual contrast with g101 (Fig. 66(c)). These observations suggest that the dislocations and loops had Burgers vector b = [010]. The dislocation segments had a mixed character and the loops were elongated along the [100] direction. Although the majority of dislocations had b = [010], occasionally dislocations with b = [001] were also observed. These features were common to both samples though they are much easier to distinguish in sample Oliver 2-2 due to the lower overall dislocation density.

Consequently, deformation of the high purity NiAl single crystals occurs by <010> dislocations, which leave behind <010> dislocation debris mainly in the form of elongated loops. The loops are formed by double cross-slip of screw components to form superjogs, and probably to a greater extent by dipole trapping of edge segments on parallel slip planes. Evidence for the operation of both of these mechanisms is visible in the deformed microstructure. Regions showing double cross-slip are marked "Y", and those showing dipole trapping of edge dislocations and their subsequent break-up into a series of smaller loops are marked "X" in Figs. 65(a) and 66(a). While determination of the slip plane was ambiguous since most of the dislocations appear to be debris not lying on specific slip planes, formation of dislocation loops aligned along <100> by both mechanisms would geometrically require a {100} type slip plane. Therefore, deformation in these crystals occurs by <010>{100}. However, the loops themselves reside on {110} planes. The loops represent debris left over from the <010>{100} slip process and would not contribute to the deformation of the alloy since their Burgers vector is not contained within the plane of the loop. The general observation of significant cross-slip at room temperature

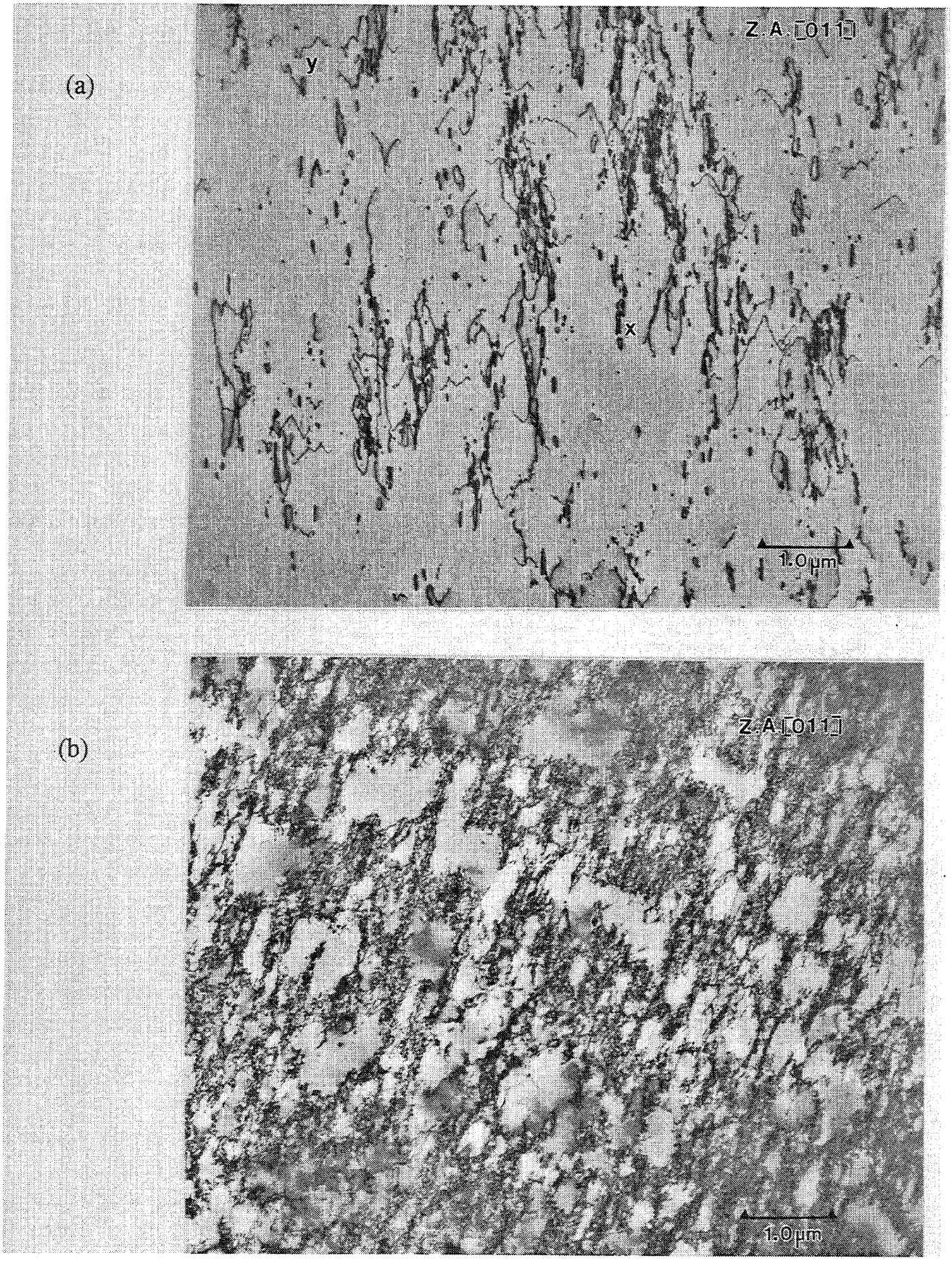

Figure 65. Bright-field images close to the [011] zone axis, showing the deformed microstructures in a) Oliver 2-2 ($\varepsilon_f = 2.1\%$), b) Oliver 2-1 ($\varepsilon_f = 12.9\%$).

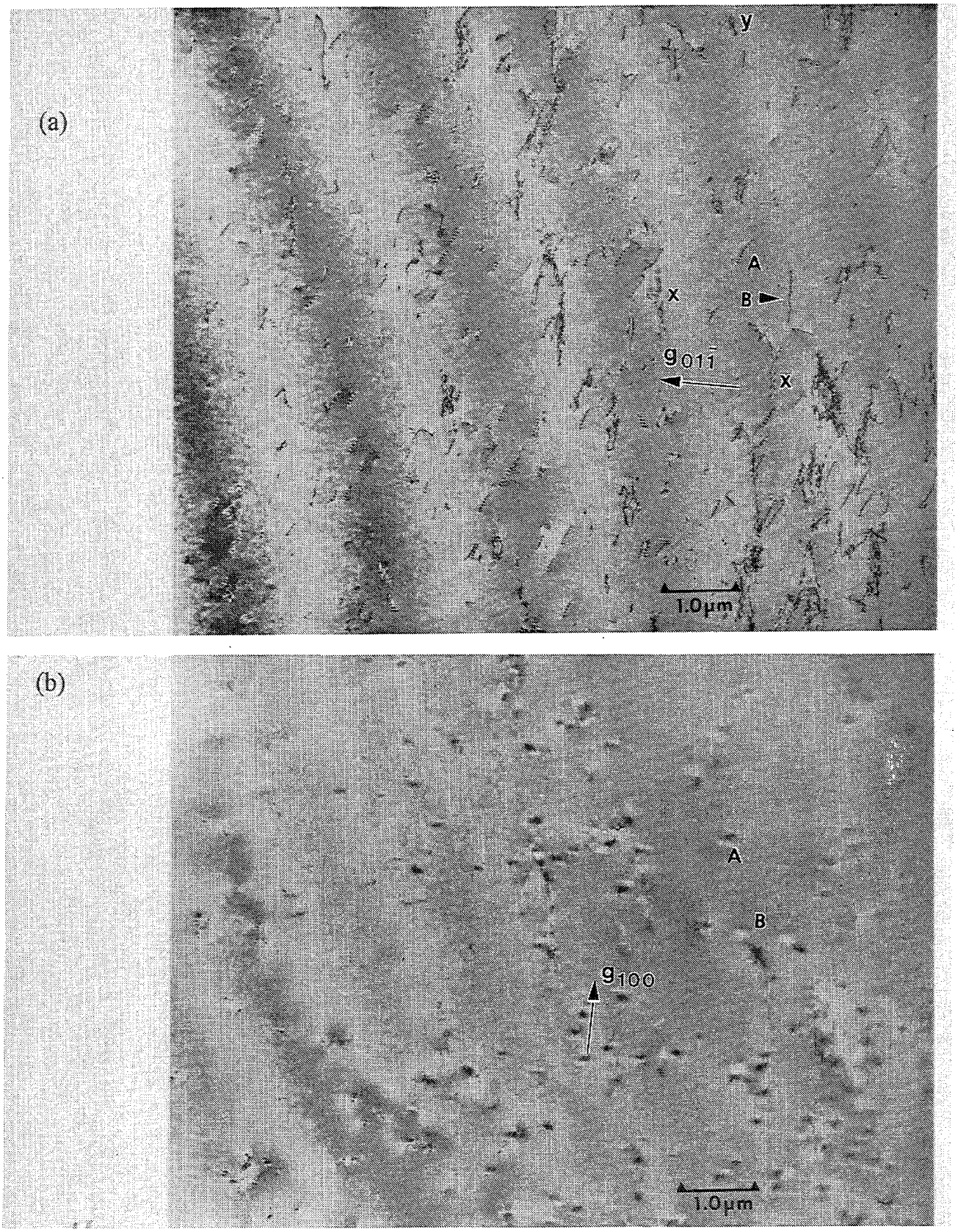

Figure 66. Dislocation contrast analysis showing a) strong visibility of dislocations with **g**01-1, b) invisibility with **g**100, c) weak residual contrast with **g**10-1, and d) strong visibility of dislocations with **g**-110. Dislocations marked "A" and "B" act as reference points.

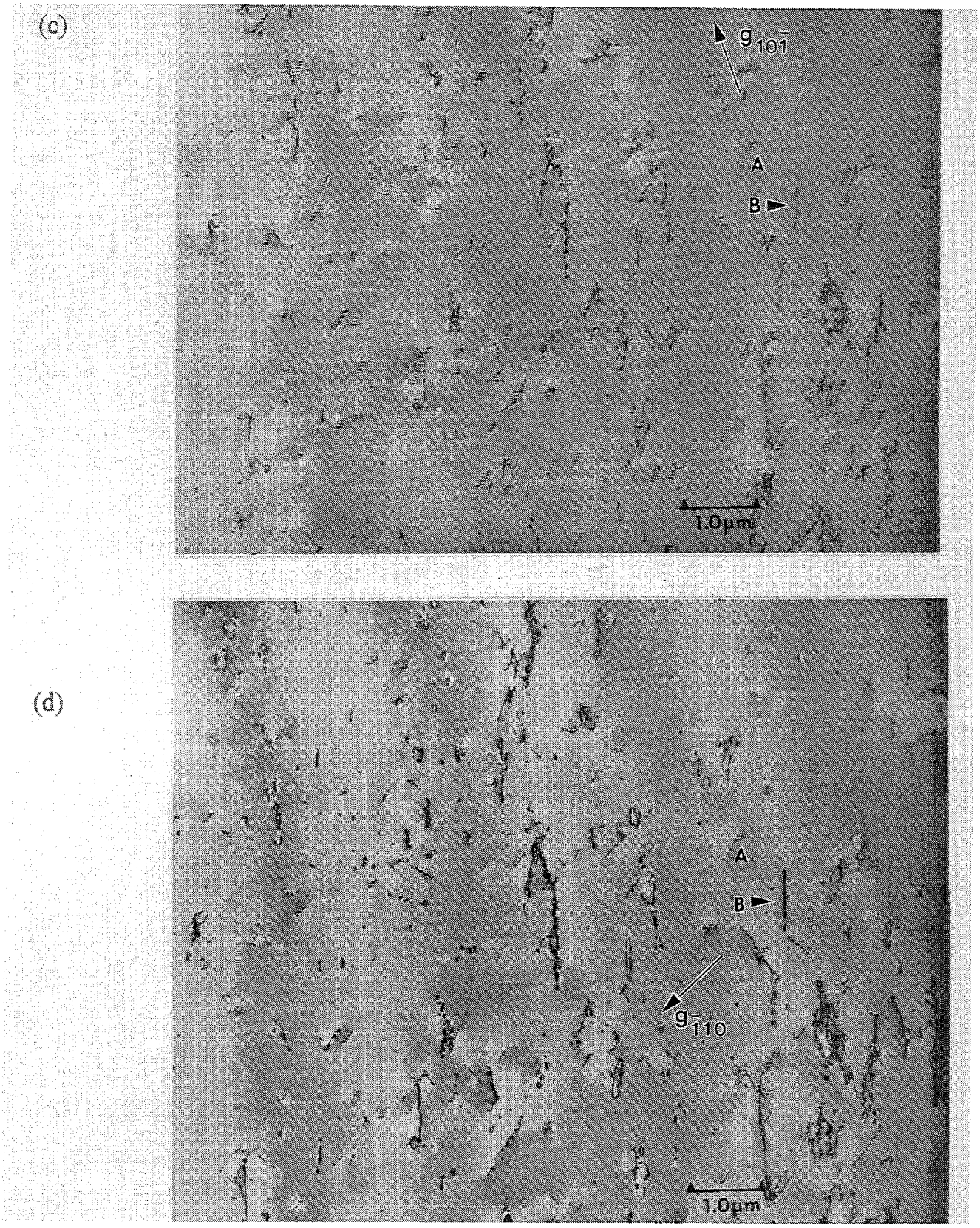

Figure 66(cont.). Dislocation contrast analysis showing a) strong visibility of dislocations with g01-1, b) invisibility with g100, c) weak residual contrast with g10-1, and d) strong visibility of dislocations with g-110. Dislocations marked "A" and "B" act as reference points.

is similar to previous observations in binary polycrystalline NiAl [35] and conventional purity single crystals [21,36]. Therefore, it is not apparent that the high purity material should have any advantage in terms of fracture behavior compared to conventional purity material.

3.11 Effect of Specimen Surface Preparation

A very extensive study was completed to understand the effect of surface polishing techniques on the room temperature tensile ductility. After the tensile specimens are ground to the specified dimensions, they are electropolished to remove grinding marks and the residual stresses on the surface of the specimen which are introduced during the grinding operation. The electropolishing conditions are described in the experimental Section 3.2. On the outset, it must be mentioned that electropolishing is an art, and highly dependent on the experience base of the technician. The prescribed electrolyte solution, temperature of the bath, voltage and current are carefully controlled by the technician. However, the electropolishing time which varies from 45 seconds to 120 seconds is determined by visual examination of the specimen surface. The technician is instructed to remove about 25 μm of surface layer. He visually looks for removal of the grinding marks as well as occurrence of etch pits. He also looks for a highly shinny surface which may not be an indication of the fact that all the grinding marks are removed. The determination of the electropolishing time is highly subjective, and has produced specimens with wide variations in the amount of surface layer removed since this removal of the surface layer is strongly time dependent. Also, if proper electropolishing conditions are not followed, excessive etch pits are introduced. These etch pits could have an adverse effect on the room temperature ductility.

A total of twenty eight specimens of D183 were evaluated. These specimens came from four different single crystal slabs. The test matrix was planned in such a way that all the initial surface preparation techniques and their variations could be evaluated on specimens from the same slab. The second slab was used to obtain additional data with the most interesting results. The third slab was used to compare test data from two different testing vendors. Therefore, ten specimens were prepared with various electropolishing conditions and times. In addition, two specimens were tested without any surface preparation to determine the effect of grinding marks and residual stresses. Thirteen specimens were chemically milled with varying milling times. The chemical milling conditions are described in Section 3.2. Chemical milling is an effective technique to remove surface material. Peaks and valleys of the grinding marks are somewhat preferentially attacked in chemical milling, leaving shallower peaks and valleys. The net result is that the stress concentration resulting from the grinding marks is reduced. Three specimens were also hand polished using diamond paste papers.

All specimens were tested at room temperature after making sure that they were properly aligned in the test fixtures at Cincinnati Testing Laboratories, Inc. (CTL). The test results are shown in Table XII A very dramatic effect of specimen surface finishing operation was observed. As can be seen from the Table XII, the room temperature tensile elongation for D183 varied from a very low value of 0.4% to a very high value of 8.2%, depending on how the specimen surface was prepared. The high plastic elongation values ranging from 6 to 8% are noteworthy because these are the highest room temperature tensile ductility values ever reported for an NiAl alloy.

Table XII. Effect of Surface Finishing Step on Room Temperature Plastic Elongation in Fe-Containing NiAl Alloy

Specimen ID	Surface Preparation	Yield Stress, MPa	Pl. El., %
D183-2449-1	Electropolish, 10% perchloric+methanol, 45 sec (3 int. 15 sec each)	183.7	2.4
D183-2449-2	Electropolish, 7% perchloric+methanol+Glycol 90 sec (6x15 sec)	181.6	0.4
D183-2449-3	Electropolish, 10% perchloric+methanol, 50 sec (15+10+10+15 sec)	181.7	1.6
D183-2449-4	Chem mill, 10 min	180.9	6.6
D183-2449-5	Chem mill, 5 min	181.8	3.8
D183-2449-6	Chem mill, 5 min	184.9	5.3
D183-2449-7	Diamond polished	178.4	0.8
D183-2449-8	Diamond polished	179.7	1.0
D183-2449-9	Diamond polished	179.9	0.5
D183-2449-10	As ground	179.9	0.7
D183-2449-12	As ground	176.6	0.4
D183-2449-11	Chem mill, 10 min	183.7	2.5
D183-2448-1	Chem mill, 5 min	174.9	1.9
D183-2448-2	Chem mill, 10 min	173.0	2.2
D183-2448-3	Chem mill, 15 min	179.1	6.8
D183-2448-4	Electropolish, 10% perchloric+methanol, 60 sec (first few intervals 3 sec each, then 15 sec each), 0.5 mil removal	182.5	5.4
D183-2448-5	Electropolish, 7% perchloric+methanol, 90 sec (first few intervals 3 sec each, then 15 sec each), 0.75 mil removal	178.9	8.2
D183-2448-6	Electropolish, 10% perchloric+methanol, 180 sec (first few intervals 3 sec each, then 15 sec each), 1.0 mil removal	176.5	7.2
D183-1676-6	Electropolish as above in 1993, 15 (3 sec) intervals	180.3	6.8
D183-2448-7	Electropolish, 7% perchloric+methanol, 75 sec (first few intervals 3 sec each, then 15 sec each), 1.0 mil removal	192.2	6.0
D183-2448-8	Same as D183-2448-7	191.7	6.6
D183-2448-9	Same as D183-2448-7	189.0	6.1
D183-2170X-1	Chem mill, 30 min	189.1	5.3
D183-2170X-2	Chem mill, 15 min	184.6	7.2
D183-2170X-3	Chem mill, 20 min	189.2	5.1
D183-2170X-A	Chem mill, 15 min, 0.7 mil removal	197.3	5.8
D183-2170X-B	Chem mill, 20 min, 0.9 mil removal	201.7	4.2
D183-2170X-C	Chem mill, 30 min, 1.15 mil removal	201.0	3.3

The as-ground specimens (D183-2449-10 and 11) without any post machining surface preparation showed essentially no plasticity. In the diamond polished specimens (D183-2449-7, 8 and 9), even though they visually look very shinny, the grinding marks were not removed These specimens also had very poor ductility ranging from 0.5 to 1.0%. Specimen D183-2449-2 was electropolished using Glycol in the electropolishing solution to avoid etch pitting. This specimen showed very little removal of the grinding marks and showed an elongation of only 0.4%.

From tests on the as-ground and diamond polished specimens, it became apparent that removal of grinding marks was essential to obtain high elongation. Subsequent electropolishing and chemical milling trials were conducted with various polishing and milling times to obtain varied degrees of grinding mark removal. For the electropolished specimens, though there are still a few unexplainable results, it appears that about 10 to 25 μm surface layer removal is necessary to eliminate detrimental effects of the grinding marks on the room temperature ductility. For example, specimen D183-2448-5 which exhibited 8.2% ductility had about 20 μm surface layer removal. The surface of this specimen is shown in Figure 67. Note a complete absence of any grinding marks in this specimen. The surface of an as-ground specimen is shown in Figure 68 for comparison. The surface of the specimen D183-2449-3 which showed 1.6% ductility is also shown in Figure 69 for comparison. The surface of the specimen D183-2448-4 which showed 5.4% ductility is shown in Figure 70. In this specimen, about 12 μm surface layer was removed by electropolishing for 60 seconds. As can be seen in Figure 70, the grinding marks are not completely removed. The surface of the specimen D183-2448-6 which showed 7.2% ductility is shown in Figure 71. In this specimen, about 25 μm surface layer was removed by eletropolishing for 120 seconds. As can be seen in Figure 71, remnants of the grinding marks are still visible. It is not clear why this specimen, even with a higher electropolishing time and more surface layer removal compared to specimen D183-2448-5, still has remnants of the grinding marks. It is known, however, that the initial surface condition of the specimen prior to electropolishing such as the depth of the grinding marks or cleanliness of the surface can affect eletropolishing behavior. It was interesting to note that these high ductility specimens contained etch pits. It appears that these etch pits were not detrimental. It was also observed that several of the high ductility specimens failed away from the gage area near the radius of the button head specimens where there is a high stress concentration indicating a potentially much higher inherent ductility of D183. It should be pointed out again that electropolishing is an art, and also depends on the surface condition of the machined specimen prior to electropolishing. Therefore, electropolishing trials with various electropolishing times are warranted with every new batch of specimens to make sure that the grinding marks are sufficiently removed.

A load vs. displacement curve for D183-2448-5 is shown in Figure 72. This curve represents behavior typical of the D183 specimens. Note the load drop near yielding in Figure 72 (see also Figure 74) which was observed in these specimens. Load drop is not seen in D5 specimens.

As was seen in the electropolished specimens, there was a large dependence of the room temperature elongation in chemically milled specimens on milling times. The elongation values ranged from 1.9 to 6.6%. Examination of the surfaces show varying degrees of grinding mark removal. Specimens chemically milled for 15 minutes and longer exhibited elongation values ranging from 5.1% to 7.2%. Figure 73 shows surfaces of two chem milled specimens, D183-

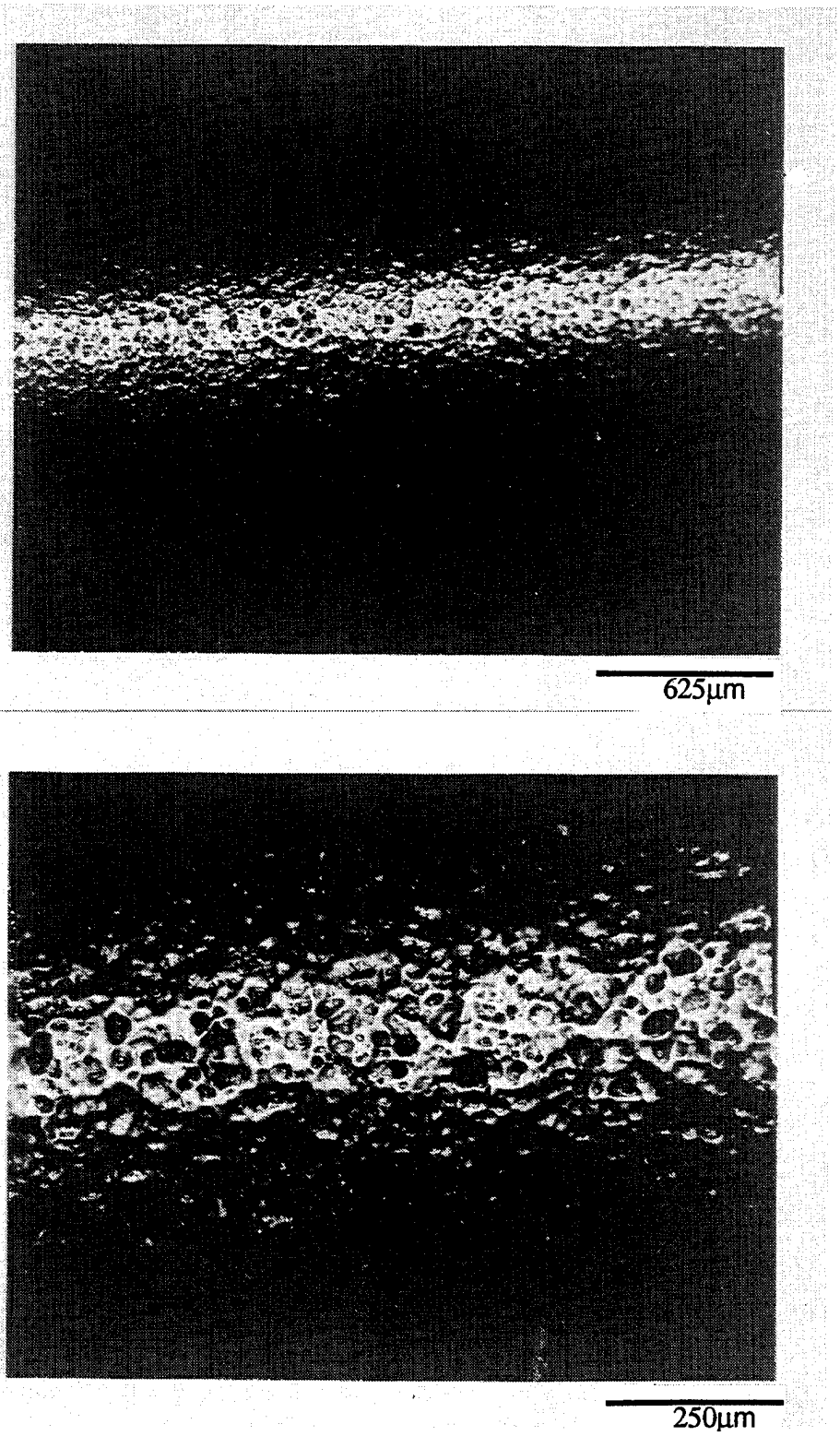

Figure 67. Optical micrographs showing surface of D183-2448-5 specimen (8.2% plastic elongation) after electropolishing. Note a complete absence of grinding marks.

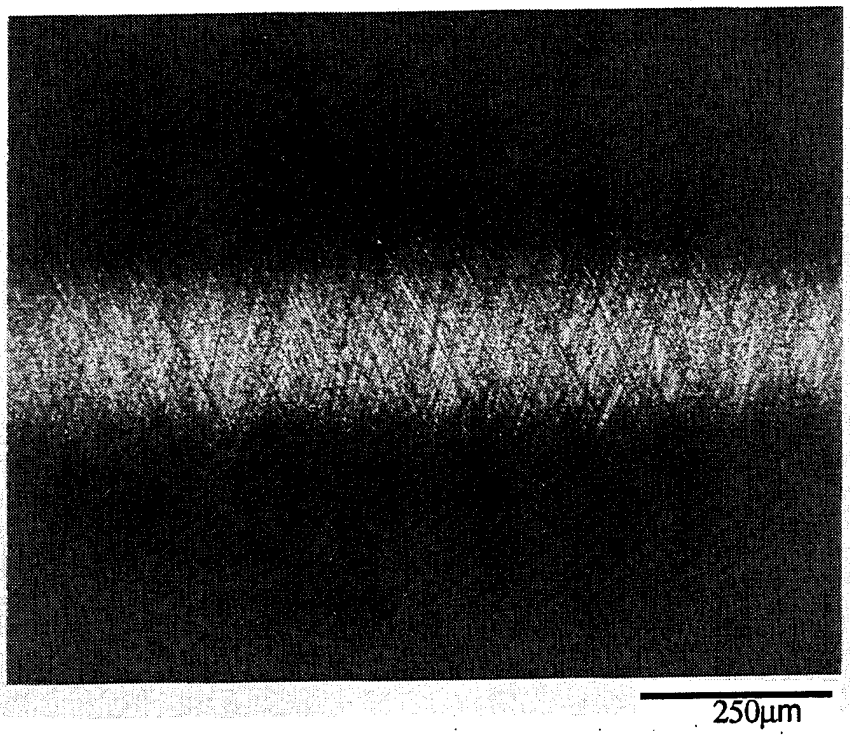

Figure 68. Optical micrograph showing surface of an as-ground specimen (D183-2449-10).

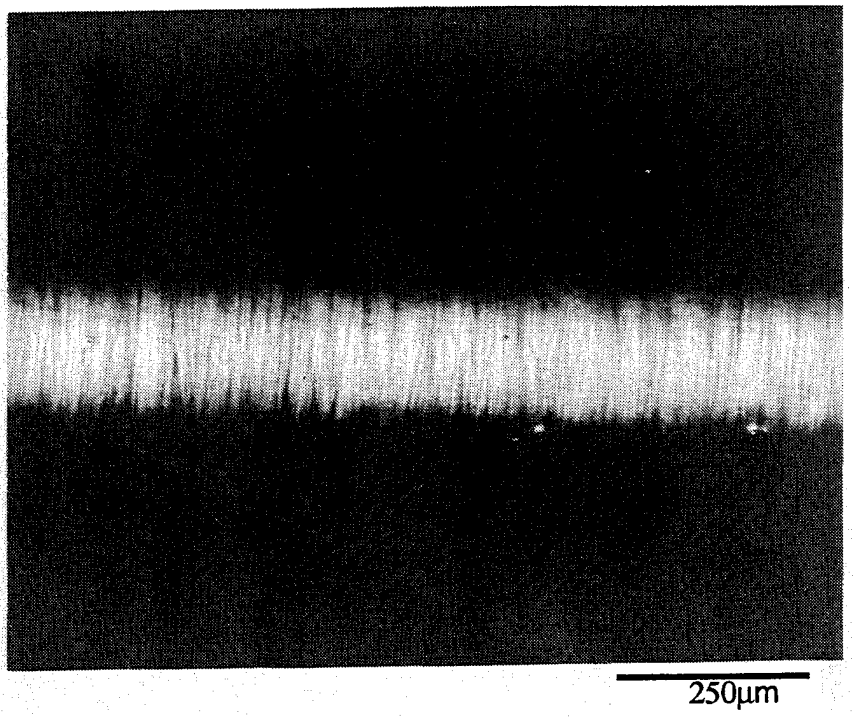

Figure 69. Optical micrograph showing surface of D183-2449-3 specimen (1.6% plastic elongation) after electropolishing.

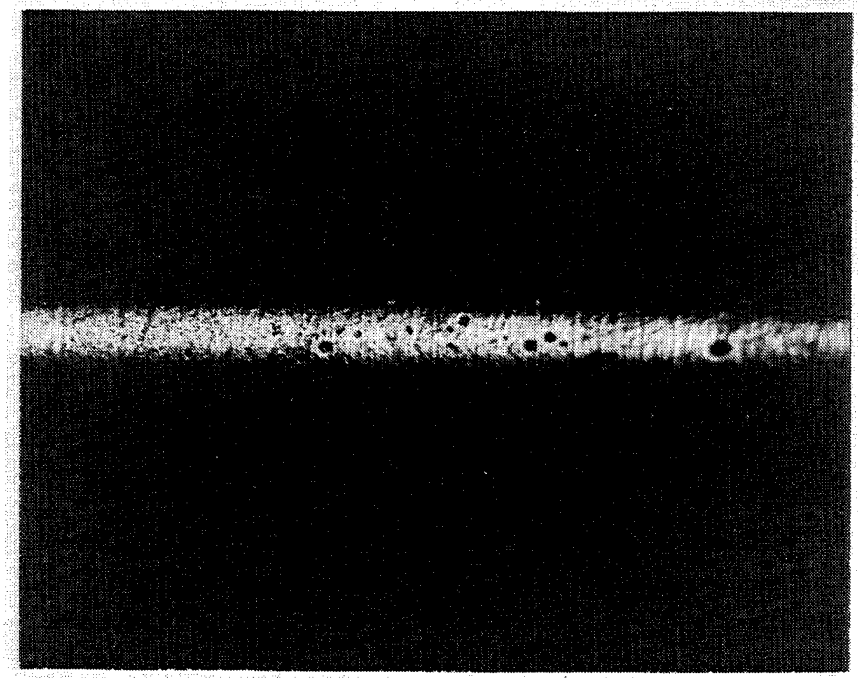

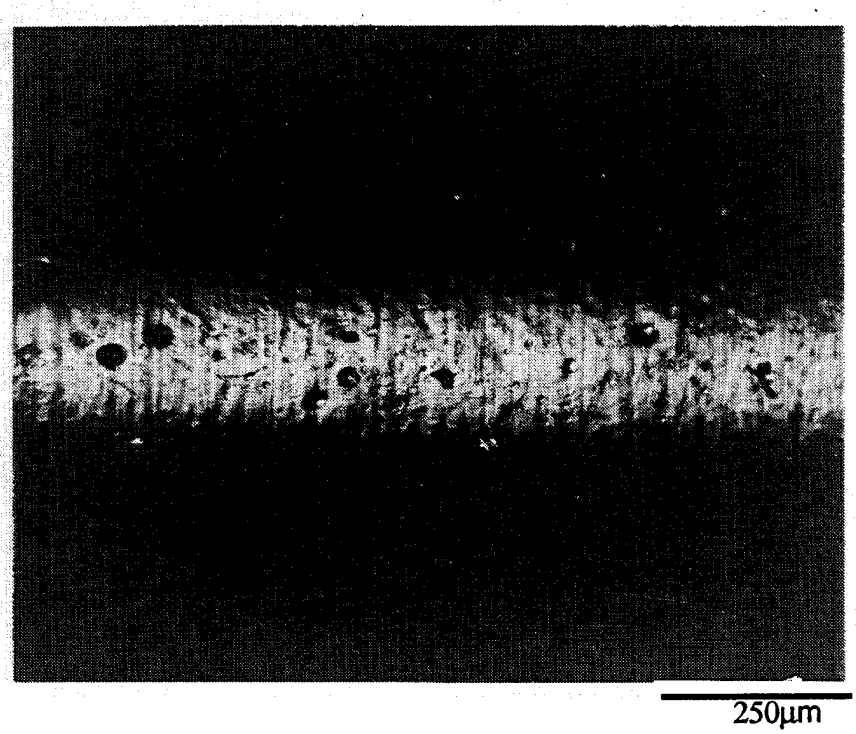

Figure 70. Optical micrographs showing surface of D183-2448-4 specimen (5.4% plastic elongation) after electropolishing. Remnants of the grinding marks are still visible.

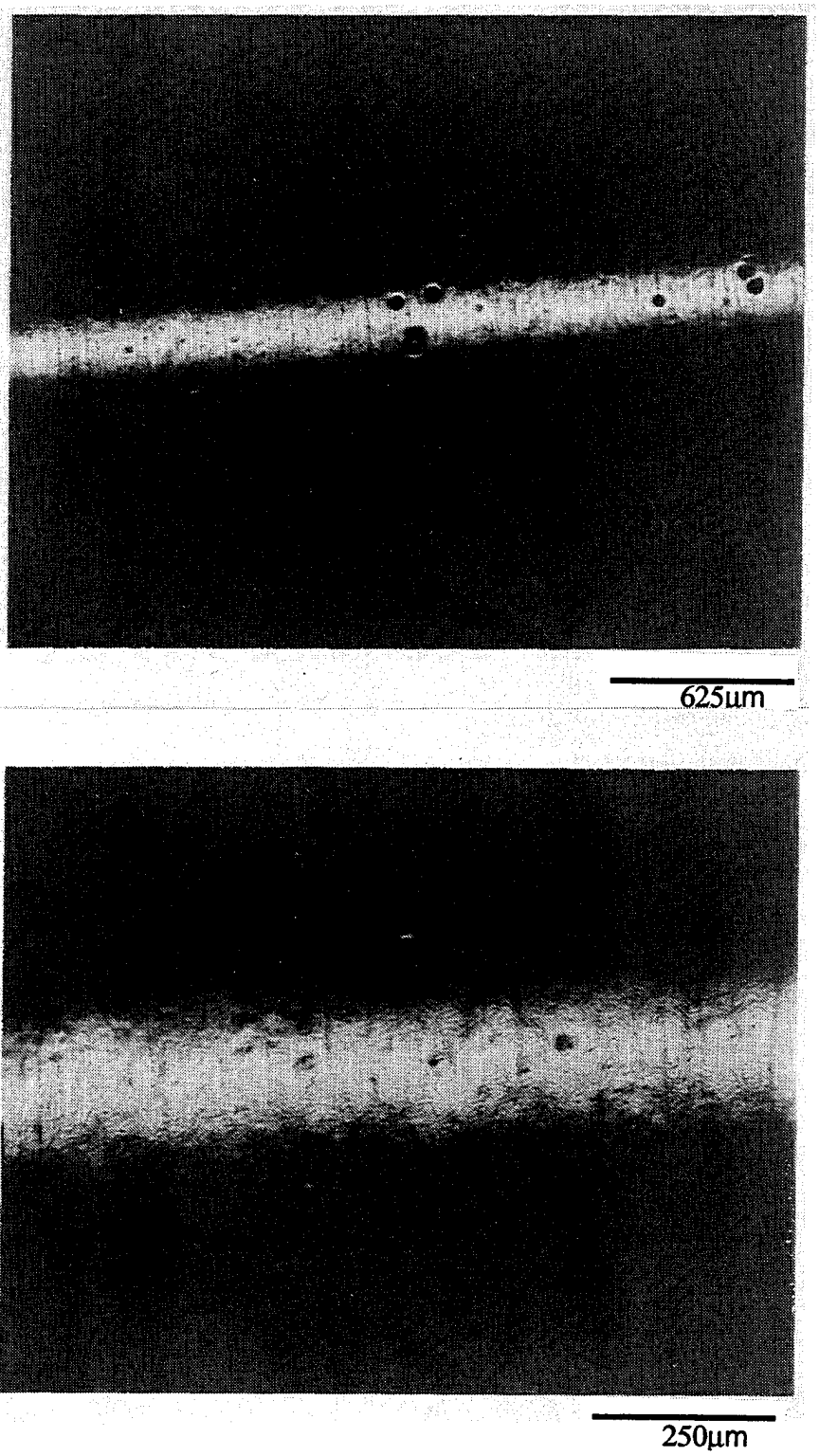

Figure 71. Optical micrographs showing surface of D183-2448-6 specimen (7.2% plastic elongation) after electropolishing. Remnants of the grinding marks are still visible.

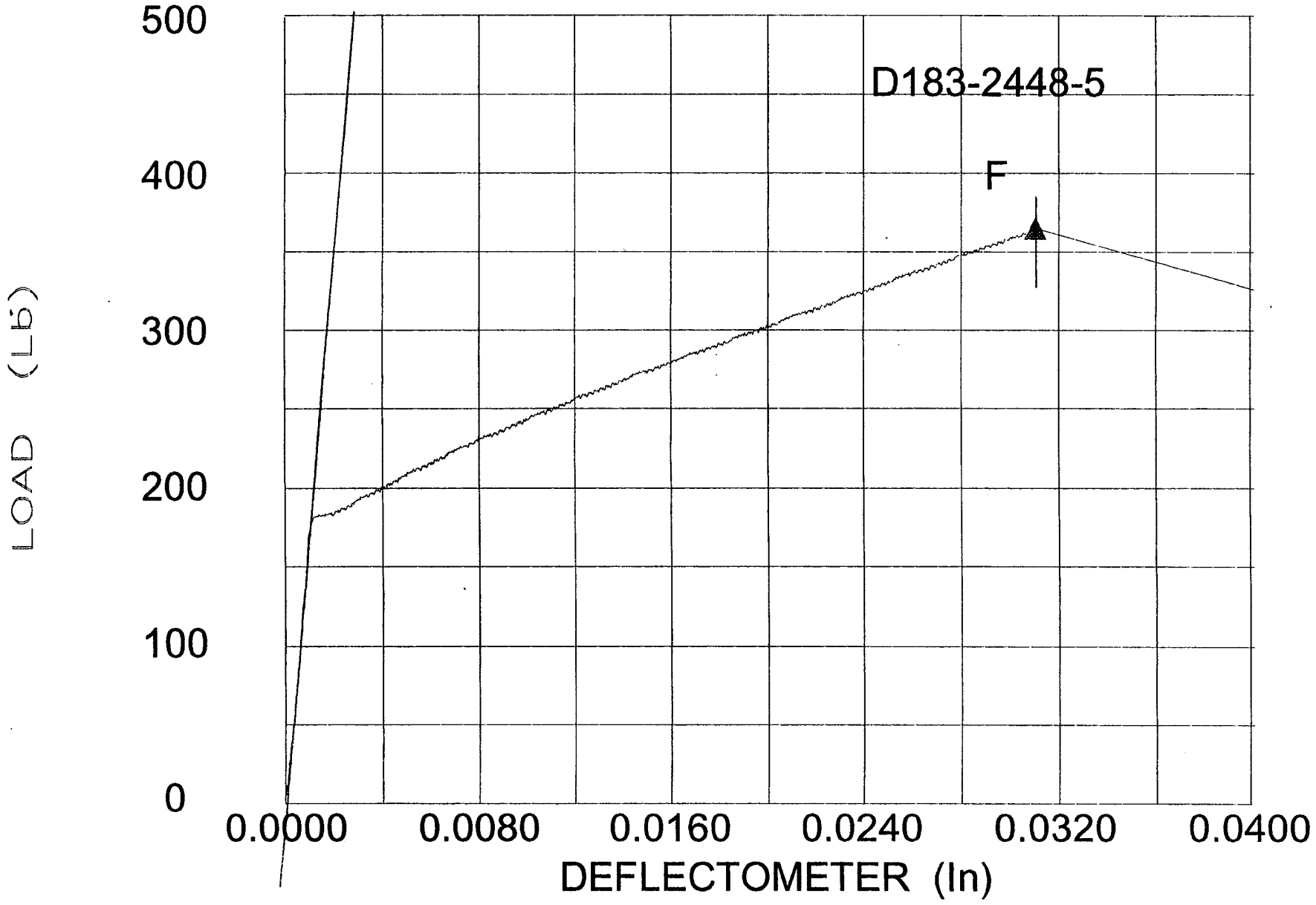

Figure 72. Load-displacement curve for a room temperature tensile test of D183-2448-5 at a strain rate of 8.3×10^{-5}/s.

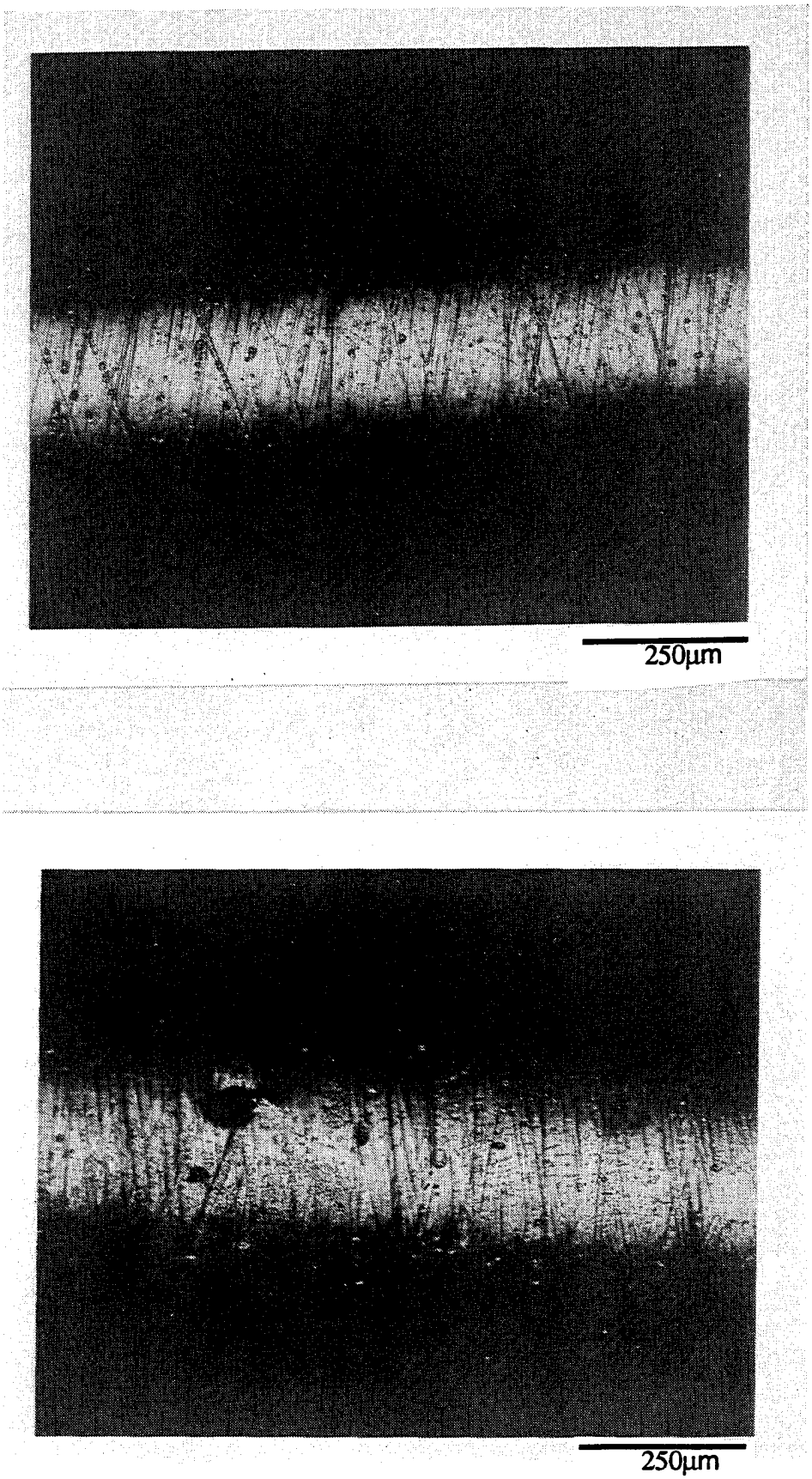

Figure 73. Optical micrographs showing surfaces of chem milled specimens. a) D183-2448-3, b) D183-2170X-2.

2448-3 and D183-2170X-2 which showed ductilities of 6.8 and 7.2%, respectively. It is interesting to note that the majority of the grinding marks are still present, but they are wider (see as ground surface in Figure 68 for comparison). A load vs. displacement curve for D183-2448-3 is shown in Figure 74. The results with the chem milled specimens also exhibit a strong dependence of room temperature elongation on surface condition. It can be concluded that the Fe-containing NiAl alloy has high inherent ductility at room temperature. However, stress concentration at the peaks and valleys of the grinding marks cause premature failure.

Six additional specimens of D183 were machined to verify the above results. Three specimens (D183-2448-7, 8, 9)were electropolished with about 25 μm surface layer removal with a time of 75 seconds. Three specimens (D183-2170X-A, B, C) were chem milled for 15 minutes (17 μm removal), 20 minutes (22 μm removal), and 30 minutes (29 μm removal), These specimens were tested at Westmoreland Mechanical Testing and Research, Inc. to see whether the results obtained at Cincinnati Testing Laboratories, Inc. (CTL) were reproducible. As can be seen in the Table XII, the three electropolished specimens yielded very consistent ductility values of 6.0, 6.6 and 6.6%. The load vs. elongation charts from these three specimens are shown in Figures 75-77. It is noteworthy that the three specimens behave very similarly with respect to yield stress, load drop, work hardening rates as well as the final room temperature elongation. The load vs. elongation charts obtained at Westmoreland Mechanical Testing and Research, Inc. are also similar to those obtained at Cincinnati Testing Laboratories, Inc. The room temperature plastic elongations from the chem milled specimens ranged from 5.8% (15 minute chem mill) to 3.3% (30 minutes). These results were similar to those obtained at CTL. The chem mill specimens still showed some scatter and the values were lower than the electropolished specimens. Surface examination of the specimens revealed that the grinding marks were mostly removed by electropolishing, whereas the remnant grinding marks were still there in the chem mill specimens even after 25 μm of surface layer removal. These differences arose from the way the two processes removed grinding marks. In the electropolishing technique, the etching/polishing action initiates at the valleys and peaks, thereby preferentially attacking them. These valleys and peaks are eventually removed with sufficient electropolishing time. In chem milling, the whole surface layer is removed with some preferential milling at the peaks and valleys. These valleys and peaks are thereby broadened reducing stress concentration at these locations. It is not very clear why longer chem milling times reduced room temperature plastic elongation.

Another interesting observation during this surface preparation study was that the specimens with high elongations tend to have well behaved stress vs. displacement curves (less instrumentation related serrations) with well defined yield drops.

An attempt was made to correlate the elongation data with the surface condition of the tested specimens. It was difficult to precisely quantify the surface topography either by optical or scanning electron microscopy. The highly polished surfaces of the round tensile specimens makes examination rather difficult. An alternate technique would be highly desirable.

These test results with various specimen surface conditions explain reasonably well the scatter in the room temperature tensile elongation data obtained for the last six years. Unfortunately, these results also cast doubt on the validity of the prior data. It can be concluded that the previously

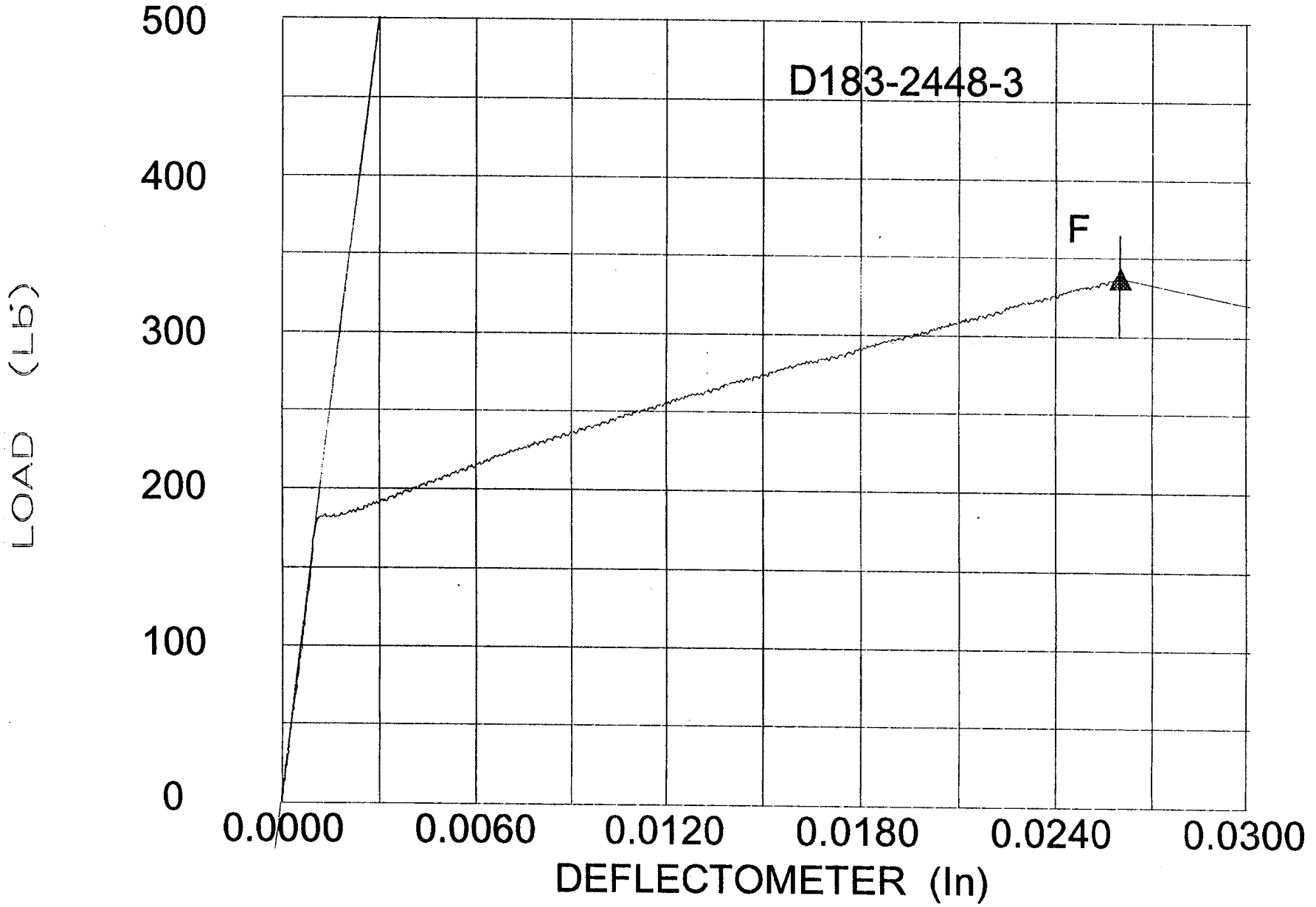

Figure 74. Load-displacement curve for a room temperature tensile test of D183-2448-3 at a strain rate of 8.3×10^{-5}/s.

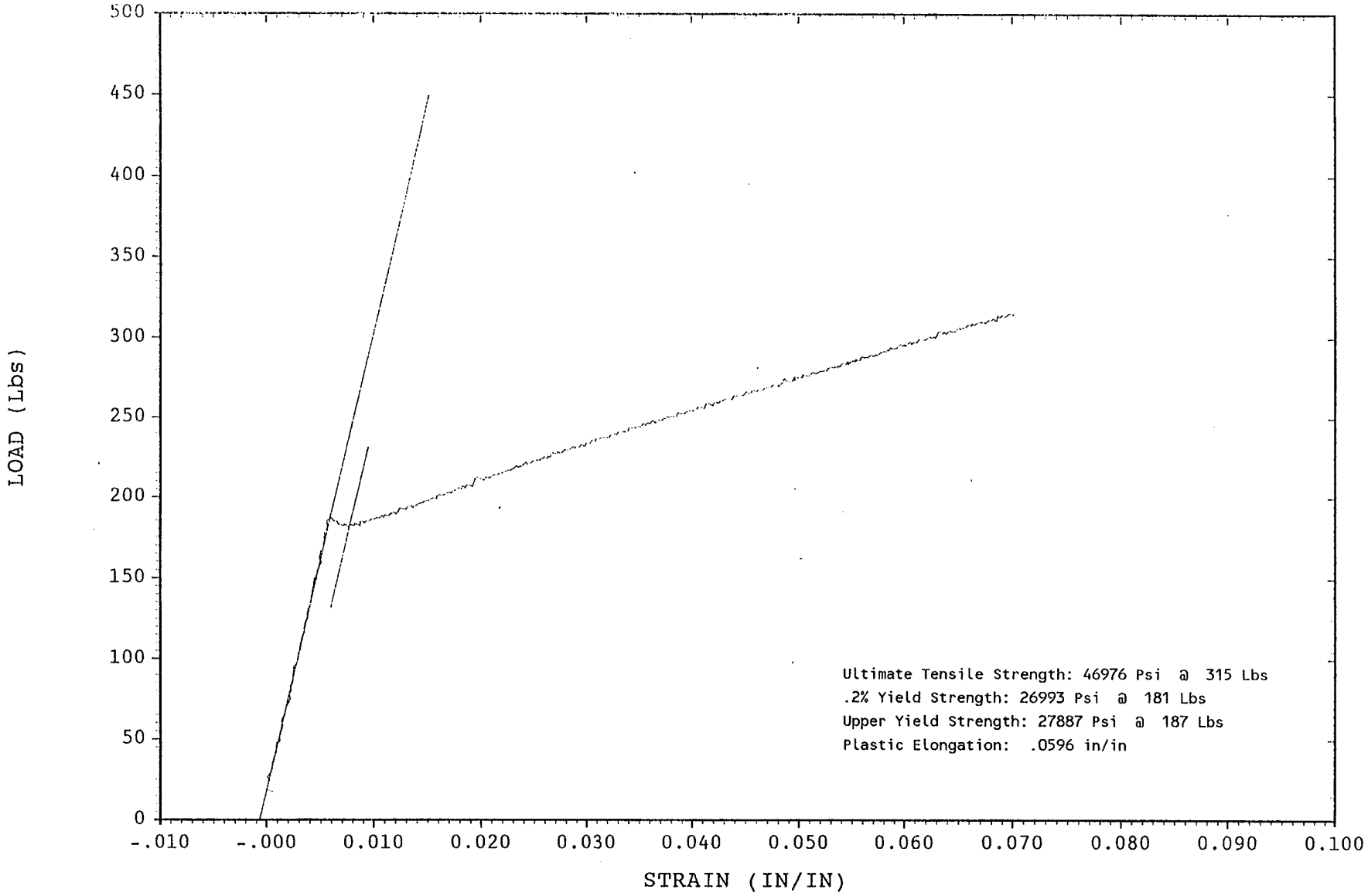

Figure 75. Load-strain curve for a room temperature tensile test of D183-2448-7 at a strain rate of 8.3×10^{-5}/s.

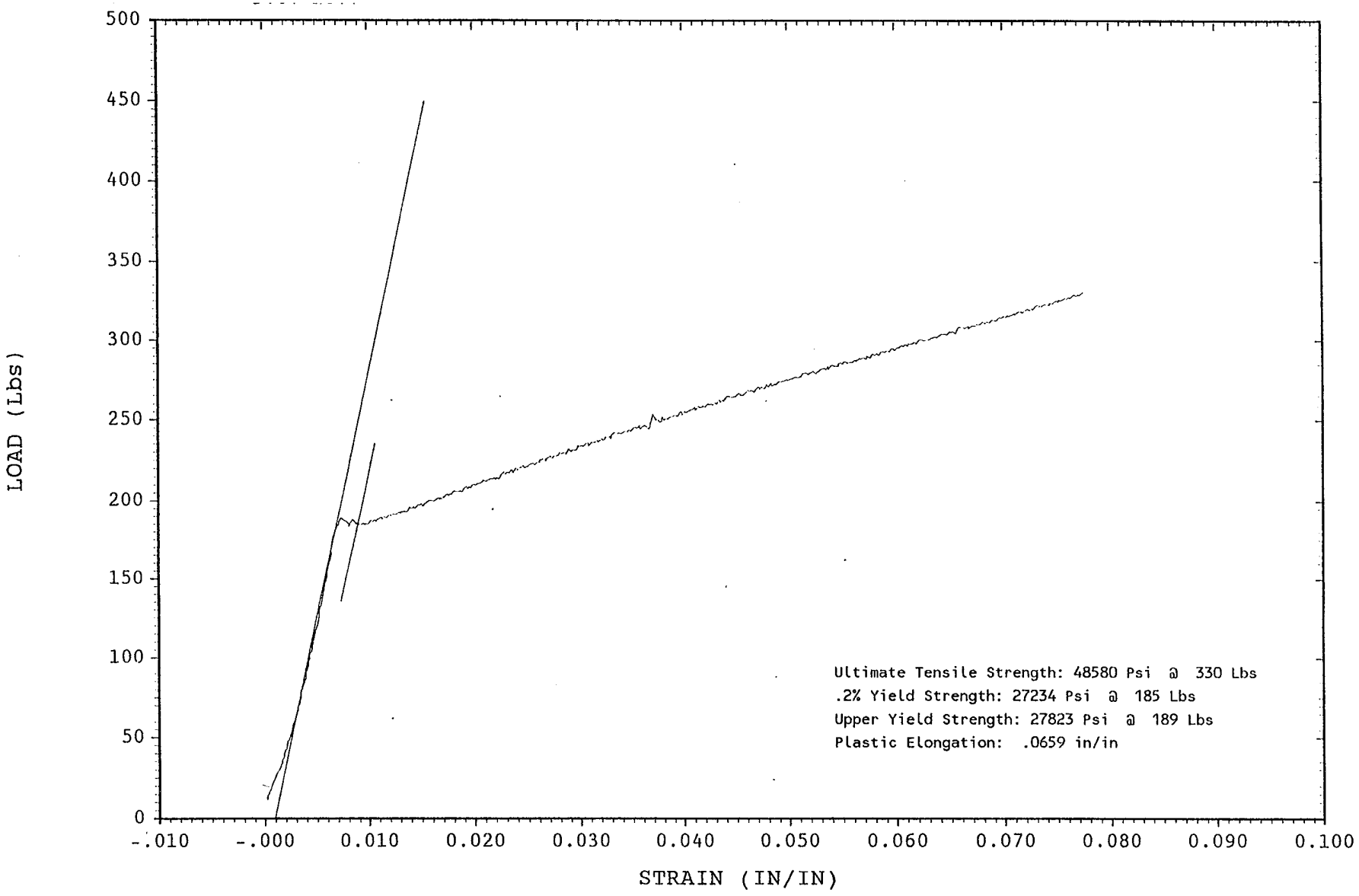

Figure 76. Load-strain curve for a room temperature tensile test of D183-2448-8 at a strain rate of 8.3×10^{-5}/s.

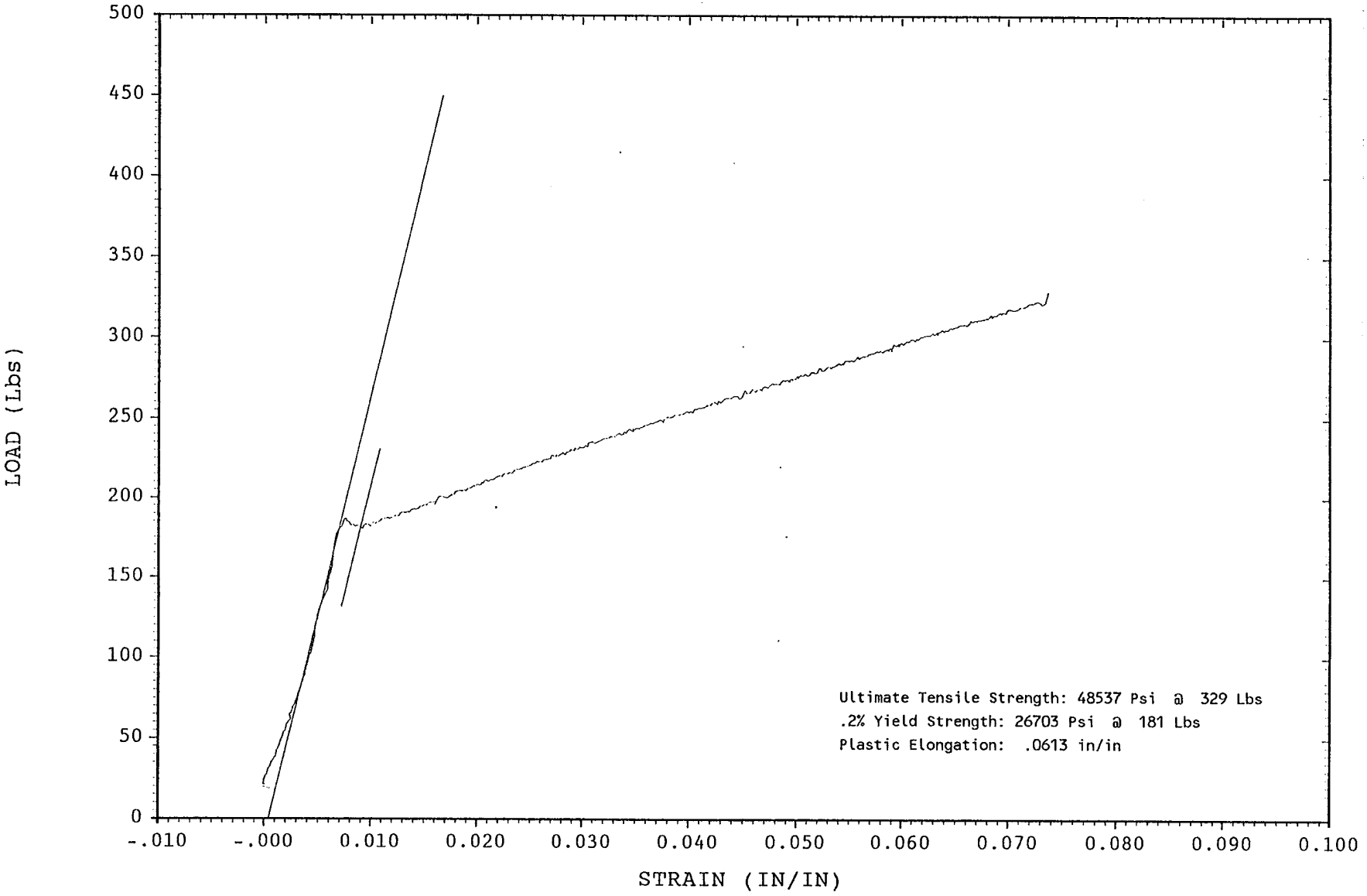

Figure 77. Load-strain curve for a room temperature tensile test of D183-2448-9 at a strain rate of 8.3×10^{-5}/s.

reported low elongation values for various NiAl alloys could have been higher if the surfaces of the specimens were properly prepared. It should, however, be pointed out that the Fe-containing NiAl specimens have, on the average, shown much higher elongation values than the stoichiometric NiAl. Also, the other aspects of deformation behavior such as yield drop, strain aging and lower flow stress of the Fe-containing alloy still makes the Fe effect in NiAl real.

3.12 Pre-Strain Effects

To study pre-strain effects, large compression blocks were machined from single crystal castings of D5 and the D176 alloy. The blocks were cut from the castings using wire EDM and the compression axis ends ground flat and parallel using low stress grinding techniques. The blocks were then pre-strained in the appropriate orientations in a vacuum hot press (backfilled with Ar) equipped with an MTS 810 test frame, with a 890KN load capacity. The tests were performed at a strain rate of approximately $8x10^{-5}/s$, the strain rate used for tensile pre-straining experiments, and the specimen was allowed to furnace cool after straining. For the D5 specimens, the tests were conducted at 538°C to approximately 1% plastic strain. For the D176 alloy, the tests were performed at 1093°C to approximately 3-5% plastic strain..

A summary of the pre-strain conditions for the individual blocks is given in Tables XIII and XIV, for the D5 and D176 alloy blocks, respectively. Following the pre-strain treatment, tensile, fracture toughness and compression specimens were machined from the blocks. For the D176 alloy, considerable cracking of the blocks occurred during the pre-straining operation. This reduced the number of tensile specimens, and thus the size of the test matrix, for this alloy. Also, priority was given to get as many toughness and tensile specimens from the compressed bars. A limited number of blanks were sent for machining of compression specimens. Unfortunately, the ends of the compression specimens were carelessly ground by the machining vendor introducing cracks at the ends. Therefore, compression tests were not carried out.

Table XIII. Data from Pre-Straining Treatments of NiAl (D5) Compression Blocks

Specimen ID	Target Strain	Actual Strain	Comments
D5-2113-1	1%	1.26%	Single Oriented <100>
D5-2113-2	1%	1.36%	Single Oriented <100>
D5-2113-3	1%	1.19%	Single Oriented <100>
D5-2154-2	1%	1.25%	Single Oriented <110>
D5-2154-2	1%	1.32%	Single Oriented <110>
D5-2108-1	1%	0.76%	Double Oriented <100>/<110>†
D5-2108-3	1%	1.40%	Double Oriented <100>/<110>†
D5-2110-1	1%	1.28%	Double Oriented <110>/<100>†
D5-2110-2	1%	1.11%	Double Oriented <110>/<100>†
D5-2108-2	1%	1.29%	Double Oriented <110>/<100>†

† First orientation is direction of pre-strain

Table XIV. Data from Pre-Straining Treatments of NiAl Alloy D176 Compression Blocks

Specimen ID	Target Strain	Actual Strain	Comments
D176-1929-1	5%	5.31	Single Oriented <100>
D176-1929-2	5%	5.36	Single Oriented <100>
D176-1929-3	5%	5.59	Single Oriented <100>
D176-1929-4	5%	5.29	Single Oriented <100>
D176-1891-1	5%	4.45	Single Oriented <110>
D176-1891-2	5%	5.37	Single Oriented <110>
D176-1891-3	5%	5.21	Single Oriented <110>
D176-1891-4	5%	5.25	Single Oriented <110>
D176-2169-1	5%	5.20	Double Oriented <100>/<110>†
D176-2169-2	5%	5.23	Double Oriented <100>/<110>†
D176-1883-1	3%	3.25	Double Oriented <110>/<100>†
D176-1883-2	3%	3.40	Double Oriented <110>/<100>†

† First orientation is direction of pre-strain

3.12.1 Tensile Tests

Tensile specimens of D5 and D176 blocks which were pre-strained in compression in either <100> or <110> orientations were machined in either the direction of pre-strain or in the other <100> or <110> orientation and tested as a function of temperature including room temperature. The test data are shown in Table XV. The plastic elongation data are also compared with values obtained from the specimens, which were pre-strained as tensile specimens (as opposed to specimens obtained from the compression pre-strained blocks) in earlier GEAE work carried out under the GEAE IRAD program. Overall, the results are similar to those earlier obtained on specimens which were pre-strained as specimens. This means that pre-strain effects are similar whether the pre-strain is done in compression or in tension. These results have technological importance because pre-straining of the blade dovetail can be accomplished by compression which is a more desirable method. Specifically, the following observations can be made for D5:

1) Pre-straining either in the <100> or <110> orientation does not provide any improvement in the room temperature plastic elongation in the <100> orientation.

2) pre-straining in the <110> orientation improves room temperature plastic elongation in the <110> orientation, whereas pre-straining in the <100> orientation does not appear to improve room temperature plastic elongation in the <110> orientation.

It should be mentioned that some scatter in the results may possibly have been caused by improper electropolishing procedure where the grinding marks may not have been completely removed.

Table XV. Tensile Elongation Data for Pre-strained D5 Specimens

Specimen ID	Pre-strain Direction	Test Direction	Test Temperature, ℃	Compression Pre-strain Plastic Elong., %	Tensile Pre-strain Plastic Elong., %
D5-2113-1-1	<100>	<100>	RT	invalid test	0
D5-2113-1-2	<100>	<100>	RT	0.0	
D5-2113-1-3	<100>	<100>	93 (200°F)	0.0	
D5-2113-1-4	<100>	<100>	204 (400°F)	0.2	
D5-2113-2-1	<100>	<100>	316 (600°F)	20.5	
D5-2113-2-2	<100>	<100>	427 (800°F)	40.4	
D5-2113-2-3	<100>	<100>	538 (1000°F)	55.6	
D5-2110-2-1	<110>	<110>	RT	7.3	7.9 (average)
D5-2110-2-2	<110>	<110>	RT	2.8	
D5-2110-2-3	<110>	<110>	93 (200°F)	2.1	
D5-2154-1-1	<110>	<110>	149 (300°F)	4.3	
D5-2110-2-4	<110>	<110>	204 (400°F)	12.5	
D5-2154-1-4	<110>	<110>	260 (500°F)	18.0	
D5-2108-1-1	<001>	<110>	RT	2.9	
D5-2108-1-2	<001>	<110>	RT	0.3	
D5-2108-1-3	<001>	<110>	93 (200°F)	1.4	
D5-2108-1-4	<001>	<110>	204 (400°F)	16.9	
D5-2108-2-1	<110>	<001>	RT	0.0	
D5-2108-2-2	<110>	<001>	RT	0.0	
D5-2108-2-3	<110>	<001>	204 (400°F)	invalid test	
D5-2108-2-4	<110>	<001>	260 (500°F)	0.03	

For the D176 specimens, the tensile tests were run at 316 (600°F), 427(800°F), 538 (1000°F), 649 (1200°F), 760 (1400°F) and 871°C (1600°F). The data are shown in Table XVI. The data are compared with data from earlier work on pre-strained and non-strained D176 specimens in Figure 78. Similar to the earlier results, pre-straining in the <100> direction increased the plastic elongation at 538°C in the <100> orientation. No plasticity is exhibited by D176 specimens at this temperature if they are not pre-strained. The test data at 649 and 760°C (no plasticity at these temperatures in the pre-strained specimens) do not agree with the prior data. These data are suspect probably due to poorly conducted tests. The specimens which were pre-strained in the <110> orientation and tested in the <110> orientation did not show any improvement in ductility. This behavior had been previously observed in earlier GEAE work carried out under the GEAE IRAD program. To understand the reasons for this behavior, an extensive collaborative study was carried out at NASA Lewis Research Center. The aim was to understand the pre-straining effects by first understanding the high temperature deformation behavior of D176. The detail results of this study are reported in Section 3.13.

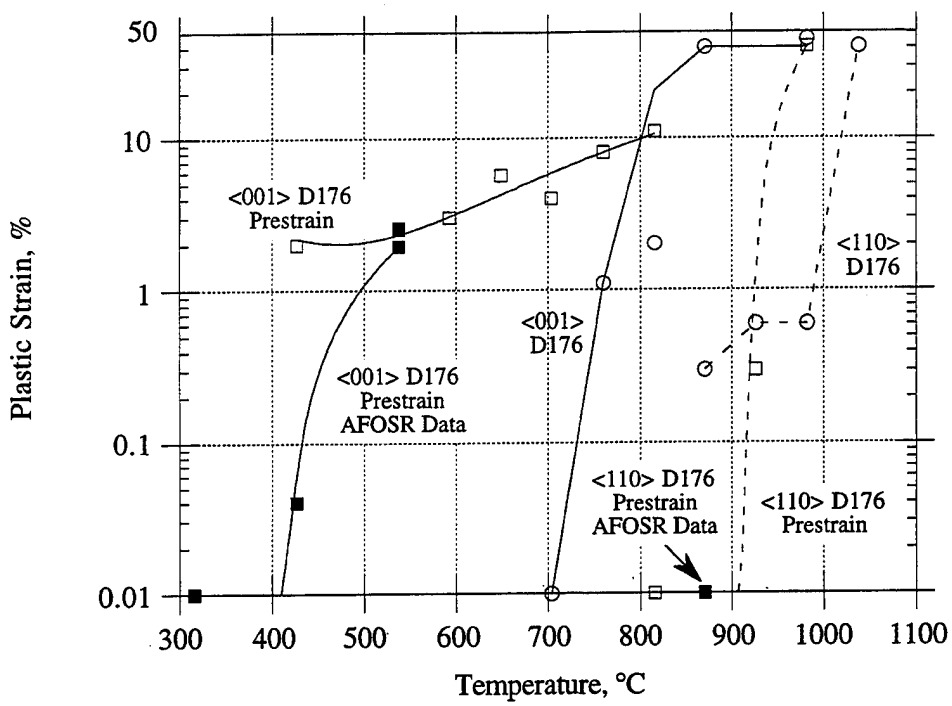

Figure 78. Plastic elongation vs. temperature curves for pre-strained and non-pre-strained D176.

Table XVI. Tensile Elongation Data for Pre-strained D176 Specimens

Specimen ID	Pre-strain Direction	Test Direction	Test Temperature, ℃	Plastic Elong., %
D176-1929-1-2	<100>	<100>	316 (600°F)	0.0
D176-1929-1-3	<100>	<100>	427 (800°F)	0.04
D176-1929-1-4	<100>	<100>	538 (1000°F)	1.93
D176-1929-4-1	<100>	<100>	649 (1200°F)	0.0
D176-1929-4-2	<100>	<100>	760 (1400°F)	0.0
D176-1891-3-1	<110>	<110>	871 (1600°F)	0.0
D176-1883-1-2	<110>	<100>	538 (1000°F)	2.55

3.12.2 Fracture Toughness Tests

Fracture toughness specimens were machined in either the direction of pre-strain or in the other <100> or <110> orientation from D5 and D176 blocks which were pre-strained in either <100> or <110> orientations and tested as a function of temperature including room temperature. Chevron notched, 3-point bend specimens with a one inch span were used for this study. The test data are shown in Table XVII for D5. The fracture toughness data are compared with values obtained from the specimens which were not pre-strained in earlier work carried out under the GEAE IRAD program. In D5, pre-straining in both <100> and <110> orientations significantly increases the fracture toughness in the <100> oriented specimens whereas the <110> oriented specimens do not seem to be affected by pre-straining in either <110> or <100> direction. It is interesting to note that, even though <100> fracture toughness is improved by pre-straining in both <100> and <110> directions, <100> plastic elongation is not improved by pre-straining. Contrary to this behavior, the <110> toughness is not improved by pre-straining in either the <100> or <110> orientation, but the plastic elongation is improved in the <110> orientations by pre-straining in the <110> orientation. Such behavior needs further study.

The fracture toughness data for the pre-strained D176 specimens are shown in Table XVIII. The fracture toughness data of specimens which were not pre-strained obtained under an AF contract F 33615-90-C-2006 [37] are also shown in Table XVIII. Several conclusions can be drawn: 1) The room temperature fracture toughness in the <100> orientation is increased by pre-straining in both <100> and <110> orientations. Surprisingly, there does not appear to be a pre-straining effect on the high temperature fracture toughness, at least near the DBTT of this alloy. Above the DBTT, the fracture toughness appears to be enhanced with pre-straining. Based on the plastic elongation data, toughness was expected to be improved at all test temperatures. For the <100> orientation, fracture toughness first increases with temperature, then decreases near DBTT before increasing again. This behavior is seen in both pre-strained and non-pre-strained specimens. Such a behavior has been previously observed by VeHoff [38] in NiAl specimens of the stoichiometric composition. The reasons for this behavior are not well understood. For the <110> orientation, no beneficial effect of pre-straining on fracture toughness is seen either at room temperature or at the elevated temperatures. This is consistent with <110> the plastic elongation data where pre-straining was found to have no effect.

Table XVII. Fracture Toughness of Pre-strained D5 Specimens

Specimen ID	Pre-strain Direction	Test Direction	Test Temp., ℃	Pre-strained K_{ic}, MPa•m$^{1/2}$	Non-Pre-strained K_{ic}, MPa•m$^{1/2}$
D5-2113-3-1	<100>	<100>	RT	13.3	7, 9, 9.3
D5-2113-3-2	<100>	<100>	RT	9.4	
D5-2113-3-3	<100>	<100>	93 (200°F)	12.7	11.5 (at 100°C)
D5-2113-3-4	<100>	<100>	149 (300°F)	24.3	
D5-2113-3-5	<100>	<100>	204 (400°F)	27.1	10.9 (at 200°C)
D5-2113-3-6	<100>	<100>	260 (500°F)	28.7	
D5-2113-3-7	<100>	<100>	316 (600°F)	35.6	19.8 (at 300°C)
D5-2113-3-8	<100>	<100>	427 (800°F)	63.6	23.6 (at 400°C)
D5-2154-2-1	<110>	<110>	RT	F.O.L.	5.5
D5-2154-2-2	<110>	<110>	RT	4.9	6.3
D5-2154-2-3	<110>	<110>	93 (200°F)	6.3	5.5 (at 100°C)
D5-2154-2-4	<110>	<110>	149 (300°F)	5.7	
D5-2154-2-5	<110>	<110>	204 (400°F)	4.9	5.5 (at 200°C)
D5-2154-2-6	<110>	<110>	260 (500°F)	10.7	
D5-2154-2-7	<110>	<110>	316 (600°F)	5.7	12.1(at 300°C)
D5-2154-2-8	<110>	<110>	427 (800°F)	41.7	12.1(at 400°C)
D5-2108-3-1	<100>	<110>	RT	4.3	
D5-2108-3-2	<100>	<110>	RT	6.3	
D5-2108-3-3	<100>	<110>	260 (500°F)	4.6	
D5-2108-3-4	<100>	<110>	316 (600°F)	8.2	
D5-2110-1-1	<110>	<100>	RT	12.5	
D5-2110-1-2	<110>	<100>	RT	15.4	
D5-2110-1-3	<110>	<100>	93 (200°F)	21.2	
D5-2110-1-4	<110>	<100>	149 (300°F)	25.2	

Table XVIII. Fracture Toughness of Pre-strained D176 Specimens

Specimen ID	Pre-strain Direction	Test Direction	Test Temp., ℃	Pre-strained K_{ic}, MPa•m$^{1/2}$	Non-Pre-strained K_{ic}, MPa•m$^{1/2}$
D176-1929-3-1	<100>	<100>	RT	5.8	3.2
D176-1929-3-2	<100>	<100>	704 (1300°F)	9.3	9.4
D176-1929-3-3	<100>	<100>	760 (1400°F)	8.4	8.0
D176-1929-4-1	<100>	<100>	816 (1500°F)	4.4	5.0
D176-1929-4-2	<100>	<100>	871 (1600°F)	6.2	4.1
D176-1929-4-4	<100>	<100>	927 (1700°F)	6.7	4.9
D176-1891-2-2	<110>	<110>	RT	2.1	2.1
D176-1891-2-3	<110>	<110>	816 (1500°F)	2.9	4.2
D176-1891-2-4	<110>	<110>	871 (1600°F)	3.0	4.6
D176-1883-2-2	<110>	<100>	RT	5.6	3.2
D176-1883-2-3	<110>	<100>	816 (1500°F)	6.5	5.0
D176-1883-2-4	<110>	<100>	871 (1600°F)	5.5	4.1

3.13 Multiple Microalloying Additions

3.13.1 Multiple Microalloying Additions: Fe and Ga

Initially two tensile test specimens of alloy D221 containing 0.1 at% Fe and 0.05 at% Ga (D221-2483-1 and 2) were tested at room temperature. Room temperature elongation values of 1.0 and 4.0% were obtained indicating that the multiple alloying addition of Fe and Ga did not provide any improvement over that obtained with the Fe addition alone. The scatter in the data was presumed to be due to test set up misalignment. Two additional specimens (D221-2483-3 and 4) were tested after the test set up was judged to be properly aligned. Again, two low values (1.0 and 2.4%) of plastic elongation were obtained. These low values led to a further search for the reasons for such discrepant data. This search led to the effect of specimen surface preparation effects described in Section 3.11. The effect of multiple alloying additions needs to be reevaluated with specimens which have been properly electropolished.

3.13.2 Multiple Microalloying Additions: Hf and Ga (at NASA Lewis Research Center)

To understand the deformation behavior of a strong alloy, alloy D176 was selected which contains 0.05 at% Ga and 0.5 at% Hf. This collaborative study was conducted at NASA Lewis Research Center, Cleveland by Drs. Ron Noebe and Anita Garg under the auspices of this program.

3.13.2.1 Characterization of the As-Homogenized Alloy D176

The microstructure of the homogenized and furnace-cooled material consisted of a B2-NiAl single crystal matrix containing a high density of very fine (~ 5-50 nm) G-phase precipitates ($N_{16}Si_6Hf_7$), as shown in a <001> zone-axis BF image in Figure 79. It should be noted that Si is not an intentional alloying addition but is picked up from reaction with the ceramic mold during directional solidification of the single crystal ingots. The G-phase precipitates nucleate coherently on $\{100\}_{NiAl}$ planes and have a cube-on-cube orientation relationship with the NiAl matrix that is clearly depicted in the selected-area diffraction-pattern shown in the right-hand corner in Figure 79. These precipitates, in general, had a cuboidal morphology and were distributed quite uniformly throughout the material. The exception to the uniform dispersion of cuboidal G-phase occurred when precipitates nucleated preferentially on the few dislocations that were observed on {100} planes. These precipitates grew at an accelerated rate along the <100> directions via pipe diffusion through the dislocation cores and formed continuous strings of precipitate plates that were surrounded by precipitate-free zones (Fig. 79). Occasional <100> dislocations were also observed in the as-homogenized microstructure and are marked with an arrow in Figure 79.

3.13.2.2 Temperature Dependence of the Yield Strength

Cylindrical bars of <001> and <011> orientations were electrodischarge machined (EDM) and centerless ground to 4 mm diameter and sectioned to 8 mm in length while making sure that the sample ends were flat and perfectly parallel in order to avoid the artifact of kinking in the high strength samples. The samples were tested in the an as-ground surface condition in a screw driven load frame at a constant cross-head velocity resulting in an engineering strain rate of $1.4x10^{-4}$ s^{-1}. The samples were tested to approximately 1-2% plastic strain between room-temperature and 1400 K in air. For the temperature scale, Kelvin (K) units are used in this section because of extensive use of the Arrhenius relationships. Stress-strain data were obtained from the load-time plots and yield stress was determined using the 0.2% offset method.

The compressive yield strength of alloy D176 as a function of temperature for both the <001> and <011> orientations is shown in Figure 80 and compared to that of binary NiAl of similar orientations. Between room temperature and 600 K the yield strength of <001> D176 is between 1600 and 1700 MPa and is essentially independent of temperature. The yield stress then drops rapidly as the temperature increases above 600 K eventually reaching about 100 MPa at 1400 K. The room temperature yield strength of <011> D176 is approximately 1060 MPa, which is much less than that in the <001> orientation. However, the yield stress in the <011> orientation decreases at a much slower rate with temperature. Due to the difference in rate of decrease of yield strength with temperature, alloy D176 in both orientations ends up with similar yield strengths at a temperature of ~1100 K. At temperatures above 1100 K (at least up to 1400 K, the highest test-temperature used in this study), <011> D176 appears slightly higher in strength than the <001> material.

Alloy D176 has a greater yield strength than binary NiAl of comparable orientation, though, the difference is much greater in the <011> orientation than in <001>. Because of the high yield strengths of NiAl single crystals in the <001> orientation, the <001> binary NiAl is actually

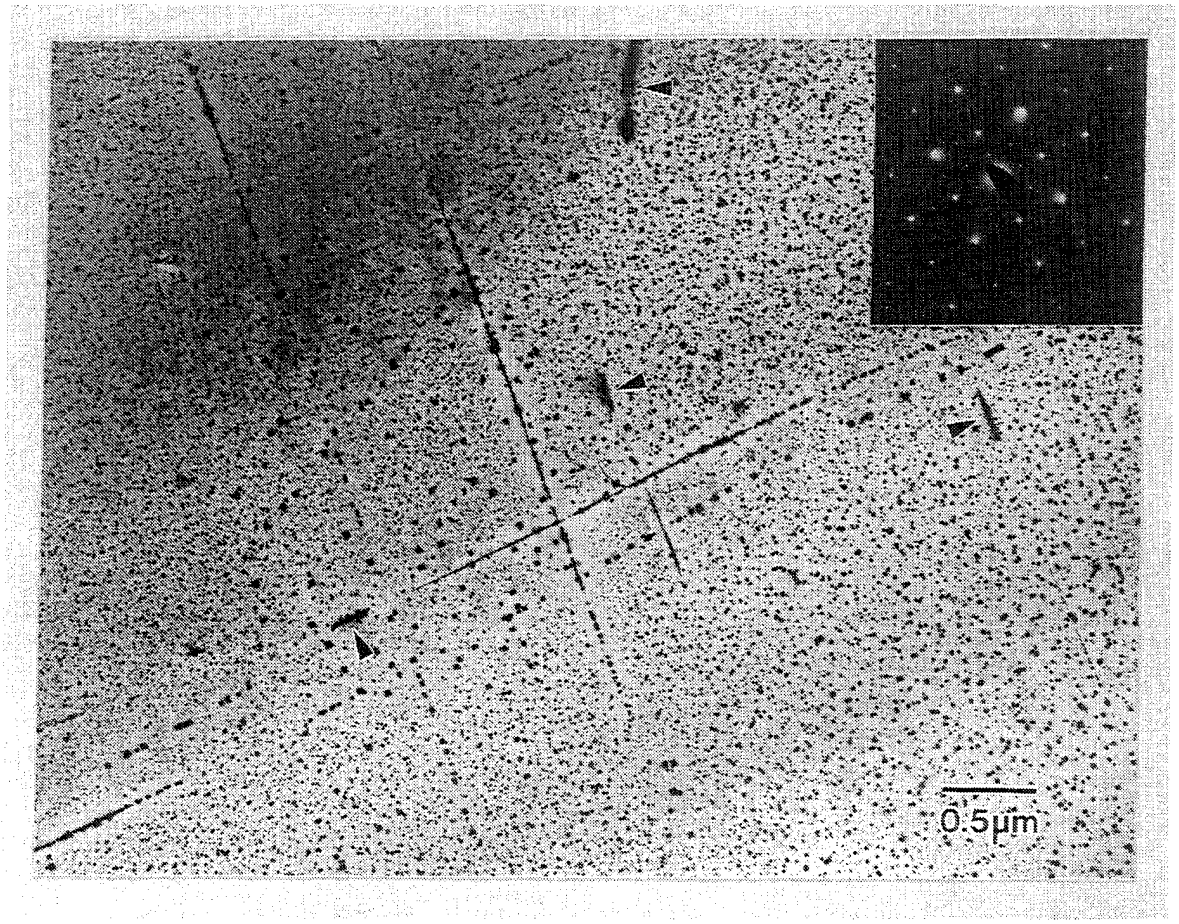

Figure 79. As-homogenized NiAl alloy D176(1695) showing the extremely high density of G-phase cuboidal precipitates in the alloy and some G-phase platelets on the edge-on {110} planes. Arrows indicate <100> dislocations.

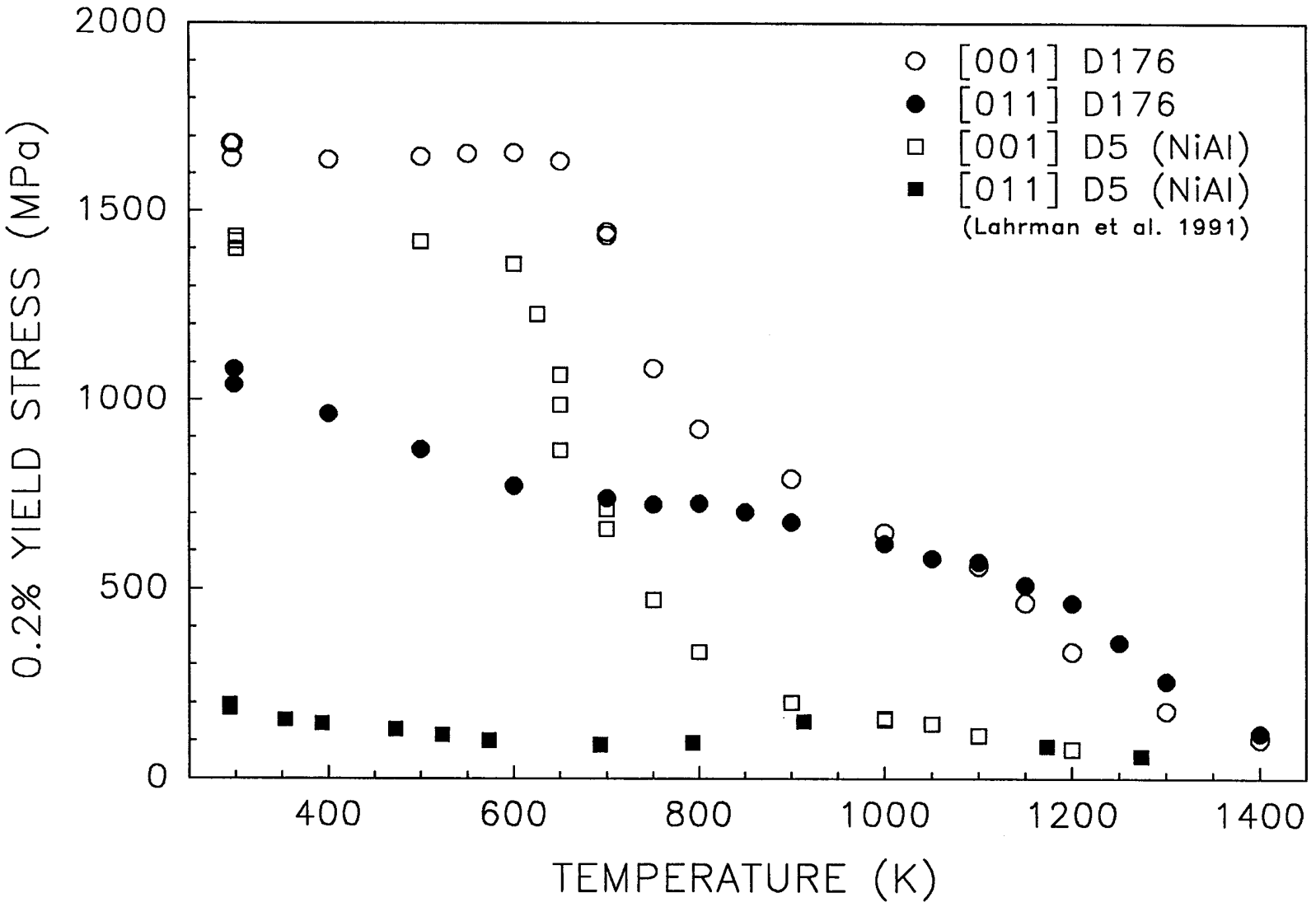

Figure 80. Yield strength of NiAl alloy D176 and binary NiAl (alloy D5) as a function of temperature for both the <001> and <011> orientations.

stronger than the <011> D176 alloy at temperatures below 700 K. The real advantage in strength of alloy D176 over binary NiAl occurs at temperatures above 700 K regardless of orientation. It is also interesting to note that the yield strength versus temperature curves exhibit a similar shape for each pair of orientations for both materials (Figure 80), the major difference is the shift of these curves towards higher yield strengths and slightly higher temperatures for the alloy D176.

3.13.2.3 Deformation Behavior of D176

Disks for TEM analysis were cut using a slow speed saw from 3 mm diameter cylinders EDM from the as-homogenized ingots and deformed compression samples. The disks were mechanically ground and then electropolished in a twin-jet Tenupol-3 polisher using a solution of 70% ethanol, 14% distilled water, 10% butycellosolve, and 6% perchloric acid cooled to -10°C. An applied potential of 20-25 V with a corresponding current of 10-15 mA produced electron transparent foils. Microstructural examination, and trace analysis was conducted in a Philips EM420 TEM equipped with a double-tilt goniometer. Dislocation analysis was carried out under bright-field (BF) and weak-beam dark-field (WBDF) conditions. Even though NiAl is elastically anisotropic, the usual invisibility criterion i.e. $g \cdot b = 0$ is applicable with residual contrast present unless $g \cdot b \times u = 0$. Under certain conditions the combination of this residual contrast and strong diffraction from the precipitates complicated the dislocation analysis, though did not affect the final conclusion as to the predominant deformation mechanism(s) in each regime.

TEM analysis was also performed on several additional <011> oriented D176 compression samples from ingots 1906 and 1902. These were samples previously tested by Cincinnati Testing Labs, Inc. at 1144 K and 1255 K, temperatures considered just above and below the DBTT (~1250 K) for this orientation of alloy D176.

3.13.2.4 Identification of Deformation Regimes

From Figure 80 it is not possible to determine the temperature range over which various deformation regimes operate or even how many different deformation regimes exist for alloy D176 of either orientation. However, it has been previously demonstrated that the use of an Arrhenius plot of yield stress can be useful in identifying the various deformation regimes that operate in polycrystalline NiAl and ternary NiAl alloys [12-14]. Therefore, a similar approach has been used with single crystal NiAl alloy D176. Figure 81 is an Arrhenius plot, $\ln(\sigma_y)$ versus 1/T, for the <001> D176 yield strength data from Figure 80. From the different slopes of this plot it is clear that three very distinct deformation regimes exist between room temperature and 1400 K. Region I is a low-temperature regime that exists from at least room temperature to 650K. Region II is an intermediate-temperature regime that exists from 650 to 1100 K and region III is a high-temperature regime that exists above 1100 K. The samples, indicated as solid symbols in Figure 81, were selected for TEM analysis to determine the operative deformation mechanisms in each of these regimes and the results are discussed in the following section.

A similar analysis was performed on the <011> D176 samples taken primarily from ingot 1910 and with additional samples taken from ingots 1902 and 1906. Figure 82 indicates good reproducibility in the yield strength of the samples taken from the three different ingots. For

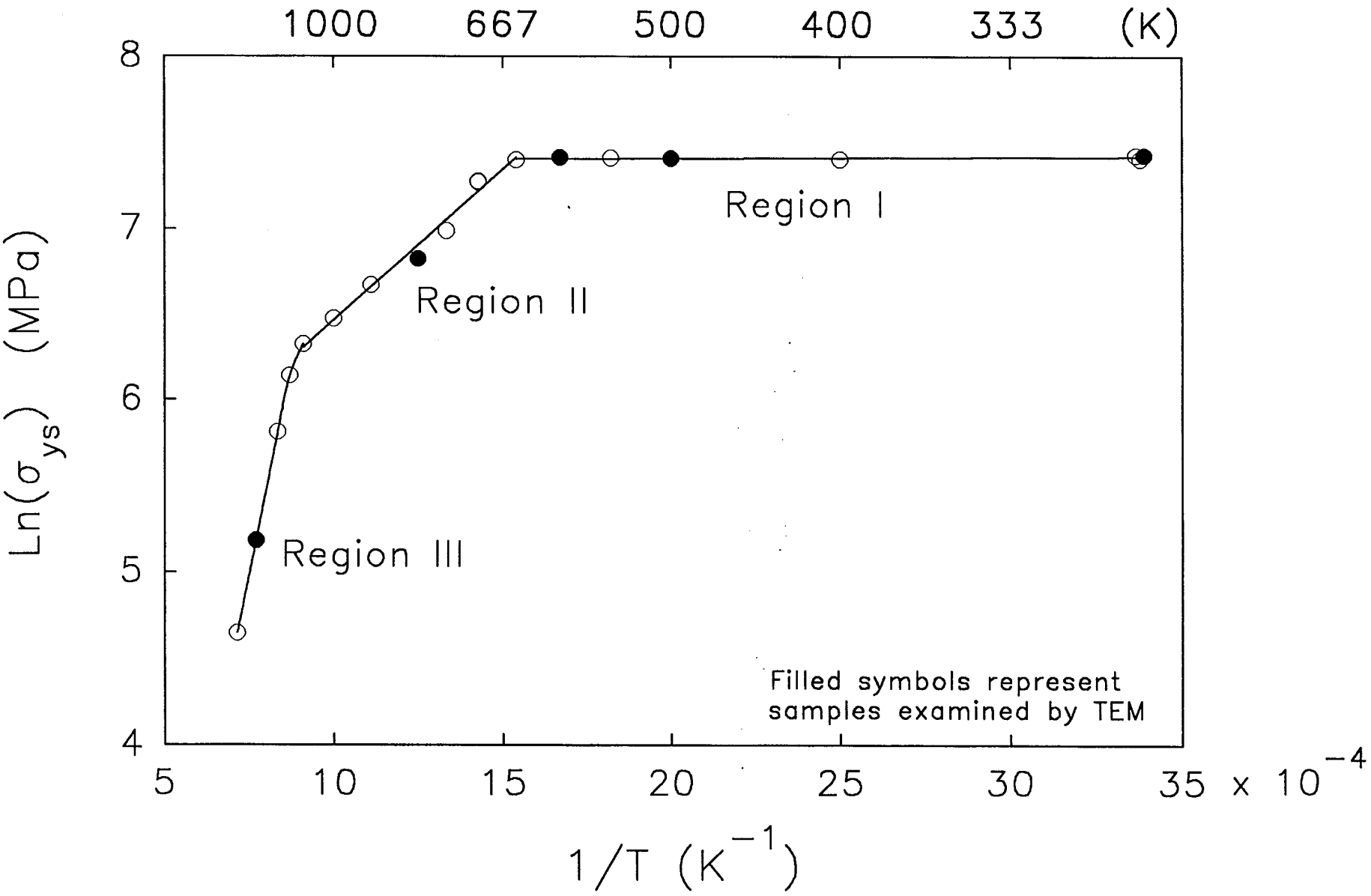

Figure 81. Arrhenius representation of the compression yield strength of <001> oriented NiAl alloy D176 showing three distinct deformation regimes. Solid symbols represent samples examined by TEM.

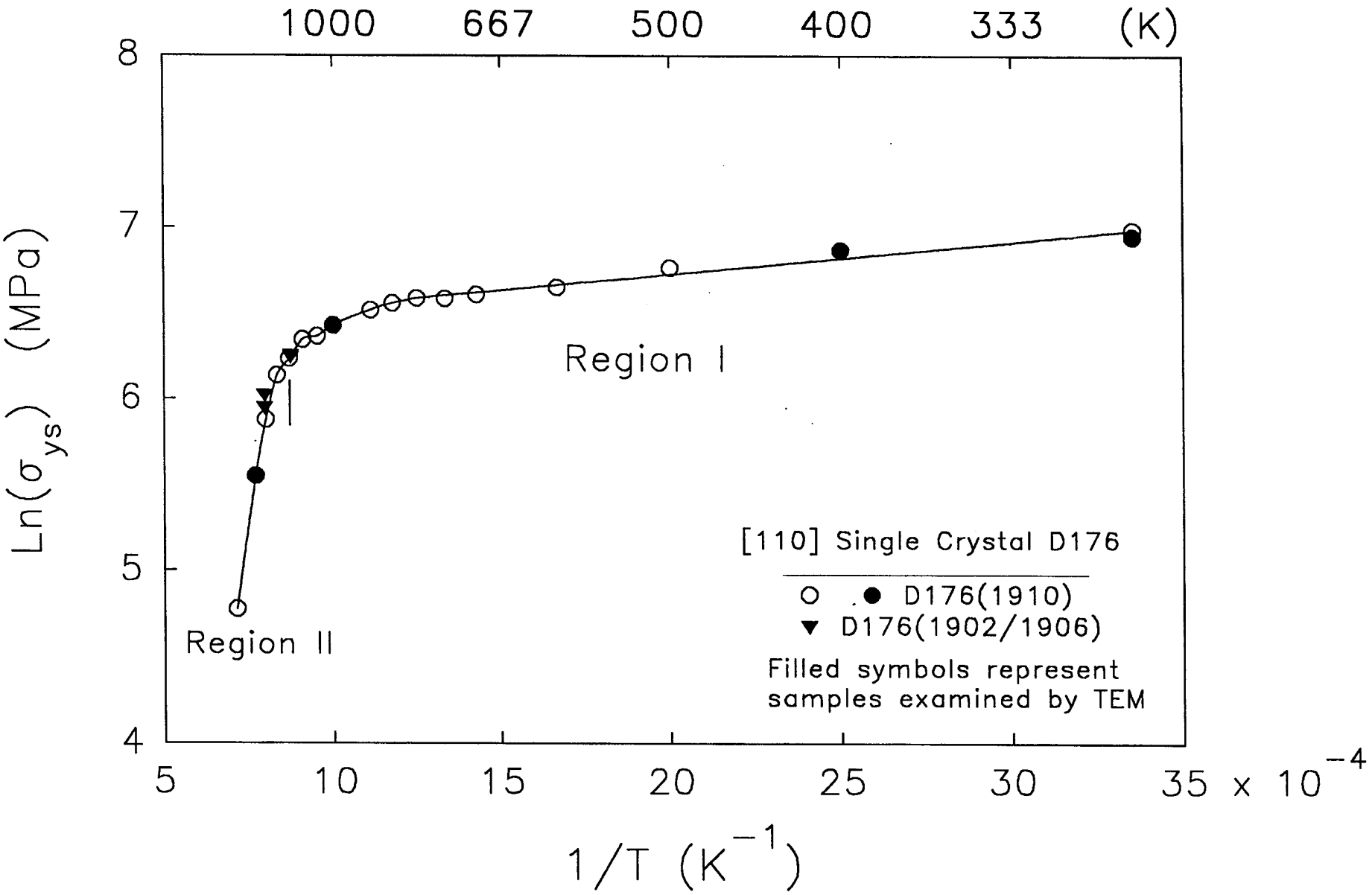

Figure 82. Arrhenius representation of the compression yield strength of <011> oriented NiAl alloy D176 showing two distinct deformation regimes with a gradual transition from region I to region II. Solid symbols represent samples examined by TEM.

<011> oriented samples the data in Figure 82 indicates the operation of only two major deformation regimes with a gradual transition from the low-temperature region I behavior to the high-temperature regime referred to as region II. Region II encompasses the temperature range above ~ 1250 K. The knee in the $\ln(\sigma_y)$ versus 1/T curve represents the transition between the two deformation regimes and, therefore, does not represent an independent deformation regime itself but is more closely related to region I behavior. The reason for this distinction will be apparent in Section 3.13.2.5. The solid symbols in Figure 82 represent those samples examined by TEM.

3.13.2.5 Deformation Processes in Each Regime

3.13.2.5.1 <001> Orientation

Region I (T = 300-650 K) : Samples tested at room temperature, 500 K, and 600 K were examined by TEM to characterize the deformed microstructure and to identify the dislocation processes responsible for deformation in region I. In this temperature range the material has limited ductility even in compression and small internal cracks aligned parallel to the compression axis were observed in room temperature samples deformed to as little as 0.5% plastic strain. Sections of the compression samples free from cracks were used to prepare TEM foils. At strains approaching 1% the room temperature samples failed catastrophically, shattering into numerous small pieces. To ensure that the deformed microstructure observed at 300 K was not an artifact of the fracture process, samples deformed at 500 and 600 K were also analyzed, since the propensity to form cracks during testing decreased and the strain before cracking occurred increased significantly with increasing test temperature. Therefore, the deformed microstructure in the 500 and 600 K samples could be attributed solely to plastic deformation associated with the induced strain during testing.

At 300K, the deformation was predominantly confined to well-defined bands that ran parallel to the traces of edge-on {110} planes in the [001] zone-axis, which was also the compression axis. A detailed dislocation analysis was performed on a sample deformed to 0.46% plastic strain. This sample contained only one type of deformation bands whose edges ran parallel to the [110] direction in the [001] zone-axis, as shown in Figure 83a. There were two types of dislocations in each deformation band, one running almost perpendicular to the band and the other type running parallel to the edges of the band. These are marked "A" and "B" respectively, in Figure 83a. These dislocations were imaged under two beam conditions with different operating reflections and the corresponding images are shown in Figure 83b-f. Dislocations of type "A" were invisible with g110 (Figure 83b), g01I (Fig. 83c), and g10I (Figure 83d), and strongly visible with g110 (Figure 83e), g011 (Figure 83f), g100 and g010. These observations indicated that the Burgers vector for dislocations of type "A" was b = [111]. Trace analysis indicated that these dislocations were of screw type gliding in (112) planes and mostly confined within the observed slip bands.

Dislocations marked "B" were irregular or wavy in appearance and were often attached to type "A" dislocations. Dislocation g•b and trace analysis indicated that the "B" dislocations were most likely [111] edge dislocations. These edge components were usually longer than the screw components and their average line direction was determined to be [I10]. The only reflection for which total invisibility of the edge components was obtained was g110 (Figure 83b), since for this

reflection both g•b and g•b x u = 0. For all other reflections with which the [111] screw dislocations disappeared, e.g. g01$\bar{1}$ and g10$\bar{1}$ (Figure 83c and 83d respectively), the edge components showed what appeared to be residual contrast due to a non-zero value of g•b x u. Otherwise, the "B" dislocations could be b = [110] edge dislocations based on the g vectors used and assuming strong visibility under g01$\bar{1}$ and g10$\bar{1}$, which really was not indicated. Furthermore, <111>{112} slip has been previously observed in binary NiAl samples deformed along <100> at room temperature [23,39,40] while <110> slip has only been reported at intermediate temperatures, at or above the DBTT in <001> binary NiAl crystals. Therefore, the observation of <111>{112} slip in <001> oriented D176 at room temperature is consistent with the deformation of binary <001> NiAl and occurs at almost similar stress levels in both materials (Fig. 80).

The waviness of the edge components is either due to cross-slip of the screw components, as observed in binary NiAl [39], and/or extensive pinning of the edge components by the G-phase precipitates. In addition to the [111] dislocations, occasional random <100> dislocations were observed mostly outside the deformation bands. These are marked "C" in Figure 83. The <100> type dislocations were few in number and believed to have an insignificant contribution to the deformation of the crystal since they were not capable of moving in a conservative fashion.

The [001] sample tested at 500 K was deformed to 1.4% plastic strain. The dislocation density at this strain was quite high and the dislocations were found to be distributed uniformly with no apparent formation of bands (Figure 84a). A g•b analysis indicated that the dislocations were strongly visible with g110 (Figure 84b), disappeared completely with g1$\bar{1}$0 (Figure 84c), displayed only residual contrast for g10$\bar{1}$ (Figure 84d) and g01$\bar{1}$, and strong contrast for g011. The dislocations were extremely wavy but trace analysis indicated that the average line direction of the dislocations was [1$\bar{1}$0]. Thus, the dislocations were identified as [111] edge dislocations similar to what was observed at room temperature. The major difference at this temperature was the absence of short [111] screw segments that were observed at 300 K. These observations suggest a greater mobility and more extensive cross-slip behavior for the [111] screw segments with increasing temperature. The wavy nature of the edge segments could be clearly seen in a foil where the dislocation density was somewhat lower (Figure 85a). A WBDF image of a similar region (Figure 85b) reveals that the waviness was associated with both a cross-slip phenomenon (e.g. at "X") and pinning of the dislocation segments by the G-phase precipitates (e.g. at "Y").

The [001] sample tested at 600 K was deformed to 1.5% plastic strain and also exhibited a uniform dislocation density. In this case, there were two types of dislocations, one running approximately along the [1$\bar{1}$0] direction marked "A", and the other running approximately along the [110] direction marked "B" in the [001] zone-axis image shown in Figure 86a. Results of g•b (Figure 86a-d) and trace analysis indicated that both types of dislocations were <111> edge dislocations. The "A" dislocations were b = [111], with an overall u = [1$\bar{1}$0], gliding in (11$\bar{2}$) plane and "B" dislocations were b = [1$\bar{1}$1], with an overall u = [110], gliding in (1$\bar{1}$2) plane. Figure 86b,c give an estimate of the density of [111] and [1$\bar{1}$1] dislocations, respectively, present in the deformed structure. In addition, some dislocations with b = <100> were also present in the microstructure and are marked "C" in Figure 86.

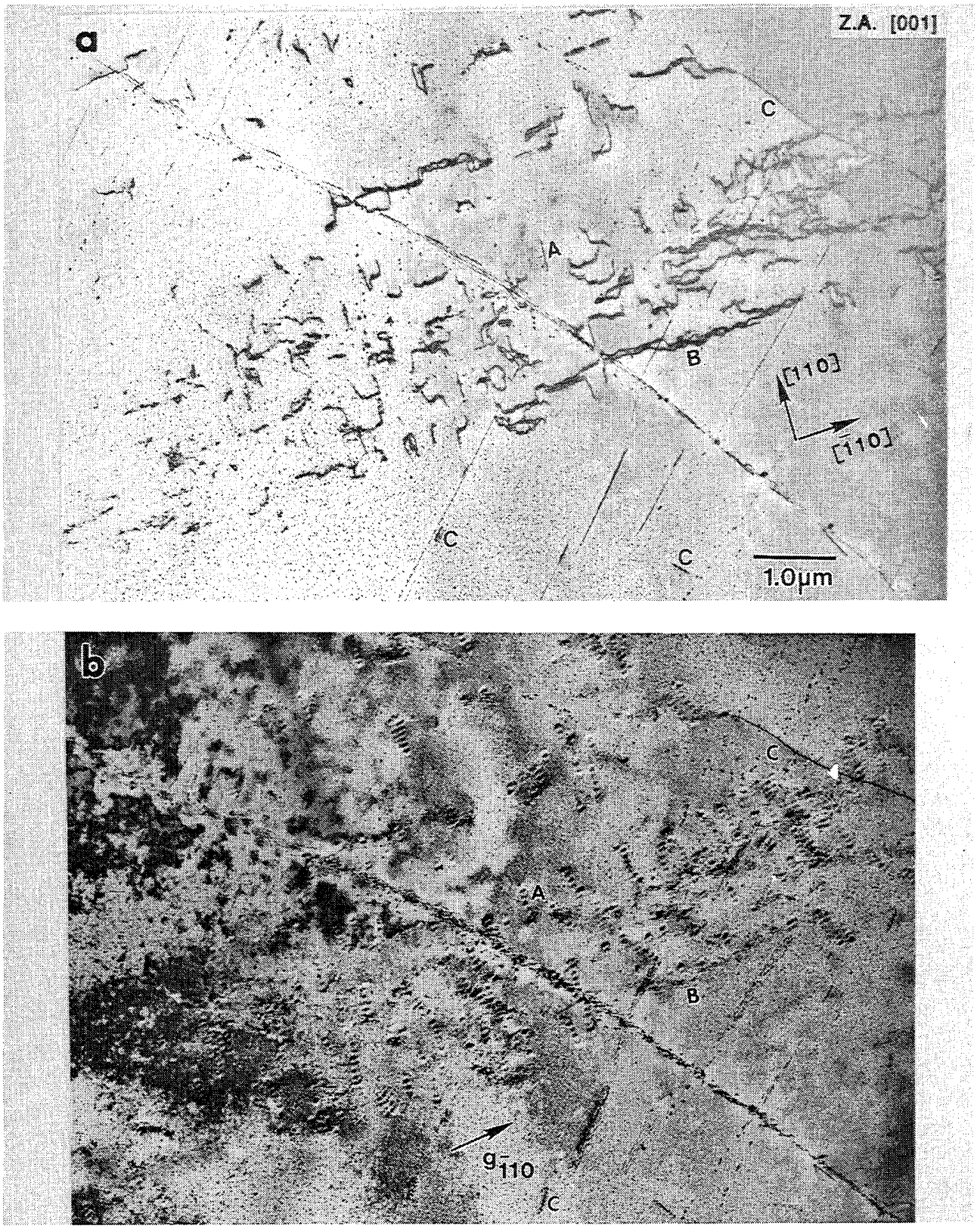

Figure 83. Dislocation structure and g•b analysis for NiAl alloy D176 deformed along [001] at room temperature. a) general area of analysis, b) gI10, c) g01I close to the Z.A. [011], d) g10I, e) g110, and f) g011 close to the Z.A. [01I].

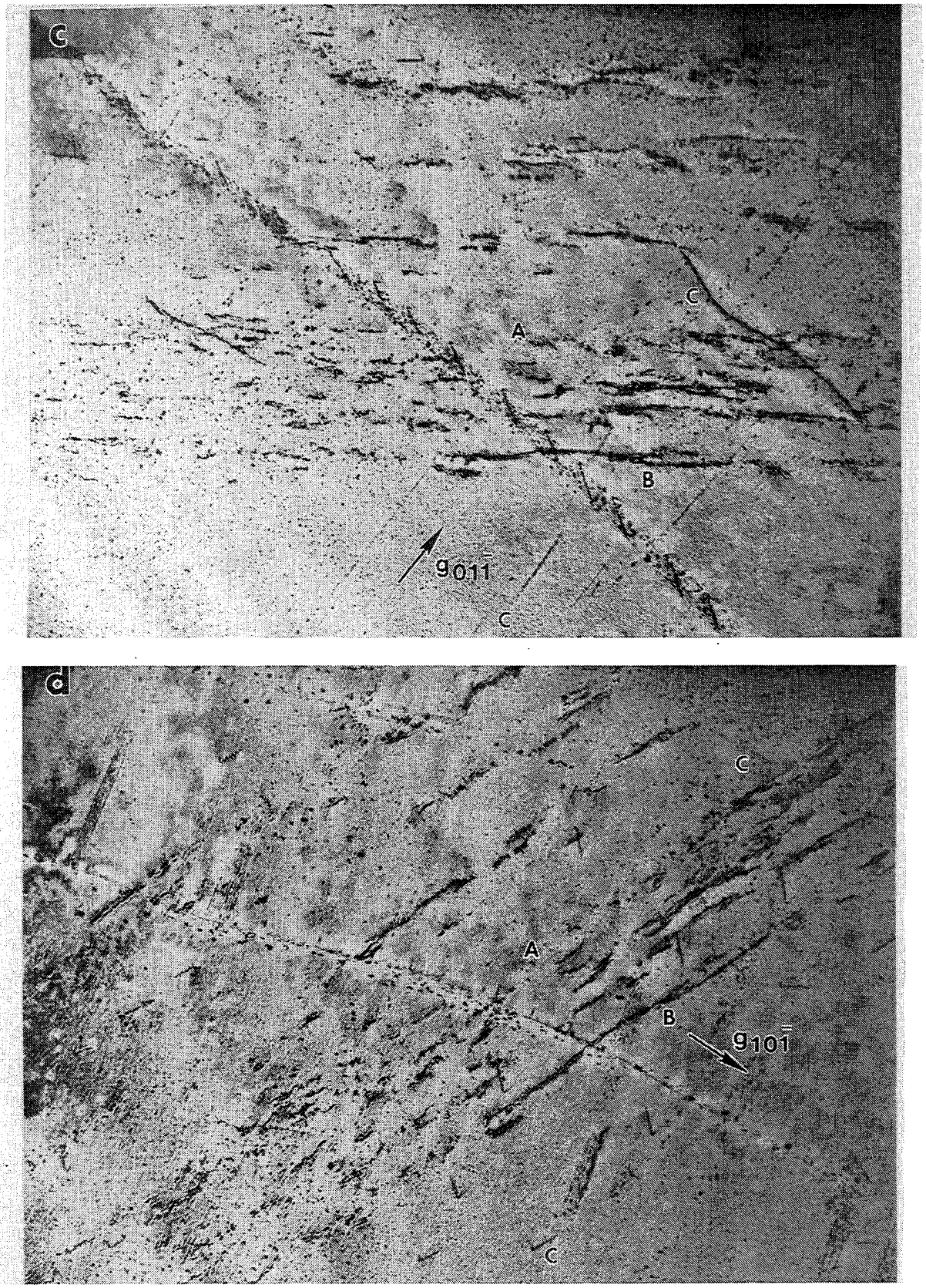

Figure 83(cont.). Dislocation structure and g•b analysis for NiAl alloy D176 deformed along [001] at room temperature. a) general area of analysis, b) gI10, c) g01I close to the Z.A. [011], d) g10I, e) g110, and f) g011 close to the Z.A. [01I].

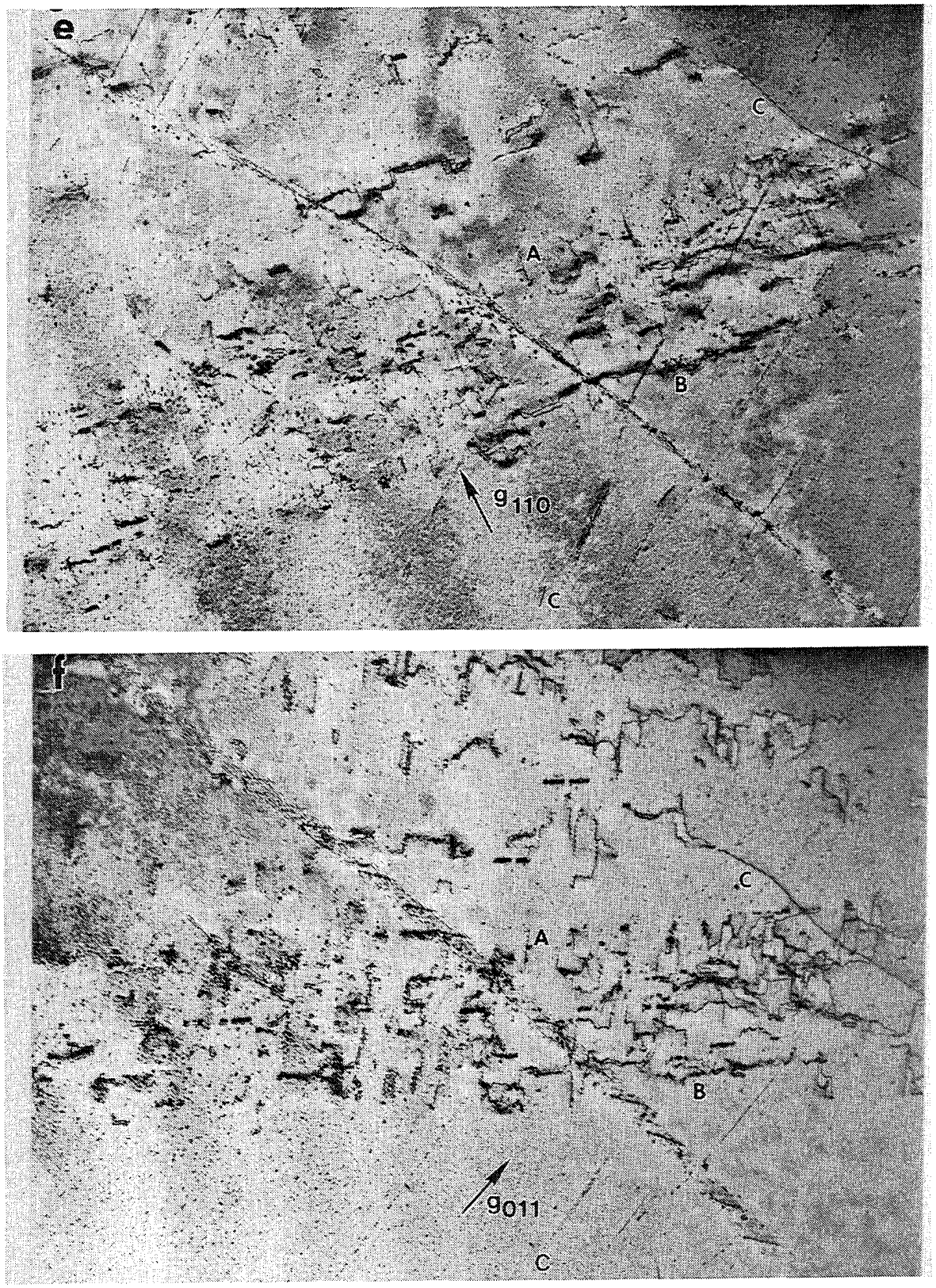

Figure 83(cont.). Dislocation structure and g•b analysis for NiAl alloy D176 deformed along [001] at room temperature. a) general area of analysis, b) g1̄10, c) g01̄1 close to the Z.A. [011], d) g10^{-}),1), e) g110, and f) g011 close to the Z.A. [01̄1].

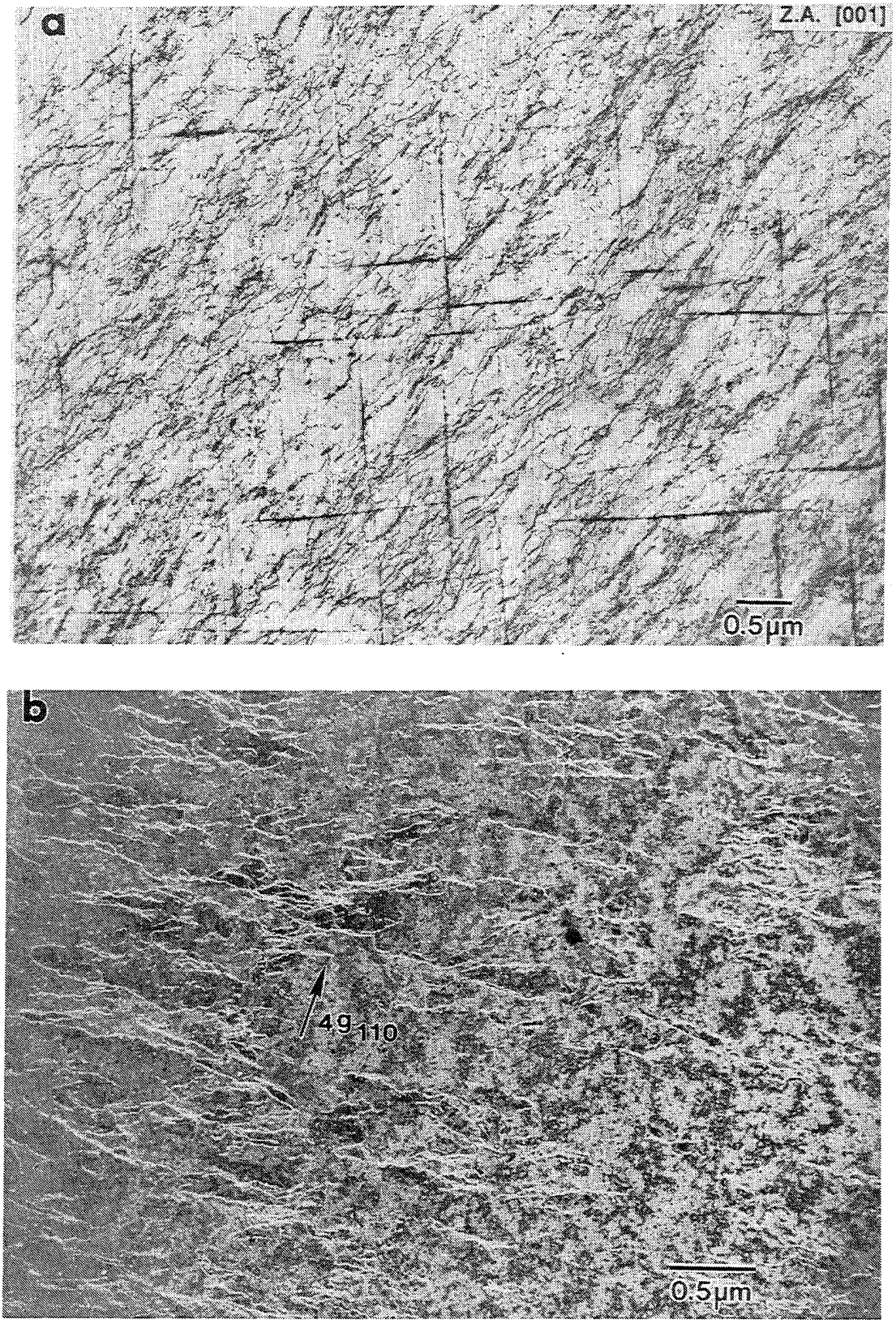

Figure 84. (a) Typical dislocation structure for [001] oriented D176 deformed at 500 K to 1.4% plastic strain. The dislocation g · b analysis is shown in: b) WBDF 4g110, c) g110, and d) g10I.

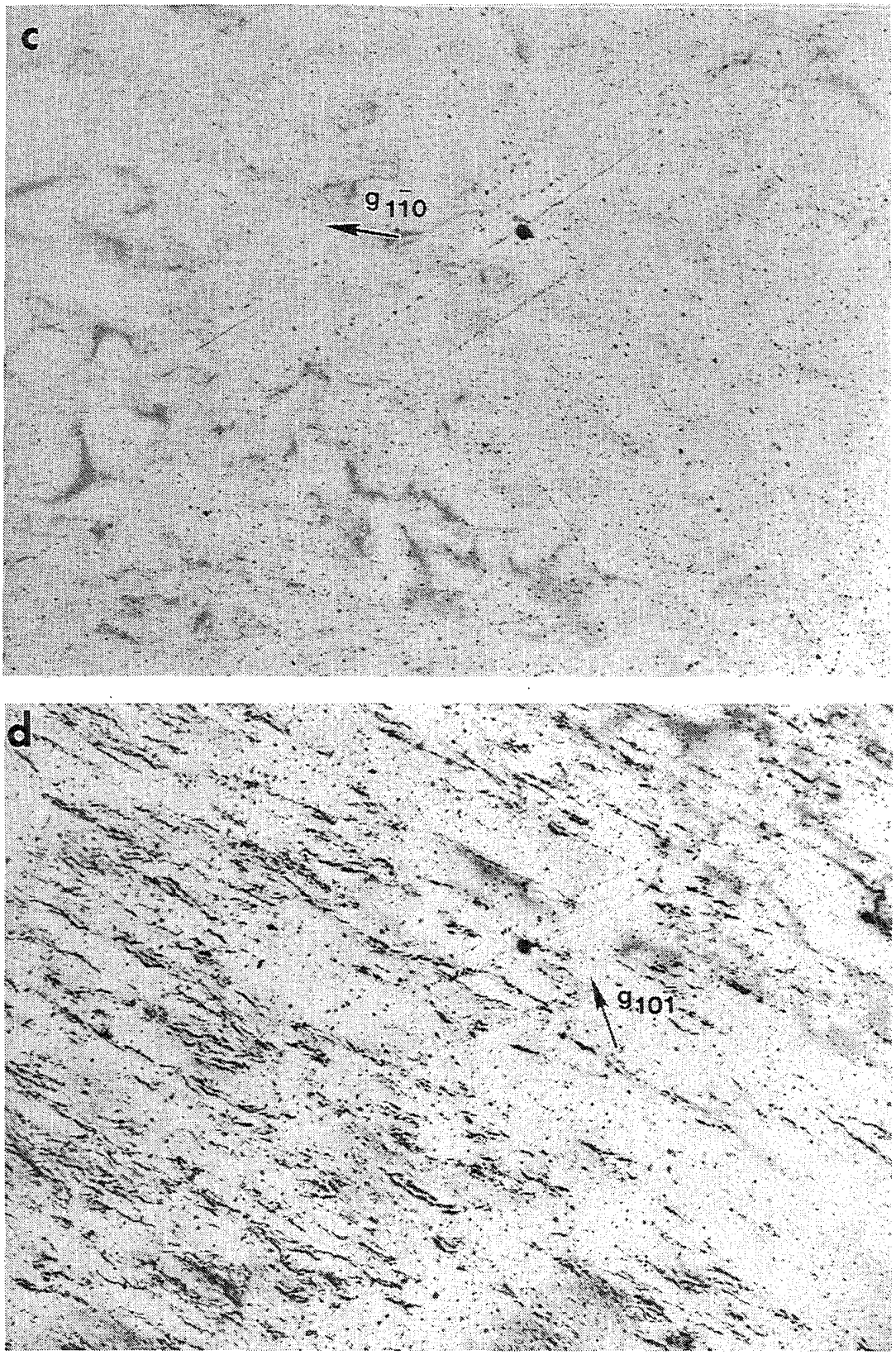

Figure 84(cont.). (a) Typical dislocation structure for [001] oriented D176 deformed at 500 K to 1.4% plastic strain. The dislocation g · b analysis is shown in: b) WBDF 4g110, c) g1I0, and d) g10I.

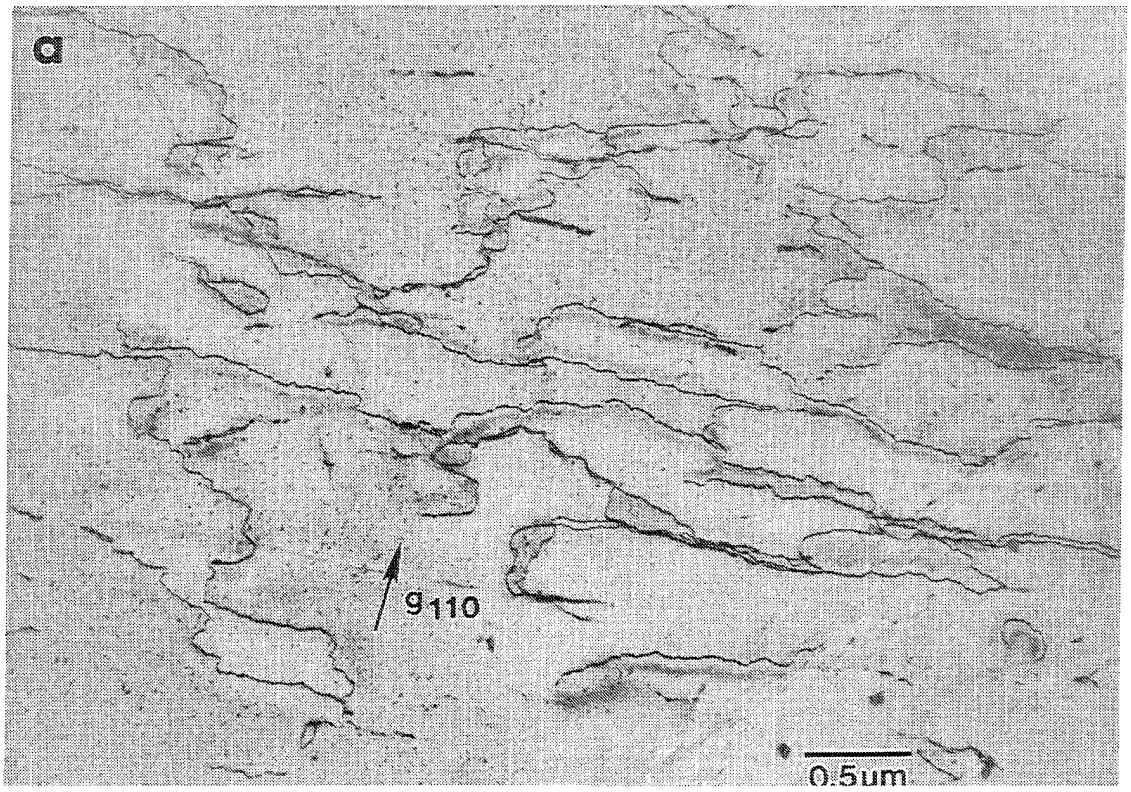

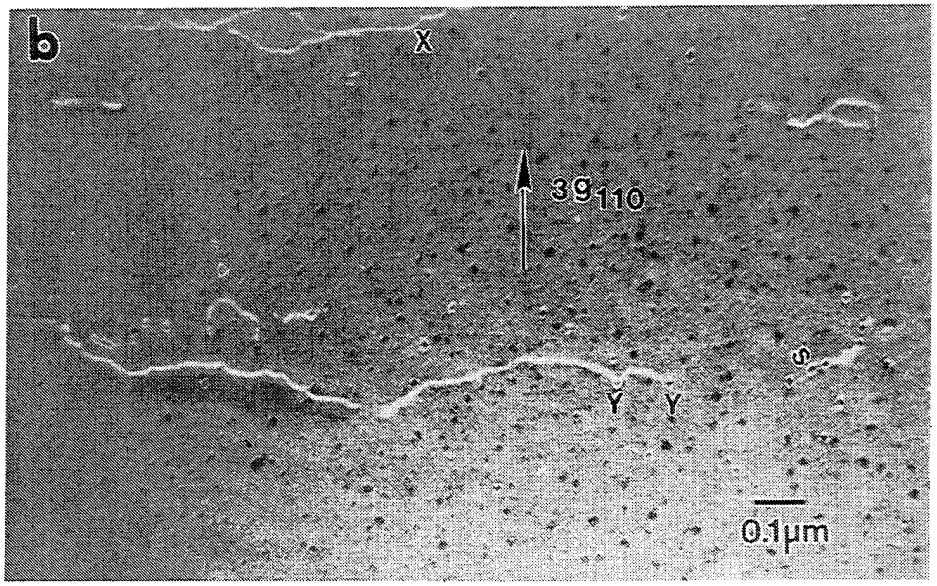

Figure 85 . The wavy appearance of the dislocations observed at 500 K. a) bright field image of a region with low dislocation density, and b) WBDF image that associates the waviness with both a cross-slip phenomenon (e.g. at "X") and pinning of the dislocation segments by the G-phase precipitates (e.g. at "Y").

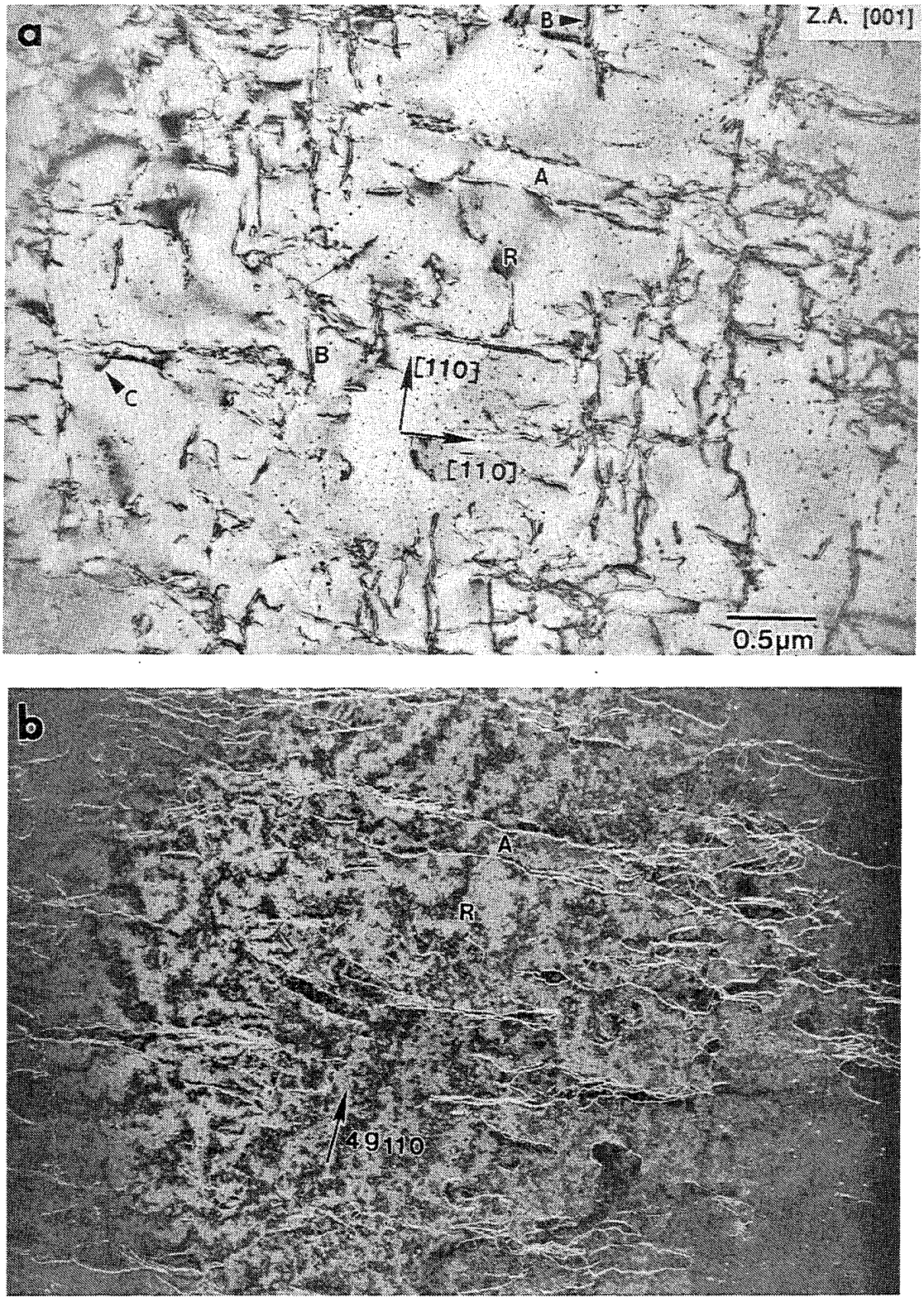

Figure 86. (a) Duplex <111> slip observed in a [001] oriented D176 sample deformed at 600 K to 1.5% plastic strain. Dislocation g•b analysis of the area shown in (a) with: b) WBDF 4g110 (A : Visible, B : Inv.), c) g1I0 (A : Inv., B : Visible), and d) g011 (A : Visible, B : Weak Contrast). R denotes the reference point in each micrograph.

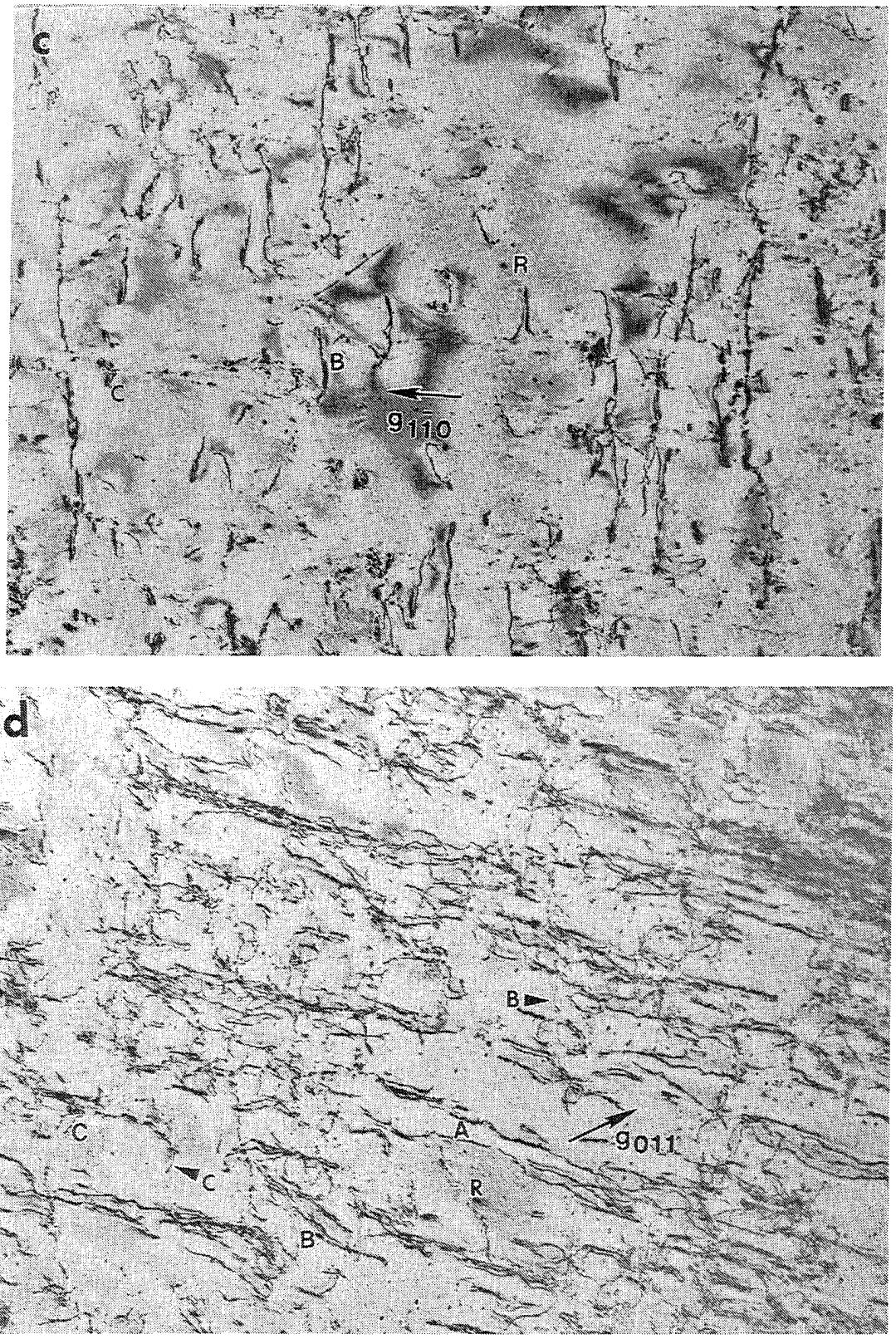

Figure 86(cont.). (a) Duplex <111> slip observed in a [001] oriented D176 sample deformed at 600 K to 1.5% plastic strain. Dislocation g•b analysis of the area shown in (a) with: b) WBDF 4g110 (A : Visible, B : Inv.), c) g110 (A : Inv., B : Visible), and d) g011 (A : Visible, B : Weak Contrast). R denotes the reference point in each micrograph.

Thus, in region I, deformation of <001> D176 crystals occurs by glide of <111> dislocations on {112} planes. For a <001> compression sample the CRSS for all four <111>{112} slip systems is the same and in a homogeneous defect-free sample with an exact orientation and precise alignment, all four slip systems would be expected to operate. However, under real life conditions, one or more of the slip systems can activate preferentially, as observed in the samples tested at 300, 500 and 600 K. Edge dislocation segments were primarily observed within the post-tested microstructures with short screw segments observed only at room temperature. The mobility of the screw components increased with temperature due probably to enhanced cross-slip and they were not observed in the microstructure above room temperature. The increased tendency for cross-slip with temperature corresponded to a small enhancement in compressive ductility observed in samples deformed in the higher temperature end of region I. The <111> edge components were observed at all temperatures within region I suggesting their limited mobility in this region. These segments were generally long and wavy due to the cross-slip of the associated <111> screw components and also pinning of the edge segments by the G-phase precipitates. The <111> screw components were apparently able to by-pass the G-phase precipitates in this regime by cross-slip.

Region II (T = 650 - 1100 K): In this region, detailed dislocation analysis was carried out on a [001] sample tested at 800 K, which was deformed to 2.1% plastic strain. The microstructure generally consisted of a high density of dislocations mostly confined to two sets of slip bands as shown in Figure 87a. The density of dislocations within the bands as well as the width of the bands, however, varied from region to region even within a single foil (Figure 87a vs. 87b). The edges of the bands ran parallel to traces of the two mutually perpendicular {100} planes parallel to the beam as shown in the [001] zone-axis images in Figure 87a,b. A WBDF image (Figure 87c) with the operating reflection 3g110 clearly shows the dislocations in the two bands and a region containing the intersection of the two bands. The microstructure in each of the two bands consisted of curved dislocations and loops (marked by arrows) elongated along <100> directions.

A detailed g•b analysis of the dislocations and loops belonging to the thin central band 1 marked with an arrow in Figure 87b was conducted and the results are presented in Figures 88a-f. This band consisted of two types of dislocations marked "A" and "B" in the [001] zone-axis image shown in Figure 88a. Most of the dislocations were of type "A" and only a small number were of type "B". Dislocations of type "A" disappeared completely with the operating reflection g100 (Figure 88b) and showed weak residual contrast with g01$\bar{1}$ (Figure 88c). These dislocations were strongly visible with g020, g1$\bar{1}$0, g110 (Figure 88d-f). The Burgers vector of dislocations "A" in band 1 was thus identified as b = [011]. Dislocations of type "B" disappeared completely with g100 (Figure 88b), but were visible with g01$\bar{1}$ (Figure 88c), suggesting that their b = [01$\bar{1}$]. The dislocation loops were elongated along the [100] direction and disappeared for g100 (Figure 88b), g10$\bar{1}$, and g101, but were visible with g020 (arrows in Figure 88d), indicating that their Burgers vector was [010]. Thus, dislocations in band 1 comprised mainly [011] dislocations and [010] loops, although a few [01$\bar{1}$] dislocation segments were also observed. A similar analysis of the dislocations in band 2 (Figure 87a,b) were found to have b = [101], a few had b = [10$\bar{1}$], and the dislocation loops had b = [100]. Trace analysis indicated that band 1 was formed on the (01$\bar{1}$) plane and band 2 on the (10$\bar{1}$) plane. Due to extensive pinning of dislocations by the G-phase precipitates, the dislocations were extremely irregular and wavy (Figure 87c) and the true line

direction of individual dislocations could not be determined. The <100> loops were found to be prismatic in nature and the loop plane was ~ 45° to their Burgers vector. In addition, a small fraction of the dislocation segments with b = <100> were also observed mostly between the bands and are marked "C" in Figure 88. These are similar to the dislocations observed in the as-homogenized material shown in Figure 79.

Thus, in region II, deformation occurred by the glide of <110> dislocations on {110} planes. In this orientation there would be four equally stressed systems of this type and indeed evidence for slip on all four systems was observed, although in the sample analyzed slip was most dominant on two oblique systems, e.g. [011](01$\bar{1}$) and [101](10$\bar{1}$). This is in contrast to many rock-salt structured crystals deformed along <001> that display latent hardening [41]. In these crystals, <110>{1$\bar{1}$0} slip will occur along two orthogonal {110} slip planes and exclude the other equally stressed pair that is oblique to the first pair, due to significant interference between slip on oblique {110} planes. While latent hardening has also been proposed to occur in [001] binary NiAl deformed at intermediate temperatures [42], it was not observed in <001> D176 deformed at low strains. It is likely that the high density of fine precipitates in the alloy is a much greater obstacle to slip than forest dislocations due to the operation of an oblique slip system. This would make slip on any {110} plane equally difficult in alloy D176, or conversely, equally likely on any given <110>{1$\bar{1}$0} system.

Because the line direction of individual dislocations was ambiguous, it was not possible to conclusively determine the type (edge vs. screw) of dislocation left within the microstructure or conversely which type of <110> dislocation was more mobile. However, work by Mills et al. [43] indicates that pure edge <110> dislocations are metastable and will likely decompose into two <100> dislocations. This decomposition is less probable for screw and mixed segments making the motion of <110> edge segments more complex due to their core decomposition resulting in locking of these dislocation segments.

The <100> dislocation loops left behind in the microstructure during deformation in region II are debris formed as a result of deformation by <110> screw dislocations. These loops could occur by several mechanisms such as edge dipole trapping or double cross-slip of <110> screw dislocations. For example, when edge segments with the same Burgers vector moving on parallel slip planes become trapped in each others stress fields, edge dipoles can form and subsequently pinch off resulting in the <100> loops. This mechanism is described in detail by Tetelman [44] and was first applied to observations in binary NiAl by Field et al. [25]. The double cross-slip of <110> screws to produce superjogs as shown in the inset to Figure 88f, is also a likely mechanism for loop formation in <001> D176, since the G-phase precipitates act as obstacles to slip forcing the <110> dislocations to cross-slip onto non-{110} planes leaving behind <100> loops.

Region III (T > 1100 K): In region III, detailed dislocation analysis was carried out on a [001] sample deformed to 2.0% plastic strain at 1300 K. The overall dislocation density in this sample was much lower than that observed in samples deformed in regions I or II, suggesting a considerable degree of recovery in region III. Along the [001] zone-axis three types of dislocations were observed (marked "1", "2" and "3" in Figure 89a), type 1 is aligned more or less vertically in the micrograph while type 3 is oriented horizontally. Dislocations of type 1 were

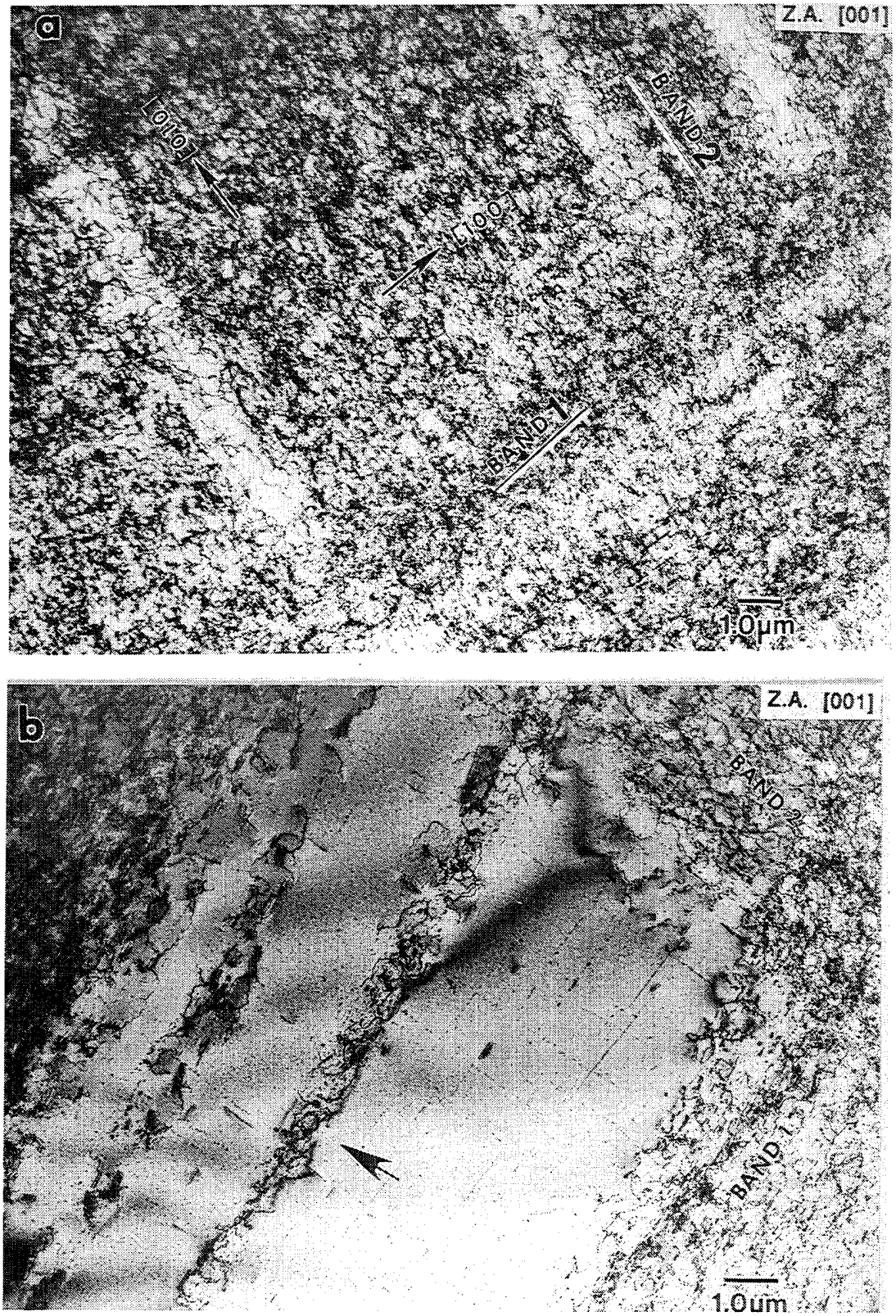

Figure 87. Typical dislocation microstructure in [001] D176 deformed to 2.1% plastic strain at 800 K. a) overall dislocation structure indicating slip on two primary systems, b) a region between slip bands where the dislocation density is low, and c) WBDF micrograph of intersecting slip bands showing the morphology of individual dislocations and loops (arrows).

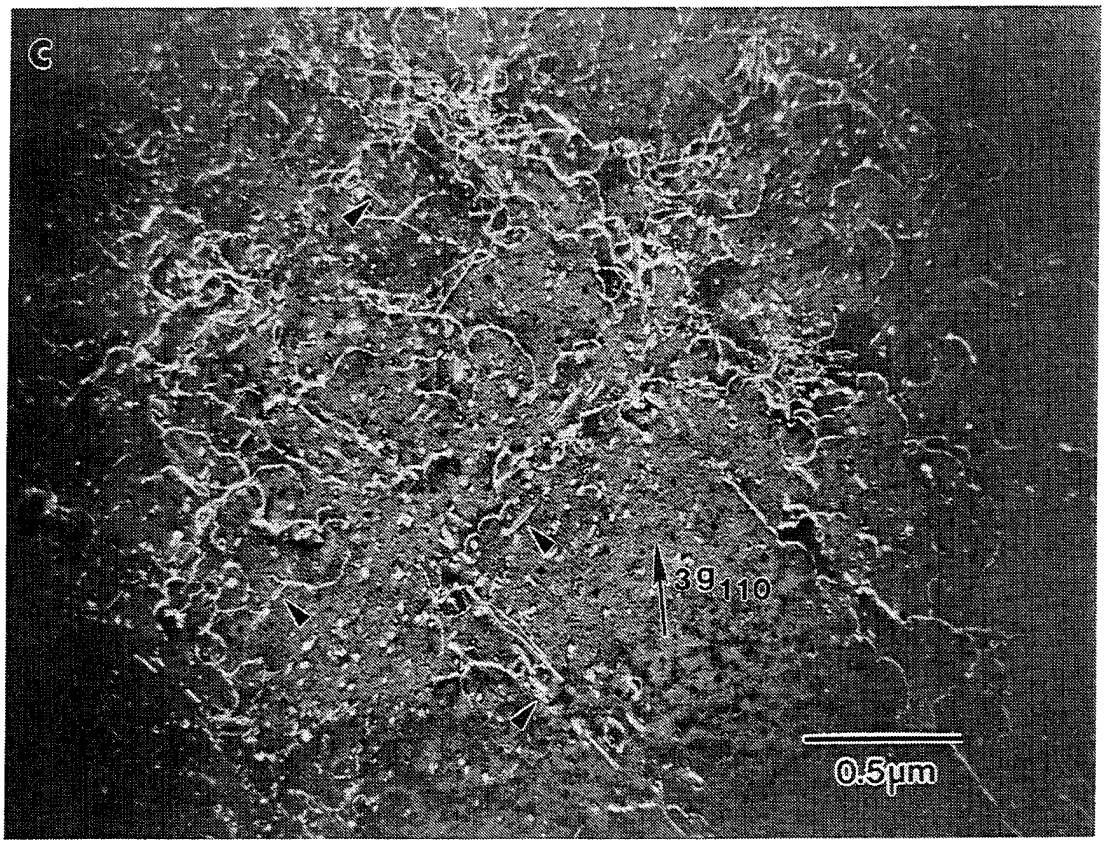

Figure 87(cont.). Typical dislocation microstructure in [001] D176 deformed to 2.1% plastic strain at 800 K. a) overall dislocation structure indicating slip on two primary systems, b) a region between slip bands where the dislocation density is low, and c) WBDF micrograph of intersecting slip bands showing the morphology of individual dislocations and loops (arrows).

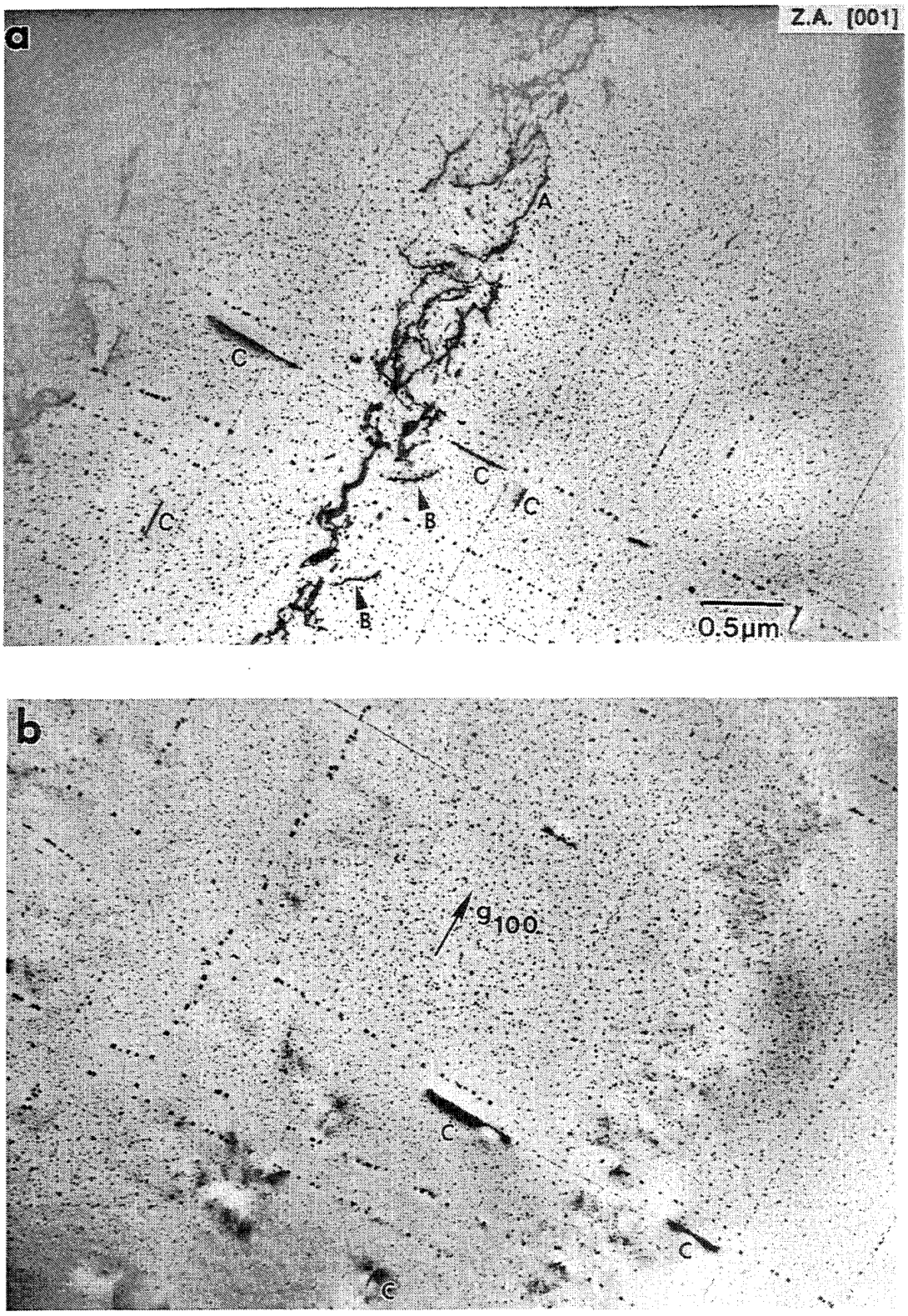

Figure 88. a) Higher magnification image of the thin band marked with an arrow in Fig. 87(b), and (b-f) dislocation g•b analysis of the area in (a) with: b) g100, c) g01$\bar{1}$, d) g020, e) g$\bar{1}$10, and f) g110.

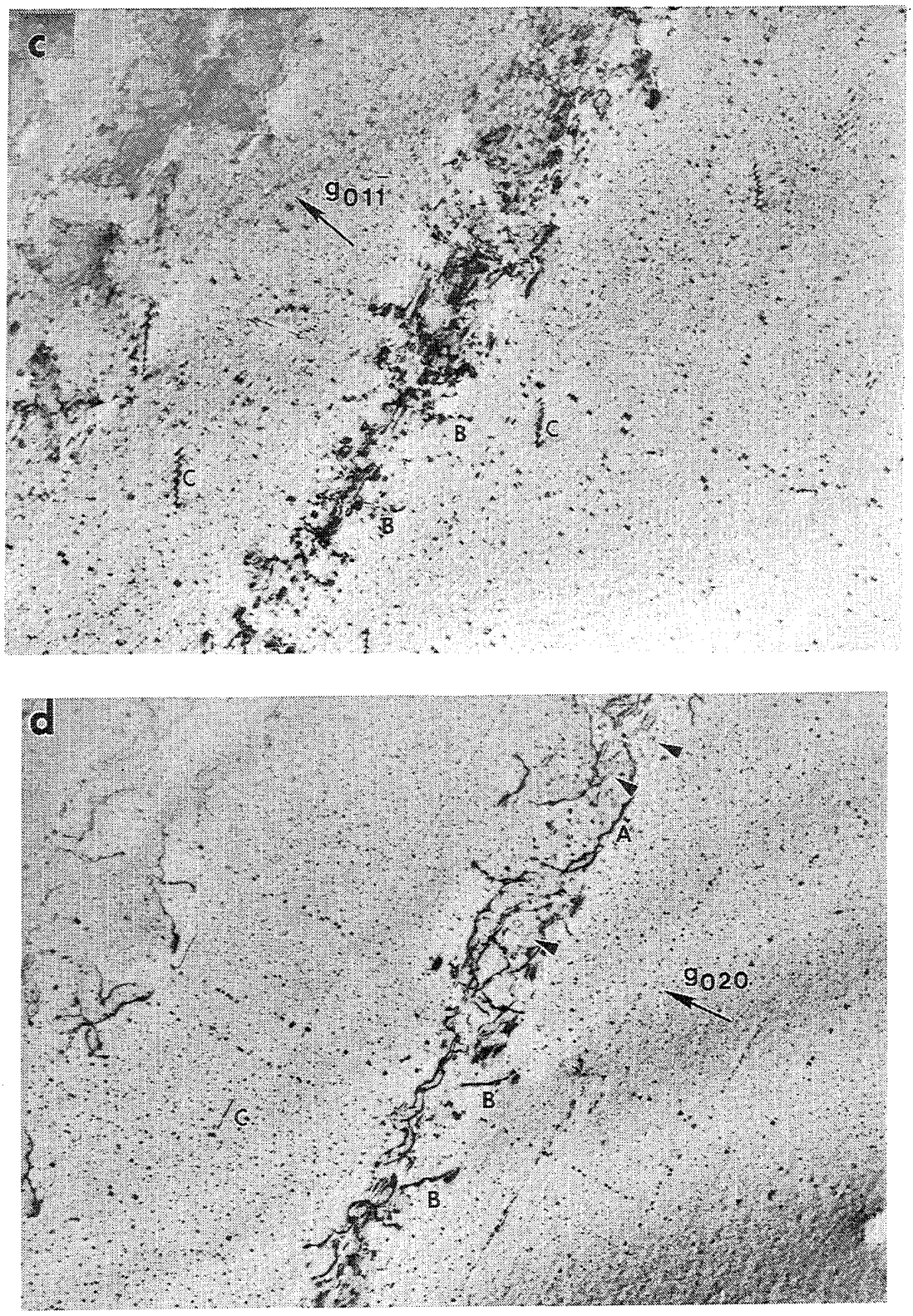

Figure 88(cont.). a) Higher magnification image of the thin band marked with an arrow in Fig. 87(b), and (b-f) dislocation g•b analysis of the area in (a) with: b) g100, c) g01I, d) g020, e) g^{-}),1)10, and f) g110.

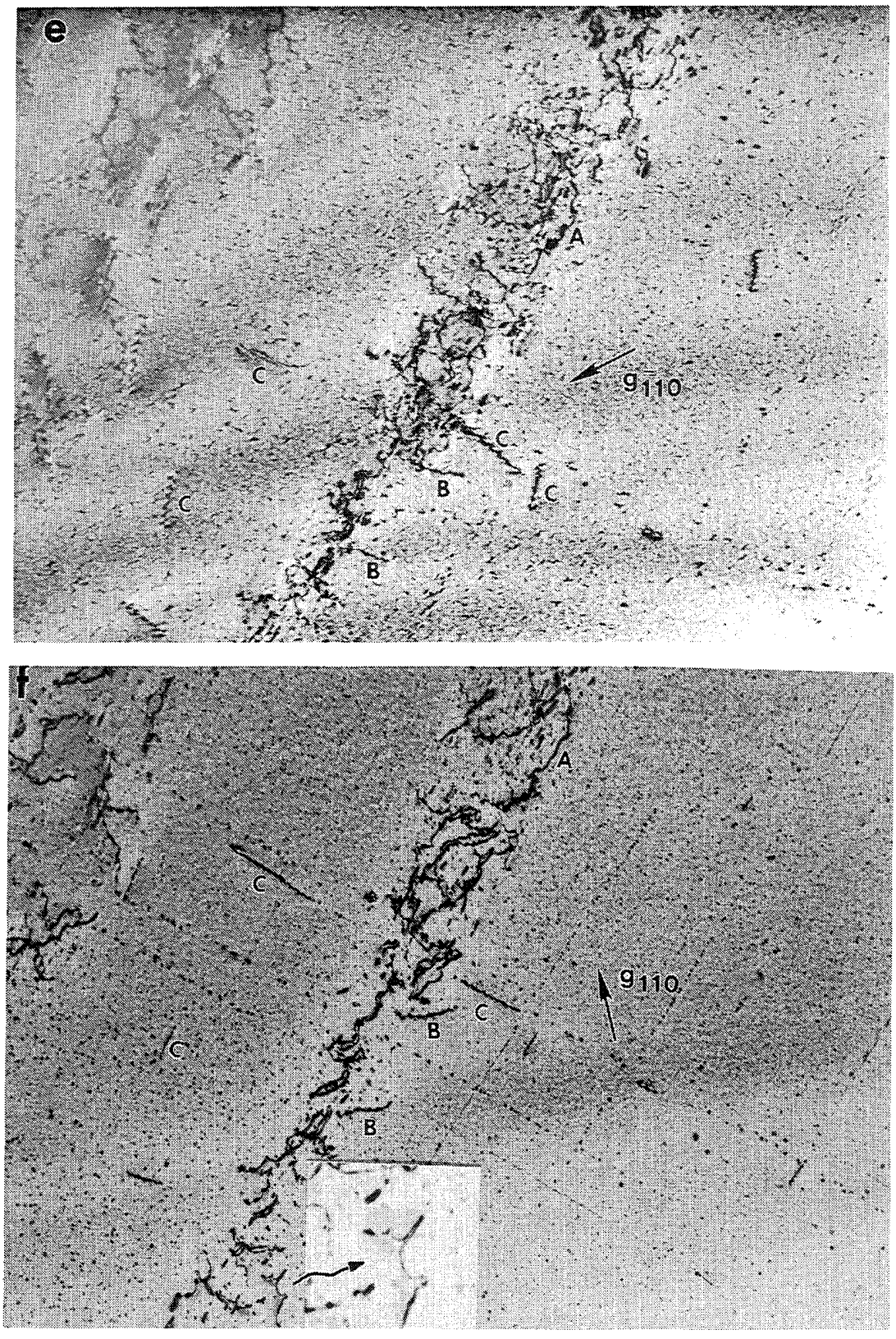

Figure 88(cont.). a) Higher magnification image of the thin band marked with an arrow in Fig. 87(b), and (b-f) dislocation g•b analysis of the area in (a) with: b) g100, c) g01I, d) g020, e) g^{-}),1)10, and f) g110.

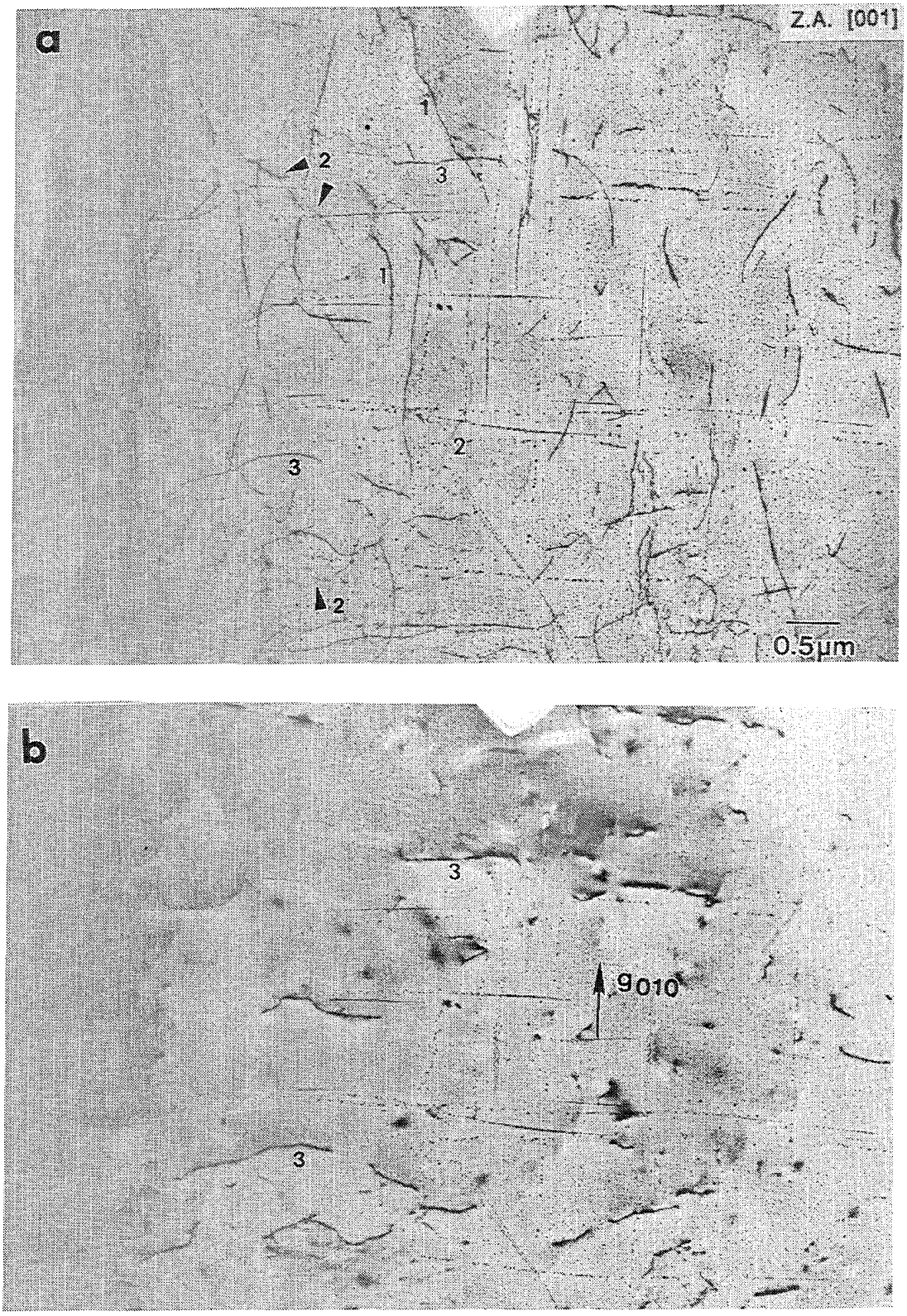

Figure 89. Typical dislocation structure for [001] D176 deformed at 1300 K to 2.0% plastic strain. a) general area of analysis, and (b-f) corresponding dislocation g•b analysis of the area with: b) g010, c) g100, d) g110, e) gI10, and f) g011.

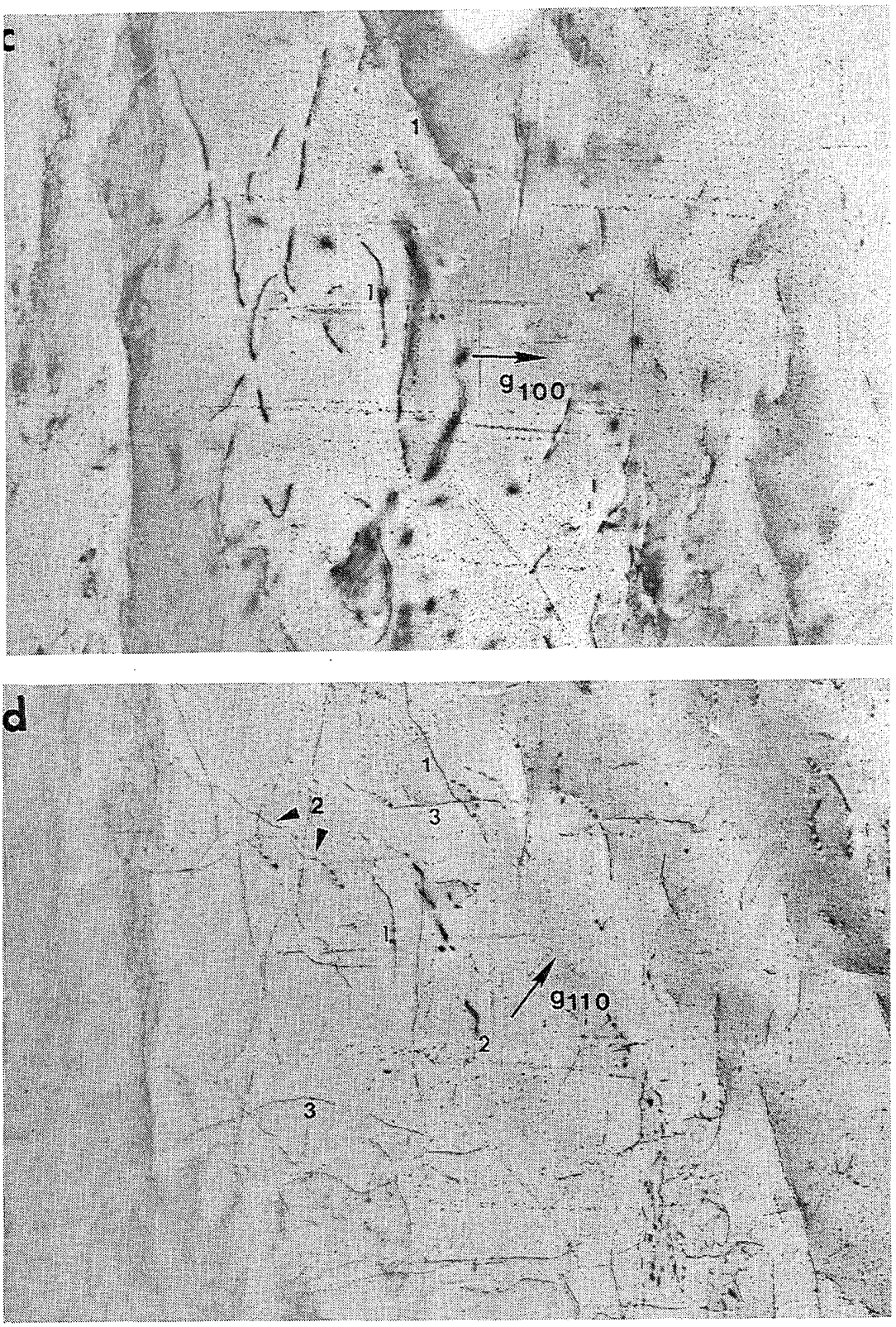

Figure 89(cont.). Typical dislocation structure for [001] D176 deformed at 1300 K to 2.0% plastic strain. a) general area of analysis, and (b-f) corresponding dislocation g•b analysis of the area with: b) g010, c) g100, d) g110, e) gI10, and f) g011.

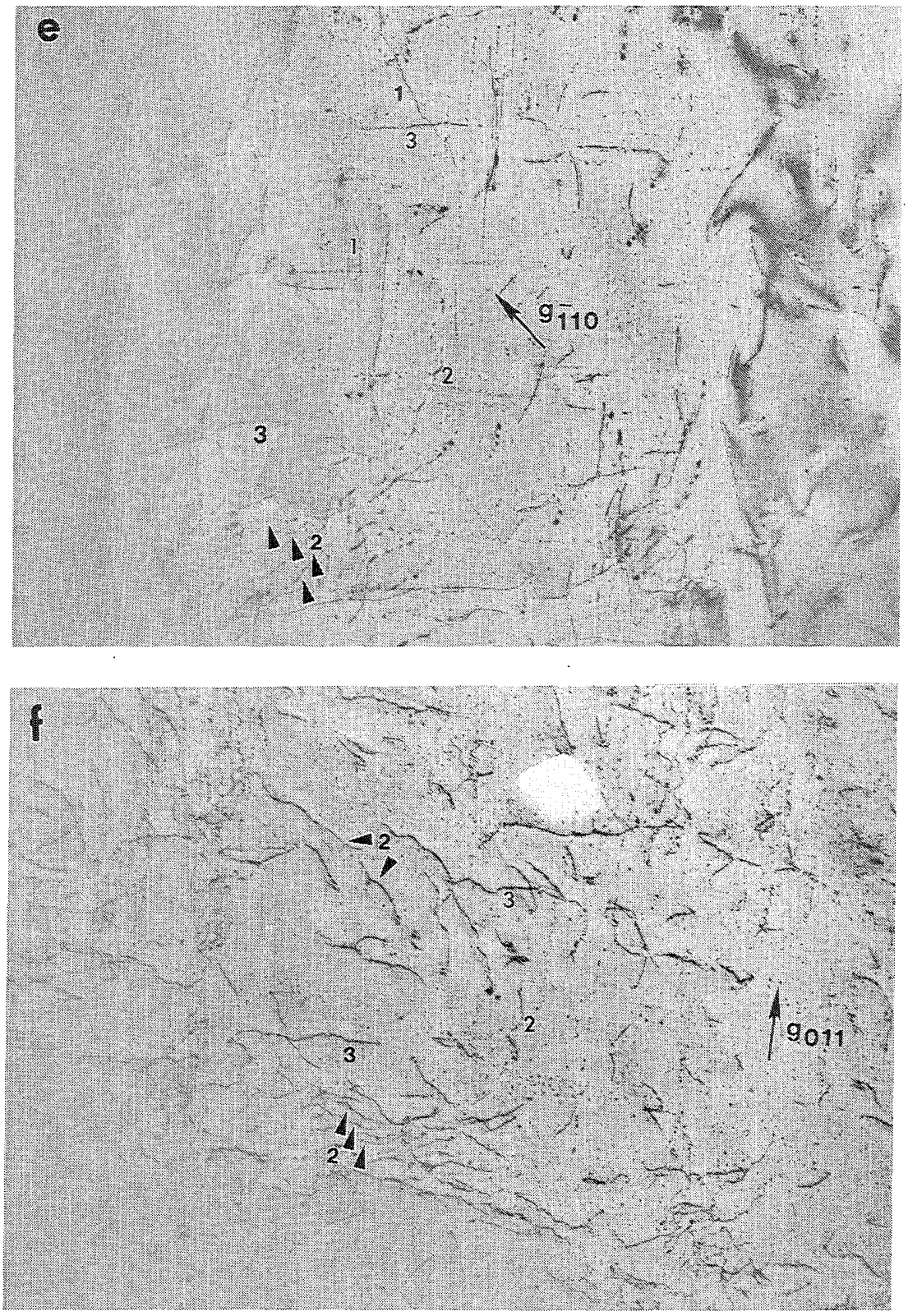

Figure 89(cont.). Typical dislocation structure for [001] D176 deformed at 1300 K to 2.0% plastic strain. a) general area of analysis, and (b-f) corresponding dislocation g•b analysis of the area with: b) g010, c) g100, d) g110, e) g$\bar{1}$10, and f) g011.

invisible with g010 (Figure 89b), whereas those of type 3 were invisible with g100 (Figure 89c). Both dislocations of type 1 and 3 were strongly visible with g110 (Figure 89d and gI10 (Figure 89e). Set 2 on the other hand showed a weak residual contrast with all the reflections in the [001] zone-axis, e.g. g100, g010, g110 and gI10, but a strong contrast with g011 (Figure 89f). Dislocations of type 1 were invisible whereas those of set 3 were visible with g011. These observations suggest that dislocations of type 1 had b = [100], type 2 were b = [001] and those of type 3 had b = [010]. The dislocations were frequently pinned by the G-phase precipitates causing a wavy appearance but it was still possible to determine an average line direction and therefore, determination of the plane in which the dislocations reside. Dislocations of type 1 had an overall line direction of [010] on (001), type 3 had a line direction of [100] on (001), and type 2 exhibited line directions of [110], [I10] and [010] on (I10), (110) and (100) planes respectively

While the post-deformation microstructure consists almost entirely of <100> edge dislocation segments, deformation probably occurs by a combination of <110> glide as in region II, in combination with non-conservative motion of the <100> dislocations. The temperature in this region is apparently high enough to cause the decomposition of <110> dislocations into two <100> segments leaving behind only indirect evidence for their operation. For example, with a [001] loading direction b = [001] dislocations would be expected to multiply by climb mechanisms. Therefore, climb of [001] dislocations would explain their high density within the crystal and provide an additional mechanism for accommodating the applied strain on the sample. However, [100] and [010] dislocations both have a near zero applied shear stress and climb force due to the applied stress (although a climb force could exist on these dislocations if a large point defect gradient were present). Therefore, there would be little reason to expect these dislocations in the high density that they were observed. However, if deformation also proceeded by <110> slip, by for example both [011] and [101] dislocations, as was observed in region II, then their eventual decomposition into <100> dislocations would result in all three Burger's vectors, i.e. b = [001], [010], and [100], which were in fact observed in the as-deformed microstructure. Therefore, deformation in region III occurs by a combination of <110> slip and non-conservative motion of <100> dislocations.

3.13.2.5.2 <011> Orientation

Region I (T= 300 - 1250 K): A sharp demarcation between the various deformation regimes as determined from the Arrhenius plot of yield strength does not exist for <011> D176 (Fig. 82) as was the case for the <001> orientation (Fig. 81). Therefore, for simplicity, all <011> samples deformed below about 1250 K will be classified as belonging to region I even though this also includes samples in the transition area between regions I and II. Samples deformed above 1250 K will be classified as belonging solely to region II. The reason for this distinction will be clear by the end of this section.

TEM analysis was performed on two [011] D176 samples tested at the low temperature end of region I. These were deformed at room temperature and 400 K and the representative dislocation structures at these temperatures are shown in Figures 90a and 90b, respectively. At room temperature, the sample was deformed to 0.3% plastic strain and deformation was confined to well defined slip bands. In most regions these bands ran along the [100] direction, parallel to the traces

of edge-on (01I) planes in the [011] zone-axis, as shown in Figure 90a. Each band contained numerous dislocations and some elongated loops (indicated by arrows), both of which were clearly visible in the [111] zone-axis image, shown in Figure 91a. A g•b analysis of the region shown in Figure 91a was performed and it was found that both dislocations and loops disappeared with the operating reflections g100 (Figure 91b), g10I (Figure 91c), and g101 (Figure 91d) but were strongly visible with g01I (Figure 91e), g020 (Figure 91f) and g110. These observations indicate that the Burgers vector of the dislocations and loops was b = [010]. The loops were small but appeared to form on {110} planes inclined 45° to their Burgers vector. The dislocations were frequently pinned by the G-phase precipitates causing them to be wavy in nature, but most had an average line direction of [010], suggesting that they were of near screw orientation.

The [011] sample tested at 400 K was deformed to a much greater strain, 1.3%. Similar to the sample deformed at room temperature, this sample also contained slip bands, which were wider and more closely spaced due to the greater strain on the sample (Fig. 90(b)). In fact, the sample was almost completely filled with bands containing a high density of dislocations after this relatively small strain indicating that the average mobility of individual dislocations was extremely low. The bands were aligned along the [100] direction in the [011] zone-axis. In this case, dislocation analysis indicated that the Burgers vector was b = [001] and trace analysis of the bands indicated that the dislocations were gliding predominantly on the (010) plane. The dislocations were generally small and curved but a large fraction of the dislocations had an overall line direction of [001], again indicating that they were of near screw orientation. However, [001] mixed and edge dislocations were also present in the microstructure. Again, the [001] loops were prismatic in nature and formed on the inclined {011} planes.

Thus, in <011> NiAl alloy D176, deformation in region I occurs by <010> dislocations, gliding predominantly on {001} planes. This is similar to the slip system observed in high purity <011> oriented binary NiAl single crystals presented elsewhere in this report, and to previous observations by Field et al. [21] for conventional purity NiAl single crystals tested at room temperature. The major difference, in the deformation behavior between <011> binary NiAl and <011> alloy D176 is the amount of cross-slip that <100> dislocations undergo. In binary NiAl cross-slip is very dominant even at room temperature and therefore, deformation does not proceed by well defined slip bands. In alloy D176 deformed in region I, slip is much more planar with cross-slip of screw dislocations contributing significantly less to the overall deformation of the crystals as compared to binary NiAl alloys.

TEM analysis was also performed on two [011] D176 samples deformed near the high temperature end of region I. Representative microstructures from these samples deformed to approximately 2% strain at 1000 and 1144 K are shown in Figure 92a and 92b, respectively. Both samples contained a high density of dislocations mostly in the form of loops or dense tangles. Detailed dislocation analysis on the sample deformed at 1000 K indicated that these dislocations and loops were invisible with g200 (Figure 93 a, and g020 (Figure 93c), but were strongly visible with g01I (Figure 93b, g002 (Figure 93d), and g101 (Figure 93e), indicating that their Burgers vector was b = [001]. The dislocations were again wavy, but there were very few dislocations present with an average line direction near [001]. Instead, many of the dislocations had an average line direction of [100], suggesting that the observed dislocations were [001] edge dislocations or

prismatic loops. A view of the (010) slip plane is shown in Figure 93f, where it was observed that [001] screw dislocations were rarely seen. However, one such dislocation in the process of leaving a [001] loop pinned by a relatively large G-phase precipitate was observed and marked with an arrow in the same figure. The presence of a large number of elongated loops, which are believed to be debris left behind by cross-slipping screw dislocations [21], and the lack of screw segments in the deformed microstructure indicate that screw dislocations are extremely mobile at these temperatures and can readily avoid being pinned by G-phase by cross-slipping around these obstacles.

Consequently, throughout the deformation regime defined as region I, deformation occurs by glide of <010> dislocations on {001} planes. However, slip is planar at the low temperature end of this regime with cross-slip becoming significant only at the high temperature end. The enhanced contribution to deformation by cross-slip of screw dislocations probably accounts for the smooth bend in the Arrhenius plot of yield strength for <011> oriented D176 crystals before the onset of region II.

Region II (T > 1250 K): TEM was performed on [011] samples deformed at 1255 and 1300 K in region II. Typical microstructures for these samples deformed to approximately 2% strain are shown in Figures 94 and 95. The first thing that becomes immediately apparent in these micrographs is the relatively low dislocation density that is retained during deformation in region II compared to deformation in region I. This indicates that significant recovery is occurring during deformation in this regime. In other words, thermally activated deformation or dislocation climb is a dominant deformation mechanism at these temperatures.

Detailed dislocation analysis of the [011] sample deformed at 1300 K indicated that there were two types of dislocations present in the microstructure, marked "A" and "B" in Figure 95a, which is a BF image close to the [111] zone-axis. Dislocations of type "A" were strongly visible and type "B" were weakly visible with g1$\bar{1}$0 (Figure 95b) and g020 (Figure 95c), whereas dislocations of type "B" were strongly visible (arrows) and type "A" were weakly visible with g10$\bar{1}$ (Figure 95d). Dislocations of type "A" completely disappeared with the operating reflection g100 (Figure 95e), whereas those of type "B" showed a weak residual contrast. Both types of dislocations were strongly visible with g01$\bar{1}$ (Figure 95f). These observations indicated that the Burgers vector of dislocations of type "A" was b = [010] and that of type "B" was b = [001]. Trace analysis indicated that the average line direction of most of the dislocations of type "A" was [100] and, thus, they were predominantly edge segments, while dislocations of type "B" had a mixed character. These observations are consistent with theoretical calculations by Glatzel et al. [45], which predict that a high energy and negative line tension of <001> screw dislocations should make them unstable at high temperatures. Figures 95b,d, provide an estimate of the proportion of type "A" and "B" dislocations respectively, which contribute to deformation at 1300 K.

Overall, in region II, deformation of <011> oriented D176 occurs by <001> dislocations. Glide still occurs on {001} planes but a significant contribution to the deformation of these single crystals occurs by climb of edge segments. Consequently, the difference between region I and region II is the significant contribution of <001> climb to the deformation of the <011> crystals.

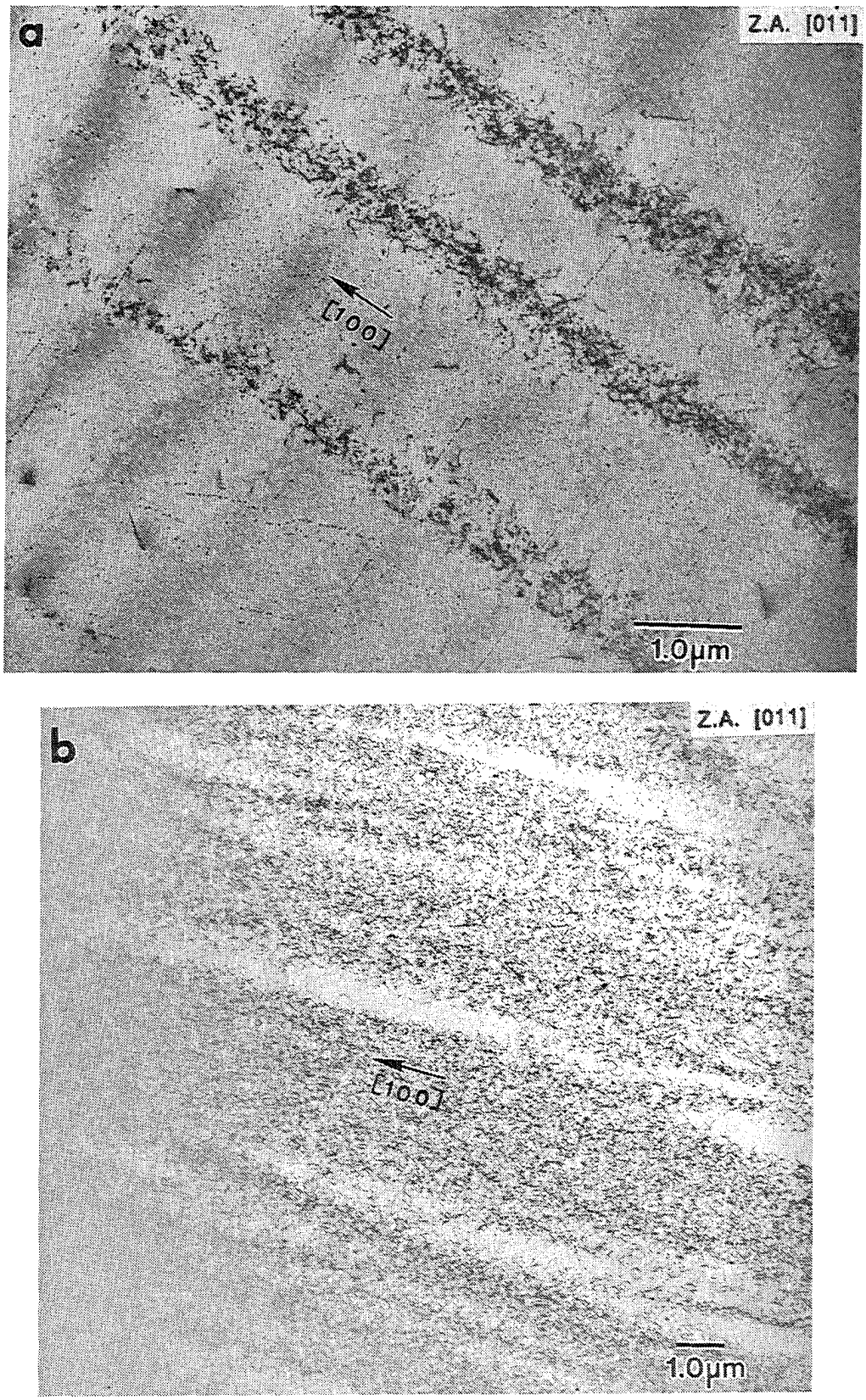

Figure 90. Dislocation structure in [011] D176 samples deformed in Region I. a) deformed at room temperature to 0.3% plastic strain and b) deformed at 400 K to 1.3% plastic strain.

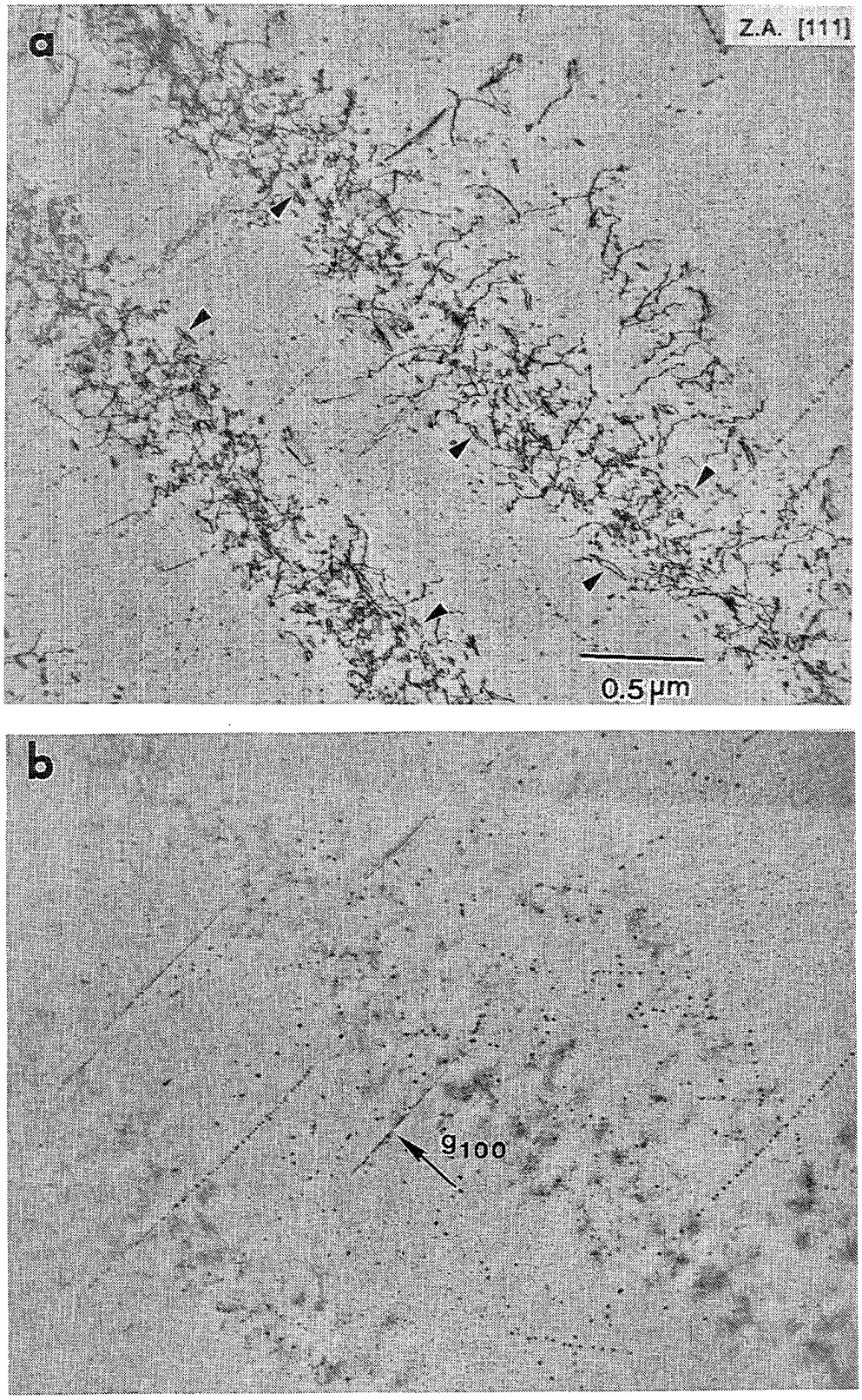

Figure 91. Dislocation g•b analysis of the [011] D176 sample tested at room temperature with: a) Z.A. [111], b) g100, c) g10I, d) g101, e) g01I, and f) g020. Arrows in (a) show the dislocation loops.

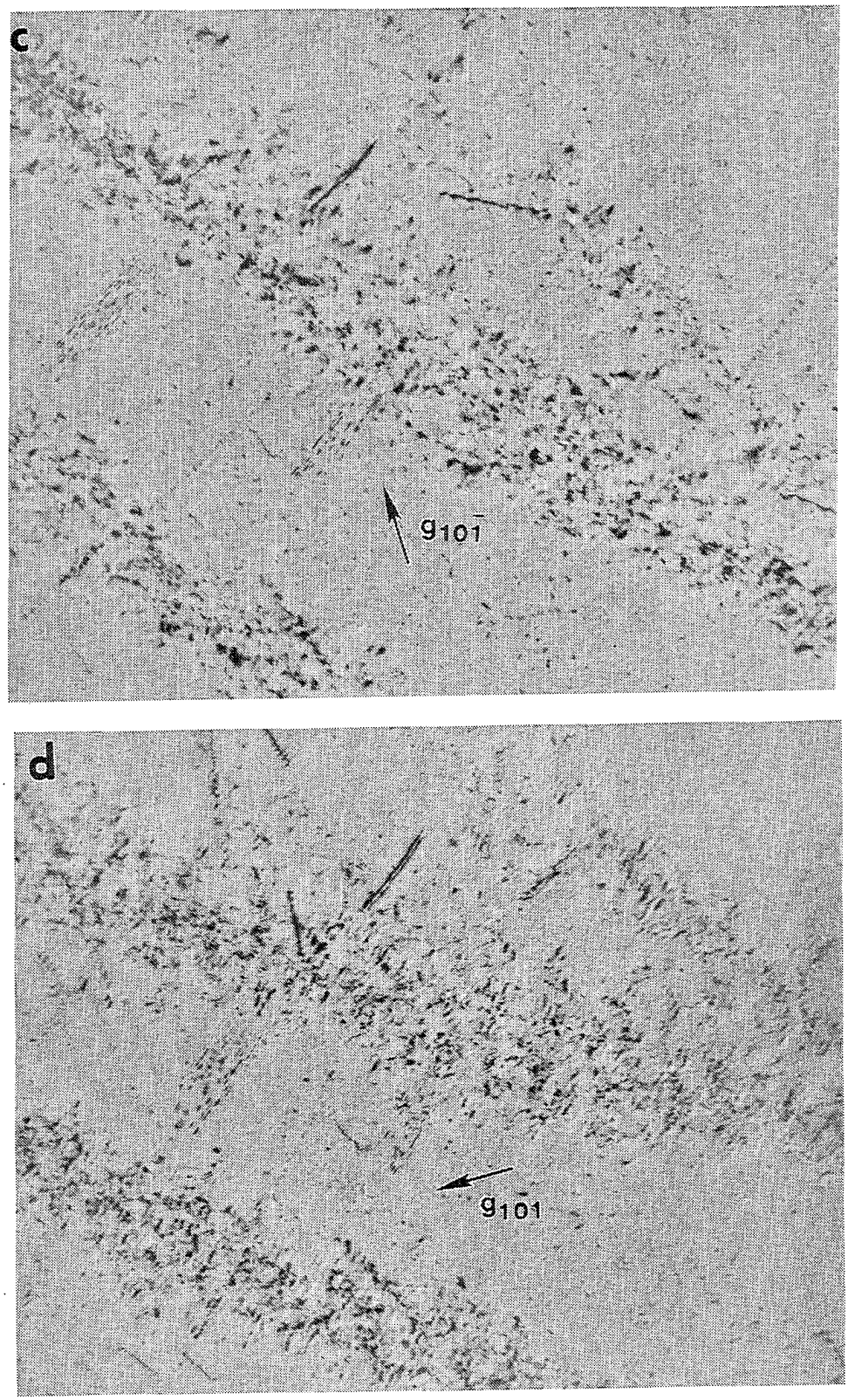

Figure 91(cont.). Dislocation g•b analysis of the [011] D176 sample tested at room temperature with: a) Z.A. [111], b) g100, c) g10I, d) g101, e) g01I, and f) g020. Arrows in (a) show the dislocation loops.

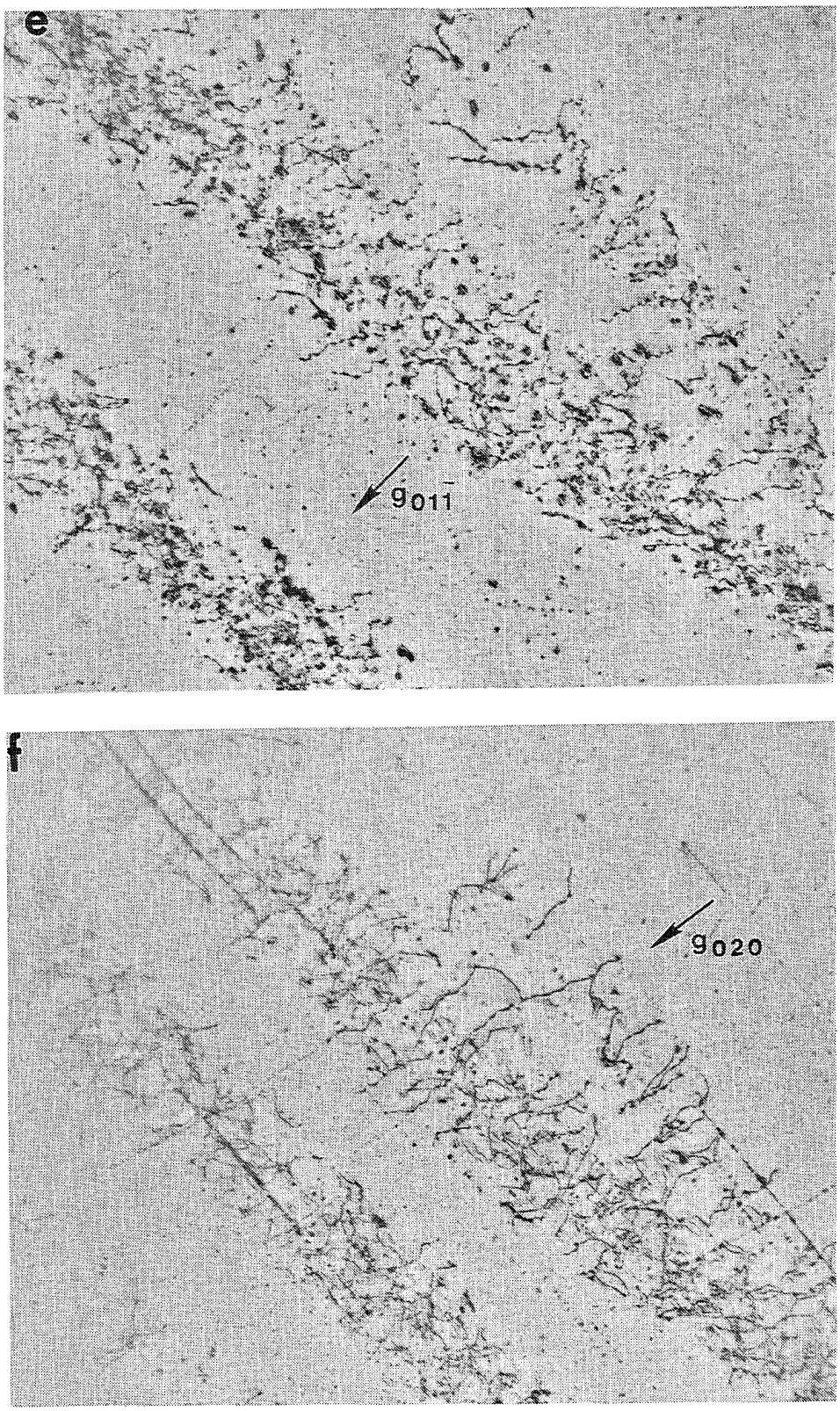

Figure 91(cont.). Dislocation g•b analysis of the [011] D176 sample tested at room temperature with: a) Z.A. [111], b) g100, c) g10I, d) g101, e) g01I, and f) g020. Arrows in (a) show the dislocation loops.

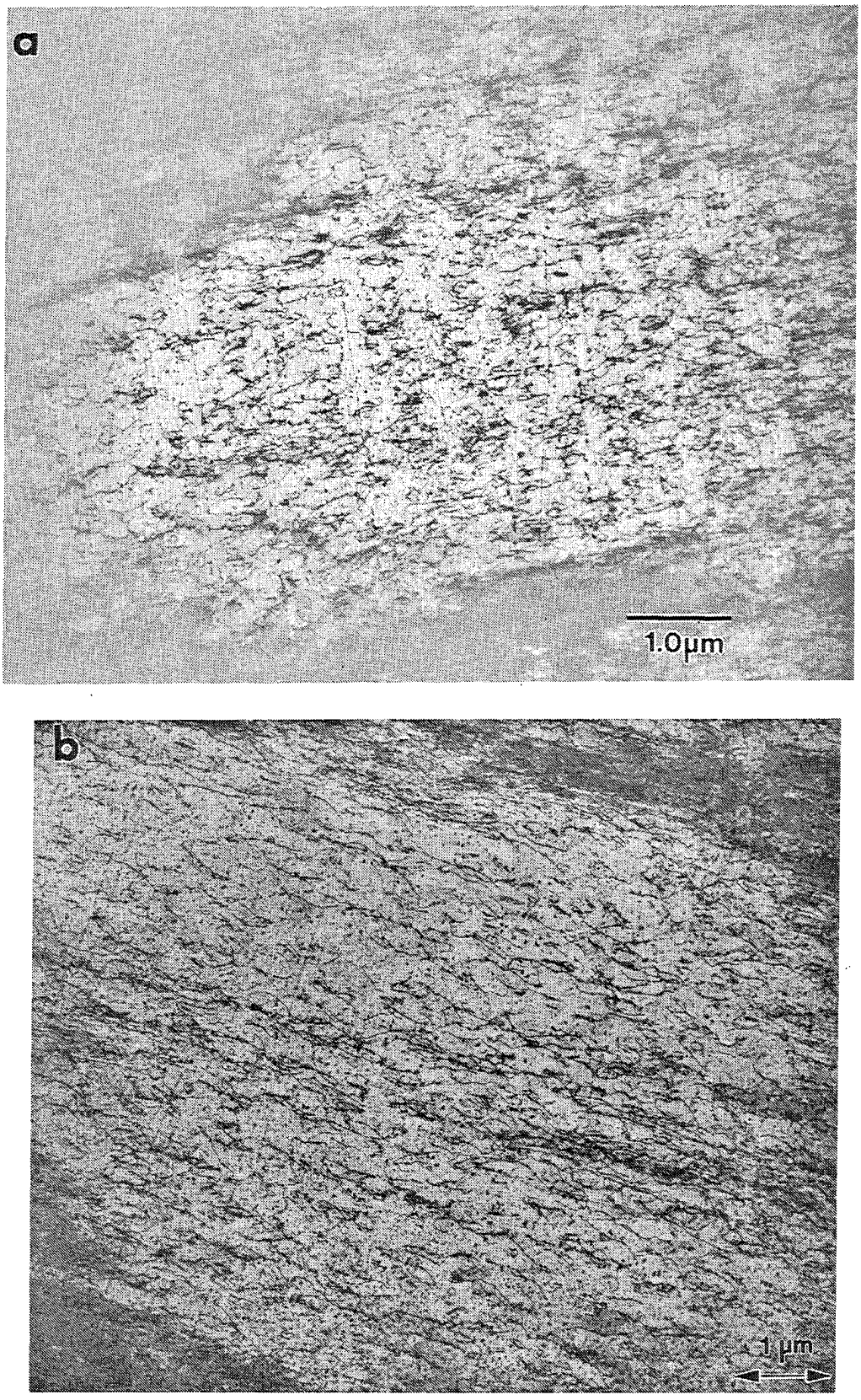

Figure 92. Dislocation structure in [011] D176 sample deformed at a) 1000 K and b) 1144 K. Both samples were deformed to approximately 2% plastic strain toward the end of region I.

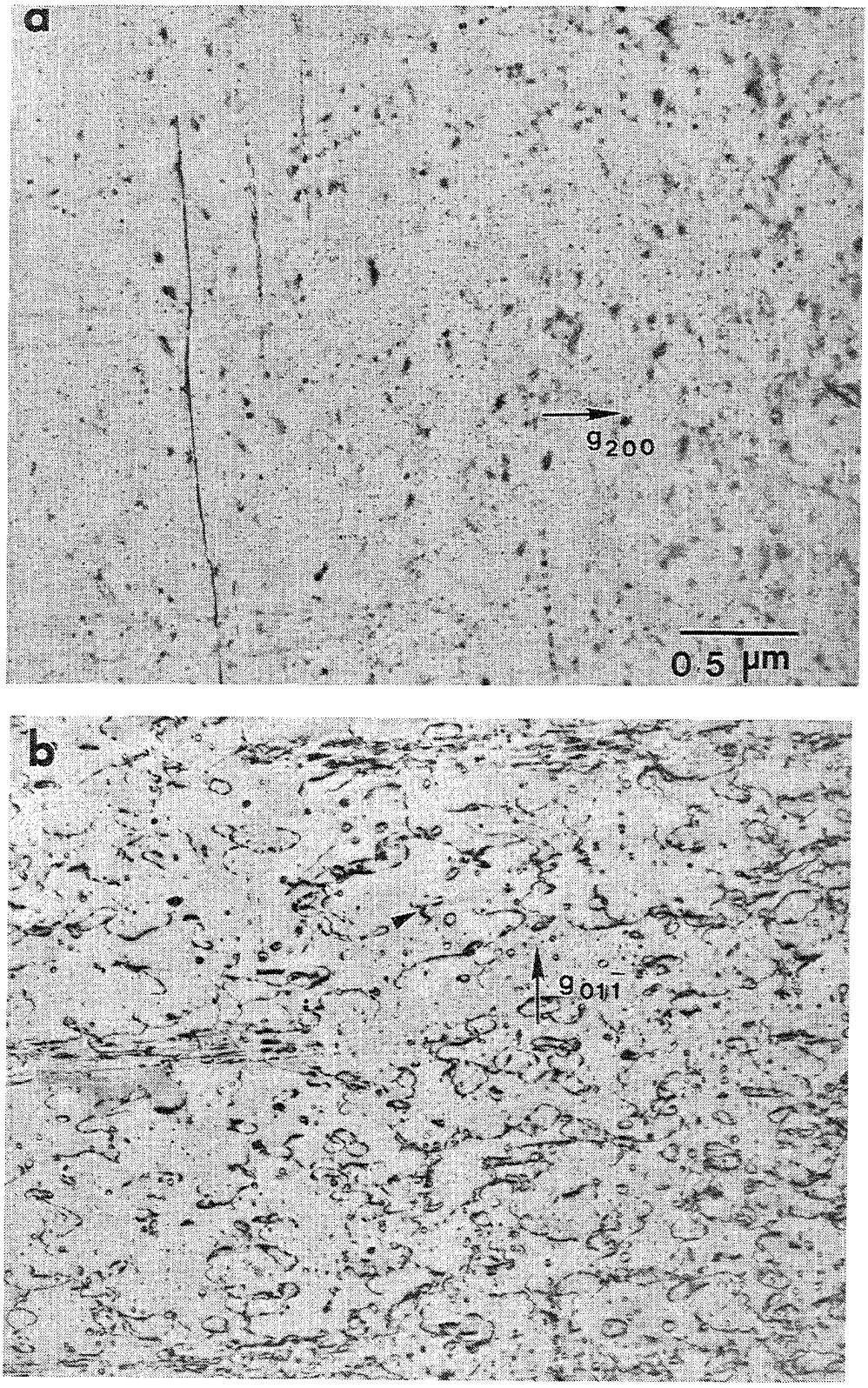

Figure 93. Dislocation g•b analysis for the [011] D176 sample tested at 1000 K with: a) g200, b) g01I, c) g020, d) g002, e) gI01. (f) shows the view of the (010) slip plane and arrow in (b, f) shows the formation of a dislocation loop by cross-slip of a screw dislocation.

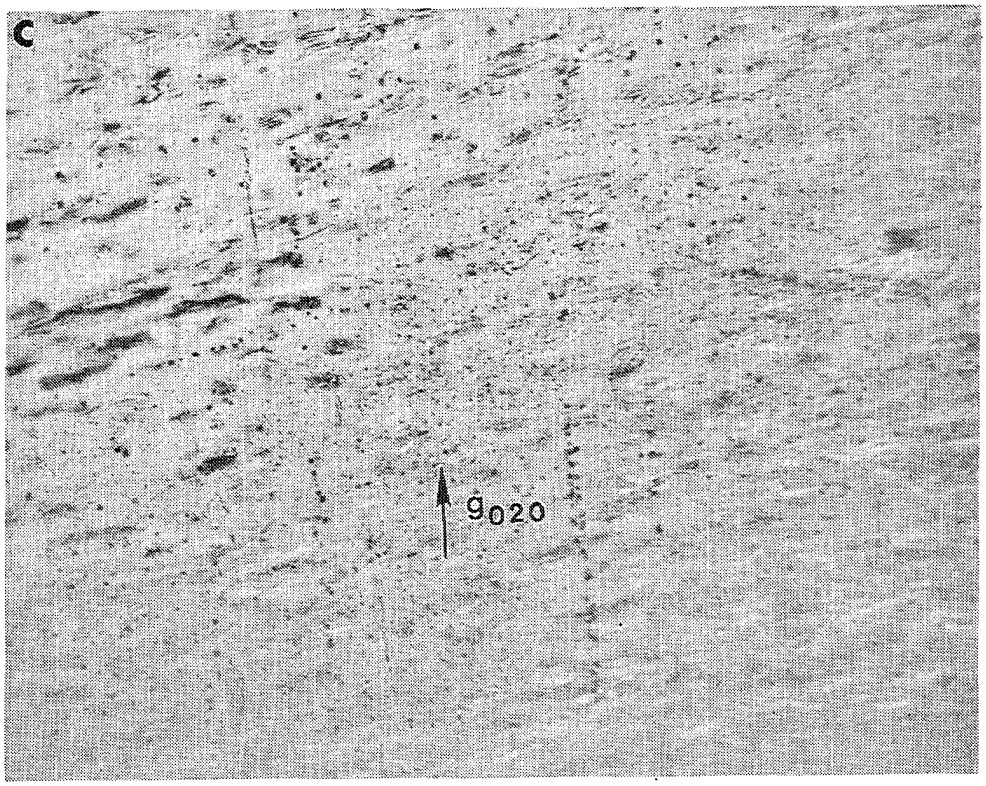

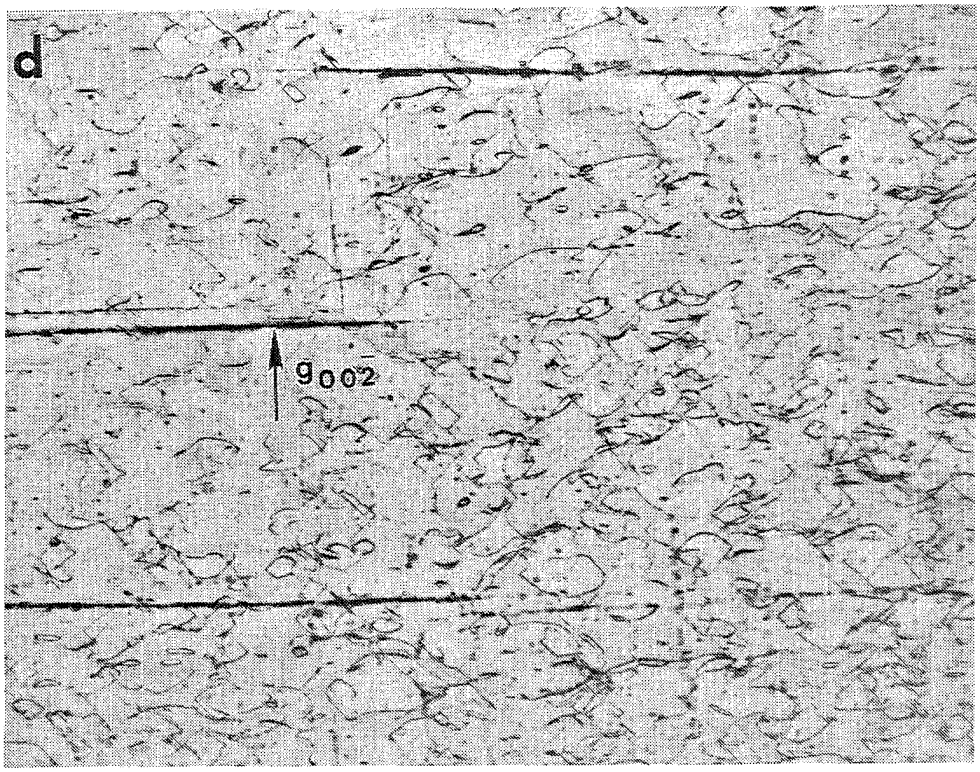

Figure 93(cont.). Dislocation g•b analysis for the [011] D176 sample tested at 1000 K with: a) g200, b) g01I, c) g020, d) g002, e) gI01. (f) shows the view of the (010) slip plane and arrow in (b, f) shows the formation of a dislocation loop by cross-slip of a screw dislocation.

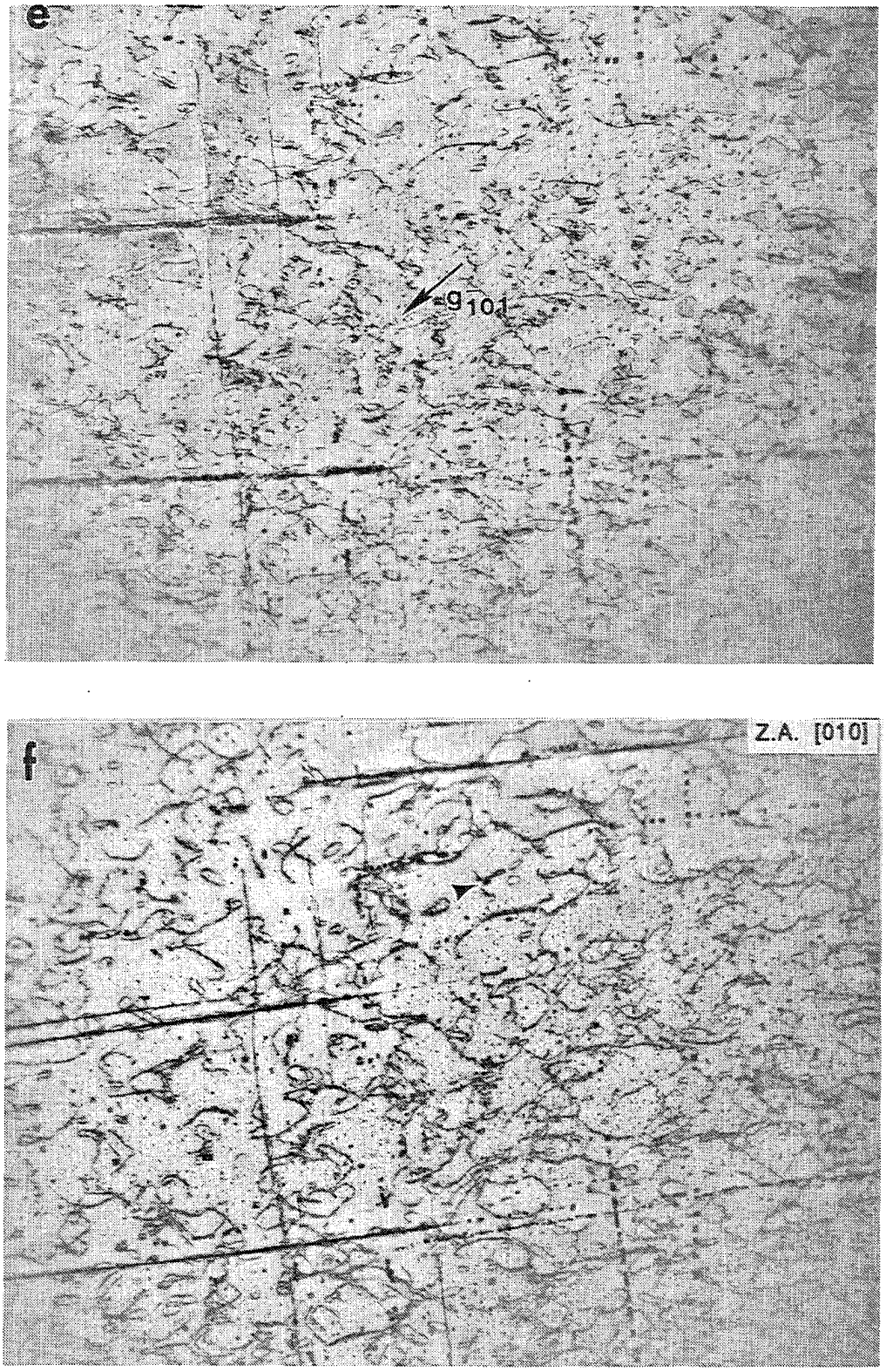

Figure 93(cont.). Dislocation g•b analysis for the [011] D176 sample tested at 1000 K with: a) g200, b) g01I, c) g020, d) g002, e) gI01. (f) shows the view of the (010) slip plane and arrow in (b, f) shows the formation of a dislocation loop by cross-slip of a screw dislocation.

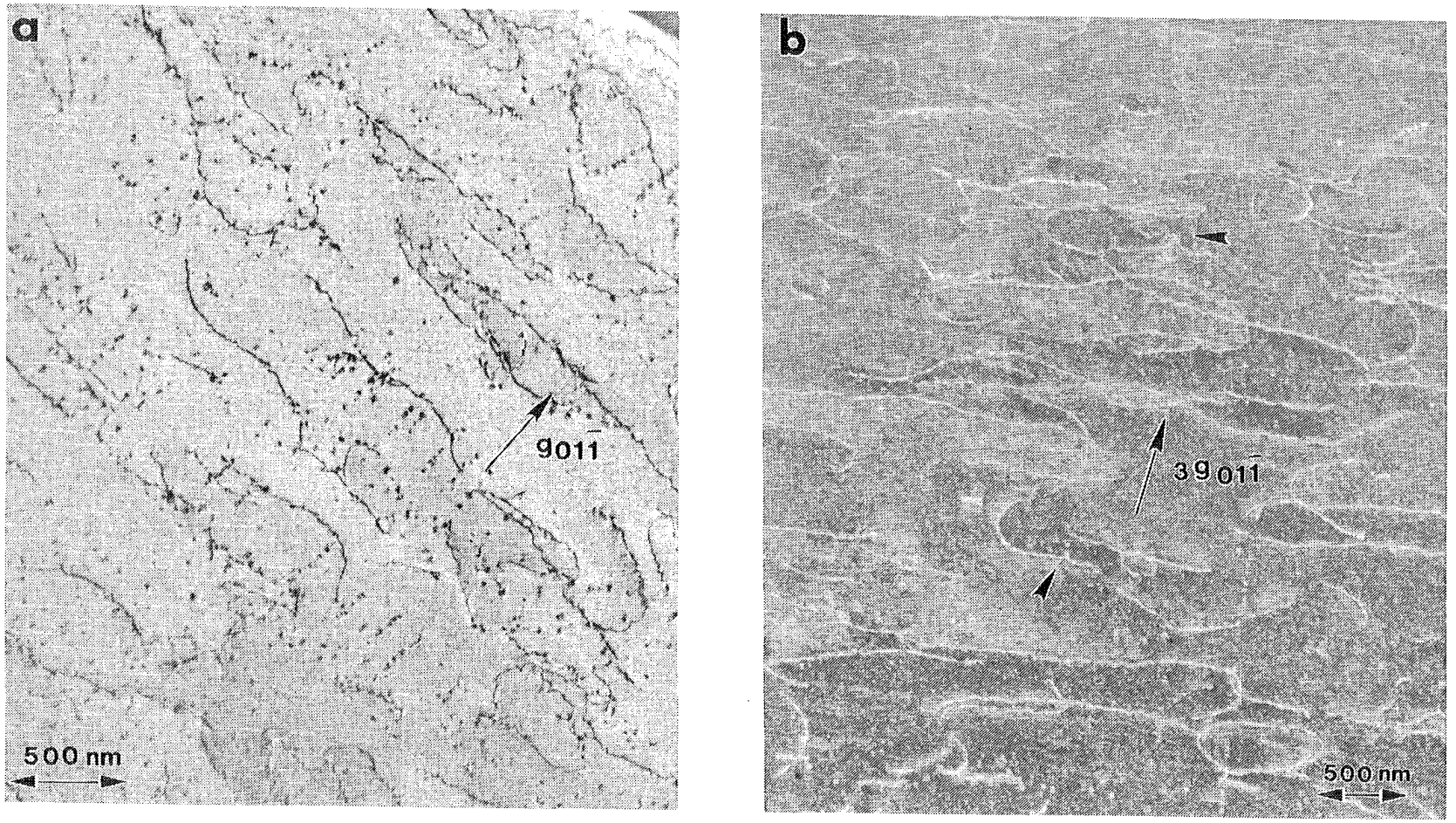

Figure 94. Dislocation structure of [011] D176 deformed at 1255 K to approximately 2% strain. a) BF micrograph showing the overall low dislocation density retained at this temperature and b) WBDF micrograph showing edge dislocations bypassing G-phase particles by Orowan looping.

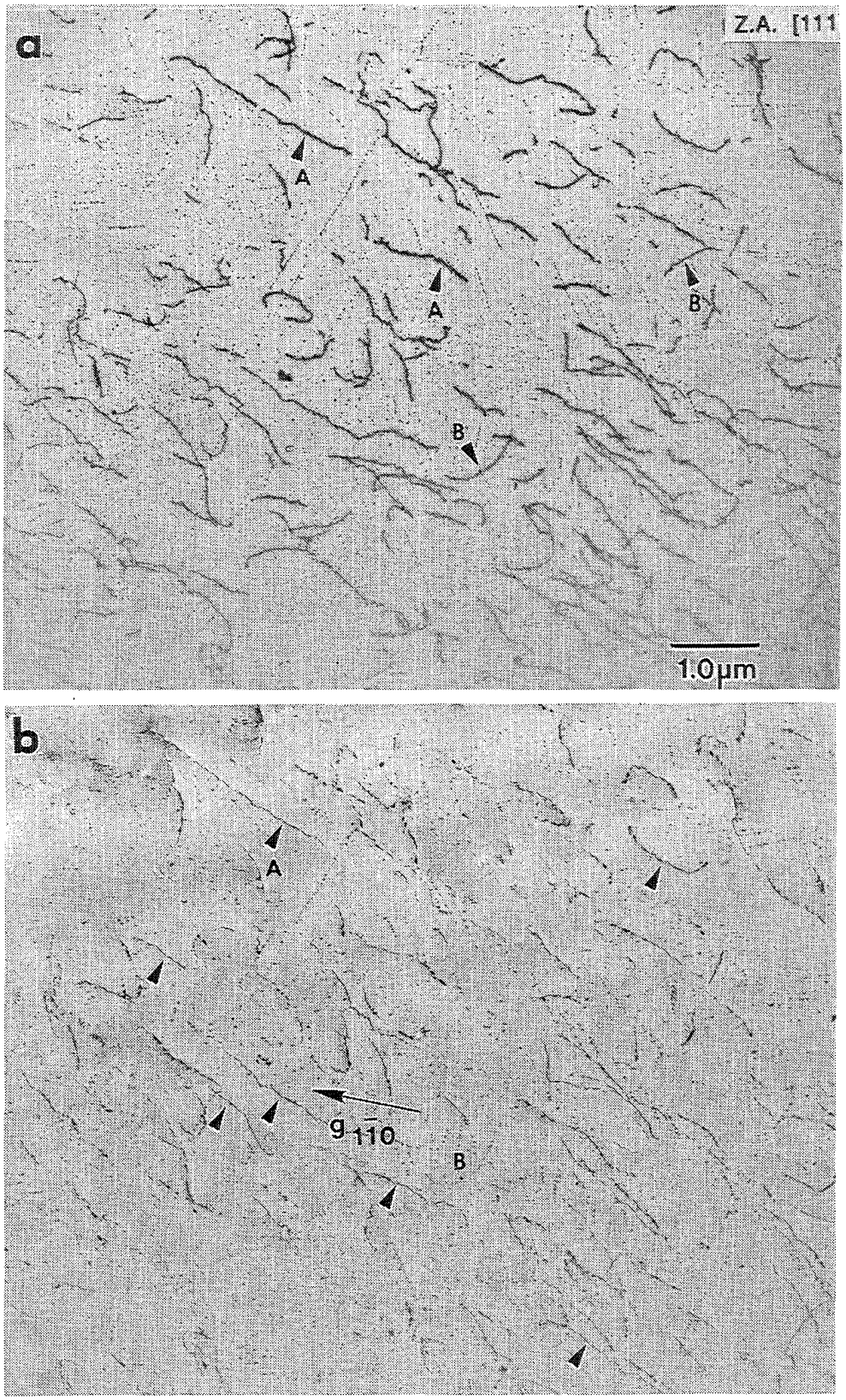

Figure 95. Typical dislocation structure and (b-f) g.b analysis with: b) g1I0, c) g020, d) g10I, e) g100, and f) g01I for the [011] D176 sample deformed at 1300 K to 2% strain. Unmarked arrows in (b, d) denote dislocations of type "B" and "A", respectively.

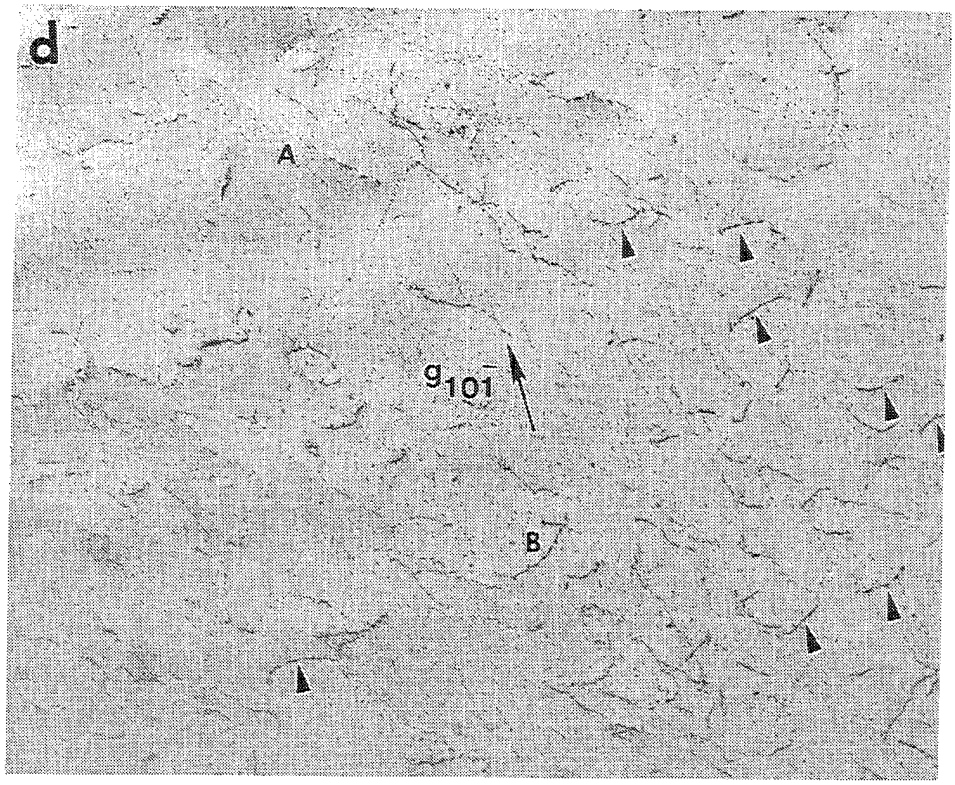

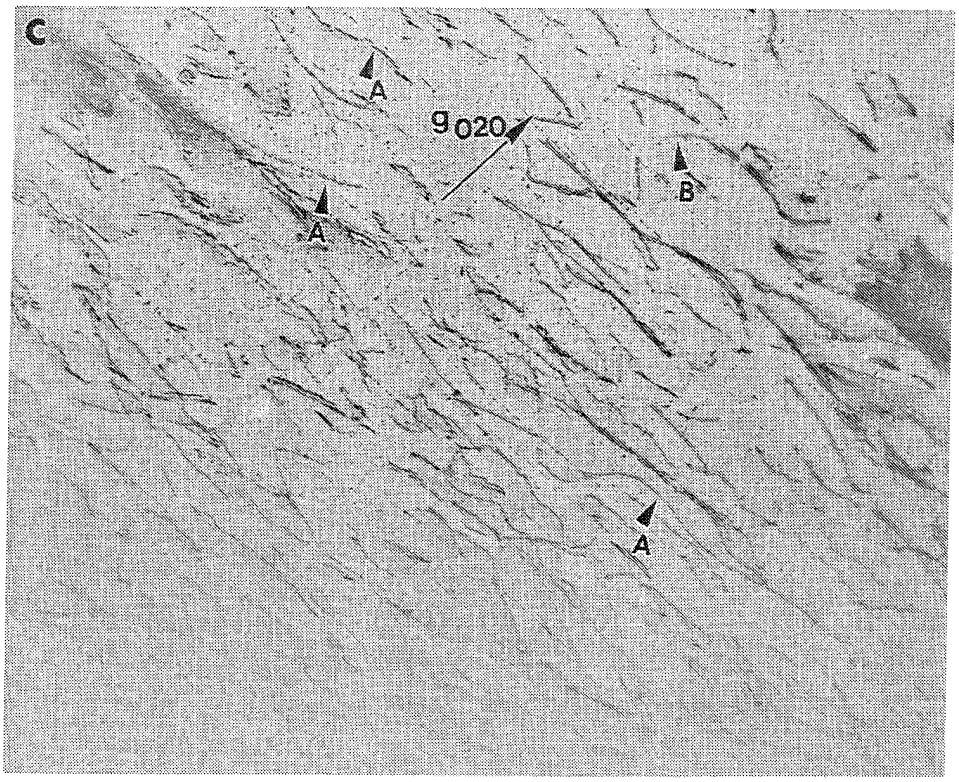

Figure 95(cont.). Typical dislocation structure and (b-f) g.b analysis with: b) g1$\bar{1}$0, c) g020, d) g10$\bar{1}$, e) g100, and f) g01$\bar{1}$ for the [011] D176 sample deformed at 1300 K to 2% strain. Unmarked arrows in (b, d) denote dislocations of type "B" and "A", respectively.

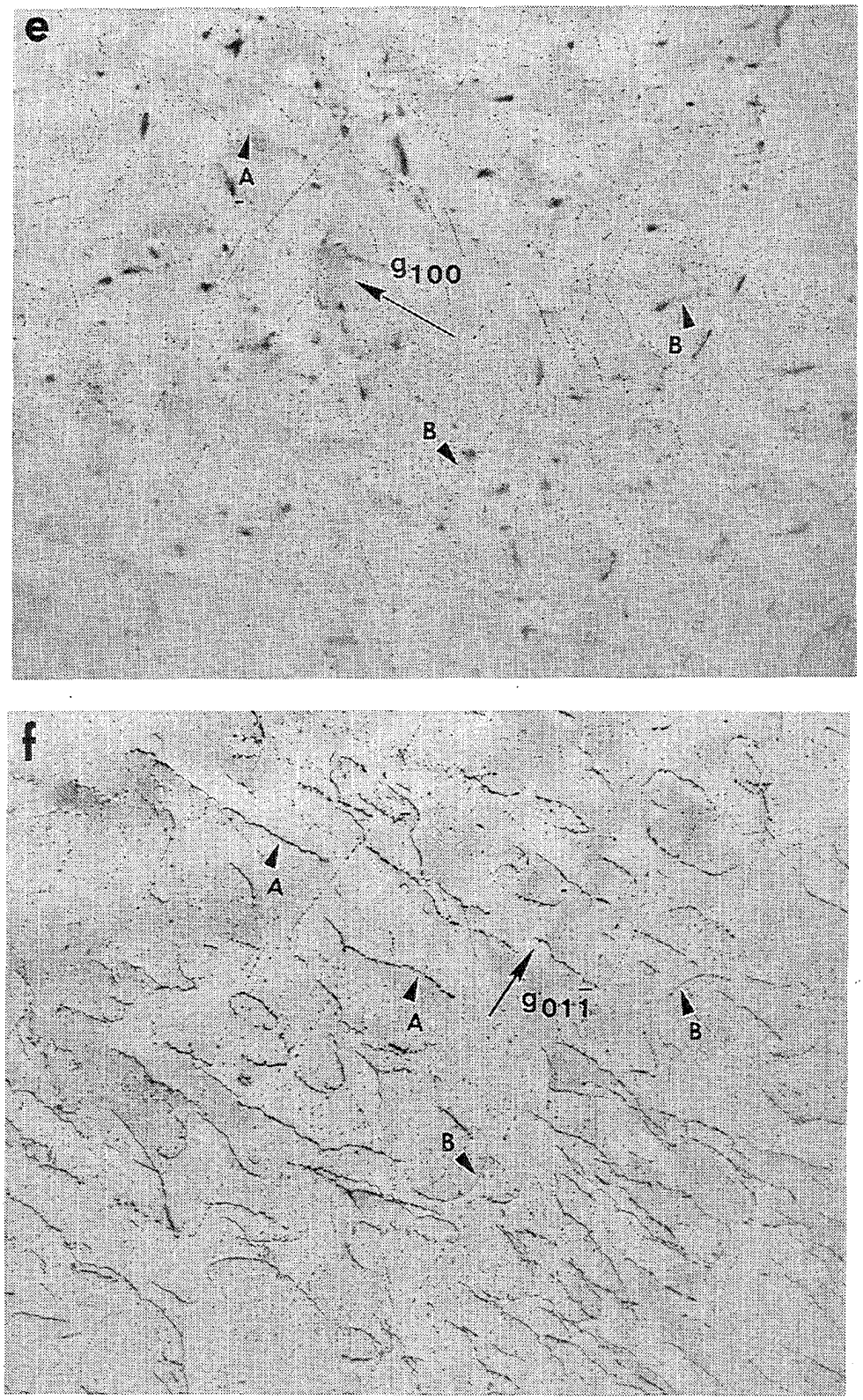

Figure 95(cont.). Typical dislocation structure and (b-f) g.b analysis with: b) g1$\bar{1}$0, c) g020, d) g10$\bar{1}$, e) g100, and f) g011 for the [011] D176 sample deformed at 1300 K to 2% strain. Unmarked arrows in (b, d) denote dislocations of type "B" and "A", respectively.

3.13.2.6 Deformation Mechanisms in Alloy D176 Versus Binary NiAl

The deformation of <001> binary NiAl [23,25,39,40,42,43,46,47] and alloy D176 are generally similar in that <111>, <110>, and <100> dislocations are observed in both types of deformed crystals over various temperature ranges. But there are also important differences in the behavior between binary NiAl and alloy D176. This is apparent by comparing Figures 96 and 97 which are the Arrhenius plots of the alloy D176 and binary NiAl data, respectively, from Fig. 80. The <001> binary NiAl exhibits only two predominant deformation regimes while <001> D176 displays three distinct deformation regimes.

The deformation behavior of binary NiAl and alloy D176 are most similar in region I. In this region, deformation of both materials is controlled by slip of <111> dislocations on {112} planes. The flow stress of the D176 alloy is only slightly higher than that of the binary NiAl (~1450 MPa vs. ~1650 MPa), indicating that a high lattice resistance to glide of <111> dislocations is the most significant strengthening mechanism at low temperatures in <001> NiAl. This is in contrast to <011> crystals where the alloying additions in alloy D176 result in a 500% increase in yield strength compared to binary NiAl over most temperatures. Furthermore, the temperature at which Region I ends in <001> crystals is also similar, 600 K for binary NiAl and 650 K for alloy D176. Therefore, the overall effect of Hf on the deformation of <001> crystals in region I is relatively negligible.

Beyond region I, the deformation behavior of binary NiAl and alloy D176 deviate significantly. In binary NiAl, deformation proceeds from the regime dominated by <111> slip directly to a regime where predominantly <100> dislocation debris is observed with an occasional observation of <110> dislocation segments [24, 25,39,46]. It is believed that <110> slip is operative during the deformation of <001> binary NiAl single crystals at these intermediate and high temperatures in addition to a significant contribution by climb of <001> dislocations. However, direct evidence for <110> dislocations in the deformed microstructure of binary NiAl is very rare. Usually all that remains in the post-deformed microstructure is <100> dislocations and debris and an occasional <110> segment [25,42]. The only direct observation of <110> slip is in a non-stoichiometric Ni-48Al single crystal by Kim and Gibala [46] who observed deformation at 800K occurring almost entirely by <110> dislocations, but with the percentage of <110> dislocations decreasing significantly at higher temperatures. Regardless of whether the observations are indirect or direct, it is generally agreed that <110> slip participates in the intermediate and high temperature deformation behavior of binary NiAl [24,25,42,43,46] However, this type of deformation behavior in binary NiAl is most comparable to region III behavior in the D176 alloy.

In alloy D176, <110> dislocations were observed directly in the microstructure over an appreciable temperature range (650-1100 K, i.e. region II). This provides direct evidence that the elevated-temperature deformation of <001> NiAl single crystals does occur by the activation of one or more {101}<101> slip systems. There is little evidence of deformation in this regime by <100> dislocations since the only <100> dislocations present in the microstructure were prismatic loops left behind as debris by moving <110> dislocations. This is in sharp contrast to region III where significant deformation occurs by <100> dislocations.

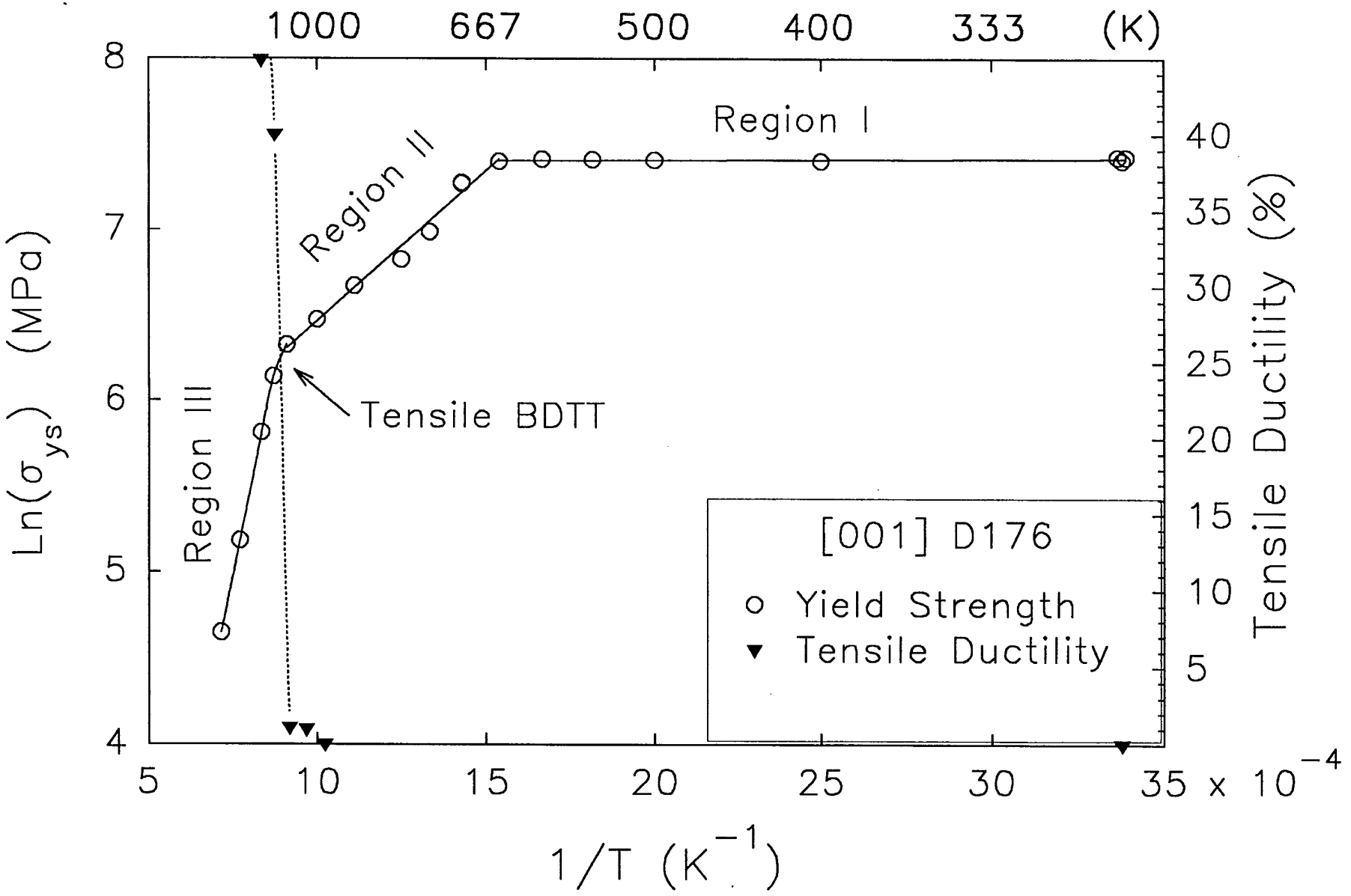

Figure 96. Correspondence of the tensile DBTT with the onset of region III deformation behavior for [001] oriented NiAl alloy D176.

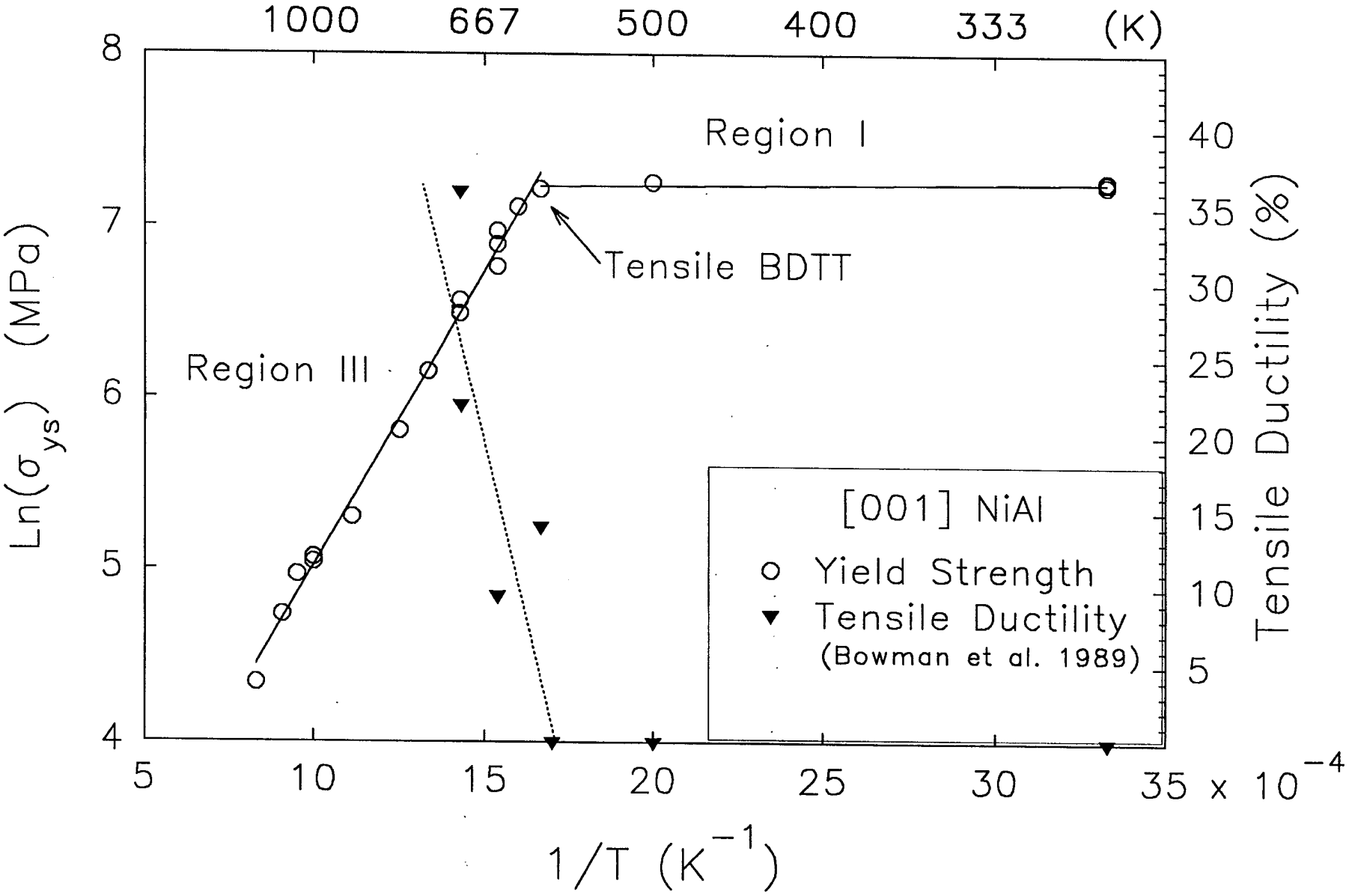

Figure 97. Observation of two distinct deformation regimes in binary NiAl and the correspondence of the tensile DBTT with the onset of region III deformation behavior for <001> oriented binary NiAl. Note that binary <001> NiAl does not exhibit a region II behavior as does alloy D176.

Therefore, the major difference between binary NiAl and alloy D176 is that the intermediate deformation regime present in alloy D176 (i.e. region II) where <110> slip alone dominates is missing in binary NiAl. Consequently, binary NiAl displays only two major deformation regimes; region I where <111> slip dominates and region III where both glide of <110> and climb of <100> dislocations occur. Alloy D176 is unique in that it also contains an appreciable deformation regime (i.e. region II) where only glide of <110> dislocations dominate the deformation behavior of the alloy. These observations suggest that the Hf addition in NiAl stabilizes the core structure of <110> dislocations in the temperature range of 650-1100 K and that more energy (higher temperature) is needed to decompose the <110> dislocations into two <100> dislocations in alloy D176 compared to binary NiAl. The unique deformation regime (region II) in alloy D176 arises as a result of this stabilization of <110> dislocations in the microstructure and shifts region III behavior, which occurs at approximately 600 K in binary NiAl, to over 1100 K in the Hf-alloyed NiAl.

In the <011> orientation, the major difference between the deformation behavior of binary NiAl and alloy D176 is the temperature that dislocation climb can readily occur in each of these crystals. Climb of <001> dislocations is thought to be significant in soft-oriented single crystals of binary NiAl at temperatures as low as 500 K and is associated with the DBTT in these materials [48]. In D176 crystals significant dislocation climb does not occur until temperatures greater than approximately 1250 K. Apart from this, the basic deformation mechanisms, <001>{010}, are the same in binary NiAl and alloy D176. The consequence of retarding climb processes until much higher temperatures is discussed in the following section.

3.13.2.7 Correlation of Deformation Behavior with the DBTT

Figures 96-98 are comparisons of the Arrhenius yield stress plots with the tensile ductility of <001> alloy D176, <001> binary NiAl, and <011> alloy D176, respectively. For both alloy D176 and binary NiAl of <001> orientation, the transition from brittle to ductile behavior occurs exactly at the onset of region III deformation behavior. Therefore, regardless of the alloy composition, tensile ductility does not become significant until the onset of thermally activated deformation processes in addition to the normal slip processes operating in <001> crystals. Change in deformation behavior from <111> slip to <110> slip by itself is not sufficient to induce ductility in the <001> D176 alloy, and in fact presents an even a worse case scenario in terms of total number of independent deformation mechanisms for relieving stress concentrations in the crystal. At least with <111> slip there are five independent slip systems for relieving stress gradients at defects in the material [49]. However, the flow stresses in these crystals are so high that fracture always intervenes before plastic deformation can occur in tensile samples tested in region I. With <110>{110} slip there are only 2 independent deformation mechanisms. Therefore, the additional deformation mechanisms provided by climb are needed to ensure compatible deformation at sites of stress concentration or at interfaces with interdendritic particles which are generally present in alloyed NiAl. In <001> D176, deformation by climb is retarded until temperatures approaching 1100 K due to the addition of 0.5% Hf to NiAl and consequently the DBTT is shifted by 500 K in temperature as well.

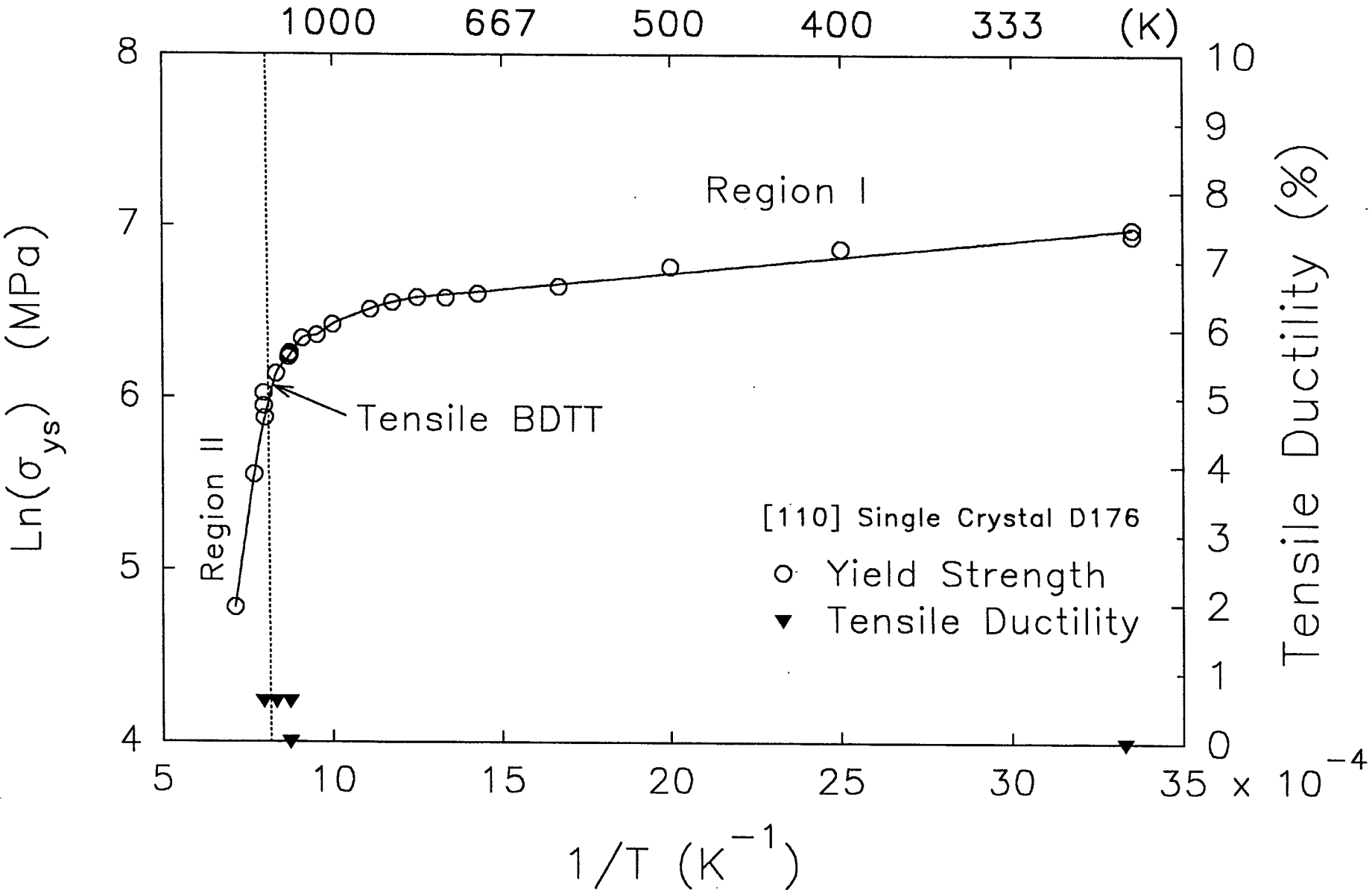

Figure 98. Correspondence of the tensile DBTT with the onset of region II deformation behavior for <011> oriented NiAl alloy D176.

The DBTT arises in <011> oriented samples for essentially the same reason. The DBTT for soft orientations of binary NiAl has been associated with the onset of dislocation climb processes at relatively low temperatures [47, 48]. Alloying with Hf has been shown in this study to inhibit the climb of <001> dislocations until temperatures greater than 1250 K, and subsequently the DBTT for D176 crystals is shifted accordingly (Fig. 98).

Alloying of polycrystalline NiAl has been shown to produce similar effects on the DBTT. Zr is extremely effective in retarding dislocation climb in polycrystalline NiAl and as a result increases the DBTT of polycrystalline material from 550 K to over 1050 K with the addition of only 0.1 at.% Zr [12, 14]. The DBTT corresponds to the onset of dislocation climb in polycrystalline NiAl or ternary alloys because <001> slip alone provides only three independent slip systems, whereas five are necessary to assure compatible deformation of a polycrystalline aggregate due to constraints across grain boundaries [50]. However, climb plus glide of <001> dislocations will account for five independent deformation mechanisms in NiAl [51] and thus fulfill the Von Mises criterion for compatible deformation of a polycrystalline aggregate resulting in ductile behavior [12]. The problem of compatible deformation across grain boundaries does not exist in single crystals. But, it is clear that the onset of thermally activated deformation processes still play a major role in the deformation and fracture of single crystal binary NiAl and its alloys. Thermally activated deformation processes are essential in the relaxation of stress concentrations that occur at surface disparities or internal defects such as pores, inclusions, or even brittle interdendritic phases (e.g. in alloyed NiAl). Dislocation glide alone, by either <100> or <110>, would not be sufficient to accommodate the complex stress states near these types of defects in single crystals. Therefore, single crystals like polycrystalline NiAl are dependent on the operation of thermally activated deformation processes before they can exhibit significant ductile behavior.

3.13.2.8 Effect of Pre-strain on the Deformation Behavior

With an understanding of the various deformation mechanisms in alloy D176, it is now possible to explain the effects of pre-strain on tensile ductility as shown in Figure 78. According to the figure, initial straining of <001> NiAl at 1366 K (2000 °F), which is inside region III, results in several percent tensile ductility when the sample is subsequently deformed anywhere in region II (temperatures as low as ~ 650 K). The initial pre-strain at 1366 K introduces a moderate density of <100> dislocations in the sample. When deformed in region II where <110> slip normally dominates, the <100> dislocations introduced by the pre-strain are apparently able to move by non-conservative processes such that the combined deformation by <110> slip and <100> climb is essentially the same as what takes place normally in region III, resulting in tensile ductility at these lower temperatures. However, the dislocations introduced by the pre-strain soon become exhausted after several percent strain, and deformation reverts back to being dominated solely by <110> slip which is insufficient to accommodate stress concentrations, resulting in brittle failure of the sample. While <100> dislocations introduced by the pre-strain are apparently able to climb at these lower temperatures (i.e., Region II), to be a viable deformation mechanism sources must also be able to nucleate additional <100> dislocations so that deformation can continue as dislocations slip out of the crystal or otherwise become immobilized. The major source for <100> dislocations in <001> crystals is the decomposition of the <110> dislocations. However, in alloy D176, <110> dislocations are stable in region II denying a source for <100>'s. Therefore, once

the original population of <100> dislocations, introduced by pre-strain in region III, become immobilized during testing in region II they no longer can contribute to deformation and brittle fracture then occurs as would normally be the situation in region II. This is also the reason why a larger pre-strain introduced in region III, as observed under the GEAE IRAD programs, produces relatively higher ductilities when the crystals are subsequently deformed in region II. Very simply, the number of <100> dislocations introduced into the sample will be greater at the greater pre-strain level permitting ductile behavior to proceed for a longer period of time. Although the Hf-addition is able to strengthen the alloy at high temperatures by solid-solution as well as precipitate hardening, unfortunately it also helps to stabilize the <110> dislocations against decomposition, thus suppressing <100> dislocation sources in the intermediate-temperature range. The real breakthrough in lowering the DBTT of <001> D176 crystals (to as low as ~ 650 K) would occur if one was able to get <100> dislocation sources to operate in region II.

According to Fig. 78, pre-strain is not effective in lowering the DBTT for <110> D176 crystals. In this case, pre-strain at 1366 K (2000 °F) also introduces <100> dislocations into the crystal. But deformation in this orientation already occurs by <100> dislocations and the <100> dislocations introduced by pre-strain at high temperature do not account for any additional deformation mechanisms. The only way to decrease the DBTT in <110> D176 crystals is to activate climb of <100> dislocations at lower temperatures, which pre-straining cannot affect.

The important question as to why climb of <100> dislocations in alloy D176 occurs at lower temperatures in <001> crystals than the <110> crystals still needs to be addressed. The answer to this question would also explain the reason for the lower DBTT for <001> D176 (1100 K) compared to <110> D176 (1250 K). The most likely explanation has to do with the assisting deformation processes in these two orientations of crystals. In <001> oriented crystals, deformation above the DBTT occurs by <110> slip at the same time climb of <001> dislocations is also occurring. The <110> dislocations in NiAl have extremely complicated core structures composed of atomic scale decompositions particularly along edge orientations [43, 52]. The fact that the edge orientations in particular can decompose and become sessile implies that simple glide of these dislocations is not possible. The movement of <110> dislocations is probably quite complicated involving glide of screw and mixed components with some type of superkink mechanism contributing to the non-conservative movement of near-edge components [43]. In fact a number of scenarios can be imagined where large concentrations of point defects would result by the "glide" of <110> dislocations. For example, cross-slip of <110> dislocations is readily observed in <001> D176 crystals and the screw dislocations leave behind jogs that can only move by leaving behind trails of vacancies or interstitial atoms [28]. Even the <110> edge dislocations will have to move by some type of non-conservative jog motion since the dislocation core decomposition occurs out of the glide plane [43]. Therefore, deformation by <110> dislocations in <001> oriented crystals is expected to provide a large non-equilibrium concentration of point defects, which can act as "fuel" for the climb of <100> dislocations throughout region II, even though this temperature is below that at which climb would normally occur for <100> dislocations due only to the normal thermal equilibrium concentration of point defects. Therefore, deformation by <110> and <100> dislocations in <001> D176 crystals could be imagined to occur in a synergistic fashion with deformation by <110> dislocations fueling the climb of <100> dislocations at temperatures as low as 650 K as must happen in pre-strained <001> alloy D176

deformed in region II. Climb of <100> dislocations is not significant until approximately 1250 K in <011> alloy D176 no matter what prior pre-strain is used since pre-straining does not influence the concentration of point defects and climb only occurs once the temperature is high enough to allow the given concentration of point defects to diffuse readily to the edge dislocations.

Therefore, in terms of the DBTT, the limiting step for achieving ductility in <001> oriented crystals is the nucleation of <100> dislocations and not their propagation. Once the <100> dislocations are introduced into the <001> crystal, climb can occur due to the synergistic glide of <110> dislocations as described above and would explain the lower DBTT for <001> alloy D176 compared to the <011> alloy. The only reason that the DBTT does not occur below 1100 K in <001> D176 is that an active source for <100>'s is absent. Therefore, the DBTT in <001> crystals, whether binary NiAl or D176, corresponds to that temperature at which <110> dislocations first become unstable against decomposition providing a ready source of <100> dislocations. In <011> oriented binary NiAl or alloy D176, deformation occurs by the glide of <100> dislocations and, therefore, <100> dislocations are already present in the crystals. Consequently, the DBTT corresponds to that temperature for which <100> dislocations can climb at a rate fast enough to contribute to the deformation of the crystal, in other words the DBTT is limited by the rate of <100> climb.

Several major conclusions can be drawn from this work. The Hf-alloying addition to NiAl single crystals is responsible for limiting the nucleation of <100> dislocations (in <001> oriented crystals) and limiting the propagation of <001> dislocations by non-conservative mechanisms such as dislocation climb (in <011> oriented crystals) at intermediate temperatures. The Hf-addition stabilizes the <110> dislocations against decomposition, thus suppressing the nucleation of <100> dislocations which could have otherwise climbed and contributed to ductility at intermediate temperatures (650-1100 K) in <001> alloy D176. The decomposition of <110> dislocations into <100> dislocations occurs at much higher temperatures in <001> alloy D176 as compared to the binary <001> NiAl, and thus, the additional contribution to deformation by climb of <100> dislocations and the onset of ductility occurs at the correspondingly higher temperature in alloy D176 than in binary NiAl. In <110> alloy D176, although <100> dislocations are available, the Hf-addition makes their climb more difficult as compared to that in the binary <110> NiAl, again shifting DBTT to higher temperature.

IV. Conclusions

The objective of this study was to determine the mechanisms for ductility improvements in NiAl resulting from low level alloying additions and low temperature heat treatments. Even though the exact mechanism(s) for these improvements was not clearly established, many findings of scientific and technological significance were made. The major findings and conclusions from this study are as follows:

1) Surface preparation of machined tensile specimens played the most critical role in affecting the measured ductility. Room temperature tensile plastic elongations varied from about zero percent (for as-ground specimens) to about 8% (for electropolished specimens when the grinding marks are completely removed) for Fe-containing NiAl specimens with various post grinding operations/surface finishes keeping all the other variables the same. Since higher elongation values were generally obtained from specimens with either a high temperature pre-strain or a 800°C heat treatment, it is likely that these treatments make test specimens less susceptible to surface condition effects.

2) Tensile test results indicated that, besides the higher room temperature ductility for the Fe-containing NiAl and the specimens given the 800°C heat treatment, the ductile to brittle transition temperature (DBTT) was also reduced A lowering of flow stress was observed in the high purity NiAl, the Fe-containing NiAl as well as in the NiAl given the 800°C heat treatment. These materials also showed distinct yield drops at all test temperatures.

3) Serrated yielding effects as a function of temperature, strain rate, and alloy/heat treatment were observed. These effects were related to impurity/dislocation interactions. A major difference in the behavior of the microalloyed and 800°C heat treated specimens, as compared to the standard heat treated NiAl specimens, was the decrease or elimination of the serrated yielding effects. Serrated yielding was also completely absent in the high purity NiAl at all test temperatures. In studying serrated yielding phenomena, it is important to clearly understand and eliminate test set up/instrumentation noise to obtain accurate and precise dynamic strain aging information.

4) The majority of the specimens with high room temperature elongations were analyzed to have low carbon. It appears that carbon affects ductility in NiAl. However, additional study with a systematic variation in carbon and other interstitial impurities is required to fully establish the carbon effect.

5) The high purity NiAl specimens did not exhibit any improvement in room temperature ductility and toughness. The propensity for cross-slip and the basic deformation processes in conventional purity and high purity NiAl are identical. Therefore, the lack of improvement in ductility can be rationalized, but the lack of improvement in fracture toughness is difficult to explain. The high purity NiAl showed an absence of strain aging as well as having much lower yield strength compared to the conventional purity NiAl.

6) The temperature dependence of the critical resolved shear stresses (CRSS) for the {100} and {110} slip planes does not appear to be significantly affected by low temperature heat treatments or Fe addition, other than an overall decrease in strength compared to the standard heat treated binary material. The CRSS data and the dislocation structures for all of the alloys/heat treatments studied indicate that the {100} and {110} slip planes are about equally active in NiAl within the temperature range from –196 to 200°C. It is also significant to point out that the deformation processes in the high purity NiAl are identical to observations on the conventional purity NiAl. It appears that the higher purity of the NiAl alloy had no observable impact on the deformation behavior of the material. Clearly, slip in NiAl is not well understood, and additional research in this area is required.

7) TEM analysis of dislocation structures in the specimens deformed as a function of alloy, heat treatment, orientation, and testing temperature showed differences in dislocation structure as a function of orientation and temperature, which could be related to the stress-strain behavior of the specimens. No effect of alloy/heat treatment was observed, with the exception of the presence of faceted loops in the 800°C heat treated material. These facets may be arising from thermal vacancy condensation. This reduction in the vacancy concentration may be responsible for the reduction in yield stress and increase in tensile ductility in these specimens. Previous work on NiAl alloys has indicated that high concentrations of thermal vacancies can be present in NiAl. Results from vacancy concentration experiments performed in this study were consistent with this finding. Resistivity measurements indicated that the stoichiometric alloy which received the 800°C heat treatment had a significantly lower total point defect concentration, consistent with a decrease in vacancy concentration. The vacancy concentration measurements made on NiAl specimens of the stoichiometric composition versus the Fe-containing NiAl specimens suggested an effect of Fe addition on vacancy concentration. However, additional experiments are needed to formulate a credible hypothesis based on this mechanism.

8) Attempts to study point defects/dislocation interaction by the ultrasonic technique were not highly successful because the technique and instrumentation require further extensive development. Preliminary measurements indicated that internal friction studies may be an useful technique.

9) Improvements in ductility and fracture toughness were observed by elevated temperature pre-straining. However, the pre-straining effect was strongly composition, orientation and temperature dependent. In binary NiAl, pre-straining improves ductility only in the <110> orientation whereas the fracture toughness is enhanced only in the <100> orientation. In the Hf-containing NiAl, pre-straining improves ductility only in the <100> orientation whereas the fracture toughness is enhanced both in the <100> and <110> orientations. Some of this behavior can be explained on the basis of the deformation behavior of the alloys. However, much additional understanding is warranted to fully explain all the observations.

10) The Hf-alloying addition to NiAl single crystals is responsible for limiting the nucleation of <100> dislocations (in <001> oriented crystals) and limiting the propagation of <001> dislocations by non-conservative mechanisms such as dislocation climb (in <011> oriented

crystals) at intermediate temperatures. The Hf-addition stabilizes the <110> dislocations against decomposition, thus suppressing the nucleation of <100> dislocations which could have otherwise climbed and contributed to ductility at intermediate temperatures in <001> alloy D176. The decomposition of <110> dislocations into <100> dislocations occurs at much higher temperatures in <001> alloy D176 as compared to the binary <001> NiAl, and thus, the additional contribution to deformation by climb of <100> dislocations and the onset of ductility occurs at the correspondingly higher temperature in alloy D176 than in binary NiAl. In <110> alloy D176, although <100> dislocations are available, the Hf-addition makes their climb more difficult as compared to that in the binary <110> NiAl, again shifting DBTT to higher temperature.

V. References

1. D. F. Lahrman, R. D. Field and R. Darolia, High Temperature Ordered Intermetallic Alloys IV, ed. L. Johnson, J. O. Stiegler and D. P. Pope, Materials Research Society Symposium Proceedings **213**, 603 (1991).
2. R. T. Pascoe and C. W. A. Newey, Met. Sci. J. **2**, 138 (1968).
3. R. Darolia, D. Lahrman and R. Field, Scripta Metall. Mater. **26**, 1007 (1992).
4. W. Wang, R. A. Dodd and P. R. Strutt, Met. Trans. **3**, 2049 (1972).
5. J. E. Hack, J. M. Brzeski and R. Darolia, Scripta Metall. Mater., 27, 1259 (1992).
6. J. E. Hack, J. M. Brzeski, R. Darolia and R. D. Field, High-Temperature Ordered Intermetallic Alloys V, ed. I. Baker, R. Darolia, J. D. Whittenberger and M. H. Yoo, Materials Research Society Symposium Proceedings, **288**, 423 (1993).
7. J. M. Brzeski, J. E. Hack, R. Darolia and R. D. Field, Mater. Sci. Eng. **A170**, 11 (1993).
8. R. W. Margevicius, J. J. Lewandowski and I. Locci, Scripta Metall. Mater. **26**, 1733 (1992).
9. W. S. Walston, R. D. Field, J. R. Dobbs, D. F. Lahrman and R. Darolia, Structural Intermetallics, ed. R. Darolia, J. J. Lewandowski, C. T. Liu, P. L. Martin, D. B. Miracle and M. V. Nathal, The Minerals, Metals & Materials Society, 523 (1993).
10. R. Darolia, Structural Intermetallics, ed. R. Darolia, J. J. Lewandowski, C. T. Liu, P. L. Martin, D. B. Miracle and M. V. Nathal, The Minerals, Metals & Materials Society, 495 (1993).
11. R. D. Noebe, R. R. Bowman and M. V. Nathal, Inter. Mater. Rev. **38**, 193 (1993).
12. R. D. Noebe, NASA TM-106534, (1994).
13. D. P. Mason, D. C. Van Aken, R. D. Noebe, I. E. Locci and K. L. King, High Temperature Ordered Intermetallic Alloys IV, ed. L. Johnson, J. O. Stiegler and D. P. Pope, Materials Research Society Symposium Proceedings, **213**, 1033 (1991).
14. R. R. Bowman, R. D. Noebe, S. V. Raj and I. E. Locci, Metall. Trans. A, **23A**, 1493 (1992).
15. R. D. Noebe: Unpublished Research, NASA LeRC, Cleveland, OH.(1989).
16. M. L. Weaver, M. J. Kaufman, and R. D. Noebe, Scripta Metall. Mater. **29**, 1113 (1993).
17. E. H. Goldman, High-Temperature Ordered Intermetallic Alloys V, ed. I. Baker, R. Darolia, J. D. Whittenberger and M. H. Yoo, Materials Research Society Symposium Proceedings, **288**, 83 (1993).
18. D. R. Johnson, S. M. Joslin, B. F. Oliver, R. D. Noebe and J. D. Whittenberger, First International Conference on Processing Materials for Properties, ed. H. Henein and T. Oki , The Minerals, Metals & Materials Society, 865 (1993).
19. N. Rusovic and E.-Th. Henig, Phys. Stat. Sol. A **57**, 529 (1980).
20. M. A. Crimp and K. Vedula, Phil. Mag. A **63**, 559 (1991).
21. R. D. Field, D. F. Lahrman and R. Darolia, High Temperature Ordered Intermetallic Alloys IV, ed.L. Johnson, J. O. Stiegler and D. P. Pope, Materials Research Society Symposium Proceedings, **213**, 255 (1991).
22. R. J. Wasilewski, S. R. Butler and J. E. Hanlon, Trans. AIME **239**, 1357 (1967).
23. M. H. Loretto and R. J. Wasilewski, Phil. Mag. **23**, 1311 (1971).
24. R. T. Pascoe and C. W. A. Newey, Phys. Stat. Sol. **29**, 357 (1968).
25. R. D. Field, D. F. Lahrman and R. Darolia, Acta Met. 39, #12, 2951 (1991).
26. R. D. Field, D. F. Lahrman and R. Darolia, Acta Met. 39, #12, 2961 (1991).

27. C. H. Lloyd and M. H. Loretto, Phys. Stat. Sol. **39**, 163 (1970).
28. J. P. Hirth and J. Lothe, Theory of Dislocations, McGraw-Hill (1968).
29. R. E. Reed-Hill, Physical Metallurgy Principles, 2nd Edition., D. Van Nostrand Co. (1973).
30. Kitano and Pollock, in Structural Intermetallics, ed. R. Darolia, J. J. Lewandowski, C. T. Liu, P. L. Martin, D. B. Miracle and M. V. Nathal, The Minerals, Metals & Materials Society, 591 (1993).
31. J. M. Brzeski, J. E. Hack and R. Darolia , High-Temperature Ordered Intermetallic Alloys VI, ed. J. A. Horton, I. Baker, S. Hanada, R. D. Noebe, and D. S. Schwartz, Materials Research Society Symposium Proceedings, **364**, 419 (1995).
32. R. D. Noebe and R. Gibala, High Temperature Ordered Intermetallic Alloys I, , ed. C. C. Koch, C. T. Liu and N. S. Stoloff, Materials Research Society Symposium Proceedings, **39**, 319 (1985).
33. K-M. Chang, R. Darolia and H. A. Lipsitt, Acta Met. **40**, 2727 (1992).
34. R. Darolia, K-M. Chang and J. E. Hack, Intermetallics, **1**, 65 (1993).
35. P. Nagpal and I. Baker, J. Mater. Sci. Lett., **11**, 1209 (1992).
36. J.T. Kim, R.D. Noebe, and R. Gibala, Intermetallic Compounds-Structure and Mechanical Properties-(JIMIS-6), ed. O. Izumi, The Japan Institute of Metals, 591 (1991).
37. W. S. Walston and R. Darolia, Intermetallic HPT Technology Development, Phase II Report, WL-TR-93-2123, Contract F33615-90-2006, 45 (1994).
38. H. Vehoff Ordered Intermetallics-Physical Metallurgy and Mechanical Behavior, ed. C. T. Liu, R. W. Cahn and G. Sauthoff, NATO ASI Series E, Applied Sciences, **213**, 299 (1992).
39. J.-T. Kim, Ph.D. Thesis, The University of Michigan, Ann Arbor, MI, 1990.
40. P. Veyssiere and R. D. Noebe, Phil. Mag. A **65**, 1 (1992).
41. T. H. Alden, AIME Trans. **230**, 649 (1964).
42. K. R. Forbes, U. Glatzel and W. D. Nix, High Temperature Ordered Intermetallic Alloys V, ed. I. Baker, R. Darolia, J. D. Whittenberger and M. H. Yoo, Materials Research Society Symposium Proceedings, **288**, 45 (1993).
43. M. J. Mills, M. S. Daw, J. E. Angelo and D. B. Miracle, High-Temperature Ordered Intermetallic Alloys VI, ed. J. A. Horton, I. Baker, S. Hanada, R. D. Noebe, and D. S. Schwartz, Materials Research Society Symposium Proceedings, **364**, 401 (1995).
44. A. S. Tetelman, Acta Met. **10**, 813 (1962).
45. U. Glatzel. K. R. Forbes and W. D. Nix, Phil. Mag. A **67**, 307 (1993).
46. J.-T. Kim and R. Gibala, High Temperature Ordered Intermetallic Alloys IV, ed. L. Johnson, J. O. Stiegler and D. P. Pope, Materials Research Society Symposium Proceedings, **213**, 261 (1991).
47. R. R. Bowman, R. D. Noebe and R. Darolia, HITEMP Review 1989, NASA CP-10039, 47-1 (1989).
48. T. Takasugi, J. Kishino, and S. Hanada, Acta Met. **41**, 1009 (1993).
49. J. D. Cotton, M. J. Kaufman and R. D. Noebe, Scripta Metall. Mater. **25**, 2395 (1991).
50. G .W. Groves and A. Kelly, Phil. Mag. **8**, 877 (1963).
51. G. W. Groves and A. Kelly, Phil. Mag. **19**, 977 (1969).
52. M. J. Mills, J. E. Angelo, M. S. Daw, J. D. Weinberg and D. B. Miracle, accepted for publication, Mater. Sci. Eng. **A** (1995).

VI. Publications

Publications from Work Sponsored by This Program

1. R. D. Field, D. F. Lahrman, and R. Darolia, "Room Temperature Deformation in "Soft" Orientation NiAl Single Crystals", High Temperature Ordered Intermetallic Alloys IV, ed. L. Johnson, J. O. Stiegler and D. P. Pope, Materials Research Society Symposium Proceedings **213**, 255 (1991).

2. R. D. Field, D. F. Lahrman, and R. Darolia, "Slip Systems in <001> Oriented NiAl Single Crystals", Acta. Met., **39**, #12, 2951, (1991).

3. R. D. Field, D. F. Lahrman, and R. Darolia, "The Effect of Alloying on Slip Systems in <001> Oriented NiAl Single Crystals", Acta. Met. **39**, #12, 2961, (1991).

4. R. Darolia, D. F. Lahrman, R. D. Field, J. R. Dobbs, K. M. Chang, E. Goldman, and D. Konitzer, "Deformation and Fracture of NiAl Alloys for High-Temperature Structural Applications", Ordered Intermetallics-Physical Metallurgy and Mechanical Behavior, ed. C. T. Liu, R. W. Cahn and G. Sauthoff, NATO ASI Series E, Applied Sciences, **213**, 679 (1992).

5. R. Darolia, D. F. Lahrman and R. D. Field, " The Effect of Iron, Gallium and Molybdenum on the Room Temperature Ductility of NiAl", Scripta Metall. Mater., **26**, #7, 1007 (1992).

6. J. E. Hack, J. M. Brzeski and R. Darolia, "Evidence of Inherent Ductility in Single Crystals of the Ordered Intermetallic Compound NiAl", Scripta Metall. Mater., **27**, 1259 (1992).

7. R.D. Field, D.F. Lahrman and R. Darolia, "A Mechanistic Study of the Microalloying Effect in NiAl Base Alloys", High-Temperature Ordered Intermetallic Alloys V, ed. I. Baker, R. Darolia, J. D. Whittenberger and M. H. Yoo, Materials Research Society Symposium Proceedings, **288**, 423 (1993).

8. J. E. Hack, J. M. Brzeski, R. Darolia and R. D. Field, "Evidence of Inherent Ductility in Single Crystal NiAl", High-Temperature Ordered Intermetallic Alloys V, High-Temperature Ordered Intermetallic Alloys V, ed. I. Baker, R. Darolia, J. D. Whittenberger and M. H. Yoo, Materials Research Society Symposium Proceedings, **288**, 1197 (1993).

9. D. F. Lahrman, R. D. Field and R. Darolia, "The effect of Crystallographic Orientation on the Mechanical Properties of a Single Crystal NiAl+Fe Alloy", High Temperature Ordered Intermetallic Alloys V, ed. I. Baker, R. Darolia, J. D. Whittenberger and M. H. Yoo, Materials Research Society Symposium Proceedings, **288**, 680 (1993).

10. R. Darolia, "NiAl for Turbine Airfoil Applications", Structural Intermetallics, ed. R. Darolia, J. J. Lewandowski, C. T. Liu, P. L. Martin, D. B. Miracle and M. V. Nathal, The Minerals, Metals & Materials Society, 495 (1993).

11. J. M. Brzeski, J. E. Hack, R. Darolia and R. D. Field, "Strain Aging Embrittlement of the Ordered Intermetallic Compound NiAl", Materials Science and Engineering, **A170**, 11 (1993).

12. M. A. Morris, J. F. Perez and R. Darolia, "Dislocation Mobility in <100> Oriented NiAl Single Crystals Containing Iron and Hafnium Additions", Phil. Mag., **69**, 485 (1993).

13. M. A. Morris, J. F. Perez and R. Darolia, "High Temperature Dislocation Configurations and Their Effect on Ductilization of NiAl Single Crystals", Phil. Mag., **69**, 507 (1993).

14. M. A. Morris, J. F. Perez and R. Darolia, "Influence of Dislocation Mobility on Room Temperature Ductility of <100> Oriented NiAl Single Crystals", High-Temperature Ordered Intermetallic Alloys VI, ed. J. A. Horton, I. Baker, S. Hanada, R. D. Noebe and D. S. Schwartz, Materials Research Society Symposium Proceedings, **364**, 413 (1995).

15. Y. Q. Sun, G. Taylor, R. Darolia and P. M. Hazzledine, "<111> Slip in NiAl Single Crystals Between 4.2K and 100K", High-Temperature Ordered Intermetallic Alloys VI, ed. J. A. Horton, I. Baker, S. Hanada, R. D. Noebe and D. S. Schwartz, Materials Research Society Symposium Proceedings, **364**, 261 (1995).

16. J. M. Brzeski, J. E. Hack and R. Darolia "Serrated Yield Behavior in NiAl Single Crystal", High-Temperature Ordered Intermetallic Alloys VI, ed. J. A. Horton, I. Baker, S. Hanada, R. D. Noebe and D. S. Schwartz, Materials Research Society Symposium Proceedings, **364**, 419 (1995).

VII. Acknowledgments

Financial support of the Air Force Office of Scientific Research to carry out this study is greatly acknowledged. Drs. Alan Rosenstein and Chuck Ward acted as the Program Monitors for this program. Several collaborative projects were carried out under the auspices of this program where there was no transfer of funds, except specimens produced under the contract were supplied to the investigators. Prof. Ben Oliver of the University of Tennessee provided high purity NiAl single crystals. Drs. Ron Noebe and Anita Garg of NASA Lewis Research Center conducted deformation studies of alloy D176 and microstructural analysis on the tested high purity single crystals. Drs. Ron Noebe and Pat Dickerson of NASA Lewis Research Center collaborated on the fractography of the high purity single crystals. Prof. John Hack of Yale University conducted the study of the strain aging effects and the effect of low temperature heat treatments on fracture toughness. Prof. Maria Morris of the University of Neuchâtel carried out TEM studies to understand the deformation behavior in stoichiometric and Fe-containing NiAl. We are grateful for these collaborative projects which led to a better understanding of the deformation behavior in NiAl. We also gratefully acknowledge the support of Dr. Mike Nathal of NASA Lewis Research Center.

Appendix A

Test Data for High Purity NiAl

Westmoreland Mechanical Testing & Research Inc.
Specialists in the Aviation and Nuclear Fields

Old Route 30, Westmoreland Drive
P.O. Box 388, Youngstown, Pa. 15696-0388 U.S.A.
Telephone: 412-537-3131 Fax: 412-537-3151

NADCAP APPROVED 10/93

General Electric Company
Aircraft Engine Business
1 Neumann Way
Box 156301
Cincinnati, OH 45215-6301
ATTN: Mr. Ram Darolia

DATE: 6/23/94

P.O. No.: 200-1Q-14V23807

WMTR REPORT NO.: 4-04708

TENSILE TEST CERTIFICATION

MATERIAL Submitted As	NiAl	NiAl	NiAl	NiAl	NiAl
SPECIMEN NUMBER	OLIVER-1-1	OLIVER-1-2	OLIVER-1-3	OLIVER-2-1	OLIVER-2-2
HEAT NUMBER	----------	----------	----------	----------	----------
HARDNESS					
TEMPERATURE, ° F	Room	Room	Room	Room	Room
SOAK TIME, minutes	----------	----------	----------	----------	----------
ULTIMATE LOAD, lbs.	201	215	232	450	209
.2 YIELD LOAD, lbs.	176	180	158	181	176
TENSILE STRENGTH, psi	28477	29952	33789	63754	30374
.2% YIELD STRENGTH, psi	24935	25076	23011	25643	25578
.02 YLD STRENGTH, psi	17001	24380	16603	22951	24416
ORIG. GAGE LENGTH, in.	.3576	.3578	.3602	.3601	.3571
FINAL GAGE LENGTH, in.	----------	----------	----------	----------	----------
ELONGATION, %*	1.26	1.36	2.38	12.85	1.14
ORIG. DIAMETER, in.	.0948	.0956	.0935	.0948	.0936
ORIGINAL AREA, $in.^2$	.00705840	.00717804	.00686615	.00705840	.00688084
FINAL DIAMETER, in.	----------	----------	----------	----------	----------
REDUCTION IN AREA, %	----------	----------	----------	----------	----------
MACHINE NO.	E4	E4	E4	E4	E4
TEST LOG NO.	041397	041398	041399	041400	041401

KNOWINGLY OR WILLFULLY FALSIFYING OR CONCEALING A MATERIAL FACT ON THIS FORM, OR MAKING FALSE, FICTITIOUS OR FRAUDULENT STATEMENTS OR REPRESENTATIONS HEREIN COULD CONSTITUTE A FELONY PUNISHABLE UNDER FEDERAL STATUTES.

jpg
T-001-03

SPECIFICATION (LABORATORY COMMENTS): All testing done at WMT&R, Inc.
ASTM E8
*Elongations were taken from the load-strain charts.
The extensometer was placed across the grips.

CERTIFIED BY: Gerald W. Boice
R & D Manager

June 23, 1994

Westmoreland Mechanical Testing & Research Inc.
Specialists in the Aviation and Nuclear Fields

Old Route 30, Westmoreland Drive
P.O. Box 388, Youngstown, Pa. 15696-0388 U.S.A.
Telephone: 412-537-3131 Fax: 412-537-3151

NADCAP APPROVED 10/93

General Electric Company
Aircraft Engine Business
1 Neumann Way
Box 156301
Cincinnati, OH 45215-6301
ATTN: Mr. Ram Darolia

DATE: 6/23/94

P.O. No.: 200-1Q-14V23807

WMTR REPORT NO.: 4-04708

TENSILE TEST CERTIFICATION

MATERIAL Submitted As	NiAl				
SPECIMEN NUMBER	OLIVER-2-3				
HEAT NUMBER	----------				
HARDNESS					
TEMPERATURE, ° F	Room				
SOAK TIME, minutes	----------				
ULTIMATE LOAD, lbs.	225				
.2 YIELD LOAD, lbs.	182				
TENSILE STRENGTH, psi	31346				
.2% YIELD STRENGTH, psi	25355				
.02 YLD STRENGTH, psi	24380				
ORIG. GAGE LENGTH, in.	.3576				
FINAL GAGE LENGTH, in.	----------				
ELONGATION, %*	1.37				
ORIG. DIAMETER, in.	.0956				
ORIGINAL AREA, in.^{2}	.00717804				
FINAL DIAMETER, in.	----------				
REDUCTION IN AREA, %	----------				
MACHINE NO.	E4				
TEST LOG NO.	041402				

KNOWINGLY OR WILLFULLY FALSIFYING OR CONCEALING A MATERIAL FACT ON THIS FORM, OR MAKING FALSE, FICTITIOUS OR FRAUDULENT STATEMENTS OR REPRESENTATIONS HEREIN COULD CONSTITUTE A FELONY PUNISHABLE UNDER FEDERAL STATUTES.

jpg
T-001-03

SPECIFICATION (LABORATORY COMMENTS): All testing done at WMT&R, Inc.
ASTM E8
*Elongations were taken from the load-strain charts.
The extensometer was placed across the grips.

CERTIFIED BY: _____ 6/23/94
Gerald W. Boice
R & D Manager
June 23, 1994

Westmoreland Mechanical Testing & Research Inc.
Specialists in the Aviation and Nuclear Fields

P.O. Box 388, Youngstown, Pa. 15696-0388
Telephone: 412-537-3131 Fax: 412-537-3151

NADCAP APPROVED 10/93

General Electric Company
G.E. Aircraft Engines
1 Neumann Way
Box 156301
Cincinnati, OH 45215-6301
ATTN: Mr. Ram Darolia

P.O. No.: 14V23807

WMT&R REPORT No.: 4-06575
DATE: 7/28/94

TENSILE RESULTS
MATERIAL: NiAl

SPECIFICATION: ASTM E8

CONDITION	SPECIMEN NUMBER	TEMP °F	UTS PSI	.2% YS PSI	ELONGATION %	ULT LOAD LBS	.2% YLD LBS	ORIG GAGE IN	ORIG DIA IN	ORIG AREA SQ IN	MACH NO	TEST LOG
*	OLIVER 3-1	Room	40377	26489	4.52	282	185	.3578	.0943	.00698415	E4	055844
*	OLIVER 3-2	Room	31690	30713	.40	227	220	.3578	.0955	.00716303	E4	055845
1475F/24 Hrs.	OLIVER 3-3	Room	23933	14641	7.68	170	104	.3585	.0951	.00710315	E5	055846
1832F/1 Hr.	OLIVER 3-4	Room	20772	20061	.47	146	141	.3557	.0946	.00702865	E5	055847

185

COMMENTS: All testing done at WMT&R, Inc.
* Prestrain 2% plastic at 1000F.
Elongations were taken from the load-strain charts.
The extensometer was placed across the grips.

Gerald W. Boice, R&D Manager

7/28/94
July 28, 1994

mls

WESTMORELAND MECHANICAL TESTING & RESEARCH, Inc.

LOAD vs STRAIN CURVE

Phone 412-537-3131

Customer: General Electric Company
WMT&R Report: 4-04708
Test Date: 05/25/94
P.O. No.: 14V23807

HEAT No.:
SPECIMEN No.: OLIVER-1-1
Temperature: Room
MATERIAL: NiAl

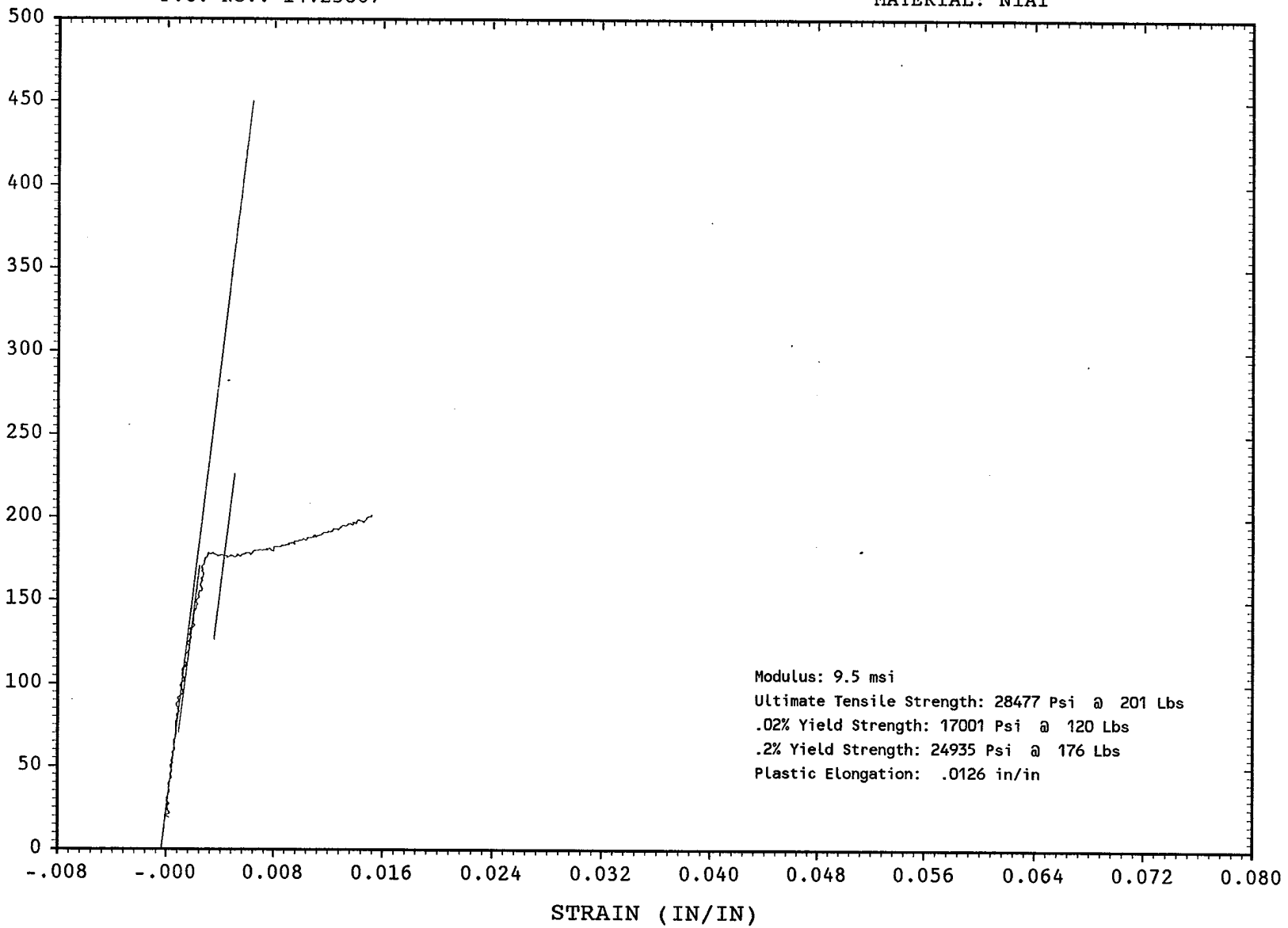

186

041397

KNOWINGLY OR WILLFULLY FALSIFYING OR CONCEALING A MATERIAL FACT ON THIS FORM OR MAKING FALSE, FICTITIOUS OR FRAUDULENT STATEMENTS OR REPRESENTATIONS HEREIN COULD CONSTITUTE A FELONY PUNISHABLE UNDER FEDERAL STATUTES.

WESTMORELAND MECHANICAL TESTING & RESEARCH, Inc.

LOAD vs STRAIN CURVE

Phone 412-537-3131

Customer: General Electric Company
WMT&R Report: 4-04708
Test Date: 05/27/94
P.O. No.: 14V23807

HEAT No.:
SPECIMEN No.: OLIVER-1-2
Temperature: Room
MATERIAL: NiAl

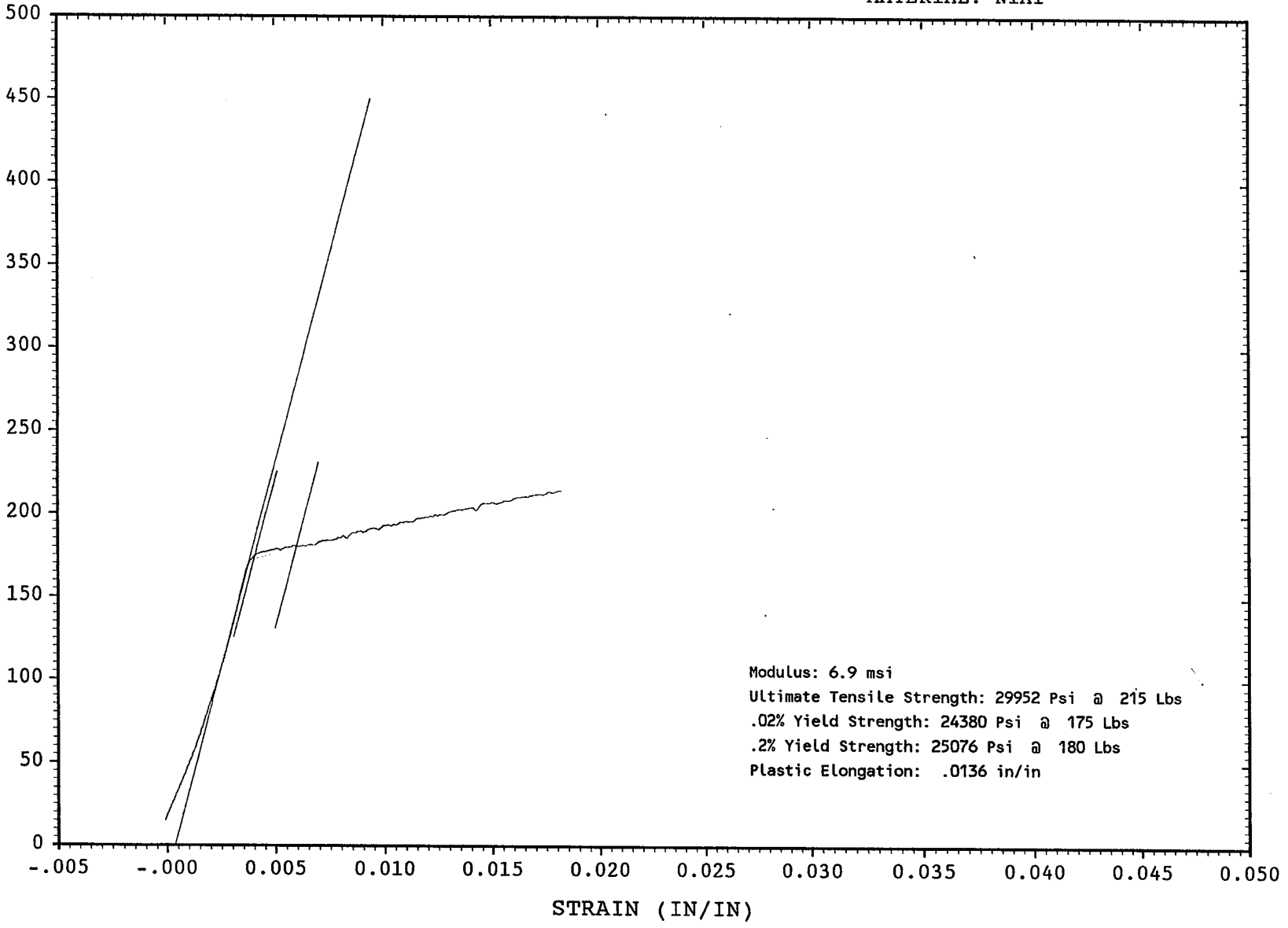

187

041398

KNOWINGLY OR WILLFULLY FALSIFYING OR CONCEALING A MATERIAL FACT ON THIS FORM OR MAKING FALSE, FICTITIOUS OR FRAUDULENT STATEMENTS OR REPRESENTATIONS HEREIN COULD CONSTITUTE A FELONY PUNISHABLE UNDER FEDERAL STATUTES.

WESTMORELAND MECHANICAL TESTING & RESEARCH, Inc.

LOAD vs STRAIN CURVE

Phone 412-537-3131

Customer: General Electric Company
WMT&R Report: 4-04708
Test Date: 06/20/94
P.O. No.: 14V23807

HEAT No.:
SPECIMEN No.: OLIVER-1-3
Temperature:
MATERIAL: NiAl

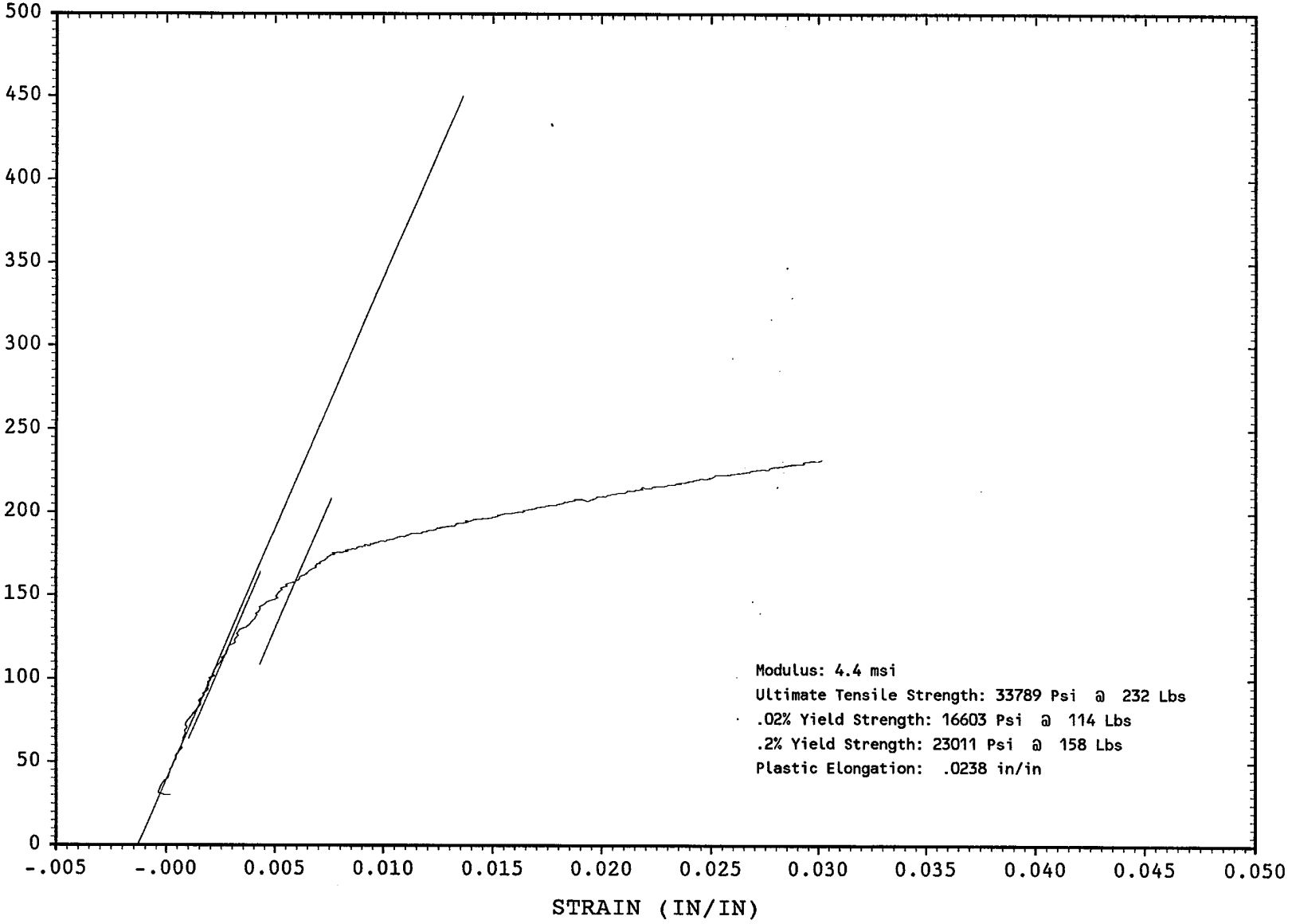

188

041399

KNOWINGLY OR WILLFULLY FALSIFYING OR CONCEALING A MATERIAL FACT ON THIS FORM OR MAKING FALSE, FICTITIOUS OR FRAUDULENT STATEMENTS OR REPRESENTATIONS HEREIN COULD CONSTITUTE A FELONY PUNISHABLE UNDER FEDERAL STATUTES.

WESTMORELAND MECHANICAL TESTING & RESEARCH, Inc.

LOAD vs STRAIN CURVE

Phone 412-537-3131

Customer: General Electric Company
WMT&R Report: 4-04708
Test Date: 05/25/94
P.O. No.: 14V23807

HEAT No.:
SPECIMEN No.: OLIVER-2-1
Temperature: Room
MATERIAL: NiAl

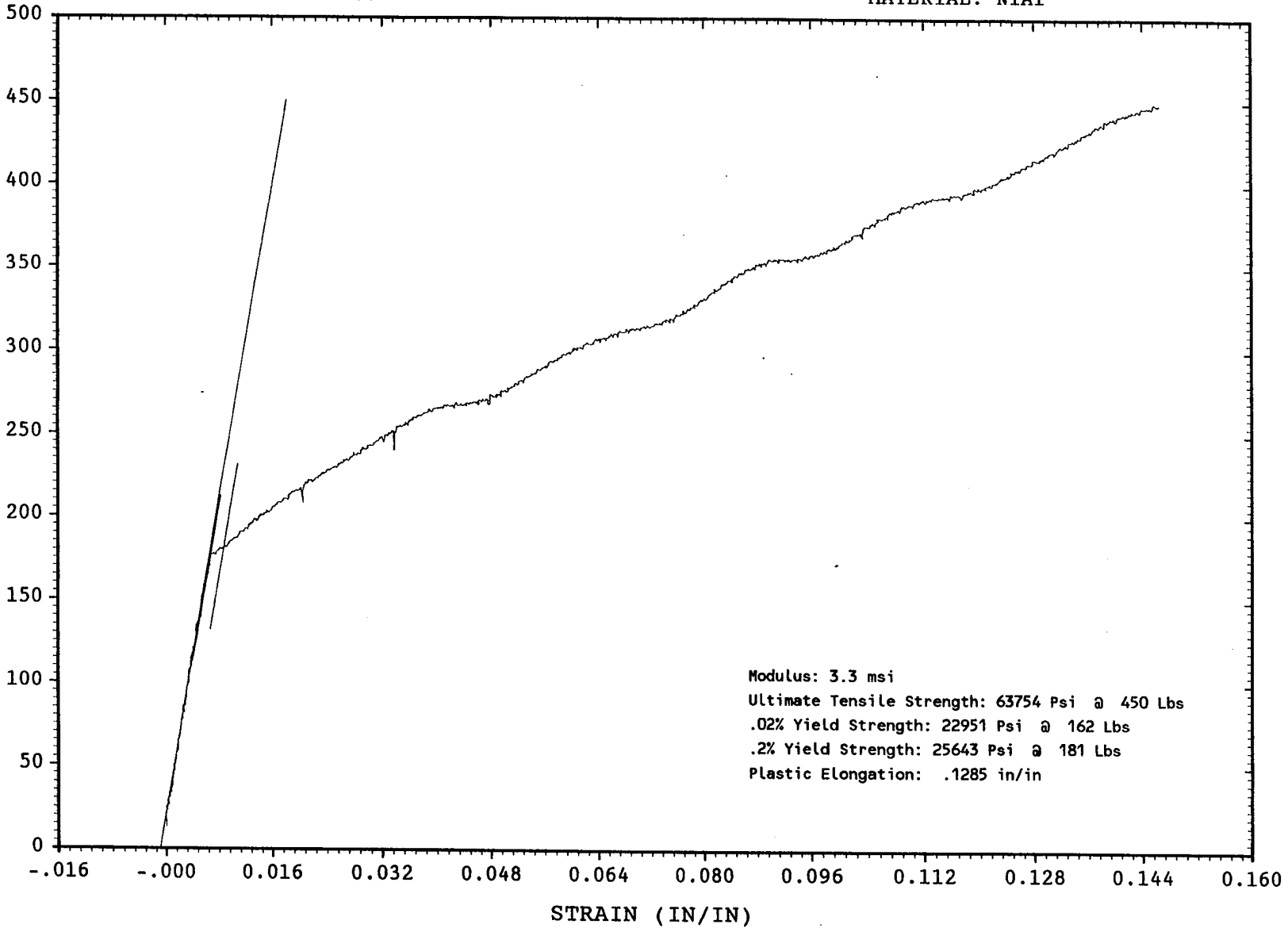

041400

KNOWINGLY OR WILLFULLY FALSIFYING OR CONCEALING A MATERIAL FACT ON THIS FORM OR MAKING FALSE, FICTITIOUS OR FRAUDULENT STATEMENTS OR REPRESENTATIONS HEREIN COULD CONSTITUTE A FELONY PUNISHABLE UNDER FEDERAL STATUTES.

WESTMORELAND MECHANICAL TESTING & RESEARCH, Inc.

LOAD vs STRAIN CURVE

Phone 412-537-3131

Customer: General Electric Company
WMT&R Report: 4-04708
Test Date: 05/27/94
P.O. No.: 14V23807

HEAT No.:
SPECIMEN No.: OLIVER-2-2
Temperature: Room
MATERIAL: NiAl

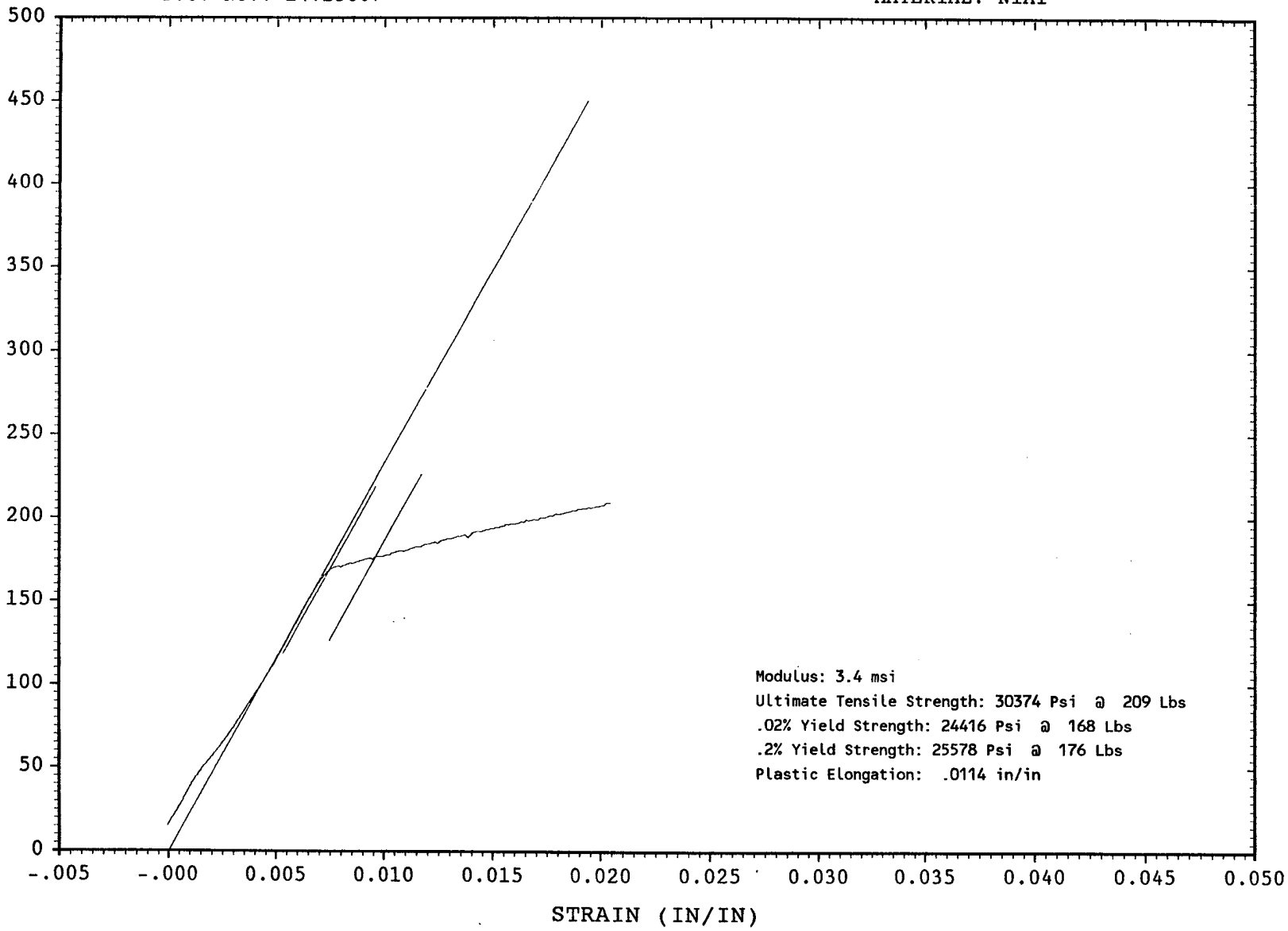

190

041401

KNOWINGLY OR WILLFULLY FALSIFYING OR CONCEALING A MATERIAL FACT ON THIS FORM OR MAKING FALSE, FICTITIOUS OR FRAUDULENT STATEMENTS OR REPRESENTATIONS HEREIN COULD CONSTITUTE A FELONY PUNISHABLE UNDER FEDERAL STATUTES.

WESTMORELAND MECHANICAL TESTING & RESEARCH, Inc.

LOAD vs STRAIN CURVE

Phone 412-537-3131

Customer: General Electric Company
WMT&R Report: 4-04708
Test Date: 06/20/94
P.O. No.: 14V23807

HEAT No.:
SPECIMEN No.: OLIVER-2-3
Temperature:
MATERIAL: NiAl

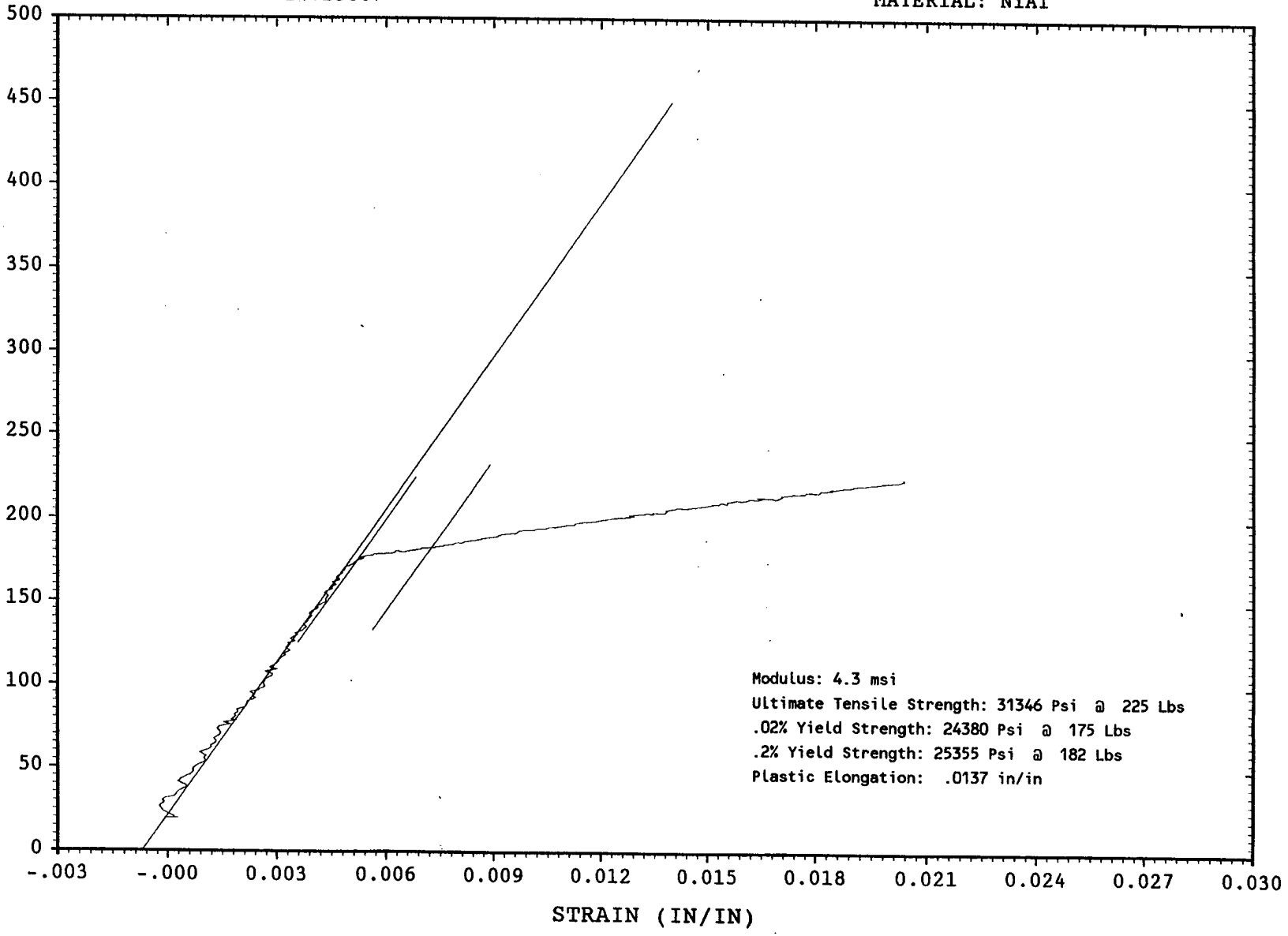

191

041402

KNOWINGLY OR WILLFULLY FALSIFYING OR CONCEALING A MATERIAL FACT ON THIS FORM OR MAKING FALSE, FICTITIOUS OR FRAUDULENT STATEMENTS OR REPRESENTATIONS HEREIN COULD CONSTITUTE A FELONY PUNISHABLE UNDER FEDERAL STATUTES.

WESTMORELAND MECHANICAL TESTING & RESEARCH, Inc.

LOAD vs STRAIN CURVE

Phone 412-537-3131

Customer: General Electric Company
WMT&R Report: 4-06575
Test Date: 07/27/94
P.O. No.: 14V23807

HEAT No.:
SPECIMEN No.: OLIVER 3-1
Temperature: Room
MATERIAL: NiAl

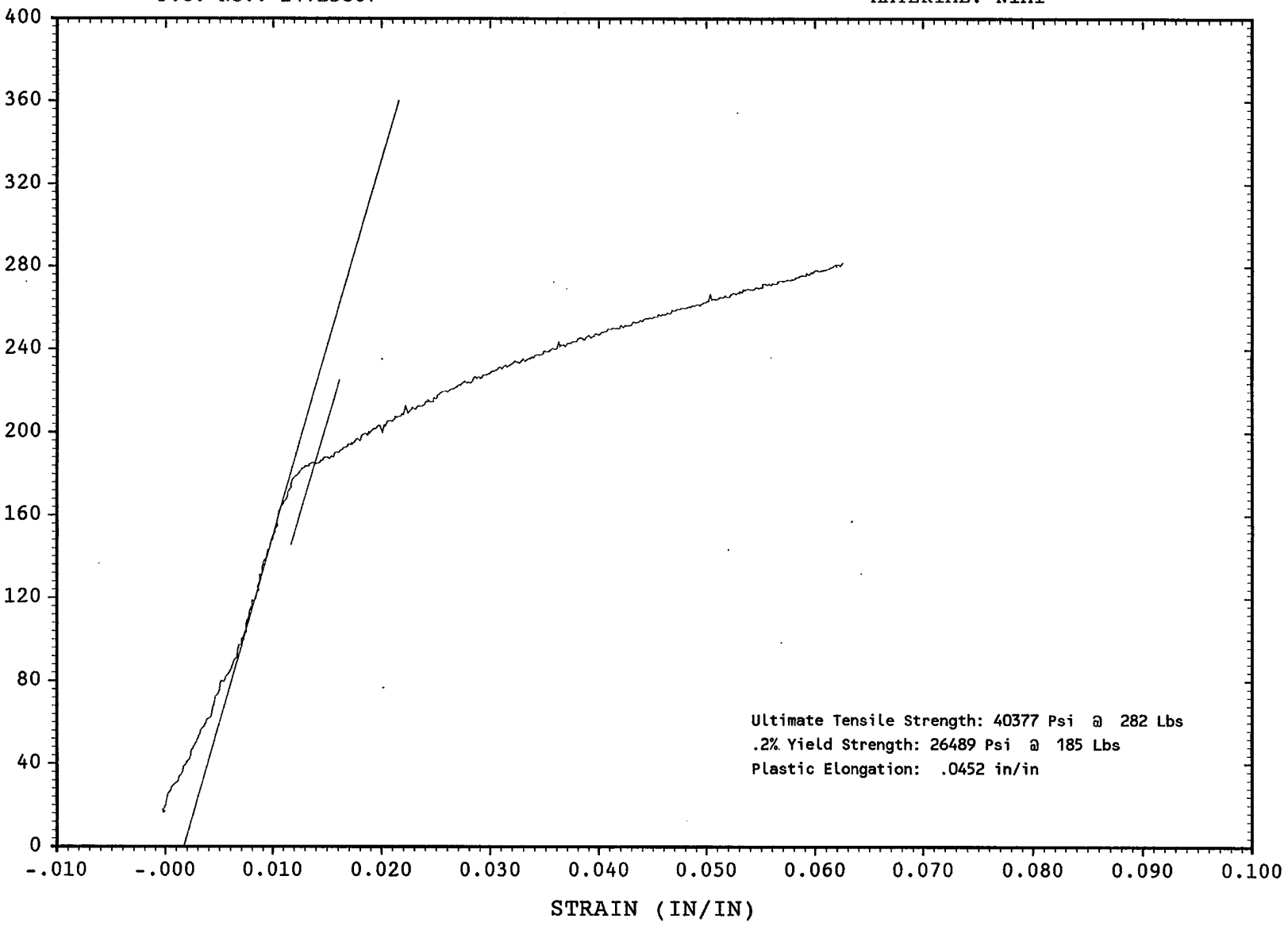

192

2.6

055844

KNOWINGLY OR WILLFULLY FALSIFYING OR CONCEALING A MATERIAL FACT ON THIS FORM OR MAKING FALSE, FICTITIOUS OR FRAUDULENT STATEMENTS OR REPRESENTATIONS HEREIN COULD CONSTITUTE A FELONY PUNISHABLE UNDER FEDERAL STATUTES.

WESTMORELAND MECHANICAL TESTING & RESEARCH, Inc.

LOAD vs STRAIN CURVE

Phone 412-537-3131

Customer: General Electric Company
WMT&R Report: 4-06575
Test Date: 07/27/94
P.O. No.: 14V23807

HEAT No.:
SPECIMEN No.: OLIVER 3-2
Temperature: Room
MATERIAL: NiAl

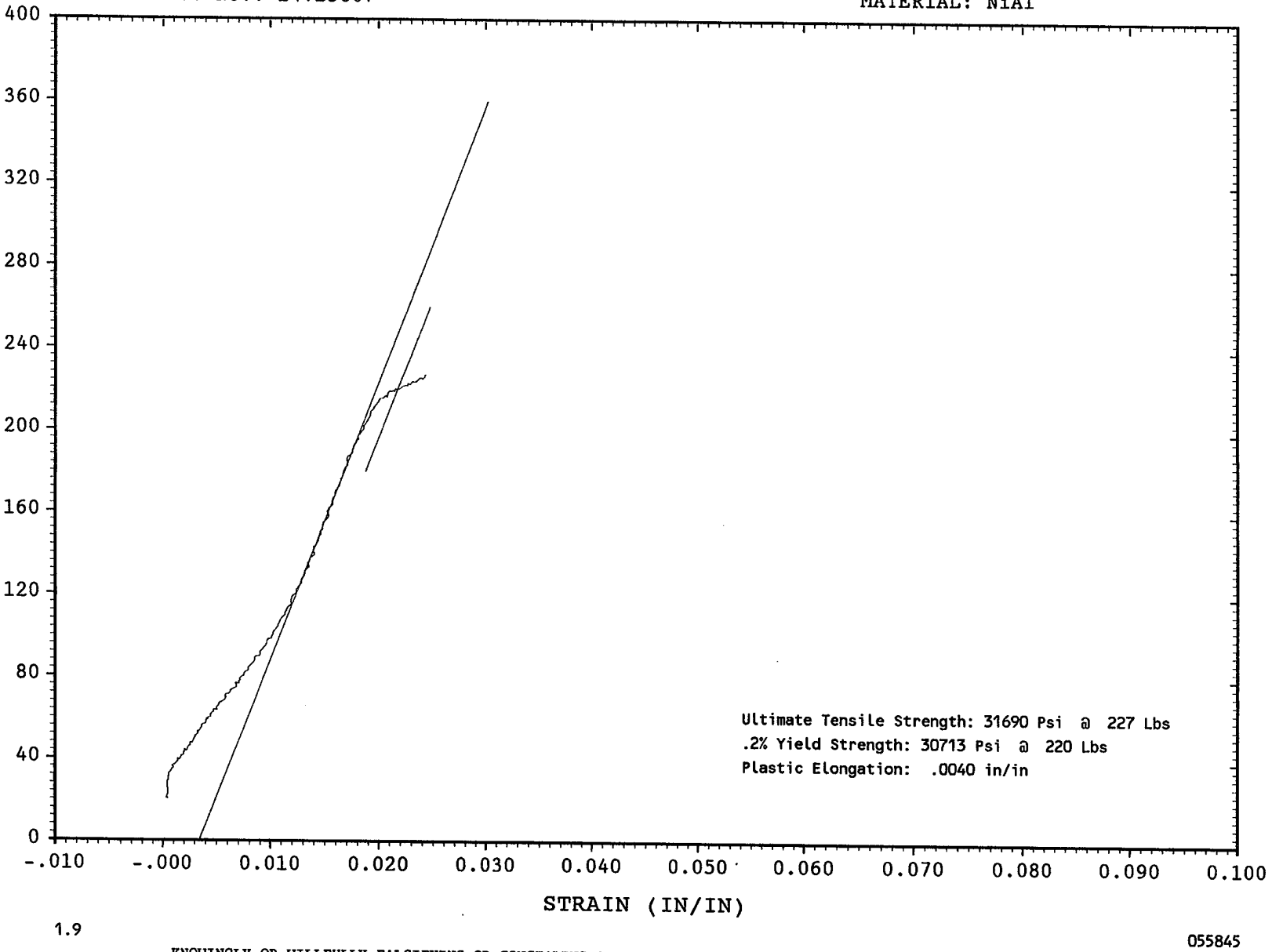

193

1.9

055845

KNOWINGLY OR WILLFULLY FALSIFYING OR CONCEALING A MATERIAL FACT ON THIS FORM OR MAKING FALSE, FICTITIOUS OR FRAUDULENT STATEMENTS OR REPRESENTATIONS HEREIN COULD CONSTITUTE A FELONY PUNISHABLE UNDER FEDERAL STATUTES.

WESTMORELAND MECHANICAL TESTING & RESEARCH, Inc.

LOAD vs STRAIN CURVE

Phone 412-537-3131

Customer: General Electric Company
WMT&R Report: 4-06575
Test Date: 07/26/94
P.O. No.: 14V23807

HEAT No.:
SPECIMEN No.: OLIVER 3-3
Temperature: Room
MATERIAL: NiAl

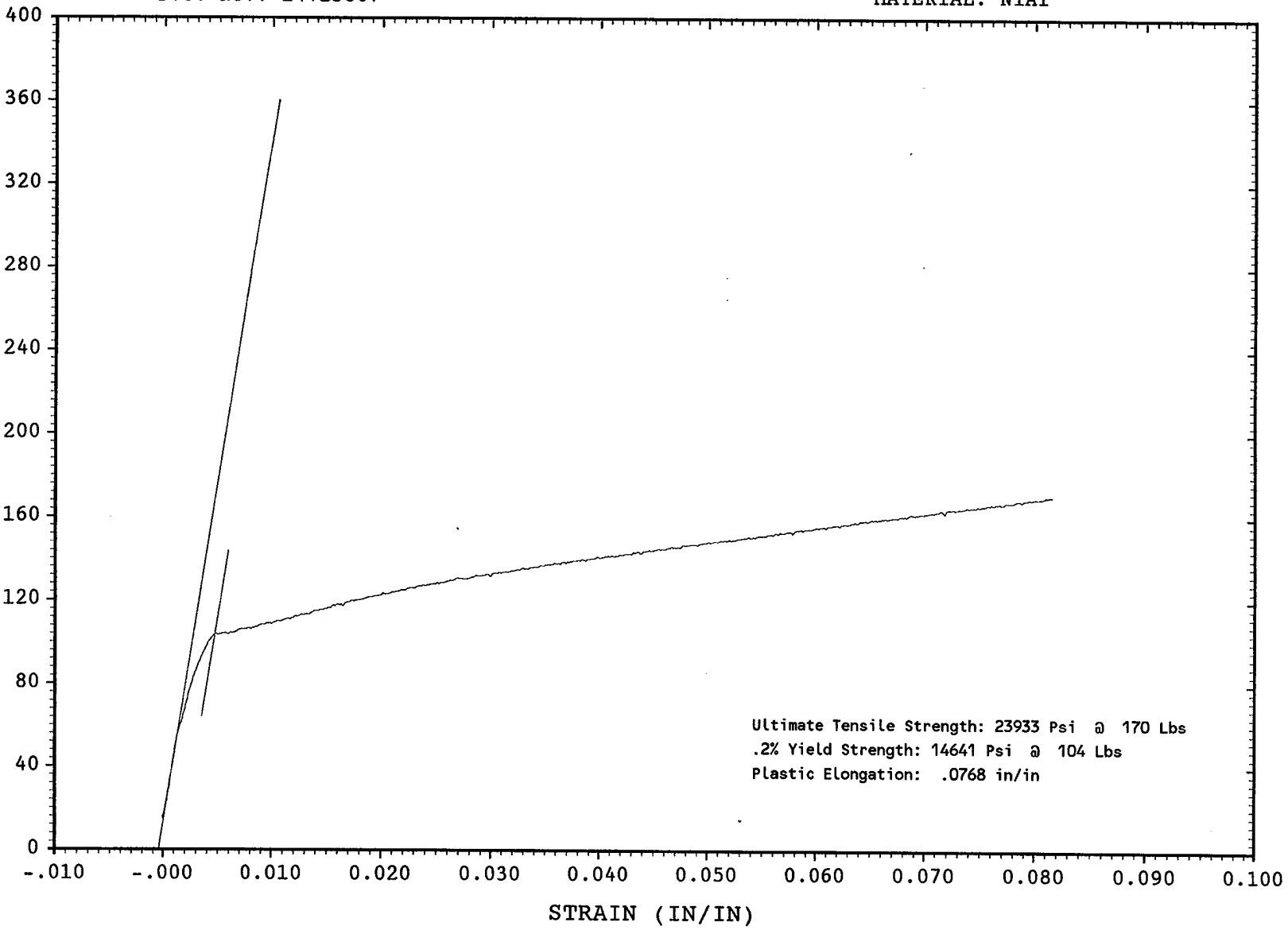

4.6

055846

KNOWINGLY OR WILLFULLY FALSIFYING OR CONCEALING A MATERIAL FACT ON THIS FORM OR MAKING FALSE, FICTITIOUS OR FRAUDULENT STATEMENTS OR REPRESENTATIONS HEREIN COULD CONSTITUTE A FELONY PUNISHABLE UNDER FEDERAL STATUTES.

WESTMORELAND MECHANICAL TESTING & RESEARCH, Inc.

LOAD vs STRAIN CURVE

Phone 412-537-3131

Customer: General Electric Company
WMT&R Report: 4-06575
Test Date: 07/26/94
P.O. No.: 14V23807

HEAT No.:
SPECIMEN No.: OLIVER 3-4
Temperature: Room
MATERIAL: NiAl

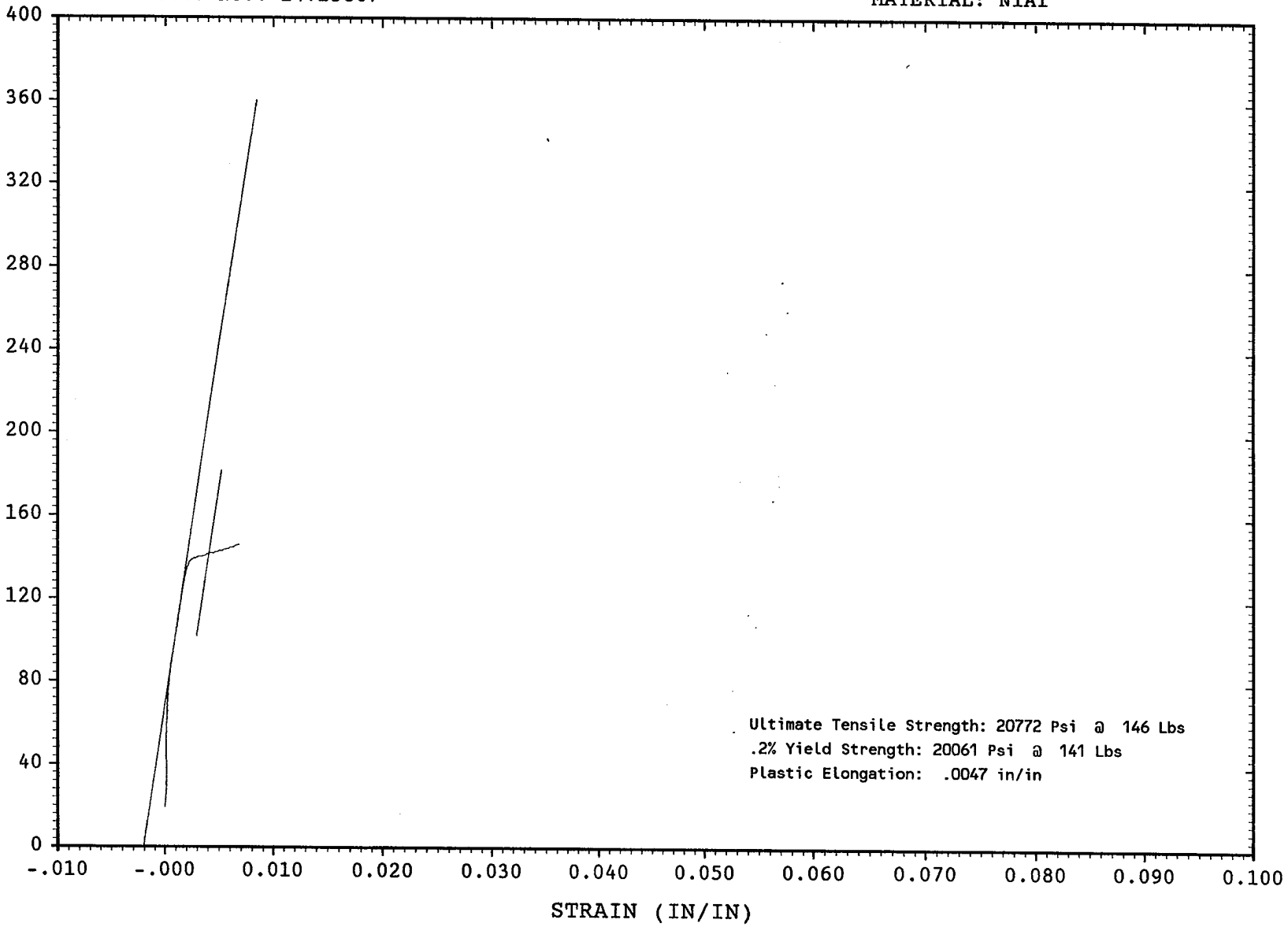

195

4.9

055847

KNOWINGLY OR WILLFULLY FALSIFYING OR CONCEALING A MATERIAL FACT ON THIS FORM OR MAKING FALSE, FICTITIOUS OR FRAUDULENT STATEMENTS OR REPRESENTATIONS HEREIN COULD CONSTITUTE A FELONY PUNISHABLE UNDER FEDERAL STATUTES.